

Madhusudhan Pandey

# Modelling Tool for Hydropower Systems, with Analysis and Design

**Dissertation for the  
degree of Ph.D**  
Process, Energy  
and Automation

Faculty of Technology, Natural  
Sciences and Maritime Studies

---

Madhusudhan Pandey

# Modelling Tool for Hydropower Systems, with Analysis and Design

A PhD dissertation in  
Process, Energy and Automation Engineering

© Madhusudhan Pandey, 2023

Faculty of Technology, Natural Sciences and Maritime Studies  
University of South-Eastern Norway  
Porsgrunn

Doctoral dissertations at the University of South-Eastern Norway no. 173

ISSN: 2535-5244 (print)  
ISSN: 2535-5252 (online)

ISBN: 978-82-7206-801-0 (print)  
ISBN: 978-82-7206-802-7 (online)



This publication is licensed with a Creative Commons license. You may copy and redistribute the material in any medium or format. You must give appropriate credit, provide a link to the license, and indicate if changes were made. Complete license terms at <https://creativecommons.org/licenses/by-nc-sa/4.0/deed.en>

Print: University of South-Eastern Norway

# Preface

This thesis is submitted to the University of South-Eastern Norway (USN) as partial fulfilment of the requirements for the degree of Philosophiae Doctor (PhD) in Process, Energy and Automation Engineering. The research was carried out with Telemark Modelling and Control Center (TMCC), USN.

The project has been under the supervision of Professor Bernt Lie and co-supervised by Associate Professor Roshan Sharma. Assistant Professor Dietmar Winkler provided good guidance and support for Modelica and programming in general.

This thesis is article-based and contains two main parts. The first part provides an introduction to the modelling of hydropower systems, and the main results from the published articles throughout the period of research work. The second part consists of five scientific articles. The work mainly emphasized modelling, design, control, and optimization of hydropower systems.

Porsgrunn, June 6, 2023

Madhusudhan Pandey





# Acknowledgements

I would like to express my sincere gratitude to my main supervisor Professor Bernt Lie. He has been my inspiration for learning, solving problems, and exploring the world around us, throughout my PhD journey. I would also like to add gratitude to my co-supervisor Associate Professor Roshan Sharma for his valuable advice and suggestions, particularly on optimization and control problems that arose during the research work.

My special thanks go to Assistant Professor Dietmar Winkler for his continuous support in sharing knowledge about hydropower systems, modeling tools, and particularly software usage. I would also like to thank Associate Professor Thomas Øyvang for sharing his knowledge regarding the thermal synchronous generator and the experimental procedures carried out for the generator. Further thanks go to Adjunct Associate Professor Kaspar Vereide at NTNU for his support and guidance while doing research work on surge tanks and their general operations.

I would like to thank my fellow PhD students Nima and Ashish for chit-chatting during break time and joining a fresh hike in the mountains on weekends. My gratitude also goes to my friends studying for master's degrees here in Porsgrunn.

I am immensely grateful to my parents Yam Prasad and Durga Devi, my brother Mohan and my sister Drona, and my wife Aleena. They always encouraged me to pursue higher education despite the challenges they faced to pursue their own. My deep love goes to my nephew Girwan and my nieces Aarusi and Toshika. Finally, a huge thanks go to the Modelica and Julia communities. Each and everyone related to the communities are working hard to produce valuable products for mankind.



# Abstract

The increased use of renewable energy sources is due to an increasing global energy need, and to counter the effects of fossil fuels on the environment. Common renewable energy sources such as solar energy and wind energy are intermittent while hydropower is dispatchable. Norwegian water reservoirs provide almost half of Europe's reservoir capacity and thus may play a significant role in balancing the variability caused by intermittent energy sources in the European interconnected grid.

The physics of generations, such as intermittent and dispatchable sources, and electric loads, are studied in the modern electric power grid. To improve the flexibility, reliability, and stability of the electricity grid in the future, we must incorporate innovative technology and market solutions. This necessitates contributions from a variety of disciplines, including physics, engineering, economics, and so on. The demand for and scope of contributions is so vast as a result of globalization that many people must participate. One approach to collaborate is to use open-source code.

In this thesis, the main contributions are developing mechanistic models of surge tanks and draft tubes for hydropower plants. These models are feature extensions of an existing open-source hydropower library — OpenHPL. The use of equation-based language Modelica is emphasized for developing modeling tools, e.g., OpenHPL. The developed models of surge tanks and draft tubes are studied for their flexible operation during electrical load rejections and acceptances in the intermittent power grid. Operational limits based on the design heights and the water mass oscillations are compared for open and closed surge tanks. Two types of draft tubes are studied, viz., conical draft tubes and Moody spreading pipes based on the pressure differences.

In addition, OpenHPL is also augmented with standard active power frequency control. Three types of power grid control are studied, viz., isochronous governor control, droop governor control, and automatic generation control (AGC) for an isolated power system. The use of AGC in a multigeneration system is also studied. Based on the grid frequency step response, two types of controllers, PI controller, and MPC, are investigated for active power frequency regulation.



# Contents

<b>Preface</b>	<b>3</b>
<b>Acknowledgements</b>	<b>5</b>
<b>Abstract</b>	<b>7</b>
<b>Contents</b>	<b>12</b>
List of Figures . . . . .	16
List of Tables . . . . .	17
<b>I Overview</b>	<b>19</b>
<b>1 Introduction</b>	<b>21</b>
1.1 Background . . . . .	21
1.2 Objectives . . . . .	23
1.3 List of Publications . . . . .	23
1.4 Outline . . . . .	24
<b>2 Literature Review</b>	<b>25</b>
2.1 Modeling Tools . . . . .	25
2.1.1 Multiphysics environment . . . . .	25
2.1.2 Hydropower libraries . . . . .	29
2.2 Modeling of Hydropower Units . . . . .	32
2.2.1 Hydropower plant . . . . .	33
2.2.2 Previous work . . . . .	34
2.2.3 Modeling of hydropower units . . . . .	35
2.2.3.1 Reservoir . . . . .	36
2.2.3.2 Intake . . . . .	37
2.2.3.3 Manifold . . . . .	38
2.2.3.4 Surge tank . . . . .	38
2.2.3.5 Penstock . . . . .	39
2.2.3.6 Turbine . . . . .	40
2.2.3.7 Discharge . . . . .	40
2.2.3.8 Tailrace . . . . .	40

## Contents

2.2.3.9	Governor	42
2.2.3.10	Aggregate	44
2.2.4	Modeling of different types of surge tanks	44
2.2.5	Modeling of draft tubes	48
2.3	Active Power Frequency Control	49
2.3.1	Linearized model	50
2.3.1.1	Generator	50
2.3.1.2	Load	50
2.3.1.3	Hydroturbine	50
2.3.1.4	Governor	51
2.3.2	Control of power grid	51
2.3.2.1	Isochronous governor control	53
2.3.2.2	Droop governor control	53
2.3.2.3	Automatic generation control (AGC)	53
2.3.3	MPC for AGC	57
2.3.3.1	MPC	58
2.3.3.2	AGC Prediction Model for MPC	59
2.3.3.3	System	61
2.3.3.4	State estimator	61
2.4	Thermal Model of Synchronous Generator	62
2.4.1	Previous work	63
2.4.2	Working principle of the thermal model	64
2.4.3	Mathematical model	64
2.4.4	State estimation	67
2.4.4.1	Recursive Bayesian filter	69
2.4.4.2	Particle filter	70
2.4.4.3	Resampling algorithms	70
2.4.4.4	Particle filter versus Kalman filter	75
<b>3</b>	<b>Main Results</b>	<b>77</b>
3.1	Surge Tanks	77
3.1.1	Modeling	77
3.1.2	Open surge tanks	79
3.1.2.1	Case study: Trollheim HPP	79
3.1.2.2	Total Load Rejection (TLR) and Water Mass Oscillation	79
3.1.2.3	Effect of the diameter of the orifice and the throat for TLR	82
3.1.2.4	Total Load Acceptance (TLA) and Water Mass Oscillation	83
3.1.2.5	TLR, TLA, and turbine pressure	84
3.1.2.6	Partial Load Rejection (PLR)	87
3.1.2.7	Partial Load Acceptance (PLA)	87
3.1.2.8	PLR, PLA, and turbine pressure	88
3.1.3	Air-cushion surge tank (ACST)	88

3.1.4	Summary . . . . .	94
3.2	Draft Tubes . . . . .	96
3.3	Active Power Frequency Control in OpenHPL . . . . .	97
3.3.1	Test case : Trollheim hydropower plant . . . . .	97
3.3.1.1	Fitting the AGC prediction model . . . . .	97
3.3.1.2	Active power frequency PI control . . . . .	100
3.3.2	Multi-generator system . . . . .	103
3.3.3	Interconnected areas . . . . .	105
3.3.4	MPC for AGC . . . . .	107
3.3.4.1	System . . . . .	107
3.3.4.2	Objective function . . . . .	110
3.3.4.3	State estimation . . . . .	111
3.3.4.4	Solving MPC formulation . . . . .	112
3.3.5	Comparing frequency step response from MPC and PI controller . . . . .	112
3.3.5.1	Integral action . . . . .	113
3.3.6	Using linearized OpenHPL Trollheim HPP model as MPC prediction model . . . . .	114
3.3.7	Output frequency constraint violation . . . . .	116
3.3.8	Computation time . . . . .	116
3.3.9	Summary . . . . .	117
3.4	State Estimation of Thermal Model using Bayesian Inference . . . . .	118
3.4.1	Metal and air temperature estimation . . . . .	118
3.4.2	Estimation with different resampling algorithms . . . . .	121
3.4.3	Estimation using UKF and EnKF . . . . .	122
3.4.4	Estimation innovation and computation time . . . . .	122
3.4.5	Summary . . . . .	122
<b>4</b>	<b>Conclusion and Future Perspectives</b>	<b>125</b>
4.1	Feature Extension of OpenHPL . . . . .	125
4.2	Other Results . . . . .	125
4.3	Future Work . . . . .	126
	<b>Bibliography</b>	<b>128</b>
<b>II</b>	<b>Publications</b>	<b>135</b>
<b>A</b>	<b>Mechanistic Modelling of Surge Tanks and Draft Tubes</b>	<b>137</b>
<b>B</b>	<b>Mechanistic Model of Air Cushion Surge Tank</b>	<b>147</b>
<b>C</b>	<b>Influence of Surge Tanks on Water Hammer</b>	<b>165</b>
<b>D</b>	<b>Bayesian Inference Part I : Parameter Estimation</b>	<b>173</b>



<b>E</b>	<b>Bayesian Inference Part II : State Estimation</b>	<b>183</b>
<b>F</b>	<b>DAEs of Surge Tanks and Draft Tubes</b>	<b>193</b>
F.1	Simple surge tank . . . . .	193
F.2	Sharp orifice type surge tank . . . . .	194
F.3	Throttle valve type surge tank . . . . .	195
F.3.1	For $\ell \leq L_t$ : When the water level is at the throat or below the throat . .	196
F.3.2	For $\ell > L_t$ : When water level inside the surge tank is above the throat .	196
F.3.2.1	For $v \geq 0$ , $\phi_{tv} = \phi_{se}$ . . . . .	196
F.3.2.2	For $v < 0$ , $\phi_{tv} = \phi_{sr}$ . . . . .	197
F.4	Conical diffuser . . . . .	197
F.5	Moody spreading pipes . . . . .	198

# List of Figures

- 2.1 A general layout of a hydropower plant taken from [1]. . . . . 34
- 2.2 Hydropower units: (a) Reservoir, (b) Intake pipe and flow diagram, and (c) Intake, surge tank, and penstock manifold diagram. . . . . 36
- 2.3 Hydropower units: (a) A simple surge tank, and (b) Turbine. . . . . 39
- 2.4 Typical efficiency  $\eta$  versus gate signal  $u_v$  for different kinds of turbine taken from [2]. . . . . 41
- 2.5 Hydropower governor. . . . . 42
- 2.6 Linear functional relationship between  $\bar{u}_{g,ref}$  and  $\bar{P}_{ref}$ . The slope of the line = 0.92 indicates that as p.u. loading of the prime mover  $\bar{P}_{ref}$  runs towards the positive x-direction, and the rise in p.u. of the gate signal  $\bar{u}_{g,ref}$  decreases in the y-direction. . . . . 43
- 2.7 Sharp orifice type fitting used for modeling the sharp orifice type surge tank. . . . . 45
- 2.8 Square expansion and square reduction type fitting used for modeling of throttle valve surge tank. . . . . 46
- 2.9 Air-cushion surge tank. . . . . 47
- 2.10 a) A conical diffuser based on [3] and b) Moody spreading pipes draft tube based on [4]. . . . . 49
- 2.11 Power frequency governor control of a power plant. . . . . 52
- 2.12 Synchronous area with the multi-generator system showing primary control to other units and secondary control to AGC unit (Unit-1). If other units take part in the secondary control, then a PI controller is used to adjust the load reference set points of the units. . . . . 54
- 2.13 Two synchronous areas represented by voltage sources and their respective power angles. The areas are connected with a lossless tie line with reactance  $X_{tie}$ . . . . . 55
- 2.14 Block diagram for AGC for two synchronous areas. . . . . 56
- 2.15 Block diagram of MPC. . . . . 58
- 2.16 Thermal model of the synchronous generator. . . . . 65
- 2.17 Experimental data for generator model from a 600 min heat-run test taken from [5]. . . . . 66
- 2.18 Bayesian inference for the state estimation. . . . . 67

List of Figures

3.1	Different types of surge tanks. (a) Simple surge tank without hydraulic resistance. (b) Sharp orifice type surge tank with an orifice of diameter $D_i$ as the hydraulic resistance. (c) Throttle valve surge tank with hydraulic resistance of diameter $D_i$ at the entry of surge tank with square expansion from diameter $D_i$ to diameter $D_o$ . The length of the throat is $L_t$ . (d) Air-cushion surge tank filled with air at pressure $p_c$ . . . . .	78
3.2	a) Layout diagram for Trollheim [6]. Nominal head, nominal discharge, and nominal power output are 370m, 40m <sup>3</sup> /s, and 130MW, respectively. The diameter for both of the penstock and the surge tank is 4m while for both the headrace and the tailrace tunnel is 6m. b) Simulation diagram implemented in OpenHPL with a hydropower governor with the gate servo motor time constant $T_{gs} = 0.2$ s and the pilot servo motor time constant $T_{ps} = 0.04$ s. For simulation studies we have considered the grid frequency of the system to be 50Hz. We have not shown the generator side or the grid side of the plant. . . . .	80
3.3	Water mass oscillation inside the open surge tanks for Trollheim HPP during TLR. The diameter of the orifice for the sharp orifice type surge tank ( $D_{so}$ ) and the diameter of the throat for the throttle valve surge tank ( $D_t$ ) are both 1m. The length of the throat for the throttle valve surge tank is 20m. . . . .	81
3.4	Maximum required height of surge tank for different diameters of the sharp orifice (SO) type and the throttle valve (TV) surge tanks. $h_{ST}^{max}$ represents the maximum amplitude of water mass oscillation during TLR. . . . .	82
3.5	Water mass oscillation inside the surge tanks for TLA. . . . .	83
3.6	Inlet turbine pressure during TLR and TLA for Trollheim HPP using different kinds of open surge tanks. . . . .	84
3.7	Water mass oscillation inside the surge tanks for PLR. In the figure, $u_v - 25\%$ represents the gate signal for a partial load rejection of 25% of the total load capacity of the plant. Similarly, $h_{ST} - 25\%$ represents water mass oscillation for a load rejection of 25%. . . . .	85
3.8	Water mass oscillation inside the surge tanks for PLA. In the figure, $u_v - 25\%$ represents the gate signal for a partial load acceptance of 25% of the total load capacity of the plant. Similarly, $h_{ST} - 25\%$ represents water mass oscillation for a load acceptance of 25% from a no-load condition. . . . .	86
3.9	Turbine pressure for various partial load rejections (PLRs) for surge tanks. . . . .	89
3.10	Turbine pressure for various partial load acceptances (PLAs) for surge tanks. . . . .	90

3.11	(a) Layout diagram for Torpa HPP. Nominal head, nominal discharge, and nominal power output are 445m, 40m <sup>3</sup> /s and 150MW, respectively. The ACST has air volume of 1300m <sup>3</sup> /s, initially pressurized at 41 · 10 <sup>5</sup> Pa. Similarly, both of the headrace and tailrace tunnels are 7m in diameter. Torpa HPP consists of two turbine units, Unit-1 and Unit-2, each rated at 75MW with rated discharge at 20m <sup>3</sup> /s. (b) Simulation model of Torpa HPP implemented in OpenHPL from the head reservoir to the tail reservoir.	91
3.12	Simulation versus real measurements for Torpa HPP, (a) turbine valve signal for Unit-1, (b) turbine valve signal for Unit-2, (c) power output for Unit-1, (d) power output for Unit-2, (e) inlet pressure of the turbine units or the outlet pressure of the penstock, (f) air cushion pressure inside the ACST, and (g) height of water level inside the ACST. Experimental data are provided by [7].	92
3.13	Hydraulic performance of the ACST for Torpa HPP for the different percentage change in the load acceptances and the load rejections, (a) turbine valve signal $u_v$ as an input to the load acceptances, (b) turbine valve signal $u_v$ as an input to the load rejections, (c) air pressure $p_c$ for the load acceptances, (d) air pressure $p_c$ for the load rejections, (e) turbine inlet pressure $p_{tr}$ for the load acceptances, (f) turbine inlet pressure $p_{tr}$ for the load rejections, (g) water level inside the ACST $h$ for the load acceptances, and (h) water level inside the ACST for the load rejections.	95
3.14	Simulated response for the inlet pressure of the conical diffuser and the Moody spreading pipes with different branching angles.	97
3.15	Fitting frequency step responses from the AGC prediction model and the Trollheim HPP from OpenHPL. $M$ , $T_w$ , $T_g$ and $R$ are the tuned parameters for the AGC prediction model with respect to the OpenHPL model.	98
3.16	Active power frequency control of Trollheim HPP implemented in OpenHPL.	101
3.17	Power frequency control of Trollheim HPP.	102
3.18	AGC in the multi-generator system. Three units: one AGC unit and two non-AGC units are operating in parallel to supply a common consumer load. A load disturbance of 10MW is created at $t = 20$ s and the frequency of the grid, and generations from the hydropower units are observed for the next 60s.	104
3.19	Frequencies, load, and generations plot for two synchronous areas after a load disturbance of 10MW in Area-1. In the figure, load disturbance of 10MW is created at $t = 20$ s and the frequencies of the grids, generations from the hydropower units, and tie line flow from Area-1 to Area-2 are observed for next 60s.	106
3.20	Frequency, load and generation responses using PI and MPC for AGC of Trollheim HPP. In the blue dashed lines, integral action has been added to MPC.	112

*List of Figures*

3.21	Responses for frequency, load and generation. Case-1: when “MPC model = the AGC prediction model”, “plant = linearized OpenHPL model”. Case-2: when “MPC model + plant = linearized OpenHPL model”. . . . .	115
3.22	Responses for frequency and generation using Ipopt and COSMO solvers.	117
3.23	Metal and air temperatures estimation using particle filter with $N_p = 200$ and Ris04 resampling. . . . .	119
3.24	Metal and air temperatures estimation using particle filter with different number of particles for Ris04, multinomial, and residual resampling. In the figure, the temperature curves have been vertically shifted (represented by $\phi_k^{15}$ and $\phi_k^2$ ) for clarity of presentation. In reality they start at same temperature. . . . .	120
3.25	Metal and air temperatures estimation using UKF and EnKF with different number of particles. In the figure, the some of the temperature curves have been vertically shifted (represented by $\phi_k^{15}$ and $\phi_k^2$ ) for clarity of presentation. In reality they start at same temperature. . . . .	121

# List of Tables

- 2.1 Multiphysics environments. . . . . 26
- 2.2 Hydropower libraries. . . . . 30
- 2.3  $\phi_{ms}^0$  for different value of  $\theta$  . . . . . 48
- 2.4 Parameters and initial operating conditions. . . . . 68
- 2.5 Generalized particle filter. Measurement co-variance  $\mathcal{V}$  is assumed constant/known. . . . . 71
- 2.6 Different resamplings pseudocodes. . . . . 72
  
- 3.1 Trollheim HPP specifications. . . . . 99
- 3.2 Trollheim HPP control model parameters. . . . . 100
- 3.3 Specifications of units in multi-generator system areas. . . . . 103
- 3.4 Control model parameters for two synchronous areas. . . . . 105
- 3.5 Operating conditions for linearization of Trollheim HPP. . . . . 107
- 3.6 Estimation algorithms, estimation innovation  $\epsilon$ , and computational time  $\tau$ . PF-Stratified, PF-Systematic, PF-RPF and PF-APF are compared relative to UKF. . . . . 123
  
- F.1  $\phi_{ms}^0$  for different value of  $\theta$  . . . . . 199



# **Part I**

## **Overview**





# 1 Introduction

This chapter provides background, objectives, and an outline of the thesis. In addition, a list of research papers that form the basis of the thesis is included.

## 1.1 Background

In 2015 United Nations General Assembly defined a set of 17 goals referred to as Sustainable Development Goals (SDGs) to be achieved by 2030. SDGs Goal 7 is on “Affordable and clean energy” which targets global access to affordable and reliable energy with an increase in renewable energy share in the global energy mix [8]. Renewable energy is a combination of dispatchable and intermittent sources. The dispatchable sources, from a control perspective, can be used to balance the electrical consumption and the generation from intermittent sources. Dispatchable sources include storage hydropower plants, pump storage hydropower plants, biomass power plants, etc., while intermittent sources include run-of-river hydropower plants, tidal power plants, solar power plants, wind power plants, etc. The most used renewable dispatchable source is a storage hydropower plant. In Norway, hydroelectric power production is about 90% of the total electric power production and it has almost half of Europe’s reservoir capacity. Reservoirs in Norway play significant role in balancing the variability caused by intermittent energy sources connected to the Nordic grid. Nordic grid is connected to the other European grids, for example, the exchange of power between Norway, Germany, and the United Kingdom with two 1400MW subsea cables. In Denmark almost 50% of its total electricity comes from wind energy sources. Denmark has a plan for increasing its electricity share from wind energy to 84% by 2035. The reservoirs of Norway are balancing more than 20% of variable energy produced from Danish wind farms in the interconnected Nordic grid. Germany is a major solar and wind energy producer in Europe. Germany has a feed-in tariffs (FiT) system. FiT is a policy that provides long-term security to renewable energy producers based on the cost of generation from renewable energy sources. The tariff for solar power production is higher as compared to wind power production. The central parts of Germany have higher annual sunshine than other locations and are suitable for PV installation. All of the 16 federal states have PV installations with the southern and eastern parts having the highest wattage per capita [9].

## 1 Introduction

Reservoirs in Norway have the potential to become a battery for balancing the variability of solar power and wind power in the European interconnected grid. In this regard, the primary focus of this thesis is on modeling tools for hydropower plants. To research the hydroelectricity production from reservoirs in Norway, a tool with a hydropower model library is required, where models of hydropower systems can be designed, simulated, and analyzed. The flexibility with which hydropower plant equipment operates during intermittent electricity injection into the grid determines its performance and reliability. Several units of hydropower plants must function efficiently under varied operating situations in order to be adaptable. From a control perspective, the development of modeling tools is of key interest. Mechanistic models contain insight into the physics of the problem. It is possible to build a mechanistic model based on the physical understanding of the system, even when the system only is in the planning stage. Approximate parameter values for the mechanistic model can be found based on very few design parameters, e.g., pressure head and volumetric flow rate. This means that it is possible to develop a mechanistic model for a system that only exists in the planning stage. In contrast, a data-driven model gives little physical insight into the problem, and cannot be developed until experimental data from the real system is available. Mechanistic models can often be represented in differential-algebraic equation (DAE) form. Mechanistic models containing partial differential equations (PDE) and integral equations can also be discretized into the form of DAE. DAE can always be represented in the form of an ordinary differential equation (ODE) by the simplification of algebraic relations into differential equations. However, the choice of DAE over ODE is due to the increase in model information from the algebraic variables. This directs us to choose a programming language for model formulation where mathematical formulas can be easily implemented. This is possible with the open-source equation-based language Modelica. Additionally, the Modelica language is preferred due to the tool's multi-physics capabilities, number of contributors, and ease-of-use. The choice of the Modelica language is well justified in [10] and in Section 2.1.1. There exists an open-source Modelica-based hydropower library — OpenHPL currently under development at University of South-Eastern Norway [USN]. OpenHPL is the outcome of a PhD study [10]. OpenHPL has units for the flow of water in filled pipes (inelastic and elastic walls, incompressible and compressible water), a mechanistic model of a Francis turbine (including design of turbine parameters), friction models, etc. The library also has draft models for surge shafts and open channel flow and a hydrology model. OpenHPL has been tested on real power plant data. The library is designed to interface with other Modelica libraries, e.g., libraries with generator models, electric grids, etc. The hydropower components are developed based on mass and momentum balances. It is of interest to further extend OpenHPL with models of other units of a hydropower plant. It is also of interest to integrate models from OpenHPL with models of intermittent energy sources from other open-source Modelica libraries. The research work presented in [10] and [5] is previous work from USN based on the state-of-the-art of flexible hydropower. Most of this thesis work is related to those previous works.

## 1.2 Objectives

Due to the need to use more renewable energy, future energy production will include a mixture of dispatchable hydropower and intermittent solar and wind power. This requires more flexibility in the operation of hydropower systems, and more extensive use of equipment to dampen variations. Quantitative studies of such integrated systems require the development of more extensive hydropower modeling libraries, as well as analysis and control/optimization tools.

The following are the main objectives of the thesis grouped into two main parts:

### Feature extension of OpenHPL

- Extend an existing library, OpenHPL, with models of surge tanks and draft tubes in order to study the flexibility of hydropower plants during load acceptance/rejection.
- Extend OpenHPL with standard active power frequency control in the electric power systems.

### Model analysis and design

The following methods are implemented in a combination of OpenModelica and Julia:

- formal tuning of models to data (parameter estimation), exemplified by a thermal model of a synchronous generator,
- on-line state estimation, exemplified by a thermal model of a synchronous generator. Such estimation is a requirement for the flexible operation of the generator,
- advance control to handle hard constraints in the operation of hydropower plants.

## 1.3 List of Publications

Following are the published research papers:

- **Appendix A.** M. Pandey and B. Lie, “Mechanistic modeling of different types of surge tanks and draft tubes for hydropower plants,” in *Proceedings of SIMS 2020 Virtual, Finland, 22-24 September 2020*. Linköping University Electronic Press, 2020, pp. 131–138.
- **Appendix B.** M. Pandey and B. Lie, “Mechanistic Model of an Air Cushion Surge Tank for Hydro Power Plants,” *Energies*, vol. 15, no. 8, p. 2824, 2022.

## 1 Introduction

- **Appendix C.** M. Pandey and B. Lie, “The influence of surge tanks on the water hammer effect at different hydro power discharge rates,” in *Proceedings of SIMS 2020 Virtual, Finland, 22-24 September 2020*. Linköping University Electronic Press, 2020, pp. 125–130.
- **Appendix D.** M. Pandey and B. Lie, “Bayesian Inference for Thermal Model of Synchronous Generator Part II : Parameter Estimation,” *IEEE Access*, 2022, <https://doi.org/10.1109/ACCESS.2022.3209232>
- **Appendix E.** M. Pandey and B. Lie, “Bayesian Inference for Thermal Model of Synchronous Generator Part II : State Estimation,” *IEEE Access*, 2022, <https://doi.org/10.1109/A>

### 1.4 Outline

The thesis consists of two main parts. In Part I an overview of the thesis is given. In Part II publications are given in appendices, together with DAEs for surge tanks and draft tubes.

Chapter 2 provides literature review. The main contributions of the thesis work are provided in Chapter 3. Conclusions of the work are given in Chapter 4, together with indications of future work.

## 2 Literature Review

This chapter includes literature review regarding:

- current modeling tools for hydropower systems,
- general modeling principle to study the dynamics of hydropower units,
- modeling of the surge tanks and draft tubes,
- active power frequency control, and
- work regarding a thermal model of a synchronous generator.

### 2.1 Modeling Tools

For the simulation of integrating dispatchable sources with intermittent sources, a modeling tool is required. The integration of intermittent and dispatchable renewable sources incorporates the physics of several domains. Studying renewable energy sources integrated with electrical generation, transmission, and distribution requires a multiphysics simulation environment.

In this section, first, a literature review on the current multiphysics simulation environment is presented. Second, a literature review on existing hydropower modeling software is given.

#### 2.1.1 Multiphysics environment

Multiphysics simulation includes physical processes commonly combined such as *thermo-hydro-concentro-mechano-dyno-chemo-electro-magneto*<sup>1</sup>. The general procedure for simulating multiphysics problems would be to identify the multi-physical processes, develop their mathematical models, discretize them with a suitable numerical solver, and solve them using languages such as MATLAB, Python, Julia, etc. The mathematical model in multiphysics includes mainly ordinary differential equations (ODEs), differential-algebraic equations (DAEs), partial differential equations (PDEs), and the mathematics of tensors,

---

<sup>1</sup>[http://www.multiphysics.us/types\\_multiphysics.html](http://www.multiphysics.us/types_multiphysics.html)

Table 2.1: Multiphysics environments.

Environment	Availability	Remarks	Support
ASCEND	open-source	- Written in: C, C++, Python - Equation-based: Yes - Domain: Chemical process - Extension: Yes - Contributors: Few	Python
Elmer	open-source	- Written in: C, C++ - Equation-based: No - Domain: Multiphysics - Extension possibility: No - Contributors: Few	C++
ModelingToolkit	open-source	- Written in: Julia - Equation-based: Yes - Domain: Multiphysics - Extension possibility: Yes - Contributors: Many	Julia
OpenModelica	open-source	- Written in: C, C++, MetaModelica - Equation-based: Yes - Domain: Multiphysics - Extension possibility: Yes - Contributors: Many	MATLAB, Python, Julia
OpenFOAM	open-source	- Written in: C++ - Equation-based: No - Domain: CFD - Extension possibility: Yes - Contributors: Many	Python
Scilab	open-source	- Written in: Scilab, C, C++, Java - Equation-based: No - Domain: Multiphysics - Extension possibility: Yes - Contributors: Very few	Java
APMonitor	commercial	- Written in: - - Equation-based: Yes - Domain: Multiphysics	MATLAB, Python, Julia
COMSOL Multiphysics	commercial	- Written in: Java - Equation-based: No - Domain: Multiphysics	MATLAB, Java
Dymola	commercial	- Written in: Modelica - Equation-based: Yes - Domain: Multiphysics	-
MapleSim	commercial	- Written in: Modelica - Equation-based: Yes - Domain: Multiphysics	Maple

functions, and fields. There exist many multiphysics simulation environments<sup>2</sup>. Among all of these multiphysics simulation environments, for simulating renewable energy integrated with end-users of electrical energy it is of interest to choose a multiphysics simulation environment that (i) is open-source, (ii) has equation-based modeling possibilities, (iii) has libraries/features extension, (iv) has a large number of contributors, and (v) is easy to use.

Table 2.1 classifies different commonly used multiphysics simulation environments based on being available as open-source or commercial, with support from modern high-level languages such as MATLAB, Python, and Julia for external processing. In addition, the multiphysics simulation environments are also classified based on the language in which the environment is written, whether the environment is built on an equation-based language or not, the domains of physics, possibilities for further extension of the environment, and the number of contributors.

ASCEND<sup>3</sup> is an open-source equation-based chemical process modeling environment developed at Carnegie Mellon University. Other than chemical process modeling, ASCEND can be used for modeling other domains. In ASCEND model development and computational solver are separated. Both a domain expert and a computational expert can work separately. ASCEND can solve dynamic systems expressed in terms of DAEs. ASCEND can also be interfaced with Python using a library — ExtPy<sup>4</sup>.

Elmer<sup>5</sup> is a multiphysics computational tool for solving physical models in fluid dynamics, electromagnetics, acoustics, and heat transfer. The models from the multiphysics problem are described using PDEs, and the model solutions are obtained using a finite element method.

ModelingToolkit<sup>6</sup> is a Julia package with equation-based modeling possibilities. It supports high-performance symbolic-numeric computation for multiphysics problems. ModelingToolkit provides modeling related to DAEs, PDEs, and optimal control problems [11]. Since ModelingToolkit is written in the host language Julia it does not require an interface like another modeling environment, e.g., ExtPy in the case of ASCEND. However, ModelingToolkit does not currently provide a graphical user interface (GUI) like other modeling environments such as ASCEND and Elmer. Except for ModelingToolkit, all the other modeling environments in Table 2.1 provide GUI for model development.

OpenModelica<sup>7</sup> is the most prominent open-source Modelica-based modeling and simula-

<sup>2</sup>[https://en.wikipedia.org/wiki/List\\_of\\_computer\\_simulation\\_software](https://en.wikipedia.org/wiki/List_of_computer_simulation_software)

<sup>3</sup><https://en.wikipedia.org/wiki/ASCEND>

<sup>4</sup><https://ascend4.org/ExtPy>

<sup>5</sup>[https://en.wikipedia.org/wiki/Elmer\\_FEM\\_solver](https://en.wikipedia.org/wiki/Elmer_FEM_solver)

<sup>6</sup><https://mtk.sciml.ai/stable/>

<sup>7</sup><https://openmodelica.org/>. Similarly, there also exists JModelica for simulation, optimization, and analysis of Modelica-based models. However, it does not contains block diagram model-development functionality like OpenModelica. OpenModelica is best suited for models and specific library devel-



## 2 Literature Review

tion environment. OpenModelica is very user-friendly for developing complex multiphysics models using block diagrams like in Simulink<sup>8</sup>; however, OpenModelica is based on an acausal paradigm, while Simulink is causal. There exist more than 30 free and commercial Modelica libraries comprising a multi-physical modeling environment [12]. OpenModelica can be interfaced with MATLAB, Python, or Julia.

OpenFOAM<sup>9</sup> is an open-source tool for solving numerical problems in CFD. OpenFOAM allows for the development of customized numerical solvers and pre/post-processing of models. OpenFOAM can be interfaced with Python using a library — PyFOAM<sup>10</sup>.

Scilab<sup>11</sup> is an open-source language for solving multiphysics problems. It is an alternative to MATLAB. For modeling and simulation of implicit and explicit dynamical systems, Scilab has a free package called Xcos. Scilab can be interfaced<sup>12</sup> with Java for processing the developed models externally. Scilab has very few contributors.

Table 2.1 also shows other multiphysics simulation environments that are commercial. The commercial environments are expensive, do not have their software development as open-source, and have very few contributors confined to a proprietary environment. It is out of the scope of this thesis to discuss commercial multiphysics simulation environments.

From Table 2.1, we see that ASCEND, ModelingToolkit, and OpenModelica are suitable modeling environments for multiphysics problems based on the software available, possibilities of feature extension, the domain of multiphysics problems that can be solved, and the number of contributors. Both OpenModelica and ModelingToolkit are better than ASCEND in terms of the domain of multiphysics problems that can be solved, and the number of contributors. It is too early to choose ModelingToolkit over OpenModelica: there is a lack of GUI for model development using ModelingToolkit, and the tool is under rapid development. Unlike ModelingToolkit, the OpenModelica environment allows for incorporating different multiphysics Modelica libraries for the integration of renewable energy sources. However, ModelingToolkit is still very interesting, because it is written in its host language Julia where advanced analysis tools can be integrated with simulation models.

We have chosen OpenModelica for continuing previous work [10] at our institution. For advanced analysis of models developed using OpenModelica, there exists OMPython<sup>13</sup> and OMJulia<sup>14</sup> which are Application Program Interfaces (APIs) built within Python

---

opment.

<sup>8</sup><https://en.wikipedia.org/wiki/Simulink>

<sup>9</sup><https://en.wikipedia.org/wiki/OpenFOAM>

<sup>10</sup><https://pypi.org/project/PyFoam/>

<sup>11</sup><https://en.wikipedia.org/wiki/Scilab>

<sup>12</sup>[https://help.scilab.org/docs/6.1.1/en\\_US/jims-getting-started.html](https://help.scilab.org/docs/6.1.1/en_US/jims-getting-started.html)

<sup>13</sup><https://openmodelica.org/doc/OpenModelicaUsersGuide/latest/ompython.html>

<sup>14</sup><https://www.openmodelica.org/doc/OpenModelicaUsersGuide/latest/omjulia.html>

and Julia, respectively. The choice of OMJulia is preferred over OMPython because the Julia language has a faster execution speed than Python.

### 2.1.2 Hydropower libraries

Section 2.1.1 lists both open-source and commercial multiphysics environments. Based on the comparison between different multiphysics environments from Table 2.1 we have chosen OpenModelica as a multiphysics environment for studying the integration of dispatchable sources with intermittent sources. It is also of interest to review hydropower modeling tools.

Table 2.2 classifies different hydropower modeling tools based on the software being available as open-source or commercial, with support from modern high-level languages such as MATLAB, Python, or Julia for external processing. In addition, the hydropower libraries are also compared based on the language in which the environment is written, whether the environment is built on equation-based language or not, the domain of the physics, possibilities for further extension of the environment, and the number of contributors. In Table 2.2, the commercial libraries are not assessed based on the number of contributors. The commercial environments have few contributors confined to a proprietary environment, however, there may be extensive company development.

CASiMiR-Hydropower<sup>15</sup> is a free hydropower simulation program that calculates energy production for a given hydropower plant based on the input parameters such as discharge, hydraulic head, flow rules, and the efficiency curve of the hydro turbines used in the plant. The energy production of the plant is calculated based on the integral of the generated power over a period of time. The main use-case of the software is to study the economic effects of hydropower production as a result of ecologically adjusted discharges in minimum flow studies<sup>16</sup>.

WHAMO is a free tool for the dynamic simulation of fluid distribution systems and hydropower plants that are subjected to water hammers [13]. WHAMO allows for studying water hammer effects and its mitigation based on minimizing water velocity through the units such as pipes, junctions, valves, pumps, surge tanks, and turbomachines. The governing equations of the unit are formulated based on 1D mass and momentum balance equations and solved using a four-point implicit finite difference representation. The software evaluates the dynamic flow rate, pressure, and head of the fluid flow system. The current version of WHAMO is Version 3.0 which is an upgraded version consisting of a GUI for modeling and simulation.

<sup>15</sup>[http://www.casimir-software.de/save\\_download.php?language=2](http://www.casimir-software.de/save_download.php?language=2)

<sup>16</sup>[http://www.casimir-software.de/data/Hydropower\\_Handb\\_EN\\_2011\\_01.pdf](http://www.casimir-software.de/data/Hydropower_Handb_EN_2011_01.pdf)

## 2 Literature Review

Table 2.2: Hydropower libraries.

Library	Availability	Remarks	Support
CASiMiR-Hydropower	open-source	- Equation-based: No - Extension possibility: No - Contributors: Few	No
WHAMO	open-source	- Equation-based: No - Extension possibility: No - Contributors: Very few	No
OpenHPL	open-source	- Written in: Modelica - Equation-based: Yes - Extension possibility: Yes - Contributors: Few but increasing	MATLAB, Python, Julia
LVTrans	free, but depend on commercial environment	- Written in: LabVIEW - Equation-based: No - Extension possibility: Yes - Contributors: Few but increasing	LabVIEW
Alab	commercial	- Written in: - - Equation-based: No - Extension possibility: No	No
Modelon HPL	commercial	- Written in: Modelica - Equation-based: Yes - Extension possibility: Yes	No
TOPSYS	commercial	- Written in: C++ - Equation-based: Yes - Extension possibility: No	No
SIMSEN	commercial	- Written in: - - Equation-based: Yes - Extension possibility: Yes	No
WANDA	commercial	- Written in: - - Equation-based: Yes - Extension possibility: Yes	No

OpenHPL<sup>17</sup> is a Modelica-based open-source tool for modeling and simulation of hydropower plants and is in the phase of development.

LVTrans<sup>18</sup> is an open-source transient simulations software for hydraulic piping systems developed using LabVIEW<sup>19</sup>. However, LabVIEW is a commercial tool. LVTrans is particularly used for the transient simulation of hydropower plants. The model is developed based on 1D mass and momentum balance equations. The governing equations are solved using the method of characteristics (MOC) numerical scheme<sup>20</sup>. The special feature of LVTrans is that it uses mechanistic models of Pelton and Francis turbines based on the nominal information of the hydropower plant, and does not require a look-up table for efficiency curve as in software such as CASiMiR-Hydropower and WHAMO. LVTrans also has a predictive hydro governor that is used for balancing power between hydropower in Norway and wind power in Denmark and Germany.

Alab<sup>21</sup> is a commercial design tool for hydropower systems. The important feature of Alab is that it provides preliminary design algorithms for designing hydropower units such as dams, intake, surge tanks, penstock, turbines, generators, transformers, governors, and reversible pump-turbines.

Modelon HPL is a commercial hydropower library for modeling and simulation based on a commercial Modelica-based environment — Dymola<sup>22</sup>. It is suitable for performance verification and control of the hydropower plant in the conceptual phase. Modelon HPL can be combined with other freely available Modelica libraries for holistic model development, control, and analysis within the Dymola framework. However, the model developed in Modelon HPL cannot be interfaced with high-level languages such as Python or Julia.

TOPSYS is a commercial hydropower library developed using 1D mass and momentum balance equations. Similar to LVTrans, TOPSYS uses MOC numerical scheme for solving the dynamic equations. TOPSYS is developed in a collaboration between Wuhan and Uppsala universities, and is used for studying Swedish and Chinese hydropower plants. The important feature of TOPSYS is a governor system model for hydropower plants running at different operating conditions [14].

SIMSEN<sup>23</sup> is a commercial tool for modeling, simulation, and control of hydraulic, electric, and adjustable speed drive systems. It is developed at École Polytechnique Fédérale de Lausanne (EPFL). SIMSEN is a widely used commercial environment for studying hydraulic transients. The hydraulic models in SIMSEN are built based on the electrical analogy of circuits comprising resistance, capacitance, and inductance [15]. The hydraulic

<sup>17</sup><https://github.com/OpenSimHub/OpenHPL>

<sup>18</sup><http://svingentech.no/index.html>

<sup>19</sup><https://www.ni.com/en-no/shop/labview.html>

<sup>20</sup>[https://en.wikipedia.org/wiki/Method\\_of\\_characteristics](https://en.wikipedia.org/wiki/Method_of_characteristics)

<sup>21</sup>[https://en.wikipedia.org/wiki/Method\\_of\\_characteristics](https://en.wikipedia.org/wiki/Method_of_characteristics)

<sup>22</sup><https://www.3ds.com/products-services/catia/products/dymola/>

<sup>23</sup><https://www.epfl.ch/research/facilities/hydraulic-machines-platform/ptmh/simsen/>

## 2 Literature Review

feature extension of SIMSEN, therefore, depends on the domain of electrical systems. The model developed in SIMSEN cannot be interfaced with high-level languages such as Python or Julia for advanced control analysis such as model predictive control (MPC).

The commercial environment WANDA<sup>24</sup> allows for advanced water hammer analysis for flow distribution systems, heat transfer, and pumping systems. It is similar to WHAMO. WANDA also has a powerful GUI that can be interfaced with SCADA systems. WANDA popular in both academic and industrial projects similar to SIMSEN.

From Table 2.2, we see that open-source hydropower libraries such as WHAMO, LVTrans, and OpenHPL are suitable for modeling, design, and analysis of hydropower systems. WHAMO has no high-level language interfaces for advanced analysis and has very few contributors. LVTrans depends on the commercial environment LabVIEW. LVTrans has a few contributors, however as the further extension of the library is maintained at Norwegian University of Science and Technology [NTNU] there is a possible number of contributors in the form of academic students using LVTrans for their projects and theses. Like LVTrans, OpenHPL has also been used for academic theses and projects at USN, and the number of general contributors is increasing. One of the prime reasons for expecting increased use of OpenHPL is that it is based on the open-source language Modelica where a large number of contributors are involved in developing other physics libraries that can be combined with OpenHPL for holistic modeling, simulation, and analysis of renewable integrated sources. Thus, in our opinion, OpenHPL could be a better choice for future modeling, simulation, control, and analysis of hydropower systems. Commercial environments such as Modelon HPL, TOPSYS, SIMSEN, and WANDA have their own special features, e.g., Modelon HPL is useful for holistic multiphysics based model development. TOPSYS has an improved model for hydropower governor systems, and SIMSEN and WANDA are popular tools used in industry and academia for multiphysics problem. Commercial hydropower tools cannot be interfaced with high-level languages for advanced control analysis such as MPC. Modelon HPL is also quite expensive compared to the other tools.

## 2.2 Modeling of Hydropower Units

This section includes literature regarding the general operation of a hydropower plant, previous work regarding the modeling of hydropower units, and the modeling of different types of surge tanks and draft tubes.

---

<sup>24</sup><https://www.deltares.nl/en/software/wanda/>

### 2.2.1 Hydropower plant

A hydropower plant converts the kinetic and/or potential energy of water into electricity. Generally in mountainous countries, water is collected from water streams and stored in a reservoir/dam. A hydropower plant using storage water for producing electricity is called a reservoir-type hydropower plant. In countries having fast-flowing rivers, only a portion of flowing water is diverted to the turbine for producing electricity, and this type of plant is called a run-of-river hydropower plant.

Figure 2.1 shows a general schematic of a reservoir-type hydropower plant. Water from the reservoir flows through the intake tunnel into the penstock. The moving water rotates the turbine which in turn rotates the electrical generator to produce electricity. The electrical power out from the generator is used for operating electrical loads. The water from the turbine outlet then flows towards the tailrace or downstream reservoir. Contrary to the reservoir-type hydropower plant, in the run-of-river type hydropower plant, the flow of water from the river is directly diverted to the intake race.

Generally, the intake is a water-filled pipe with a small slope, with, however, a much longer length based on the suitability of the location of the penstock and power house including the turbine and generator. The flowing water from the intake is then directed towards a steep slope penstock to the turbine. There is a large pressure difference between the inlet and outlet of the penstock pipe due to the steep slope. Furthermore, an effect known as a water hammer or hydraulic shock phenomenon can arise in the penstock when the turbine valve is rapidly opened/closed during an electrical load disturbance. The water hammer effect is due to the larger momentum change of water from the reservoir to the end of the penstock. In order to reduce the water hammer effect, the movement of mass in the intake race and penstock are decoupled by installing a surge tank as in Figure 2.1. Surge tanks can be open type or closed type. An open type surge tank has free water surface, while a closed type surge tank has water surface in contact with pressurized air. In Section 2.2.4, literature review for three different kinds of open type surge tanks and an air cushion surge tank is provided.

Based on the total height difference and flow rate or discharge of the power plant, turbines are classified in two types: impulse turbine and reaction turbine. In the impulse turbine, only the kinetic energy of water is used to rotate the turbine whereas in the reaction turbine both the kinetic and pressure energy of water is used to rotate the turbine. The most common example of the impulse turbine is the Pelton turbine, typically used for height differences in the ranges of 300 – 4000 m and flow rate  $< 30\text{m}^3/\text{s}$ . The most common examples of the reaction turbine are the Francis turbine and the Kaplan turbine with height differences in the ranges of 20 – 600 m and flow rate  $< 1000\text{m}^3/\text{s}$ .

## 2 Literature Review

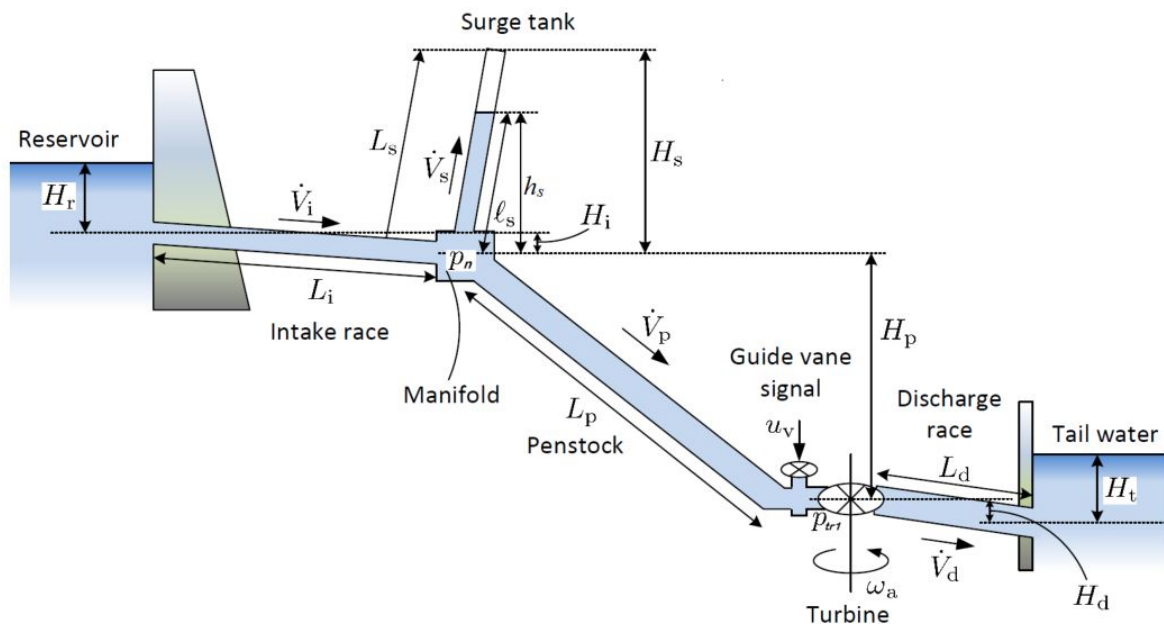


Figure 2.1: A general layout of a hydropower plant taken from [1].

### 2.2.2 Previous work

Previous work regarding modeling of OpenHPL hydropower units includes Sharif (2011) [16], Zhou (2017) [17], Splavska (2017) [18], and Vytvytskyi (2019) [10].

Sharif (2011) developed models of hydropower units based on the mass and momentum balances. In modeling for control, an ODE formulation of mass and momentum balances can be used for models of hydropower units, such as reservoir, intake, penstock, etc. However, to take into account the effect of water compressibility and elasticity in the hydropower units, such as the penstock, in the overall generation from the plant, a more detailed model would be required. A model of the penstock in the case of water compressibility and wall elasticity consists of PDEs. Sharif (2011) used the finite volume method for studying the behavior of a penstock when the elasticity of the penstock walls and the compressibility of the water are taken into account. The modeling and simulation results were obtained using MATLAB scripts.

Similarly, Zhou (2017) studied the behavior of the penstock using different numerical schemes for discretizing penstock PDEs, viz., finite volume method (FVM), electrical equivalent circuit (EEC), and method of characteristic (MOC). Zhou (2017)'s results indicate that all the numerical schemes produced similar results. Zhou's (2017) used the ODE model of penstock for control application, such as a model predictive controller. All the numerical schemes were implemented using MATLAB scripts.

In Splavska (2017), mechanistic models of hydropower units developed from ODE formulations of mass and momentum balances were implemented in an object-oriented modeling language — Modelica. The models of hydropower units were implemented in OpenModelica which supports a graphical user interface for the “drag-drop” of the units as in MATLAB and Simulink. However, Splavska (2017) did not consider the effect of water compressibility and penstock pipe elasticity. The work from Splavska (2017) is further extended in a PhD study by Vytvytskyi (2019).

Vytvytskyi (2019) was a key contributor to the development of the open-source hydropower library — OpenHPL. Vytvytskyi (2019) used the Kurganov-Petrova numerical scheme [19] for discretizing PDEs to include the effect of water compressibility and penstock pipe elasticity. OpenHPL is under development at USN. Currently, OpenHPL has units for the flow of water in filled pipes (inelastic and elastic walls, incompressible and compressible water), a mechanistic model of a Francis turbine (including design of turbine parameters), friction models, etc. The library also has draft models for a Pelton turbine, a surge shaft, open channel flow, and a hydrology model. In addition, some accompanying work on analysis tools has been developed in scripting languages (Python, Julia) related to state estimation, structural analysis, etc. The library has been tested on real power plant data. The library is designed to interface with other Modelica libraries, e.g., libraries with generator models, electric grids, etc.

This thesis work, regarding the modeling of hydropower units, mostly focuses on:

1. the extension of OpenHPL with mechanistic models of different kinds of surge tanks and draft tubes, and
2. the extension of OpenHPL with standard active power frequency control.

### 2.2.3 Modeling of hydropower units

A hydropower plant is numerically defined based on its nominal head and the nominal volumetric discharge. The nominal head  $H^n$  and the nominal discharge  $\dot{V}^n$  are the minimum requirements to model, simulate, and optimize a hydropower plant. A hydropower plant consists of several hydropower units, e.g., a reservoir, an intake, a surge tank, a penstock, a turbine, a tailrace, etc., as shown in Figure 2.1.

A hydropower unit can be described using mechanistic equations based on conservation principles. Mass and linear momentum are conserved, and we use the mass and linear momentum balances.

The mass balance is

$$\frac{dm}{dt} = \dot{m}_i - \dot{m}_e \quad (2.1)$$



## 2 Literature Review

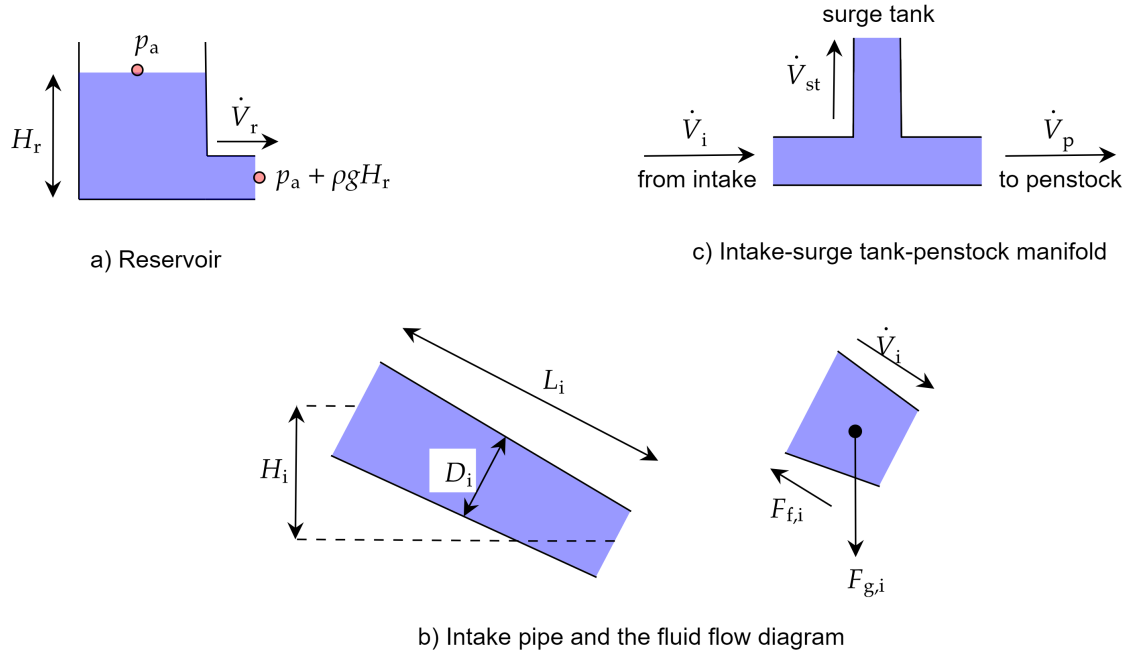


Figure 2.2: Hydropower units: (a) Reservoir, (b) Intake pipe and flow diagram, and (c) Intake, surge tank, and penstock manifold diagram.

where  $m$  is the accumulated mass in the system volume within the hydropower unit,  $\dot{m}_i$  is the influent mass flow rate of water through the unit, and  $\dot{m}_e$  is the effluent mass flow rate of water out of the unit.

The linear momentum balance is

$$\frac{d\mathcal{M}}{dt} = \dot{\mathcal{M}}_i - \dot{\mathcal{M}}_e + F \quad (2.2)$$

where  $\mathcal{M}$  is the accumulated linear momentum in the system volume within the hydropower unit,  $\dot{\mathcal{M}}_i$  is the influent momentum flow rate of water through the unit,  $\dot{\mathcal{M}}_e$  is the effluent momentum flow rate of water out of the unit, and  $F$  is the force acting on the fluid within the hydropower unit.

### 2.2.3.1 Reservoir

Consider a reservoir with water level  $H_r$  as shown in Figure 2.2 a). The mass balance for the reservoir is

$$\frac{dm_r}{dt} = \dot{m}_{r,i} - \dot{m}_{r,e} \quad (2.3)$$

where  $m_r$  is the mass of water in the reservoir,  $\dot{m}_{r,i}$  is the influent mass flow rate, and  $\dot{m}_{r,e}$  is the effluent mass flow rate. Assuming homogeneous density  $\rho$  in the reservoir, and the same density in the influent and effluent flows, the mass balance can be simplified to

$$\frac{dH_r}{dt} = \frac{\dot{V}_{r,i} - \dot{V}_{r,e}}{A_r}, \quad (2.4)$$

here,  $H_r$  is the reservoir water level above the intake<sup>25</sup>,  $\dot{V}_{r,i}$  is the influent volumetric flow rate,  $\dot{V}_{r,e}$  is the effluent volumetric flow rate, and  $A_r$  is an assumed constant cross-sectional area.

The level variation in the reservoir is normally much slower (from days to years) than the dynamics in the power plant, and it is common to assume a constant reservoir level in hydropower simulations.

Equations 2.3 and 2.4 give the model of the reservoir with water level  $H_r$ .

### 2.2.3.2 Intake

An intake tunnel can be considered as a simple pipe as shown in Figure 2.2 b) with the fluid flow diagram. If we consider a filled, rigid pipe with constant density, the rate of accumulated mass within the unit is *zero*. Then the influent and effluent mass flows are equal, and likewise the volumetric flow rates, and the average linear velocities are also equal. Consequentially, influent and effluent momentum flow rates are equal, and the momentum balance reduces to Newton's law,

$$\frac{dm_i}{dt} = 0 \quad (2.5)$$

$$\frac{d\mathcal{M}_i}{dt} = F_{p,i} + F_g - F_{f,i}. \quad (2.6)$$

In Eqs. 2.5 and 2.6, further algebraic equations are needed for a complete model.

The mass of water inside the intake race is  $m_i = \rho V_i$  where the volume of water inside the pipe is given as  $V_i = A_i L_i$ . The momentum of the water in the pipe is  $\mathcal{M}_i = m_i v_i$  where  $v_i$  is the *average* velocity of water through the pipe given as  $v_i = \frac{\dot{V}_i}{A_i}$ . The pressure force for the unit is

$$F_{p,i} = (p_{i,i} - p_{e,i}) A_i$$

with influent pressure of the intake pipe  $p_{i,i}$  given as

$$p_{i,i} = p_a + \rho g H_r,$$

<sup>25</sup>The real level is  $H'_r = H_r + H_i$ , where  $H_i$  is the vertical distance from the bottom of the reservoir to the intake, and we assume that  $H'_r \geq H_i$ .

## 2 Literature Review

and effluent pressure of the intake pipe  $p_{e,i}$ . The force due to gravity in the direction of fluid flow  $\dot{V}_i$  is expressed as

$$F_g = m_i g \frac{H_i}{L_i}.$$

The fluid frictional force  $F_{f,i}$  can be expressed using Darcy's friction factor  $f_{D,i}$  as

$$F_{f,i} = \frac{1}{2} \rho v_i |v_i| A_{w,i} \frac{f_{D,i}}{4} \quad (2.7)$$

where  $A_{w,i}$  is the wetted area of the intake pipe. In general the Darcy's friction factor  $f_D$  is expressed in terms of Reynolds' number as

$$f_D = \begin{cases} \frac{64}{N_{Re}} & N_{Re} < 2100 \\ aN_{Re}^3 + bN_{Re}^2 + cN_{Re} + d & 2100 \leq N_{Re} \leq 2300 \\ \frac{1}{\left(2 \log_{10} \left( \frac{\varepsilon}{3.7D} + \frac{5.7}{N_{Re}^{0.9}} \right)\right)^2} & N_{Re} > 2300 \end{cases}$$

where Reynolds' number  $N_{Re}$  is

$$N_{Re} = \frac{\rho v D}{\mu},$$

$\mu$  is the dynamic viscosity of the fluid,  $\varepsilon$  is the pipe roughness height. For the region  $2100 \leq N_{Re} \leq 2300$ ,  $f_D$  is calculated by using cubic interpolation with coefficients  $a, b, c$ , and  $d$ , differentiable at the boundaries.  $D$  is the average diameter of the unit.

Equations 2.5 and 2.6 with algebraic equations represent a DAE model for an intake pipe.

### 2.2.3.3 Manifold

The manifold is small (typically around  $50\text{m}^3$ ), and is filled with water. Even assuming compressible water makes the dynamics extremely fast compared to the dynamics of all other units. Because of this the manifold is considered an ideal connection point where the mass flows into the manifold sums to zero, and the pressure is the same for all the connecting units. Figure 2.2 c) shows the intake-surge tank-penstock manifold.

### 2.2.3.4 Surge tank

The model of the surge tank can be similarly developed as in the case of the model of the intake pipe. Figure 2.3 a) shows the schematic diagram of the open surge tank. The

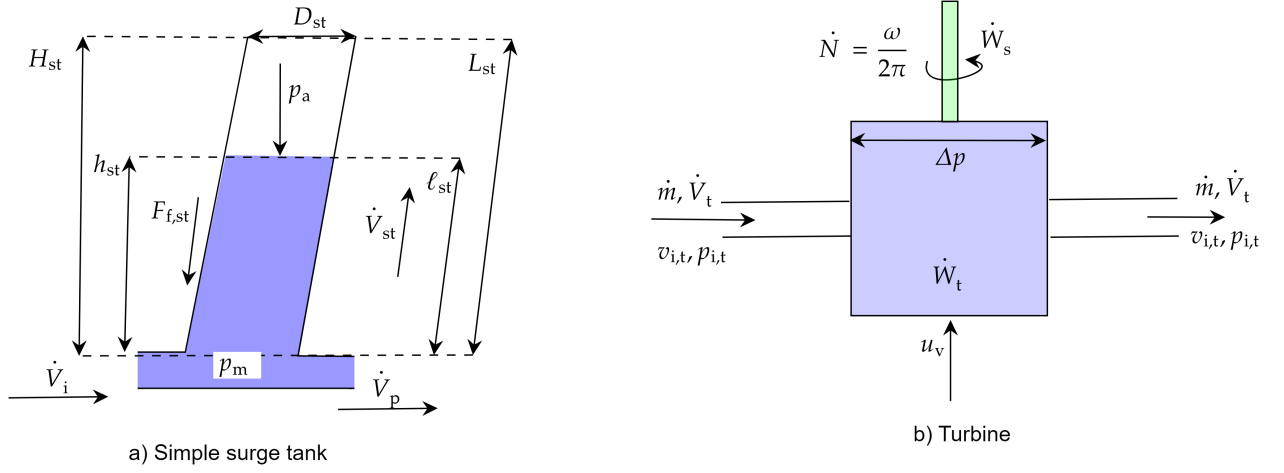


Figure 2.3: Hydropower units: (a) A simple surge tank, and (b) Turbine.

mass and the momentum balances for the tank are

$$\begin{aligned}\frac{dm_{st}}{dt} &= \dot{m}_{i,st} - \dot{m}_{e,st} \\ \frac{d\mathcal{M}_{st}}{dt} &= \dot{\mathcal{M}}_{i,st} - \dot{\mathcal{M}}_{e,st} + F_{st}\end{aligned}$$

where the mass of the water inside the surge tank is expressed as

$$\begin{aligned}m_{st} &= \rho V_{st} \\ V_{st} &= A_{st} \ell_{st},\end{aligned}$$

the influent mass flow rate  $\dot{m}_{i,st} = \rho \dot{V}_{st}$ , effluent mass flow rate  $\dot{m}_{e,st} = 0$ , influent momentum flow rate  $\dot{\mathcal{M}}_{i,st} = \frac{\rho \dot{V}_{st}}{A_{st}}$ , effluent momentum flowrate  $\dot{\mathcal{M}}_{e,st} = 0$ , and the total force action on the surge tank  $F_{st} = F_{p,st} - F_g - F_{f,st}$ . The pressure force is expressed as  $F_{p,st} = (p_m - p_a)A_{st}$ , the force due to gravity is calculated as  $F_g = m_{st}g \frac{H_{st}}{L_{st}}$ . The frictional force due to the fluid flow can be calculated as in Eq. 2.7 for the case of intake. Here, the intake losses due to change of direction of flow and/or change of diameter, and the losses when liquid is entering/leaving the tank are assumed negligible.

### 2.2.3.5 Penstock

A penstock pipe can be considered as a simple circular filled pipe with diameter  $D$ . Thus, the model of the intake pipe developed in Section 2.2.3.2 can be considered as the model of a penstock pipe.

### 2.2.3.6 Turbine

Figure 2.3 b) shows a general schematic of a turbine. The water flowing through the turbine with mass flow rate  $\dot{m}_t$  and volumetric flow rate  $\dot{V}_t$  experiences a pressure drop  $\Delta p_t = p_{i,t} - p_{e,t}$  and a velocity change  $v_{i,t} \rightarrow v_{e,t}$ ; we assume zero elevation change in the flows. The conservation of energy at the influent and effluent of the turbine gives

$$\frac{1}{2}\dot{m}_t v_{i,t}^2 + p_{i,t}\dot{V}_t = \frac{1}{2}\dot{m}_t v_{e,t}^2 + p_{e,t}\dot{V}_t + \dot{W}_t \quad (2.8)$$

where  $\dot{W}_t$  is the power imparted out of the moving fluid. Equation 2.8 is further simplified to give

$$\dot{W}_t = \Delta p_t \dot{V}_t + \frac{\dot{m}_t}{2} (v_{i,t}^2 - v_{e,t}^2). \quad (2.9)$$

The power imparted out of the fluid  $\dot{W}_t$  expressed in terms of efficiency of the turbine  $\eta$  and power available at the turbine shaft

$$\eta = \frac{\dot{W}_s}{\dot{W}_t}.$$

The efficiency of the turbine, considering a simplistic case, can be expressed as a function of actuator signal or the gate signal to control the fluid flow through the turbine  $u_v$ .

For reaction turbines such as low head Francis turbine or Kaplan turbine, the pressure drop term dominates in  $\dot{W}_t$  giving

$$\dot{W}_t \approx \Delta p_t \dot{V}_t.$$

The shaft power then can be expressed as

$$\dot{W}_s = \eta \Delta p_t \dot{V}_t. \quad (2.10)$$

The efficiency  $\eta$  of the turbine can be expressed as a function of gate signal  $u_v$  as shown in Figure 2.4.

Previous work [10] has studied models of Francis turbine validated with experimental data for Trollheim HPP. More specific models of turbines such as Pelton, Francis, and Kaplan are also studied in [20].

### 2.2.3.7 Discharge

The model of the discharge is similar to the model of the intake pipe.

### 2.2.3.8 Tailrace

The model of the tailrace is an exact mirror replica of the reservoir model.

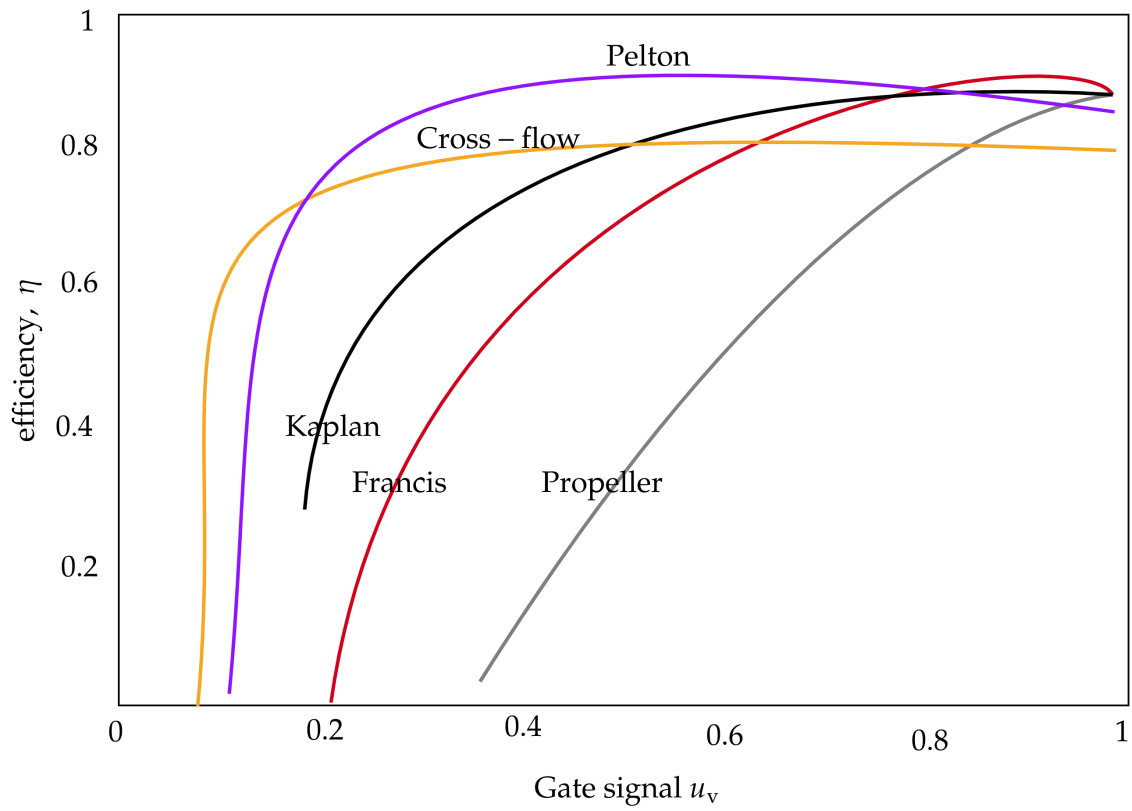


Figure 2.4: Typical efficiency  $\eta$  versus gate signal  $u_v$  for different kinds of turbine taken from [2].

## 2 Literature Review

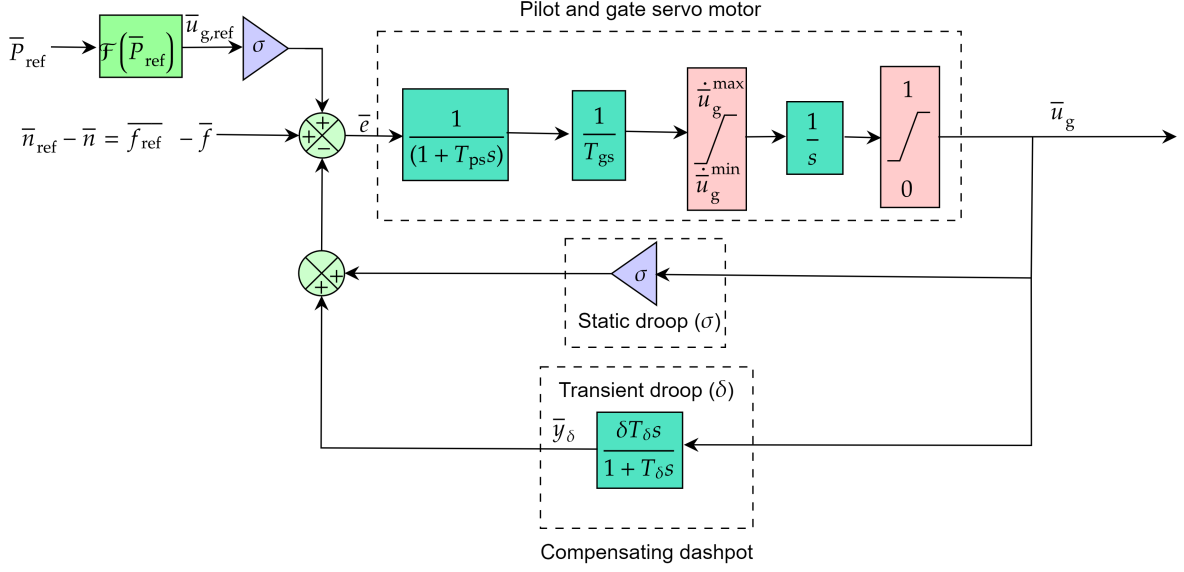


Figure 2.5: Hydropower governor.

### 2.2.3.9 Governor

Figure 2.5 shows the hydropower governor model formed by combining the differential equations of the pilot servo motor, the gate servo and the compensating dashpot [21]. The pilot and the gate servo motors form an open loop governor model with the differential equations

$$T_{gs} \frac{d\bar{u}_g}{dt} = \begin{cases} 0 & \text{if } \bar{u}_g \leq \bar{u}_g^{\min} \text{ \& } \bar{x}_g < 0 \\ 0 & \text{if } \bar{u}_g \geq \bar{u}_g^{\max} \text{ \& } \bar{x}_g > 0 \\ -\dot{\bar{u}}_g^{\min} & \text{if } \bar{x}_g \leq -\dot{\bar{u}}_g^{\min} \\ \dot{\bar{u}}_g^{\max} & \text{if } \bar{x}_g \geq \dot{\bar{u}}_g^{\max} \\ \bar{x}_g & \text{else} \end{cases}$$

$$T_{ps} \frac{d\bar{x}_g}{dt} + \bar{x}_g = \bar{e}$$

where  $T_{gs}$  is the gate servo motor time constant and  $T_{ps}$  is the pilot servo motor time constant.  $\bar{u}_g$  is the per unit gate signal out of the governor for the turbine, i.e.,  $\bar{u}_g = \bar{u}_v$ . A per unit quantity can be defined as the ratio of the actual quantity and the base quantity in which the system is evaluated. The per unit system is also defined in the forthcoming Section 2.3. The gate servo motor is constrained with the rate of the gate opening between the minimum rate of the gate opening  $\dot{\bar{u}}_g^{\min}$  and the maximum rate of the gate opening  $\dot{\bar{u}}_g^{\max}$ .  $\bar{x}_g$  is the internal state for the open loop governor model.  $\bar{e}$  is the error signal to the pilot and gate servo motors.

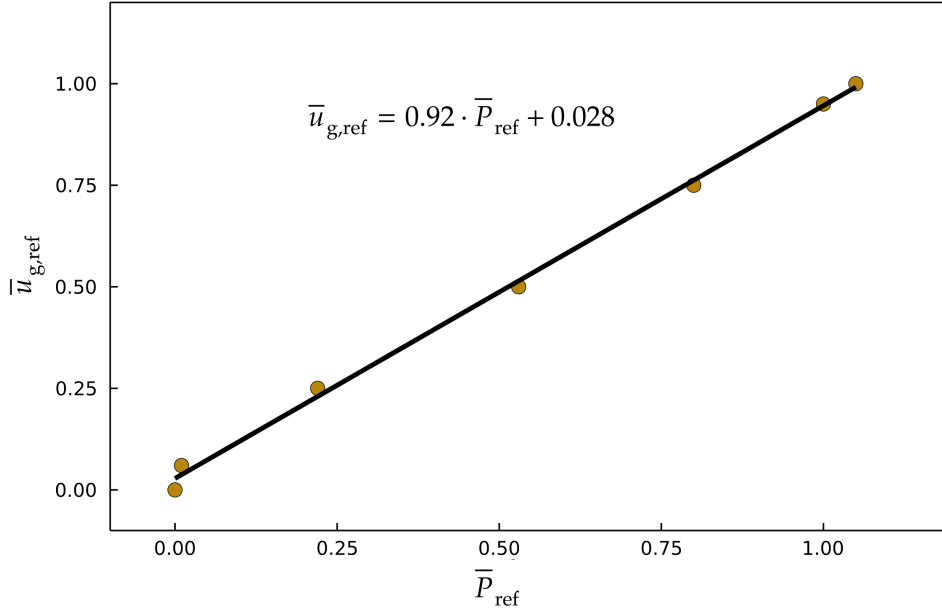


Figure 2.6: Linear functional relationship between  $\bar{u}_{\text{g,ref}}$  and  $\bar{P}_{\text{ref}}$ . The slope of the line = 0.92 indicates that as p.u. loading of the prime mover  $\bar{P}_{\text{ref}}$  runs towards the positive x-direction, and the rise in p.u. of the gate signal  $\bar{u}_{\text{g,ref}}$  decreases in the y-direction.

In Figure 2.5, the compensating dashpot has the transient droop coefficient  $\delta$ , and the needle valve settling time constant  $T_\delta$ . The governing equation of the dashpot is

$$T_\delta \frac{d\bar{x}_\delta}{dt} + \bar{x}_\delta = \delta \bar{u}_g$$

$$\bar{y}_\delta + \bar{x}_\delta = \delta \bar{u}_g$$

where  $\bar{x}_\delta$  is a state for the transient droop due to dashpot's working fluid. The error signal is generated based the frequency deviation and active power deviation, the static droop, and the transient droop as

$$\bar{e} = \frac{\bar{f}_{\text{ref}} - \bar{f}}{\bar{f}_{\text{ref}}} + \sigma (\bar{u}_{\text{g,ref}} - \bar{u}_g) - \bar{y}_\delta$$

$$\bar{u}_{\text{g,ref}} = \mathcal{F}(\bar{P}_{\text{ref}}).$$

The functional relationship between reference per unit gate signal  $\bar{u}_{\text{g,ref}}$  and per unit mechanical power reference  $\bar{P}_{\text{ref}}$  can be found as in [22]. Figure 2.6 shows a typical graph of  $\bar{P}_{\text{ref}}$  versus  $\bar{u}_{\text{g,ref}}$ , for instance, in the case of Trollheim hydropower plant with rated power 130MW.



### 2.2.3.10 Aggregate

The aggregate consists of the turbine and the synchronous generator. The aggregate can be modeled using the swing equation

$$\begin{aligned}\frac{d\delta}{dt} &= \omega - \omega_0 \\ J\omega \frac{d\omega}{dt} &= P_m - P_e \\ P_e &= P_\ell + D \frac{d\omega}{dt}\end{aligned}$$

where  $\delta$  is the rotor angle,

$\omega_0$  is a constant reference angular velocity,  $\omega$  is the angular velocity of the machine,  $J$  is the inertia of the coupled turbine-generator,  $P_m$  is the mechanical power out of the machine.  $P_e$  is the electrical power.  $D$  is the load damping factor.

### 2.2.4 Modeling of different types of surge tanks

The increasing use of intermittent renewable energy in modern electric power grid requires more flexible operation of hydropower. Hydropower can tackle a higher percentage of load acceptance and rejection. Surge tanks play an important role in reducing water hammer effects on pressure tunnels by acting as a buffer. The model of hydraulic transients inside the surge tank has a well-established theory using Newton's second law [23, 24].

Sudden changes in hydropower production leads to oscillations in the surge tank level, and larger changes gives larger amplitude. Higher mean hydropower production gives increased pressure loss in the intake race, which is balanced by an increased level in the surge tank. Presence of intermittent energy sources in the grid necessitates continuous changes in hydropower production. This implies an increased level of oscillations in the surge tank. Decrease in intermittent power implies an increase in hydropower, and therefore, higher level. If the decrease is substantial, this implies a) increased level, b) large amplitude in the oscillations. This requires a long surge shaft.

Because of geological challenges, the length of the surge tank may be limited. The amplitude of the water-mass oscillation can be reduced by using hydraulic resistance in the surge tank's input. There are two critical variables to consider: i) damped amplitude, and ii) turbine pressure. Surge tanks come in a variety of styles. The application of hydraulic resistances at the surge tank's input helps to prevent water hammer effects in the surge tank-turbine manifold.

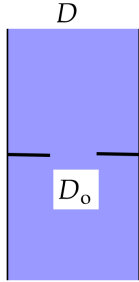
$$\begin{aligned}
 & N_{\text{Re}} < 2500 : \\
 & \phi_{\text{so}} = \left[ 2.72 + \left( \frac{D_o}{D} \right)^2 \left( \frac{120}{N_{\text{Re}}} - 1 \right) \right] \cdot \phi_{\text{so}}^0 \\
 & N_{\text{Re}} \geq 2500 : \\
 & \phi_{\text{so}} = \left[ 2.72 + \left( \frac{D_o}{D} \right)^2 \left( \frac{4000}{N_{\text{Re}}} \right) \right] \cdot \phi_{\text{so}}^0 \\
 & \text{where} \\
 & \phi_{\text{so}}^0 = \left[ 1 - \left( \frac{D_o}{D} \right)^2 \right] \left[ \left( \frac{D}{D_o} \right)^4 - 1 \right] \\
 & F_f \approx \frac{1}{2} \rho v |v| \left( A_w \frac{f_D}{4} + A \phi_{\text{so}} \right)
 \end{aligned}$$


Figure 2.7: Sharp orifice type fitting used for modeling the sharp orifice type surge tank.

Different types of surge tanks designed with respect to hydraulic resistances are presented in [25]. The time evolution equations for developing a mechanistic model of the surge tank are given in [26]. The hydraulic resistance at the inlet of different kinds of surge tanks can be studied from [26, 27]. Surge tanks are typically classified as open or closed. It is worthwhile to investigate the simple surge tank, the sharp orifice type surge tank, and the throttle valve surge tank. The frictional force caused by the orifice and throat of the surge tank's inflow can be corrected to design sharp orifice and throttle valve surge tanks.

The sharp orifice type surge tank can be modeled by considering frictional force due to the generalized friction factor for a sharp orifice type fitting as shown in Figure 2.7. The model of the simple surge tank developed in Section 2.2.3.4 can be used to develop a model of the sharp orifice type surge tank by adding the frictional force due to the sharp orifice. The overall frictional force for the sharp orifice type surge tank is given as

$$F_f = \frac{1}{2} \rho v |v| \left( A \frac{f_D}{4} + A \phi_{\text{so}} \right), \quad (2.11)$$

where  $A$  is the cross-sectional area of the surge tank,  $v$  is the average velocity of the water inside the tank,  $f_D$  is the Darcy's friction factor, and  $\phi_{\text{so}}$  is a generalized friction factor.  $\phi_{\text{so}}$  depends on  $N_{\text{Re}}$ , the diameter of the surge tank  $D$ , and the diameter of the orifice  $D_o$ . Figure 2.7 shows the generalized friction factor for different ranges of Reynolds numbers.

## 2 Literature Review

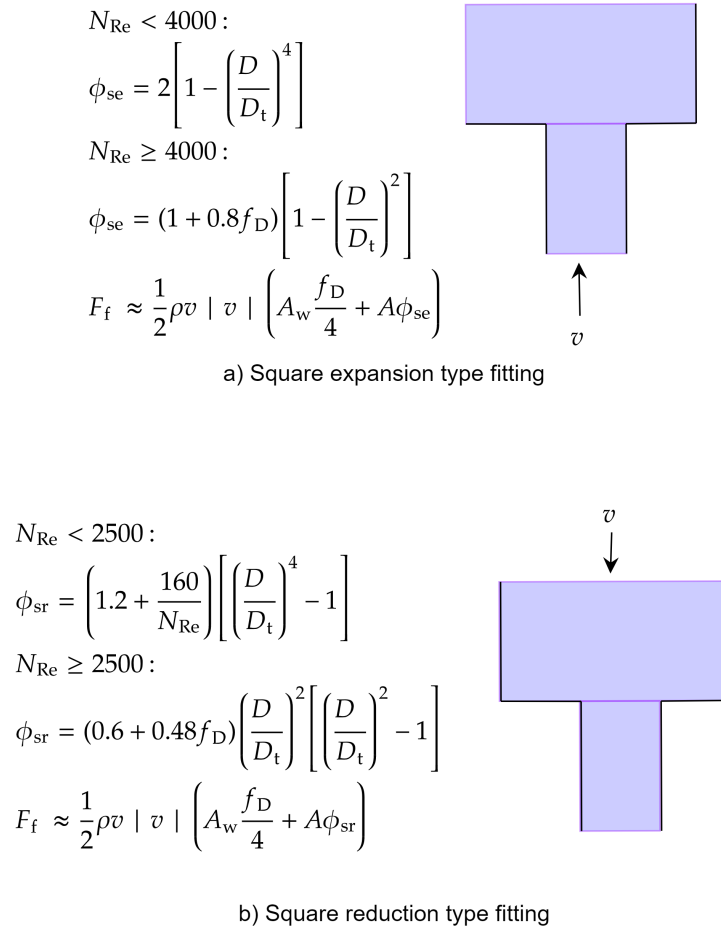


Figure 2.8: Square expansion and square reduction type fitting used for modeling of throttle valve surge tank.

Similarly, the model of the throttle valve surge tank can be modeled using square expansion and the reduction type fittings as shown in Figure 2.8.

The general schematic of an air-cushion surge tank is shown in Figure 2.9. The free water surface inside the surge tank is connected to pressurized air making it a closed type surge tank.

The pressure wave during a *load rejection* travels from a *high pressure region* (at the end of penstock) to the a *low pressure region* (near free water surface, i.e., through the surge tank in hydro power systems). During this period, water mass inside the surge tank oscillates driven by pressure waves traveling back and forth between the higher pressure region and free-water surface. The larger the amplitude of water mass oscillation is, the higher should be the physical height of the surge tank. For reducing the amplitude of

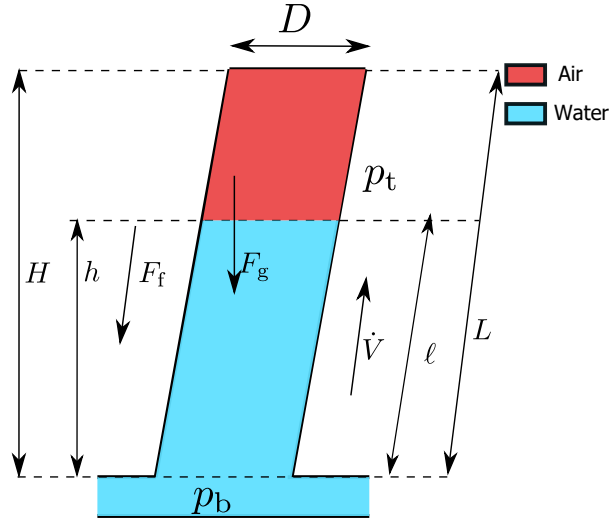


Figure 2.9: Air-cushion surge tank.

water oscillation inside the surge tank, pressurized air is placed inside the surge tank making a closed surge tank. This will cause the air to compress and expand adiabatically [7], and the energy due to high pressure is released as a form of work done for compression and rarefaction of the air. For an ideal gas, with reversible compression/decompression, we have,

$$pV^\gamma = \text{constant}, \quad (2.12)$$

where  $p$ ,  $V$ , and  $\gamma$  is the pressure, volume, and ratio of specific heats at constant pressure and at constant volume, respectively, for air. The mechanistic model of an air cushion surge tank is similar to that of a simple surge tank, however with correction terms for  $m$  and  $p_t$  for a simple surge tank.

The mass of water and air inside the surge tank is given as,

$$m = \rho A \ell + m_a, \quad (2.13)$$

and the air pressure inside the surge tank is given by,

$$p_t = p_c \left( \frac{L - \ell_0}{L - \ell} \right)^\gamma, \quad (2.14)$$

where  $m_a$  is the mass of air inside the surge tank given by expression,

$$m_a = \frac{p_c A (L - \ell_0) M_a}{R T^o}. \quad (2.15)$$

In Eq. 2.14,  $p_c$  is the initial air cushion pressure when the initial slant height of liquid level inside the surge tank is  $\ell_0$ . The expression shown in Eq. 2.14 is derived from Eq. 2.12 equalizing the *initial* and *final* expression. In Eq. 2.15,  $M_a$  represents the molar mass of air,  $R$  is the universal gas constant, and  $T^o$  is the temperature of the air inside the surge tank.

Table 2.3:  $\phi_{ms}^0$  for different value of  $\theta$  .

$\theta$	15	30	45	60	90
$\phi_{ms}^0$	0.04	0.16	0.36	0.64	1

### 2.2.5 Modeling of draft tubes

A draft tube is a diverging pipe placed at the exit of the turbine's runner, and it utilizes the kinetic energy of water available at the exit of the turbine. Draft tubes are only used in reaction type turbines, for example, the Francis turbine and the Kaplan turbine. The pressure at the turbine's outlet can be reduced by inserting a draft tube, which increases the effective pressure change across the turbine, hence increasing the power production and the turbine efficiency.

In OpenHPL, a simple model of a draft tube is considered using a mechanistic model of a simple pipe as studied in previous work [6]. It is of interest to study two different kinds of draft tubes, viz., conical diffuser type draft tube and Moody spreading pipes as a feature extension of OpenHPL.

Figure 2.10 shows two different kinds of filled pipes. Figure 2.10 a) shows a circular diffuser that can be used as a conical diffuser type draft tube. The generalized friction factor due to the diffusion for the conical diffuser is expressed as [3]

$$\phi_{cd} = k \left( 1 - \frac{D_i}{D_o} \right)^2$$

where  $k$  is a constant that depends on the angle of diffusion from the smaller input diameter to the larger output diameter. For a maximum efficiency conical diffuser, an  $8^\circ$  diffusion angle is generally considered with  $k \approx 0.23$  [3]. If the length of the conical diffuser is not suitable for a hydropower plant, a model of the Moody spreading pipes can be used which will reduce the extra excavation required for installing longer conical diffuser.

Figure 2.10 b) shows a bifurcation pipe that can be used for modeling the Moody spreading pipes type draft tube where the generalized friction factor due to the bifurcation angle  $\theta$  is given as

$$\phi_{ms} = 1 + \frac{v_b}{v_m} - 2 \frac{v_b}{v_m} \cos \theta - \phi_{ms}^0 \left( \frac{v_b}{v_m} \right)^2$$

where  $v_m$  is the entry velocity in the main part and  $v_b$  is the velocity of water in the bifurcated branches. The diameter of both branches is considered equal.  $\phi_{ms}^0$  is calculated as in Table 2.3.

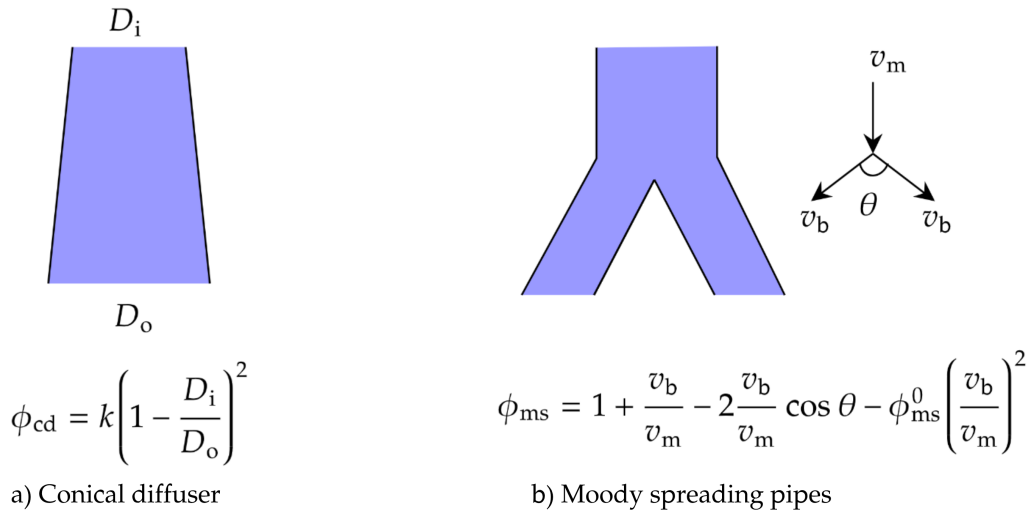


Figure 2.10: a) A conical diffuser based on [3] and b) Moody spreading pipes draft tube based on [4].

## 2.3 Active Power Frequency Control

An electric power system network should maintain its frequency and voltage within the permissible limits during disturbances such as load add/loss, generation loss/add, etc. In this thesis only algorithms for maintaining the frequency of the grid are implemented. The frequency of the grid is maintained by controlling the water flow based on which the power plant's governor's active power set-points are changed to balance between the load and the generation. However, the voltage of the network grid is maintained by controlling the reactive power out of the generator.

It is of interest to implement a standard method for an active power frequency control loop in OpenHPL. To study the active power frequency control of the grid, a *per unit* based linearized model of the network can be formed using transfer functions as in [28] and [29]. A per unit quantity, generally abbreviated as **p.u.**, is expressed as

$$\text{p.u.} = \frac{\text{actual quantity}}{\text{base quantity}}. \quad (2.16)$$

In this section, literature regarding control of the power grid is provided. Two types of controllers are discussed, viz., a PI controller and an MPC.

### 2.3.1 Linearized model

The following are the linearized models for the components of the electric power system grid.

In the sequel,  $x^\delta \triangleq x - x_0$  where  $x^\delta$  is the deviation of variable  $x$  from the operating point  $x_0$ . Furthermore,  $\bar{x}^\delta$  is the per unit deviation of the variable.

#### 2.3.1.1 Generator

A linearized model of a generator can be formed using the swing equation. The per unit rate of change of deviation in frequency of the generator is expressed as

$$\frac{d\bar{f}^\delta}{dt} = \frac{\bar{P}_m^\delta - \bar{P}_e^\delta}{M} \quad (2.17)$$

where  $\bar{P}_m^\delta$  is the per unit change in mechanical power,  $\bar{P}_e^\delta$  is the per unit change in electrical power, and  $M$  is the machine constant. Taking the Laplace transform of Eq. 2.17, we get

$$sM\bar{f}^\delta(s) = \bar{P}_m^\delta(s) - \bar{P}_e^\delta(s)$$

where  $s$  is the Laplace variable, and  $\bar{P}_e^\delta(s)$  may depend on  $\bar{f}^\delta(s)$ .

#### 2.3.1.2 Load

The electrical load is the sum of frequency dependent and independent loads. Resistive loads are frequency independent, while motor loads, etc. are frequency dependent. Particularly, in the context of modern smart grids all loads behind an inverter are independent of the grid frequency, even if they drive a non-resistive load such as a compressor.

The electrical load is given as

$$\bar{P}_e^\delta = \bar{P}_\ell^\delta + D\bar{f}^\delta$$

where  $D$  is the load damping factor expressed as per unit change in load divided by per unit change in frequency.

#### 2.3.1.3 Hydroturbine

A linearized model of a hydroturbine can be found relating per unit change in mechanical power  $\bar{P}_m^\delta$  with per unit change in turbine valve position  $\bar{P}_v^\delta$  and expressed as

$$\bar{P}_m^\delta(s) = \frac{1 - T_w s}{1 + \frac{T_w s}{2}} \bar{P}_v^\delta(s)$$

where  $T_w$  is the water starting time at rated load [29]. The water starting time is expressed in terms of the nominal head  $H^n$  and the nominal volumetric flow rate  $\dot{V}^n$  as

$$T_w = \frac{L_p \dot{V}^n}{g A_p H^n}$$

where  $L_p$  and  $A_p$  are the length and the cross-sectional area of the penstock.

### 2.3.1.4 Governor

Similar to the hydroturbine transfer function model, the per unit change in governor power  $\bar{P}_g^\delta$  can be related to the per unit change in turbine valve position  $\bar{P}_v^\delta$  as

$$\bar{P}_v^\delta(s) = \frac{1}{1 + T_g s} \bar{P}_g^\delta(s)$$

where  $T_g$  is the governor's servo motor time constant.

The differential equations for the governor can be written as

$$\frac{d\bar{P}_v^\delta}{dt} = \frac{\bar{P}_g^\delta - \bar{P}_v^\delta}{T_g}$$

and the differential equation of the hydro-turbine is given as

$$\frac{T_w}{2} \frac{d\bar{P}_m^\delta}{dt} + \bar{P}_m^\delta = \bar{P}_v^\delta - T_w \frac{d\bar{P}_v^\delta}{dt},$$

which can be further expressed by inserting expression for  $\frac{d\bar{P}_v^\delta}{dt}$  as

$$\frac{d\bar{P}_m^\delta}{dt} = 2 \left( \frac{1}{T_w} + \frac{1}{T_g} \right) \bar{P}_v^\delta - \frac{2}{T_g} \bar{P}_g^\delta - \frac{2}{T_w} \bar{P}_m^\delta.$$

## 2.3.2 Control of power grid

Based on the operation of a power plant either in isolated mode or in interconnected mode, three kinds of active power frequency control modes are described for the power plant. They are: isochronous governor control, droop governor control, and automatic generation control.



2 Literature Review

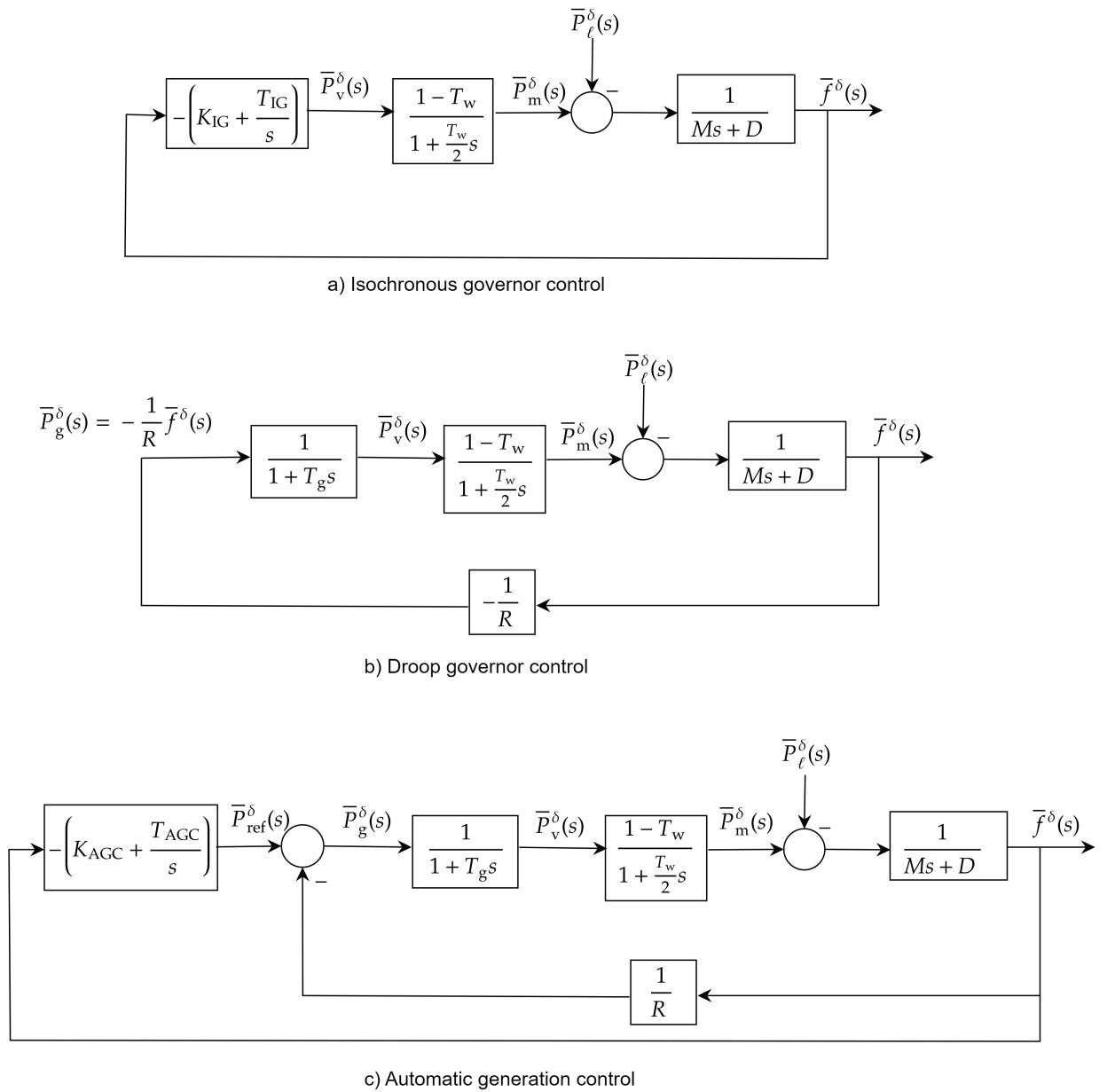


Figure 2.11: Power frequency governor control of a power plant.

### 2.3.2.1 Isochronous governor control

In isochronous governor control of a hydropower plant, the hydroturbine is directly controlled by sensing the change in frequency of the grid. The per unit change in the turbine valve signal is given as

$$\bar{p}_v^\delta(s) = - \left( K_{IG} + \frac{T_{IG}}{s} \right) \bar{f}^\delta(s).$$

where  $K_{IG}$  is the proportional gain and  $T_{IG}$  is the integral time constant. An isochronous governor is simply a PI controller with parameters  $K_{IG}$  and  $T_{IG}$ . Figure 2.11 a) shows the block diagram of an isochronous governor. An isochronous governor is used mostly in island operation of a power plant.

### 2.3.2.2 Droop governor control

If an isochronous governor is used in a multi-generator system supplying a common consumer load, each governor will try to control system frequency. Because the grid frequency is given by the difference between the total generation and load, it is only possible to have a single integral controller in the system. In a multi-generator system governors are provided with speed-droop/frequency-droop characteristics so that the speed drops as the load is increased, and vice-versa. Figure 2.11 b) shows the droop governor control or often termed as the *primary control* of a power plant. In Figure 2.11 b)  $R$  is simply termed as droop or regulation. The droop  $R$  can be defined as the ratio of the change in per unit frequency to the change in per unit turbine valve position expressed as

$$R = \frac{\bar{f}^\delta}{\bar{p}_v^\delta}.$$

The droop parameter  $R$  is often expressed in percentage (%). For instance,  $R = 5\%$  droop means that a 5% frequency deviation will cause 100% change in turbine valve position.

### 2.3.2.3 Automatic generation control (AGC)

In a droop governor control (or primary control) of a multi-generator system supplying a common consumer load, after the load disturbance, the system frequency attains a new steady-state value. Based on the droop characteristics of the generating units, the overall change in the generation will be shared among all the generating units.

In the droop governor control, the frequency of the grid is not restored to nominal frequency or 50Hz because the droop controllers do not have integral action. The frequency of the grid is only restored after the supplementary control or secondary control by adjusting the load reference set-point (governor power set-point). Figure 2.11 c) shows the

## 2 Literature Review

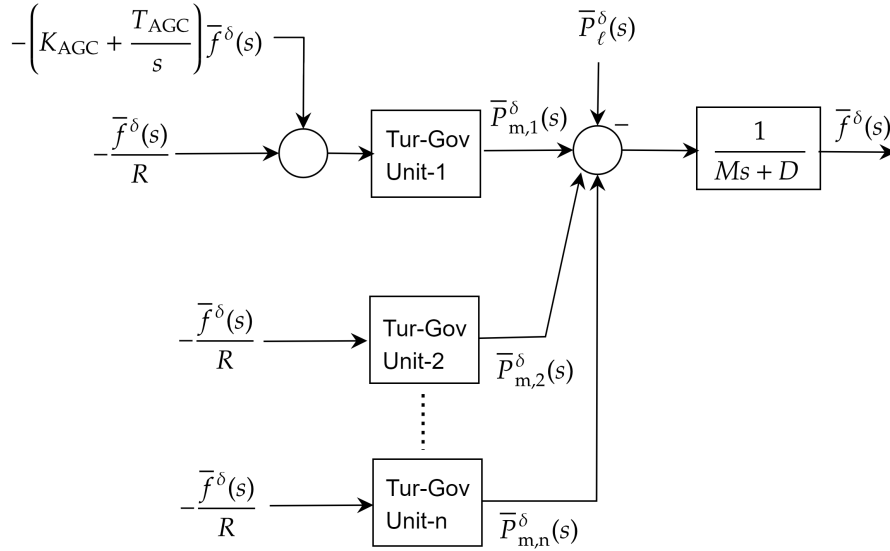


Figure 2.12: Synchronous area with the multi-generator system showing primary control to other units and secondary control to AGC unit (Unit-1). If other units take part in the secondary control, then a PI controller is used to adjust the load reference set points of the units.

AGC of a power plant for an isolated power system network. The load reference set-point  $\bar{P}_{ref}^\delta$  is expressed in terms of a PI controller where the integral control action ensures zero frequency error in steady-state. The expression for  $\bar{P}_{ref}^\delta$  is given as

$$\bar{P}_{ref}^\delta(s) = - \left( K_{AGC} + \frac{T_{AGC}}{s} \right) \bar{f}^\delta(s).$$

### AGC in an isolated power grid

Figure 2.11 c) shows AGC for an isolated power system network that can be used for the system where multi-generators are supplying a common consumer load. A power system network with multiple generators supplying a common consumer load is often termed a *single area* or a *synchronous area*. Figure 2.12 shows a synchronous area showing supplementary control to AGC unit<sup>26</sup> (Unit-1) using a PI controller to restore the grid frequency to nominal operating conditions. In the figure, all others units are considered to be non-AGC units.

As the load disturbance occurs in the area:

1. all the generating units will have primary control/droop governor actions and the frequency attains a new steady state

<sup>26</sup>Unit that takes part in the supplementary control or secondary control is called an AGC unit.

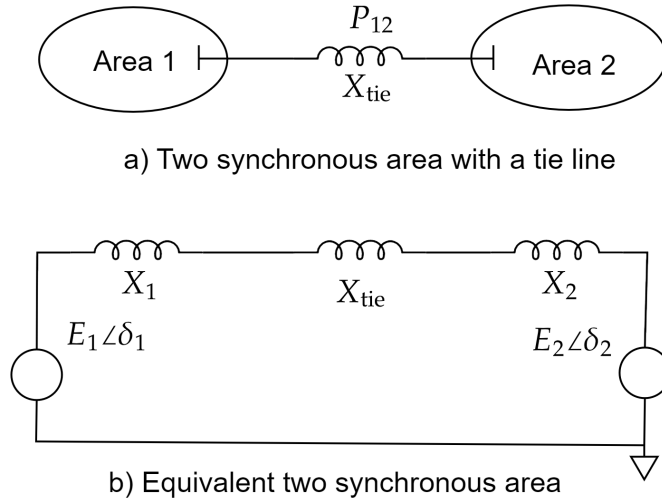


Figure 2.13: Two synchronous areas represented by voltage sources and their respective power angles. The areas are connected with a lossless tie line with reactance  $X_{\text{tie}}$ .

2. the total generation change to cope with the total load variation is shared among all the generating units based on their droop characteristics.

To correct the deviation in the grid frequency from the nominal operating point, supplementary control or *secondary control* is done to the AGC units in the area. The secondary control will ensure:

1. restoration of the grid frequency to the nominal operating point
2. all the units other than AGC units will return to their own scheduled values.

### AGC in interconnected power grid

Figure 2.13 a) shows an interconnected network with two synchronous areas. Each synchronous area has primary control units and AGC units. The two areas are connected with a tie line reactance  $X_{\text{tie}}$ . The power frequency control study of two area systems can be extended to any  $n$ -area system.

The active power transferred over a tie line is given as

$$P_{12} = \frac{|E_1| |E_2|}{X_{12}} \sin \delta_{12} \quad (2.18)$$



where  $X_{12} = X_1 + X_{\text{tie}} + X_2$  and  $\delta_{12} = \delta_1 - \delta_2$ . Equation 2.18 can be linearized for a small deviation in the tie line flow in per unit as  $\bar{P}_{12}^\delta$  from nominal value as

$$\begin{aligned}\bar{P}_{12}^\delta &= \left. \frac{\partial \bar{P}_{12}}{\partial \bar{\delta}_{12}} \right|_{\bar{\delta}_{120}} \bar{\delta}_{12}^\delta \\ &= \bar{P}_s \bar{\delta}_{12}^\delta\end{aligned}$$

where  $\bar{P}_s$  is the synchronizing power coefficients given as

$$\begin{aligned}\bar{P}_s &= \left. \frac{\partial \bar{P}_{12}^\delta}{\partial \bar{\delta}_{12}} \right|_{\bar{\delta}_{120}} \\ &= \frac{|\bar{E}_1| |\bar{E}_2|}{\bar{X}_{12}} \cos \bar{\delta}_{120}^\delta.\end{aligned}$$

The tie line power deviation is then expressed as

$$\bar{P}_{12}^\delta = \bar{P}_s \bar{\delta}_{12}^\delta.$$

For  $\bar{\delta}_1^\delta > \bar{\delta}_2^\delta$  the tie line power flows from area 1 to area 2 and vice-versa. Figure 2.14 shows the block diagram of AGC for two synchronous areas. The function of AGC in the interconnected areas is to:

- keep the frequencies of areas around the nominal value
- keep the scheduled tie-line power flow between the areas.

The AGC control for a single area as shown in Figure 2.11 c) restores the grid frequency to the nominal value by changing the load reference set-point of the AGC unit in the area. For two area control the AGC minimizes the area control error  $\bar{\epsilon}$ . The area control errors are given as

$$\begin{aligned}\bar{\epsilon}_1 &= \bar{P}_{12}^\delta + B_1 \bar{f}_1^\delta \\ \bar{\epsilon}_2 &= \bar{P}_{21}^\delta + B_2 \bar{f}_2^\delta.\end{aligned}$$

### 2.3.3 MPC for AGC

Due to the increasing use of intermittent sources in the power grid, the conventionally tuned-based PI controller may not be sufficient to guarantee stability and reliable power supply during large disturbances. Since, MPC can handle hard constraints in both output frequency and generation rate, it is of interest to compare the frequency response from PI control and MPC for AGC during a large disturbance.

## 2 Literature Review

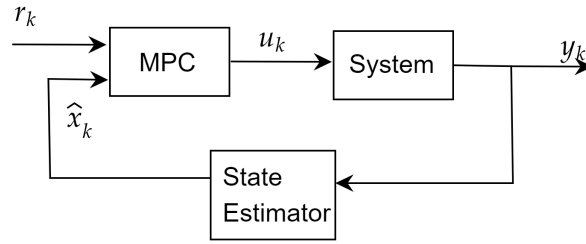


Figure 2.15: Block diagram of MPC.

### 2.3.3.1 MPC

Figure 2.15 shows an MPC controller used for generating input signal  $u_k$  at time step  $k$  to control the system to track the desired reference  $r_k$ . The MPC controller solves an optimization problem at each time step to find the optimal system input over a fixed time horizon with respect to an objective function  $J(\cdot)$ . The first element of the optimal input over the horizon is applied to the system, and this process continues as the time step progresses. An estimator such as Kalman filter [30] is used for estimating state  $\hat{x}_k$  from measurement  $y$ .

An objective function of a reference tracking MPC, sum of the running cost over the horizon and the terminal cost, can be given as

$$\min_{e,u} J = \left( \sum_{k=1}^{N_p-1} e_k^T Q e_k + \Delta u_k^T R \Delta u_k \right) + e_{N_p}^T S e_{N_p} \quad (2.19)$$

*s.t*

$$x_{k+1} = Ax_k + Bu_k + Gw_k$$

$$y = Cx_k$$

$$e_k = y_k - r_k$$

$$x_0 = \text{given}$$

(2.20)

$$x_{\min} \leq x_k \leq x_{\max}$$

$$\dot{x}_{\min} \leq \dot{x}_k \leq \dot{x}_{\max}$$

$$u_{\min} \leq u_k \leq u_{\max}$$

$$\dot{u}_{\min} \leq \dot{u}_k \leq \dot{u}_{\max}$$

(2.21)

where the objective function is subjected to the state space model of an input/output system, error between the output and the reference trajectory/set-point, and the terminal constraints.

In Eq. 2.19,

- $e_k$  is the error from the reference trajectory at time step  $k$
- $Q$  and  $R$  are the weighting matrices for the running cost over the prediction horizon  $N_p$
- $S$  is the weighting matrix for the terminal cost
- $Q, R$  and  $S$  are all assumed to be symmetric
- $R$  is assumed to be positive definite, whereas  $Q$  and  $S$  are positive semi-definite
- the cost is subjected to the discrete linearized system with state transition matrix  $A$ , control matrix  $B$ , disturbance matrix  $G$ , and output matrix  $C$
- constraints that includes bounds on the state and input.

Furthermore, in MPC it is also possible to put constraints on the rate of change of state and input, i.e.,  $\dot{x}_{\min} \leq \dot{x}_k \leq \dot{x}_{\max}$  and  $\dot{u}_{\min} \leq \dot{u}_k \leq \dot{u}_{\max}$ , respectively.

### 2.3.3.2 AGC Prediction Model for MPC

The transfer function based linearized model in Section 2.3.1 can be transformed into time domain equation by taking the inverse Laplace transform. Any first order transfer function can be written in the form of input  $u(s)$ , output  $y(s)$ , and time constant of the system  $T$  as

$$y(s) = \frac{1}{Ts+1}u(s)$$

Taking inverse Laplace transform, the result is a first order differential equation

$$T \frac{dy}{dt} + y = u$$

where  $u$  is the input and  $y$  is the output in the time domain.

The following are the time domain equations for the components of the electric power system from Section 2.3.1

$$\frac{d\bar{f}^\delta}{dt} = \frac{\bar{P}_m^\delta - \bar{P}_\ell^\delta - D\bar{f}^\delta}{M} \quad (2.22)$$

$$\frac{d\bar{P}_m^\delta}{dt} = 2 \left( \frac{1}{T_w} + \frac{1}{T_g} \right) \bar{P}_v^\delta - \frac{2}{T_g} \bar{P}_g^\delta - \frac{2}{T_w} \bar{P}_m^\delta. \quad (2.23)$$

$$\frac{d\bar{P}_v^\delta}{dt} = \frac{\bar{P}_g^\delta - \bar{P}_v^\delta}{T_g}. \quad (2.24)$$

Equation 2.22 combines the models of generators in the grid and the electrical power. Equation 2.23 shows the time domain equation of the mechanical power and Eq. 2.22



## 2 Literature Review

represents the time domain linearized model of the governor. For the AGC as shown in Figure 2.11 c), the per unit change in governor power  $\bar{P}_g^\delta$  is expressed as

$$\bar{P}_g^\delta = \bar{P}_{\text{ref}}^\delta - \frac{\bar{f}^\delta}{R}. \quad (2.25)$$

Putting expression of Eq. 2.25 in Eq. 2.23, the Eq. 2.23 can be further expressed as

$$\frac{d\bar{P}_m^\delta}{dt} = 2 \left( \frac{1}{T_w} + \frac{1}{T_g} \right) \bar{P}_v^\delta - \frac{2}{RT_g} \bar{f}^\delta - \frac{2}{T_w} \bar{P}_m^\delta - \frac{2}{T_g} \bar{P}_{\text{ref}}^\delta.$$

Similarly, from the Eq. 2.24 we get

$$\frac{d\bar{P}_v^\delta}{dt} = \frac{1}{T_g} \bar{P}_{\text{ref}}^\delta - \frac{1}{RT_g} \bar{f}^\delta - \frac{1}{T_g} \bar{P}_v^\delta.$$

Equations 2.22 to 2.25 can be written as. the following linear time invariant (LTI) system

$$\frac{d\bar{x}}{dt} = \bar{A}_m \bar{x} + \bar{B}_m \bar{u} + \bar{G}_m \bar{w} \quad (2.26)$$

$$\bar{y} = \bar{C}_m \bar{x} \quad (2.27)$$

with  $\bar{x} = (\bar{f}^\delta, \bar{P}_m^\delta, \bar{P}_v^\delta)$ ,  $\bar{u} = \bar{P}_{\text{ref}}^\delta$ ,  $\bar{w} = \bar{P}_\ell^\delta$ , and  $\bar{y} = \bar{f}^\delta$ , respectively. The system matrices of the AGC prediction model for MPC are given as

$$\bar{A}_m = \begin{bmatrix} -\frac{D}{M} & \frac{1}{M} & 0 \\ -\frac{2}{RT_g} & -\frac{2}{T_w} & 2 \left( \frac{1}{T_w} + \frac{1}{T_g} \right) \\ -\frac{1}{RT_g} & 0 & -\frac{1}{T_g} \end{bmatrix}$$

$$\bar{B}_m = \begin{bmatrix} 0 \\ -\frac{2}{T_g} \\ \frac{1}{T_g} \end{bmatrix}$$

$$\bar{G}_m = \begin{bmatrix} -\frac{1}{M} \\ 0 \\ 0 \end{bmatrix}$$

$$\bar{C}_m = [ 1 \ 0 \ 0 ].$$

Equations 2.26 and 2.27 are the continuous time domain model. For MPC, a discrete time domain model is used at sampling time  $\Delta t$ . The discrete time domain can be obtain using exact discretization<sup>27</sup> as

$$\bar{A}_{\text{md}} = e^{\bar{A}\Delta t} \quad (2.28)$$

$$\bar{B}_{\text{md}} = \left( e^{\bar{A}\Delta t} - I \right) \bar{A}^{-1} \bar{B} \quad (2.29)$$

$$\bar{G}_{\text{md}} = \left( e^{\bar{A}\Delta t} - I \right) \bar{A}^{-1} \bar{G} \quad (2.30)$$

where output matrices are equal in both continuous and discrete time domains, i.e.,  $\bar{C}_{\text{md}} = \bar{C}_{\text{m}}$ .

Expressions 2.28, 2.29, and 2.30 can now be used in the constraints of the objective function in Eq. 2.19.

### 2.3.3.3 System

For emulating a real system (or a real plant), we will use the linearized model of hydropower plant developed in OpenHPL. Models developed in OpenHPL are linearized as in [31]. The continuous time linearized models from OpenHPL is converted into the discrete time domain and used for finding current output measurement  $y_k$  at time step  $k$ .

### 2.3.3.4 State estimator

At each time step  $k$ , MPC required knowledge of all the states for the prediction model. A linear Kalman filter can be used for AGC. A linear system with system disturbance  $w$  and process noise  $\mathbf{v}$ , and measurement  $y$  with measurement noise  $\mu$  is given as

$$x_{k+1} = Ax_k + Bu_k + Gw_k + \mathbf{v}_k \quad (2.31)$$

$$y_k = Cx_k + \mu_k. \quad (2.32)$$

In Eq. 2.31  $\mathbf{v}$  is considered with zero mean and co-variance  $\mathcal{V}$ , and in Eq. 2.32  $\mu$  is considered with zero mean and co-variance  $\mathcal{U}$ , i.e.,  $\mathbf{v}_k \sim \mathcal{N}(\mathbf{0}, \mathcal{V})$  and  $\mu_k \sim \mathcal{N}(0, \mathcal{U})$ .

A linear Kalman filter has two steps:

- Prediction:

$$\hat{x}_{k|k-1} = Ax_{k-1|k-1} + Bu_k + Gw_k$$

$$\hat{\mathcal{X}}_{k|k-1} = A\mathcal{X}_{k-1|k-1}A^T + \mathcal{V},$$

<sup>27</sup><https://en.wikipedia.org/wiki/Discretization>

- Update:

$$\begin{aligned}\hat{x}_{k|k} &= \hat{x}_{k|k-1} + K_k \varepsilon_k \\ \varepsilon_k &= y_k - C \hat{x}_{k|k-1} \\ K_k &= \hat{\mathcal{X}}_{k|k-1} C^T \mathcal{E}_k^{-1} \\ \mathcal{E}_k &= C \hat{\mathcal{X}}_{k|k-1} C^T + \mathcal{U}\end{aligned}$$

$$\hat{\mathcal{X}}_{k|k} = (I - K_k C) \hat{\mathcal{X}}_{k|k-1}$$

$\hat{x}_{k|k-1}$  is the predicted *a priori* state estimate using the prior  $x_{k-1|k-1}$ ,  $\hat{x}_{k|k}$  is the *a posteriori* state estimate,  $\hat{\mathcal{X}}_{k|k-1}$  is the *a priori* estimate of the state co-variance using the prior  $\mathcal{X}_{k-1|k-1}$ , and  $\hat{\mathcal{X}}_{k|k}$  is the *a posteriori* estimate of the state co-variance.  $K_k$  is the Kalman gain,  $\varepsilon_k$  is the innovation residual, and  $\mathcal{E}_k$  is the innovation co-variance at time step  $k$ .

## 2.4 Thermal Model of Synchronous Generator

Electricity generation from intermittent sources is rapidly increasing in modern electric power system networks. The intermittency in these sources causes the power system networks to operate in different operating conditions. Dispatchable sources such as hydro power can be used for removing the variability in the system's power production caused by intermittent sources [32, 33]. A concept of *flexible* hydropower is coined in [34] for modern intermittent power system networks. Thus, in a modern power system, the hydro generators play a significant role in the flexible operation of the intermittent grid. The performance of the synchronous generator depends on its *capability diagram* [5]. The capability diagram provides information about the operating regimes of the synchronous generator in case of the various operational limits, viz., armature current limit, field current limit, and under-excitation [35]. In [36], an instance of exploiting more active power from the hydro generator is studied by controlling the internal temperature of the machine. By monitoring the temperature of the rotor copper, stator copper, and stator iron, it will be possible to adjust the armature current limit and the field current limit, which will lead to a reduction in the resistance of the armature and the field winding. Furthermore, because of an increase in the active current through the synchronous generator, more active power can be exploited. The temperature of the machine is controlled by the cooled air circulation through the generator's internal surfaces. The cooled air is supplied through a heat exchanger in a closed loop.

In this section:

- First, previous research work is provided regarding the thermal model of the synchronous generator
- Second, literature regarding the working principle of the thermal synchronous generator is provided
- Third, a mathematical mechanistic model of the thermal synchronous generator is provided, and
- The literature is extended with the inclusion of literature regarding the state estimations using Bayesian inference.

### 2.4.1 Previous work

A brief review of thermal analysis of electrical machines is given in [37]. Lumped-parameter thermal network (LPTN) models of the thermal machines are provided in [38, 39]. Finite element analysis (FEM), and computational fluid dynamics (CFD) models were studied in [40]. More recently, a totally enclosed thermal model of an air-cooled hydro generator has been developed in [41] using a closed-loop heat exchanger model for cooling heated air from the outlet of the generator.

Prior work at USN on a thermal model of a synchronous generator involves the concept of enhancing the capability diagram of the synchronous generator by monitoring the internal temperature of the machine to increase power system stability in the modern electric grid supplied by intermittent sources; Øyvang (2018) [5]. Øyvang (2018) studied the interplay between the current, voltage, and power production of a synchronous machine. Øyvang (2018) proposed a model predictive control system for exploiting maximum performance out of the generator's thermal capacity by monitoring the metals and air temperatures of the generator. For experimental purposes, Øyvang (2018) used a 103 MVA air-cooled hydrogenerator from Åbjøra HPP in Norway. Øyvang (2018) developed a thermal model of a totally enclosed air-cooled hydrogenerator by using a closed loop water-cooled heat exchanger for cooling heated air from the outlet of the generator. For estimating states in the model predictive control system for the thermal synchronous generator, Øyvang (2018) used the Unscented Kalman Filter (UKF). In predictive control systems, model improvement and state estimation are important.

Similar modeling work was carried out by Lie (2018) with a more general structure of the thermal circuit of the machine, and the inclusion of a more efficient heat exchanger description. In addition, Pandey (2019) also extended the thermal model from Lie (2019) with temperature dependent specific heat capacities of fluid (air+water) inside the machine and temperature dependent copper resistances (stator+rotor copper resistances). The extended models were then used in Pandey (2019) for comparing several variations of UKF, as well as introducing of Ensemble Kalman Filter (EnKF). It was too early,

## 2 Literature Review

then, to make a conclusion about the choice of models in Pandey (2019) due to computational issues with the temperature dependent thermal models for on-line use. It was also emphasized that there is a need for the parameter tuning and the model refinement for eradicating computational issues as the effect the temperature dependence in the heat capacities has a noticeable effect on the solution of the model. Aleikish (2020) [42] studied hybrid (mechanistic+data-driven) models for the thermal model of the synchronous generator. The data-driven model was developed by solving a two point boundary value problem for the heat exchanger multiple times under different conditions, and then fitting a data-driven model (linear and non-linear regression) to this data. The numerical computation for the models with specific heat capacities in Pandey (2019) was made approximately 2000 times faster using hybrid models in Aleikish (2020). Furthermore, the feasibility of the use of machine learning and recurrent neural networks for parameter estimation of the thermal model of the synchronous generator is studied in Melfald (2020) [43]. It is of interest to further extend the work with inclusion of Bayesian inference for improving estimation of parameters, model fitting, and state estimation using the thermal model from Pandey (2019). In this thesis work, the main focus is on state estimation using Bayesian inference.

### 2.4.2 Working principle of the thermal model

Figure 2.16 shows the thermal operation of an air-cooled synchronous generator. The cold air out of the heat exchanger is blown by a fan into the rotor/stator air gap. The air is heated by heat flow from the rotor, air gap windage, and bearing friction. Furthermore, the air is forced into the iron cores which then get heated by the heat flow from the iron cores. The heated air is now collected at the stator's outlet and passed through the heat exchanger. The heated air is then cooled to the desired temperature using continuous cold water circulation in the heat exchanger and then fed again into the air gap as a continuous process. The heat exchanger is fed with cold water, with mass flow rate  $\dot{m}_w$  at temperature  $T_w^c$ . The air mass flow rate is  $\dot{m}_a$  with temperature  $T_a^h$  at the stator outlet and heat exchanger entry. The rotor copper heat source,  $\dot{Q}_r^\sigma$ , is due to rotor field current,  $I_f$ . Similarly, the stator copper heat source,  $\dot{Q}_s^\sigma$  is due to stator terminal current  $I_t$ .  $\dot{Q}_{Fe}^\sigma$  is the stator iron heat source, and  $\dot{Q}_f^\sigma$  is the heat generated due to friction in the stator/rotor air gap. The thermal operation of the air-cooled synchronous generator is mainly influenced by  $\dot{m}_w$ ,  $\dot{m}_a$ ,  $T_w^c$ ,  $\dot{Q}_{Fe}^\sigma$ ,  $\dot{Q}_f^\sigma$ ,  $I_t$  and  $I_f$ . It is of interest to see the behavior of rotor, stator, and iron core temperatures indicated by  $T_r$ ,  $T_s$  and  $T_{Fe}$ , respectively.

### 2.4.3 Mathematical model

The mathematical equations governing generator metal temperatures taken from [44] are

## 2.4 Thermal Model of Synchronous Generator

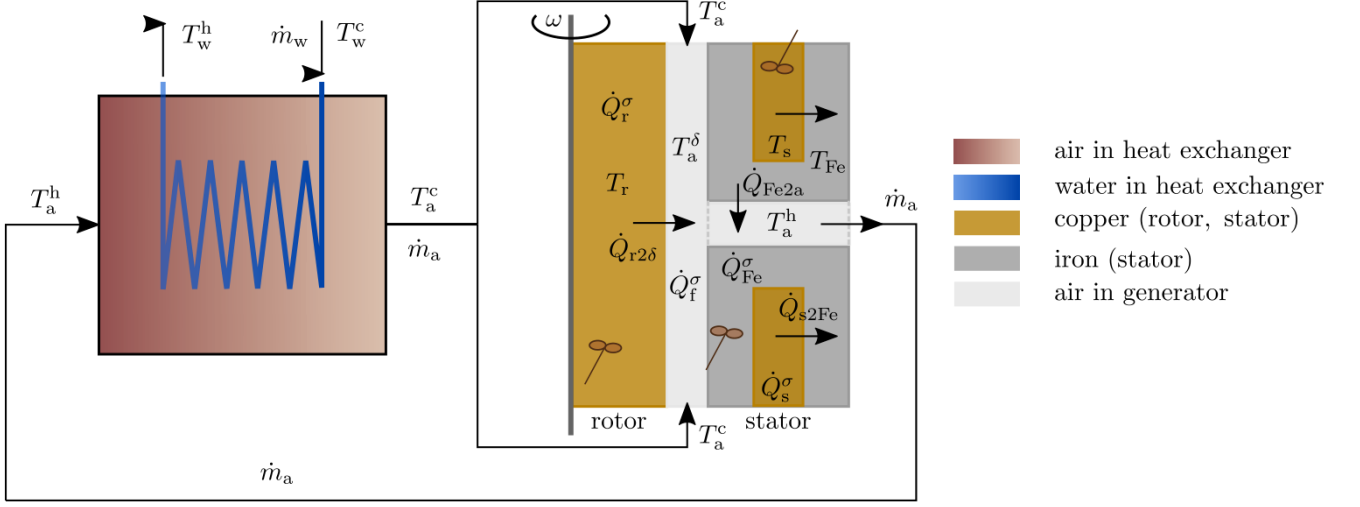


Figure 2.16: Thermal model of the synchronous generator.

$$m_r \hat{c}_{p,Cu} \frac{dT_r}{dt} = 1.1R_r I_f^2 - \mathcal{U} A_{r2\delta} (T_r - T_a^\delta) \quad (2.33)$$

$$m_s \hat{c}_{p,Cu} \frac{dT_s}{dt} = 3R_s I_t^2 - \mathcal{U} A_{s2Fe} (T_s - T_{Fe}) \quad (2.34)$$

$$m_{Fe} \hat{c}_{p,Fe} \frac{dT_{Fe}}{dt} = \mathcal{U} A_{s2Fe} (T_s - T_{Fe}) \quad (2.35)$$

$$- \mathcal{U} A_{Fe2a} (T_{Fe} - T_a^h) + \dot{Q}_{Fe}^\sigma. \quad (2.36)$$

In Eq. 2.33, the total rotor copper losses is given as  $P_r = 1.1R_r I_f^2$  which includes the DC power loss  $R_r I_f^2$  and the 10% loss from the static excitation system as recommended by IEEE. Similarly, in Eq. 2.34, the three phase DC stator copper losses is given as  $P_s = 3R_s I_t^2$  [41, p. 58].

Similarly, the algebraic equations for air inside the generator are

$$0 = \dot{m}_a \hat{c}_{p,a} (T_a^c - T_a^\delta) + \mathcal{U} A_{r2\delta} (T_r - T_a^\delta) + \dot{Q}_f^\sigma \quad (2.37)$$

$$0 = \dot{m}_a \hat{c}_{p,a} (T_a^\delta - T_a^h) + \mathcal{U} A_{Fe2a} (T_{Fe} - T_a^h) \quad (2.38)$$

and the heat exchanger is modeled as

$$(N_{St}^w - N_{St}^a e^{-N_{St}^\Delta}) T_a^c = N_{St}^\Delta T_a^h + N_{St}^a (1 - e^{-N_{St}^\Delta}) T_w^c. \quad (2.39)$$

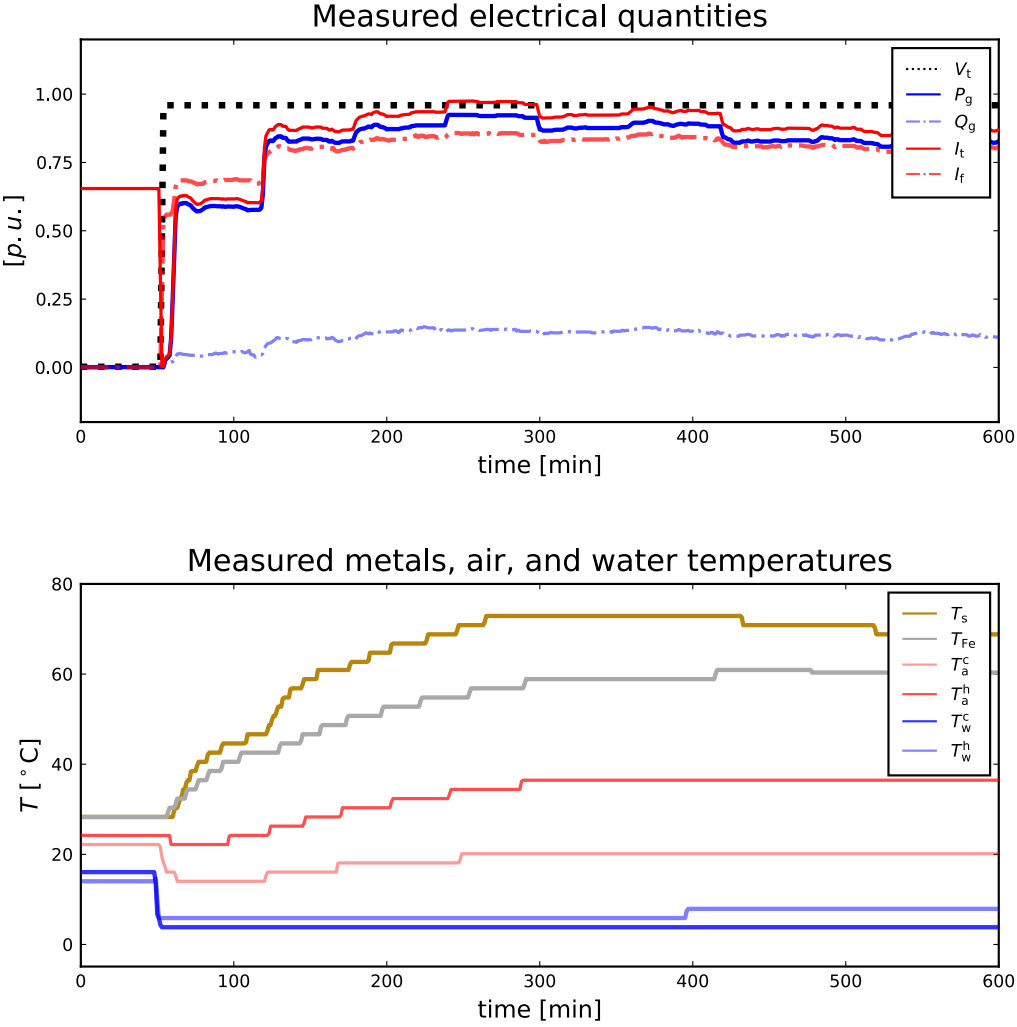


Figure 2.17: Experimental data for generator model from a 600 min heat-run test taken from [5].

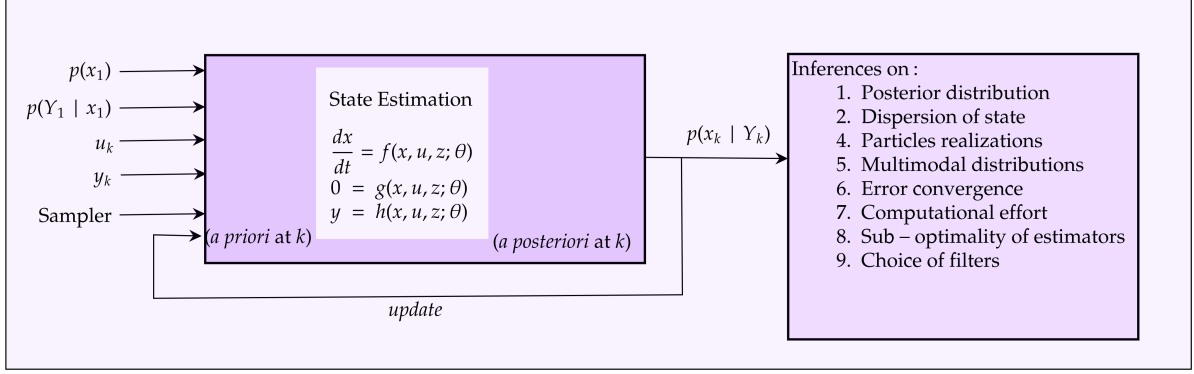


Figure 2.18: Bayesian inference for the state estimation.

In Eq. 6  $N_{St}^i$  is a Stanton-like number relating heat transfer coefficient, density, heat capacity, and velocity<sup>28</sup> where  $i \in \{\mathbf{w}, \mathbf{a}, \Delta\}$  refers to water, air, and their differences.

Equations 2.33–2.39 can be written in Differential Algebraic Equations (DAEs) form as

$$\begin{aligned} \frac{dx}{dt} &= f(x, z, u; \theta) \\ 0 &= g(x, z, u; \theta) \\ y &= h(x, z, u; \theta) \end{aligned} \quad (2.40)$$

where  $x = (T_r, T_s, T_{Fe})$ ,  $z = (T_a^c, T_a^\delta, T_a^h)$ ,  $u = (I_f, I_t, T_w^c)$ ,

$$\theta = (m_r, m_s, m_{Fe}, R_r, R_s, \hat{c}_{p,Cu}, \hat{c}_{p,Fe}, \hat{c}_{p,a}, \dot{m}_a, \mathcal{U}_{A_{r2\delta}}, \mathcal{U}_{A_{s2Fe}}, \mathcal{U}_{A_{Fe2a}}, \dot{Q}_{Fe}^\sigma, \dot{Q}_f^\sigma, N_{St}^a, N_{St}^w, N_{St}^\Delta).$$

Nominal parameters and operating conditions are given in Table 2.4.

Out of the three states,  $T_s$  and  $T_{Fe}$  are measured, while it is of interest to estimate the temperature of rotating rotor copper  $T_r$ . Similarly, out of three algebraic variables,  $T_a^c$  and  $T_a^h$  are measured, and it is also of interest to estimate air gap temperature  $T_a^\delta$ . The measured inputs, states, and algebraic variables are shown in Figure 2.17.

#### 2.4.4 State estimation

Figure 2.18 shows the Bayesian framework for the inferences about the states of a dynamical system. In the figure,  $x, u, z, \theta$ , and  $y$  are the states, inputs, algebraic variables,

<sup>28</sup>Formally, the Stanton number is  $St = \frac{h}{\rho v c_p}$ . Replacing the heat transfer coefficient  $h$  by the overall heat transfer coefficient  $\mathcal{U}$ , assuming a circular heat exchanger pipe of length  $L$  and diameter  $d$  gives  $N_{St} = \frac{4L}{d} \cdot St$ .



## 2 Literature Review

Table 2.4: Parameters and initial operating conditions.

Quantities	Symbols	Values
Mass of rotor copper, stator copper and stator iron	$m_r, m_s, m_{Fe}$	9260kg, 6827kg, 71200kg
Ohmic resistances of rotor copper and stator copper	$R_r, R_s$	0.127 $\Omega$ , 1.95 m $\Omega$
Specific heat capacities of copper and iron	$\hat{c}_{p,Cu}, \hat{c}_{p,Fe}$	0.385 kJ/kg/K, 0.465 kJ/kg/K
Specific heat capacities of air and water	$\hat{c}_{p,a}, \hat{c}_{p,w}$	1.15 kJ/kg/K, 4.2 kJ/kg/K
Air and water mass flow rates	$\dot{m}_a, \dot{m}_w$	49.2 kg/s, 53.9 kg/s
Heat transfer, rotor to air gap, stator copper to iron, and stator iron to air	$\mathcal{U} A_{r2\delta}, \mathcal{U} A_{s2Fe}, \mathcal{U} A_{Fe2a}$	2.7 kW/K, 20 kW/K, 14.3 kW/K
Stator iron generated heat	$\dot{Q}_{Fe}^\sigma$	212 kW
Friction heating	$\dot{Q}_f^\sigma = 0.8 \cdot \dot{W}_f$	422.4 kW
Friction work	$\dot{W}_f$	528 kW
Stanton number, air	$N_{St}^a = \frac{\mathcal{U} A_x}{\hat{c}_{p,a} \dot{m}_a}$	0.785
Stanton number, water	$N_{St}^w = \frac{\mathcal{U} A_x}{\hat{c}_{p,w} \dot{m}_w}$	0.196
Stanton number, difference	$N_{St}^\Delta = N_{St}^w - N_{St}^a$	-0.589
Heat transfer, air to water	$\mathcal{U} A_x = 1 / \left( \frac{1}{h_a A_x} + \frac{1}{h_w A_x} \right)$	44.46 kW/K
Heat transfer, solid to air	$h_a A_x$	55.6 kW/K
Heat transfer, solid to water	$h_w A_x$	222 kW/K
Initial value of rotor copper, stator copper, and stator iron temperatures	$T_a^c(t=0), T_s(t=0), T_{Fe}(t=0)$	28°C, 28°C, 28°C
Initial value of cooled air, air-gap, and hot air temperatures, stator copper, and stator iron temperatures	$T_a^c(t=0), T_a^\delta(t=0), T_a^h(t=0)$	14°C, 18°C, 22°C

parameters, and outputs, respectively. For the state estimation shown in Figure 2.18,  $x$  and  $z$  are estimated when  $u, \theta$ , and  $y$  are given.  $p(x_1)$  is the prior distribution of the initial conditions of the states,  $p(Y_1 | x_1)$  is the initial likelihood and  $p(x_k | Y_k)$  is the estimated posterior distribution of states by formulating a recursive relation considering measurement available at each instance of measurement data for outputs where  $Y_k = [y_1, y_2, \dots, y_k]$ . The numerical implementation of the recursive Bayesian filter draws random values from a known initial probability density function for the state ( $p(x_1)$ ). Each random value is considered a *particle*. The model is then solved for each of these particles, with some measurement update. The particle evolution allows for the numerical approximation of the posterior of the Bayesian estimator at each time instance; this is often termed a particle filter.

In the figure, it is indicated that Bayesian state estimation allows posterior distribution of the state, particles realization needed in the state estimation, the relationship between the parameters with the multimodal posterior distribution, and the choice of particle or ensemble type filters, inference on particles realization with error convergence and computational effort, and sub-optimality comparison between different estimators.

#### 2.4.4.1 Recursive Bayesian filter

The Bayesian state estimation at time instant  $k$  conditioned with measurement up to  $Y_k$  is given as

$$p(x_k | Y_k) = \frac{p(y_k | x_k) p(x_k | Y_{k-1})}{p(y_k | Y_{k-1})} \quad (2.41)$$

where  $p(y_k | x_k)$  and  $p(y_k | Y_{k-1})$  are the likelihood and the evidence, respectively, known from the information of the measurement noise density.  $p(x_k | Y_{k-1})$  is the prior and calculated as

$$p(x_k | Y_{k-1}) = \int p(x_k | x_{k-1}) p(x_{k-1} | Y_{k-1}) dx_{k-1}. \quad (2.42)$$

For a state estimation for measurement  $y = [y_1, y_2, \dots, y_k, \dots, y_N]$  with the initial state density function given as

$$p(x_1 | Y_1) = \frac{p(Y_1 | x_1) p(x_1 | Y_0)}{p(Y_1)}, \quad (2.43)$$

a recursive state estimation problem can be formulated. In practice, the analytical solution for the posterior density function  $p(x_k | Y_k)$  given by Eq. (2.41) exists for only a few special cases. The analytical derivation considering a linear system with additive Gaussian noise leads to the optimal linear Kalman filter. Further information about the Kalman filter and its derivatives for state estimation can be found in [30]. However, for a non-linear system and systems where analytical solutions are impossible, we formulate a numerical solution considering a sample drawn from the known initial states' density function and recursively obtain the numerical solution using Eqs. (2.41-2.43) for the posterior distribution.

#### 2.4.4.2 Particle filter

The particle filter algorithm taken from [30] is given in Table 2.5.  $p(x_1)$ ,  $p(w_1)$ , and  $p(v_1)$  are the initial prior densities of the states, process noise, and the measurement noise. For  $i = 1 : N_p$ ,  $x_{k|k-1}^i$  are *a priori* particles obtained by propagating the prior particles through the process equations. Similarly,  $y_{k|k-1}^i$  are the predicted measurements used for calculating the innovation  $\epsilon_i$ . The innovation is used for calculating the likelihood  $q_i$ . A simple expression for the likelihood is found by considering measurement noise as  $v_k \sim \mathcal{N}(0, \mathcal{V})$ , i.e., normal distribution with zero-mean  $\bar{v} = 0$  and co-variance  $\mathcal{V}$ . After this, the likelihood is normalized. The normalized likelihood is then resampled to obtain the posterior density.

Resampling is a key step for success of the particle filter. There are several methods for resampling. The particles drawn from the posterior distribution are called *a posteriori* estimates, and considered as the sub-optimal estimates. The optimality of the estimates increases as the number of particles increases.

Due to numeric degeneracy, *a priori* particles may get clustered in certain regions, and diluted in other important regions. This leads to uneven *weighing* when computing statistics, and leads to estimates with too large variance. This makes resampling necessary, and is done to make sure all particles have equal weights to minimize the estimate variance. Particles with low weight are replaced with higher weight to distribute particles evenly on the basis of their weights. This process of distributing of particles evenly on the basis of weights is often termed resampling. Resampling is done based on the resampling quality, computational cost, and ease of implementation. The resampled particles are denoted *a posteriori* particles from which any statistical moments, like mean and standard deviation, are updated to recursively run the filter.

#### 2.4.4.3 Resampling algorithms

A simple resampling algorithm is taken from [45], given in Table 2.5, and this algorithm is named *Ris04* for distinguishing it from other algorithms. In the *Ris04* algorithm, we first generate a uniformly distributed random number  $r$  as  $r \sim \mathbb{U}(0, 1]$ . Then we find the cumulative sum of the likelihood  $q^+$  in each iteration. If  $q^+$  is less than or equal to the generated random number, we then set the *a priori* particles as the *a posteriori* particles as shown in Table 2.6. *Ris04* algorithm is not very efficient [30] to distribute particles evenly based on their weights. Several other more efficient resampling algorithms are available. In this thesis, we focus on multinomial resampling, stratified resampling, residual resampling, and systematic resampling. These resampling algorithms are taken from [46], [47] and [48].

Table 2.5: Generalized particle filter. Measurement co-variance  $\mathcal{V}$  is assumed constant/known.

<b>Initialization, <math>k = 1</math> :</b> Draw $N_p$ particles for states, process and measurement noise from initial probability distribution $p(x_1)$ , $p(w_1)$ and $p(v_1)$ . $x_{1 1}^i \sim p(x_1)$ , $i \in \{1, 2, \dots, N_p\}$ $w_1^i \sim p(w_1)$ $i \in \{1, 2, \dots, N_p\}$ $v_1^i \sim p(v_1)$ $i \in \{1, 2, \dots, N_p\}$
for $k = 2, 3, \dots$
<b>Propagation step:</b> Propagate particles through process model ( <i>a priori</i> particles) $x_{k k-1}^i = f(x_{k-1 k-1}^i, u_{k-1}, w_{k-1}^i)$ $i \in \{1, 2, \dots, N_p\}$
<b>Information update:</b> 1. Propagate <i>a priori</i> particles through measurement model (predicted measurement particles) $y_{k k-1}^i = h(x_{k k-1}^i, u_{k-1}, v_{k-1}^i)$ $i \in \{1, 2, \dots, N_p\}$ 2. Calculate relative <i>likelihood</i> $q_i$ i.e. $p(y_k   x_{k k-1})$ from innovation $\epsilon_i = y_k - y_{k k-1}^i$ $q_i \sim \frac{1}{(2\pi)^{\frac{m}{2}}  \mathcal{V} ^{\frac{1}{2}}} e^{-\left(\frac{\epsilon_i^T \mathcal{V}^{-1} \epsilon_i}{2}\right)}$ , $m$ is dimension of the measurement equation and $\mathcal{V}$ is measurement co-variance 3. Normalize $q_i$ $q_i = \frac{q_i}{\sum_{j=1}^{N_p} q_j}$ 4. Resampling for <i>a posteriori</i> estimate Pseudo code for a simple ‘‘Ris04’’ resampling: <b>loop</b> $i = 1 : N_p$ $r \sim \mathbb{U}(0, 1]$ $q^+ \leftarrow 0$ <b>loop</b> $j = 1 : N_p$ $q^+ \leftarrow q^+ + q_j$ <b>if</b> $(q^+ < r)$ $x_{k k}^i \leftarrow x_{k k-1}^j$ <b>end</b> <b>end</b>
5. <i>A posteriori</i> mean update $\hat{x}_{k k} = \frac{1}{N_p} \sum_{i=1}^{N_p} x_{k k}^i$

Table 2.6: Different resamplings pseudocodes.

<p>(1) Multinomial</p> $q^+ = \text{cumsum}(q_i)$ $r_i \sim \text{sort}(\mathbb{U}(0, 1]), i \in 1 : N_p$ $j = 1$ <b>loop</b> $i = 1 : N_p$ <b>while</b> $q_j^+ < r_j$ $j = j + 1$ <b>end</b> $x_{k k}^i \leftarrow x_{k k-1}^j$ <b>end</b>	<p>(2) Residual</p> $q_i^* = \frac{N_p q_i - \lfloor N_p q_i \rfloor}{N_p - \sum_{i=1}^{N_p} \lfloor N_p q_i \rfloor}$ $q^+ = \text{cumsum}(q_i^*)$ $r_i \sim \text{sort}(\mathbb{U}(0, 1]), i \in 1 : N_p$ $j = 1$ <b>loop</b> $i = 1 : N_p$ <b>while</b> $q_j^+ < r_j$ $j = j + 1$ <b>end</b> $x_{k k}^i \leftarrow x_{k k-1}^j$ <b>end</b>
<p>(3) Stratified</p> $q^+ = \text{cumsum}(q_i)$ $s_i \sim \mathbb{U}\left(\frac{i-1}{N_p}, \frac{i}{N_p}\right]$ $s_{N_p+1} = 1$ $i = 1; j = 1$ <b>while</b> <b>if</b> $s_i < q_j^+$ $x_{k k}^i \leftarrow x_{k k-1}^j$ $i = i + 1$ <b>else</b> $j = j + 1$ <b>end</b> <b>end</b>	<p>(4) Systematic</p> $q^+ = \text{cumsum}(q_i)$ $r \sim \mathbb{U}\left(0, \frac{1}{N_p}\right]$ $s_j = r + \frac{j-1}{N_p}, j \in 1 : N_p$ $s_{N_p+1} = 1$ $i = 1; j = 1$ <b>while</b> <b>if</b> $s_i < q_j^+$ $x_{k k}^i \leftarrow x_{k k-1}^j$ $i = i + 1$ <b>else</b> $j = j + 1$ <b>end</b> <b>end</b>

### Multinomial resampling

For multinomial resampling, we first generate a vector of  $N_p$  uniformly distributed numbers  $\mathbb{U}(0, 1]$  and sort them in increasing order. Then, we use this sorted vector to select the *a priori* particles with higher weights based on the index of ordered random numbers, see Table 2.6-(1) for details. The multinomial resampling algorithm is similar to Ris04 resampling. In the algorithm,  $q^+$  represents the cumulative sum of the likelihood  $q_i$ ,  $\text{cumsum}(\cdot)$  gives the cumulative sum and  $\text{sort}(\cdot)$  represents the sorting function for creating an ordered sequence. Both  $\text{cumsum}(\cdot)$  and  $\text{sort}(\cdot)$  are available as built-in functions in most high level programming languages such as Python, Julia, etc.

### Residual resampling

The residual resampling technique works based on a modification of normalized likelihoods. The modified likelihood  $q_i^*$  captures the residual from the normalized likelihood  $q_i$  based on the *floor* function of the product of  $N_p$  and  $q_i$ , i.e.,  $\lfloor N_p q_i \rfloor$ . The modified likelihood is then given as

$$q_i^* = \frac{N_p q_i - \lfloor N_p q_i \rfloor}{N_p - \sum_{i=1}^{N_p} \lfloor N_p q_i \rfloor}.$$

The modified likelihood can then be used for resampling through the Ris04 or the multinomial resampling. Pseudo code for residual resampling is given in Table 2.6-(2).

### Stratified resampling

The stratified resampling algorithm differs from Ris04 and multinomial resampling in that the procedure for generating the sequence of random numbers is different. The algorithm for the stratified resampling algorithm is given in Table 2.6-(3). For  $i \in 1 : N_p$  we generate the random number as  $s_i \sim \mathbb{U}\left[\frac{i-1}{N_p}, \frac{i}{N_p}\right)$  and each of these generated numbers  $s_i$  are called *strata*. These strata divides the interval  $[0, 1)$  into  $N_p$  disjoint sub-intervals  $\left(0, \frac{1}{N_p}\right] \cup \left(\frac{1}{N_p}, \frac{2}{N_p}\right] \cup \left(\frac{2}{N_p}, \frac{3}{N_p}\right] \cup \dots \cup \left(\frac{N_p-1}{N_p}, 1\right]$  [47].

### Systematic resampling

Systematic resampling is a modified and computationally more robust algorithm than the stratified resampling algorithm. The random number is generated as  $r \sim \mathbb{U}\left(0, \frac{1}{N_p}\right]$  and the strata are calculated deterministically using the index  $j$  as

$$s_j = r + \frac{j-1}{N_p}, j \in 1 : N_p.$$

## 2 Literature Review

Note that the random number is only generated once in the systematic resampling algorithm. This reduces the computational cost as compared to the other resampling algorithms. The pseudo code for the systematic resampling is given in Table 2.6-(4).

### Sample impoverishment in particle filter

The *a priori* particles are distributed according to the distribution function  $p(x_k | y_{k-1})$ . These particles are resampled using the posterior density function  $p(y_k | x_k)$ . In practice, if the high particles density region of the state space of the posterior density  $p(y_k | x_k)$  does not overlap with the high-density state-space region of the prior density  $p(x_k | y_{k-1})$  then only a few *a priori* particles with higher weights are selected to become the *a posteriori* particles during resampling. This process in which there is a significant decrement in the volume of the *a priori* particles to become *a posteriori* particles after the resampling is called *sample impoverishment*. If the sample impoverishment persists with a fewer number of the *a priori* particles becoming the *a posteriori* particles, eventually, all the particles would collapse to the same value. This phenomenon is called a *black hole* in particle filtering. One way of eradicating this phenomenon is using a large number of particles, however, this increases computational cost. Several solutions are provided to deal with sample impoverishment. Roughening, prior editing, regularized particle filter (RPF), Markov Chain Monte Carlo resampling, and auxiliary particle filter (APF) are some of the common methods explained in [30]. This thesis will mainly focus on roughening, RPF, and APF.

### Roughening

Roughening or *jittering* is a procedure where random noise is added to the *a posteriori* particles after they are resampled. This increases the volume of the distinct *a posteriori* particles and the problem of sample impoverishment is improved. Roughening creates diversification in resampled particles which are distributed evenly based on their weights. For the *a posteriori* estimates roughening can be done as

$$x_{k|k}^i \leftarrow x_{k|k}^i + w_r^i,$$

where  $w_r$  is random noise drawn from a Gaussian distribution with zero-mean and given as

$$w_r \sim \left( 0, K \cdot M \cdot N_p^{-\left(\frac{1}{n_x}\right)} \right),$$

where  $n_x$  is the number of dimensions of the state space.  $K$  is a scalar tuning factor usually set to 0.2 and  $M$  is the vector containing differences between the maximum and the minimum values of the particles before roughening, given as,

$$M = \max(x_{k|k-1}) - \min(x_{k|k-1}).$$

The roughening procedure will spread the clustered particles, and more even weights. Roughening also improves statistical moments that we infer from the *a posteriori* particles.

### Regularized Particle Filter (RPF)

The sampling algorithms presented in Table 2.6 are discrete in time. However, RPF assumes a probability density function using a continuous distribution. The algorithm for regularized particle filter is taken from [30].

### Auxiliary Particle Filter (APF)

For an auxiliary particle filter (APF) we modify the likelihood obtained in Table 2.5 by using the following formula,

$$q_i \leftarrow \frac{(\alpha - 1)q_i + \bar{q}}{\alpha} \quad (2.44)$$

where  $\alpha$  is a tuning parameter for increasing the diversity in the likelihood. A typical value of  $\alpha$  for APF is 1.1 [30]. During resampling, particles that are outliers having a lower likelihood in the region of the state space are replaced with particles having a higher likelihood. The eradication of these lower weight particles will reduce the diversity of distribution of the particles. APF addresses this issue by assigning outliers with a higher likelihood and this is done with Eq. (2.44). APF is used mostly with highly non-linear systems to address the issues of outliers in the estimation of the posterior distribution.

#### 2.4.4.4 Particle filter versus Kalman filter

As described in Section 2.4.4.1, Eqs. (2.41-2.43) are solved recursively to obtain state estimates. The analytical solution for Eq. (2.41) only exists for a few special cases. For instance, if we consider both the process and measurement dynamics as linear functions, and process and measurement noises as Gaussian distribution, then the analytical solution is the optimal linear Kalman filter (KF). However, the optimal Kalman filter cannot be derived from the Bayesian formulation for linear dynamical systems with non-Gaussian noises. Kalman filter can also be derived from the least-squares error method as in original KF [49] and it preserves optimality in the case of both Gaussian and non-Gaussian noises for linear systems.



### Kalman filter and its variants

There are several variants of the original KF. As the non-linearity increases in any dynamical system, linear KF fails. For a nonlinear system with Gaussian/non-Gaussian noises, state estimation algorithms like Extended Kalman Filter (EKF), Unscented Kalman Filter (UKF) [50], and Ensemble Kalman Filter (EnKF) [51] are employed; UKF and EnKF have several variants with different performances. However, for a non-linear system with non-Gaussian noise, these variants of the KF cannot guarantee a true estimate if the true posterior distribution is multimodal and unsymmetrical around the mean [46]. In reality, the multimodal *a posteriori* distribution can be approximated by summing up weighted Gaussian for each modal distribution as described in [52]. The Gaussian sum [53] can also be applied to other variants of KF, for instance, Gaussian Sum-UKF (GSUKF). Several variants of the KF are compared in [54] for a case study to estimate the state of charge in lithium-ion cells. From the paper, it was shown that in addition to the selection of filter algorithm for a particular problem, the tuning of the filter also plays an important role in the estimation accuracy. Similarly, in [55] different variants of EnKF are compared and analyzed for determining the synthetic experiments required to determine the difference in root mean square errors (RMSE) between the variants.

In this thesis, we are more focused on implementing and comparing UKF and EnKF with particle filters for the thermal model of the synchronous generator. We follow the same notations of our previous work on state estimation for the thermal model of the synchronous generator in [44] where UKF and EnKF algorithms are succinctly defined.

## 3 Main Results

This chapter summarized the main results and contributions of the thesis work. The major part of the work is related to the papers provided in the Appendices. First, modeling of different types of surge tanks and draft tubes is studied for the open-source library — OpenHPL. The work is also extended with the inclusion of the standard active power frequency control in OpenHPL. Furthermore, the work also includes parameter and state estimation of the thermal model of the synchronous generator.

### 3.1 Surge Tanks

#### 3.1.1 Modeling

Figure 3.1 shows four different kinds of surge tanks. The sharp orifice type surge tank and the throttle valve type surge tanks are modeled by modifying the expression for the overall fluid frictional force of the simple surge tank. Appendix F lists DAEs of different types of surge tanks. These DAEs are implemented in the OpenHPL library, and further analysis of the performance of the surge tanks is based on the simulated performance of surge tanks based on the hydroturbine's load acceptances and rejections.

The detailed modeling of the different types of open type surge tanks, viz., the simple surge tank, the sharp orifice type surge tank, and the throttle valve type surge tank are provided in the paper presented in Appendix A. The paper presented in Appendix A also shows simulated responses for the open type surge tanks when the hydroturbine is loaded from half load to full load. Similarly, Appendix A also provides the modeling of closed type surge tank (air-cushion surge tank). Furthermore, the paper presented in Appendix B provides modeling of the air-cushion surge tank with the inclusion of an access tunnel that connects to the main air-chamber. The air-cushion surge tank model is further enhanced with the inclusion of Darcy's friction force for air inside the surge tank.

The paper presented in Appendix C provides simulated responses for the open and the closed type surge tanks during various percentage changes in the hydroturbine's load acceptances and rejections.

It is of interest to:

### 3 Main Results

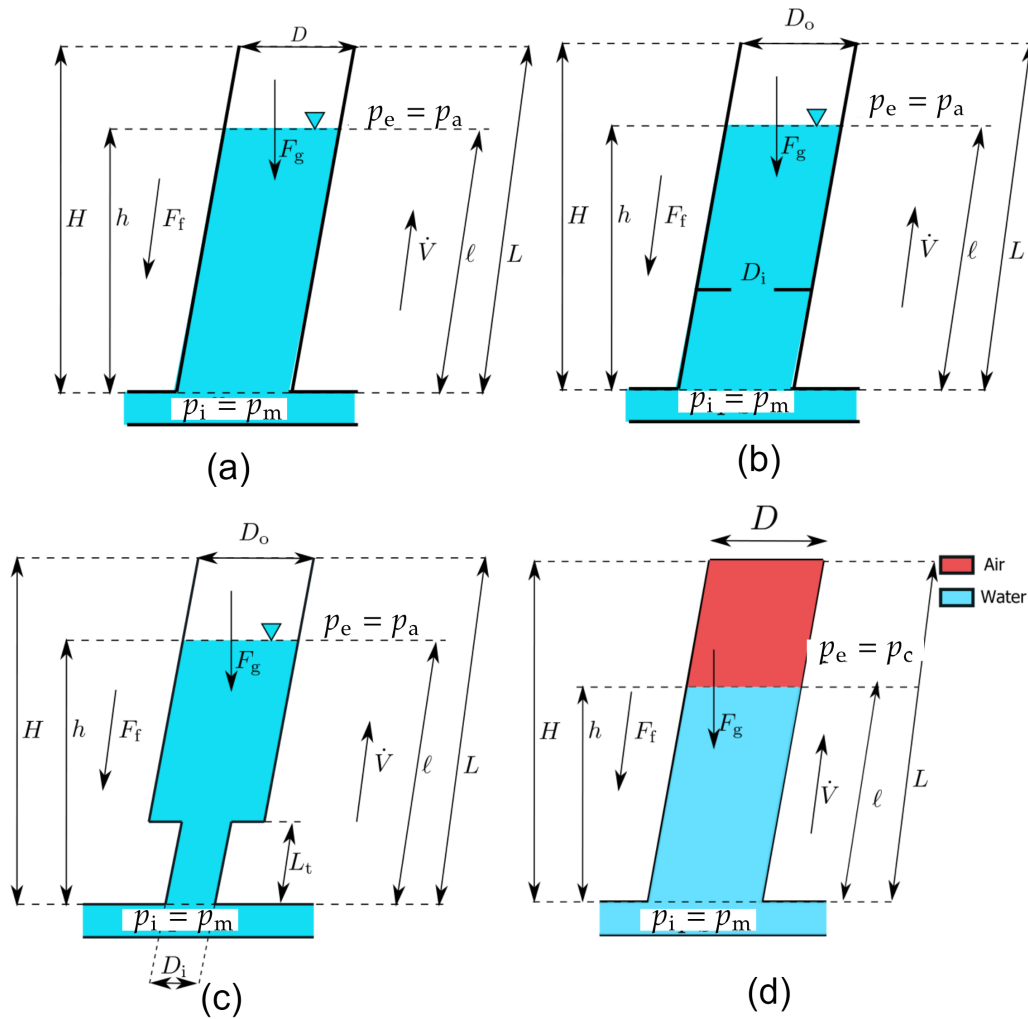


Figure 3.1: Different types of surge tanks. (a) Simple surge tank without hydraulic resistance. (b) Sharp orifice type surge tank with an orifice of diameter  $D_i$  as the hydraulic resistance. (c) Throttle valve surge tank with hydraulic resistance of diameter  $D_i$  at the entry of surge tank with square expansion from diameter  $D_i$  to diameter  $D_o$ . The length of the throat is  $L_t$ . (d) Air-cushion surge tank filled with air at pressure  $p_c$ .

- evaluate the maximum required height of the open surge tanks for restriction of water spilling out from the surge tank during load acceptances and rejections
- see the effect of the load acceptances and the load rejections on the water mass oscillation and the turbine inlet pressure inside the surge tank.

### 3.1.2 Open surge tanks

#### 3.1.2.1 Case study: Trollheim HPP

The case study includes simulated responses for the different types of open surge tanks at different discharge rates for Trollheim HPP. The general layout of the Trollheim HPP is shown in Figure 3.2 a). The corresponding simulation model created in OpenHPL is shown in Figure 3.2 b).

#### 3.1.2.2 Total Load Rejection (TLR) and Water Mass Oscillation

First, we consider a case of a simple surge tank for Trollheim HPP for the layout shown in Figure 3.2 for a total load rejection. The maximum required height of a simple surge tank for restriction of water-spilling from the surge tank is given by the expression

$$H_{ST} = H_{res} + H_{in} + Y_{max} \quad (3.1)$$

where  $Y_{max}$  is the maximum surge or maximum water mass oscillation height during total load rejection [23] evaluated as

$$Y_{max} = \frac{\dot{V}_n}{A_{in}} \sqrt{\frac{L_{in}}{g} \left( \frac{A_{in}}{A_{ST}} \right)}, \quad (3.2)$$

where  $H_{ST}$ ,  $H_{in}$ , and  $H_{res}$  are height difference for surge tank, intake, and reservoir, respectively.  $A_{in}$  and  $L_{in}$  are the cross-sectional area and the length of the intake pressure tunnel, respectively.  $\dot{V}_n$  is the nominal discharge, while  $g$  is the acceleration due to gravity. From Figure 3.2 we have  $H_{res} = 50\text{m}$ ,  $H_{in} = 20\text{m}$ , and  $Y_{max}$  is calculated using Eq. 3.2 with  $Y_{max} \approx 45\text{m}$ . Thus, the height of the surge tank for avoiding water spillage from a simple surge tank for Trollheim HPP during total load rejection, is **115m**.

Figure 3.3 shows the turbine valve signal creating a TLR at 1500s. A TLR is created using control signal

$$u_v = \begin{cases} 1 & 0 < t \leq 1500 \text{ s} \\ 0 & 1500 \text{ s} < t \leq 3000 \text{ s} \end{cases}$$

### 3 Main Results

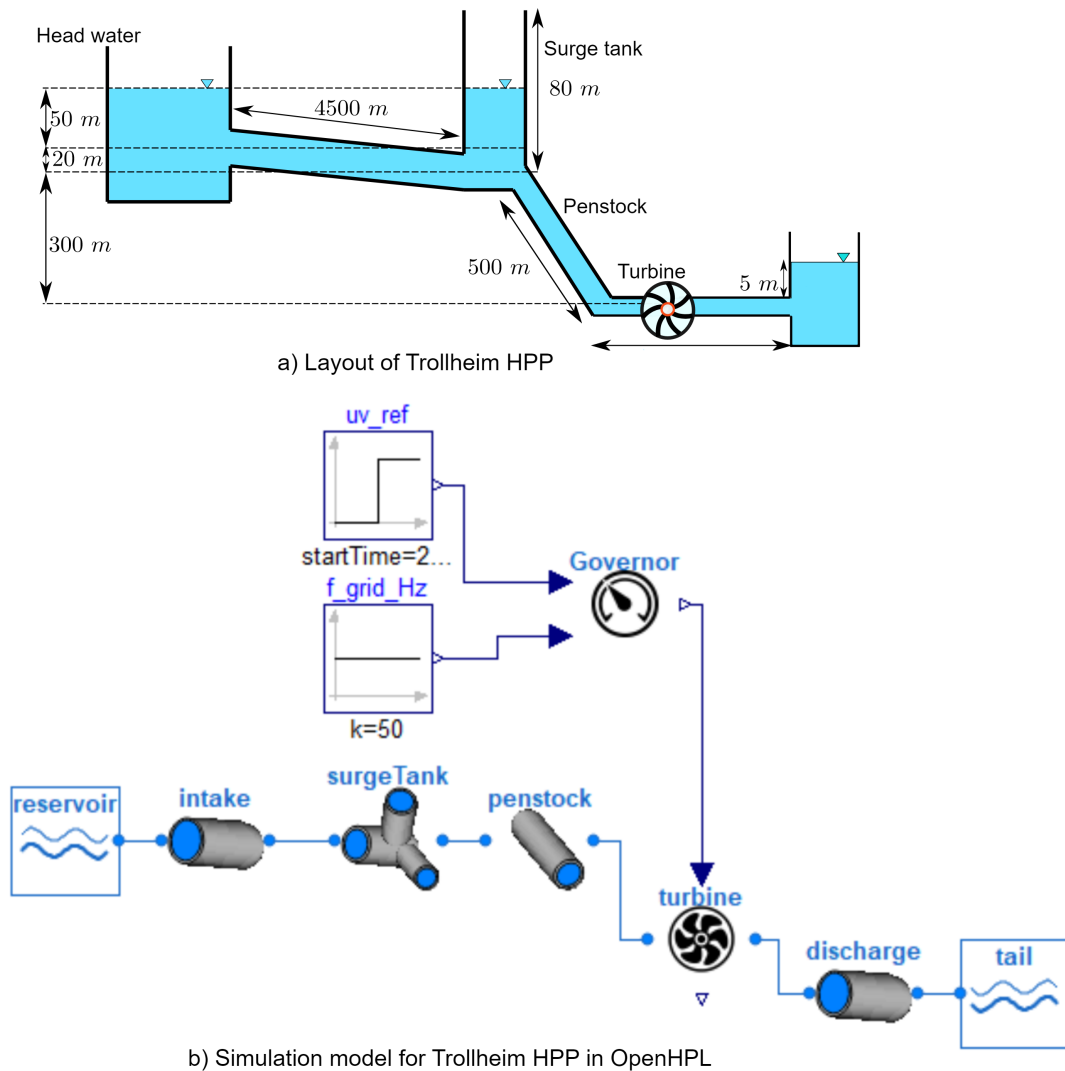


Figure 3.2: a) Layout diagram for Trollheim [6]. Nominal head, nominal discharge, and nominal power output are 370m, 40m<sup>3</sup>/s, and 130MW, respectively. The diameter for both of the penstock and the surge tank is 4m while for both the headrace and the tailrace tunnel is 6m. b) Simulation diagram implemented in OpenHPL with a hydropower governor with the gate servo motor time constant  $T_{gs} = 0.2$ s and the pilot servo motor time constant  $T_{ps} = 0.04$ s. For simulation studies we have considered the grid frequency of the system to be 50Hz. We have not shown the generator side or the grid side of the plant.

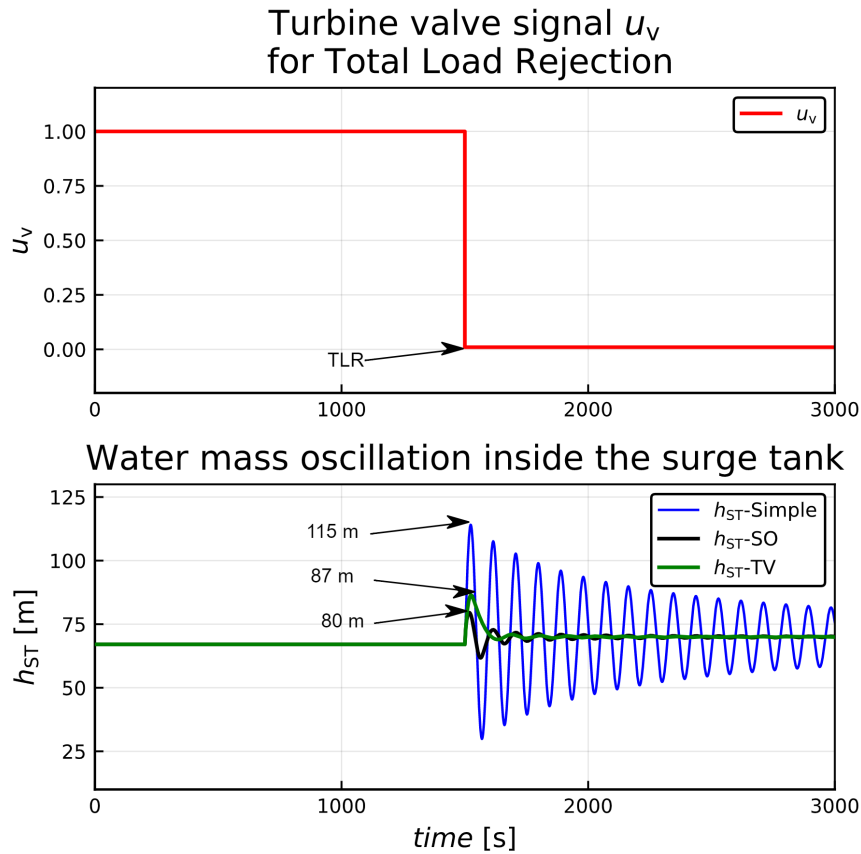


Figure 3.3: Water mass oscillation inside the open surge tanks for Trollheim HPP during TLR. The diameter of the orifice for the sharp orifice type surge tank ( $D_{so}$ ) and the diameter of the throat for the throttle valve surge tank ( $D_t$ ) are both 1 m. The length of the throat for the throttle valve surge tank is 20 m.

### 3 Main Results

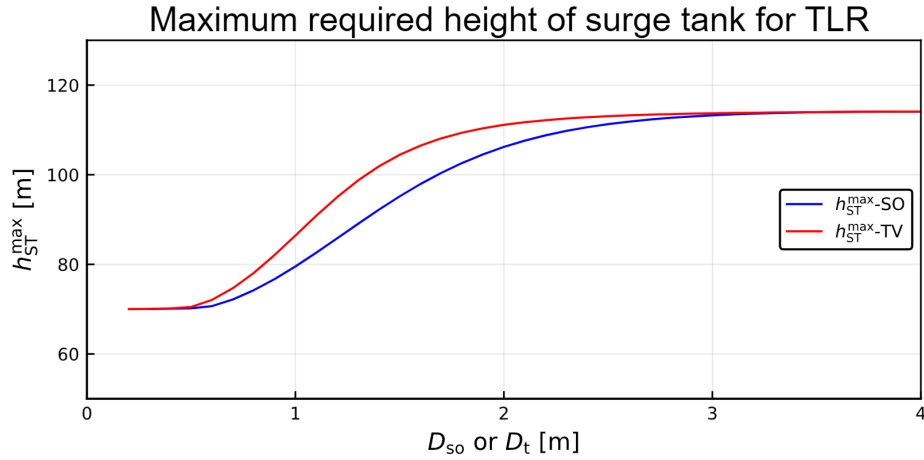


Figure 3.4: Maximum required height of surge tank for different diameters of the sharp orifice (SO) type and the throttle valve (TV) surge tanks.  $h_{ST}^{max}$  represents the maximum amplitude of water mass oscillation during TLR.

at time 1500s. In the figure, SO and TV denote the sharp orifice type and the throttle valve surge tank, respectively. The maximum amplitude of water mass oscillation  $h_{ST}$  is 115m at around 1500s for the simple surge tank. While for the sharp orifice type and the throttle valve type surge tanks, the maximum amplitude of water mass oscillations are 80m and 87m, respectively. This shows that hydraulic resistances in the case of the sharp orifice type and the throttle valve type surge tanks dampen out the mass oscillation quicker than in the case of the simple surge tank. The maximum required height of the surge tank for avoiding water spillage from the surge tank is smaller for the sharp orifice type surge tank as compared to other types of open surge tanks during the TLR.

#### 3.1.2.3 Effect of the diameter of the orifice and the throat for TLR

The maximum required height of the surge tanks for avoiding the water spillage from the surge tank can be decreased by decreasing the diameter of the orifice in the case of the sharp orifice type surge tank, and the diameter of the throat in the case of the throttle valve type surge tank as shown in Figure 3.4. As the diameter of hydraulic resistances like sharp orifice or throat at the entry of the surge tank is decreased, the maximum height of the water mass oscillation decreases. For example, when  $D_t$  and  $D_{so}$  both are 1 m,  $h_{ST}^{max}$  for sharp orifice type surge tank is 80m and for throttle valve surge tank is 87 m.

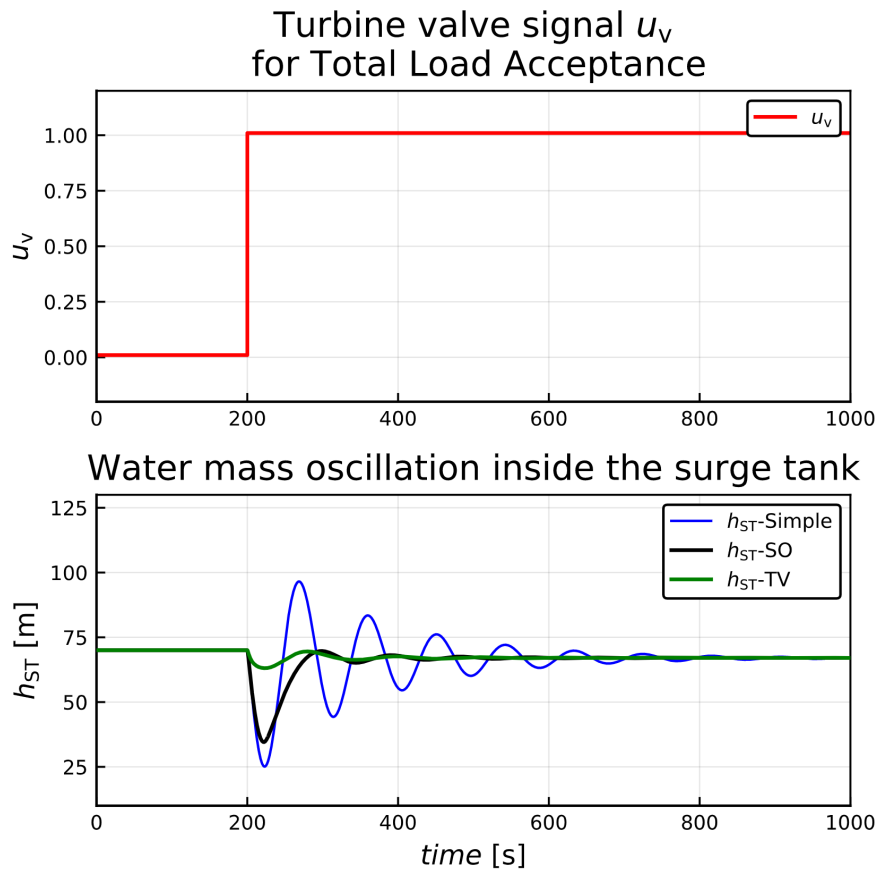


Figure 3.5: Water mass oscillation inside the surge tanks for TLA.

#### 3.1.2.4 Total Load Acceptance (TLA) and Water Mass Oscillation

A case of total load acceptance study is created using turbine guide valve control signal

$$u_v = \begin{cases} 0 & 0 < t \leq 200 \text{ s} \\ 1 & 200 \text{ s} < t \leq 1000 \text{ s} \end{cases}$$

at time 200s. The simulated response for water mass oscillation for the simple, sharp orifice, and throttle valve type surge tanks, are shown in Figure 3.5. The water mass oscillation dies out quicker in the case of both the sharp orifice type and the throttle valve type surge tanks.



### 3 Main Results

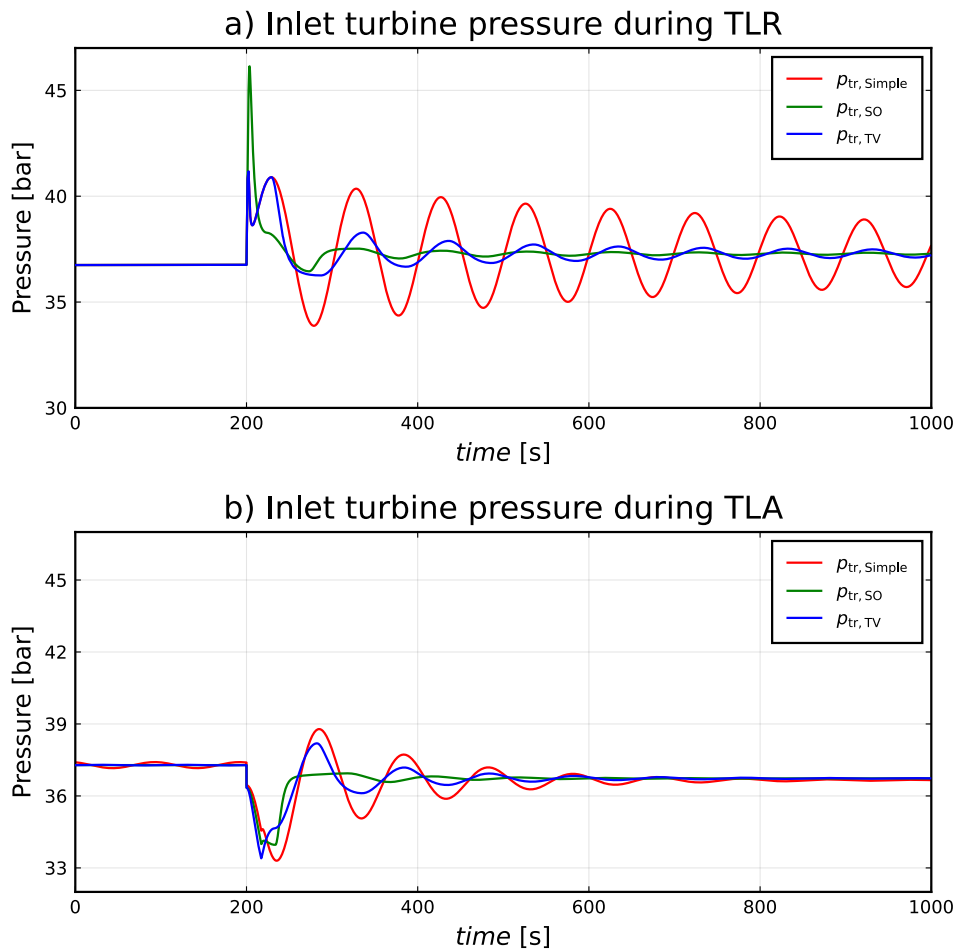


Figure 3.6: Inlet turbine pressure during TLR and TLA for Trollheim HPP using different kinds of open surge tanks.

#### 3.1.2.5 TLR, TLA, and turbine pressure

Figure 3.6 a) shows the turbine pressure during the TLR study. During the TLR study, the turbine pressure is larger in the case of the sharp orifice type surge tank as compared to the simple and the throttle valve type surge tanks. However, the pressure oscillation dies out quicker in the case of the sharp orifice type surge tank than the other open surge tanks. Figure 3.6 b) shows the turbine pressure during the TLA study.

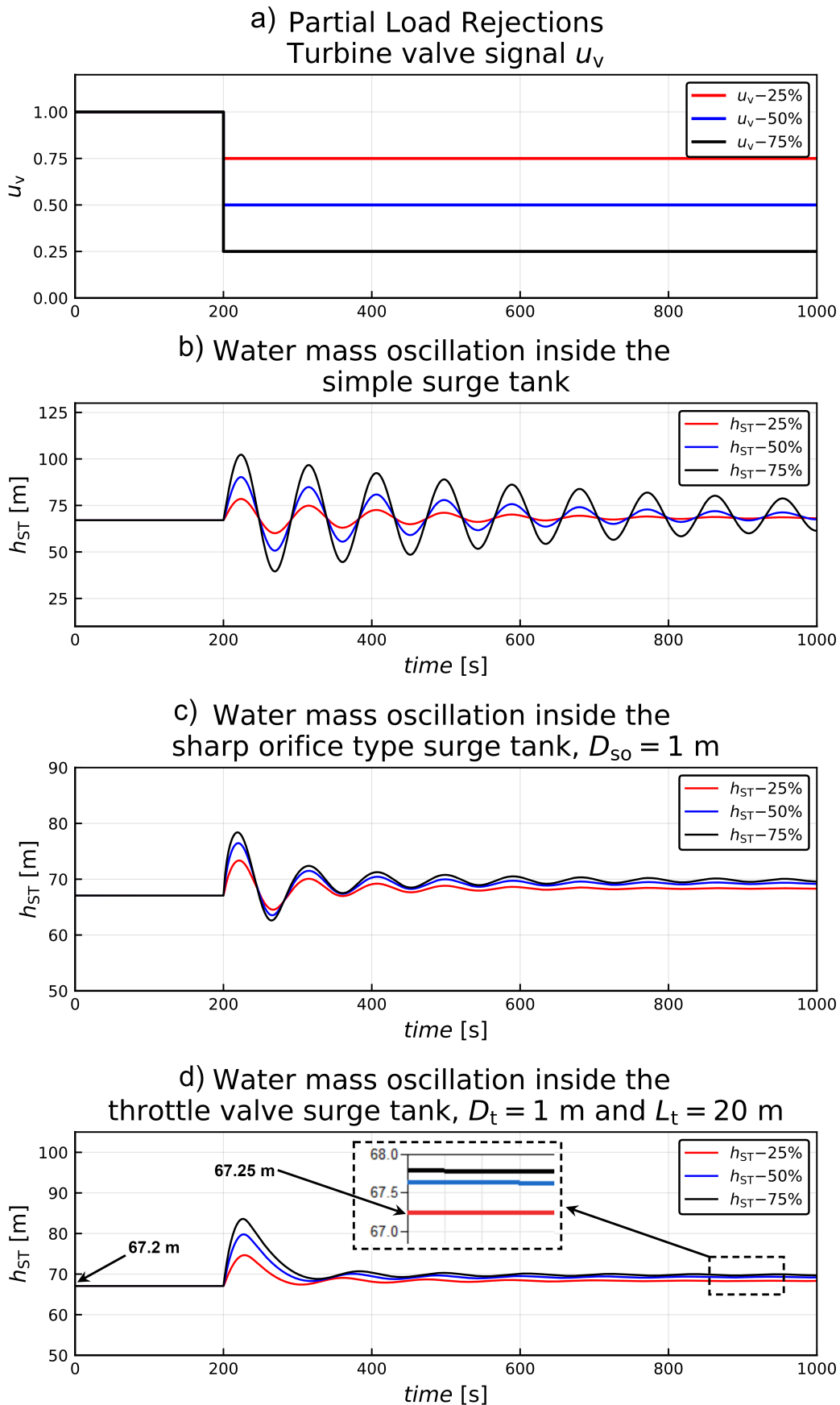


Figure 3.7: Water mass oscillation inside the surge tanks for PLR. In the figure,  $u_v - 25\%$  represents the gate signal for a partial load rejection of 25% of the total load capacity of the plant. Similarly,  $h_{ST} - 25\%$  represents water mass oscillation for a load rejection of 25%.

### 3 Main Results

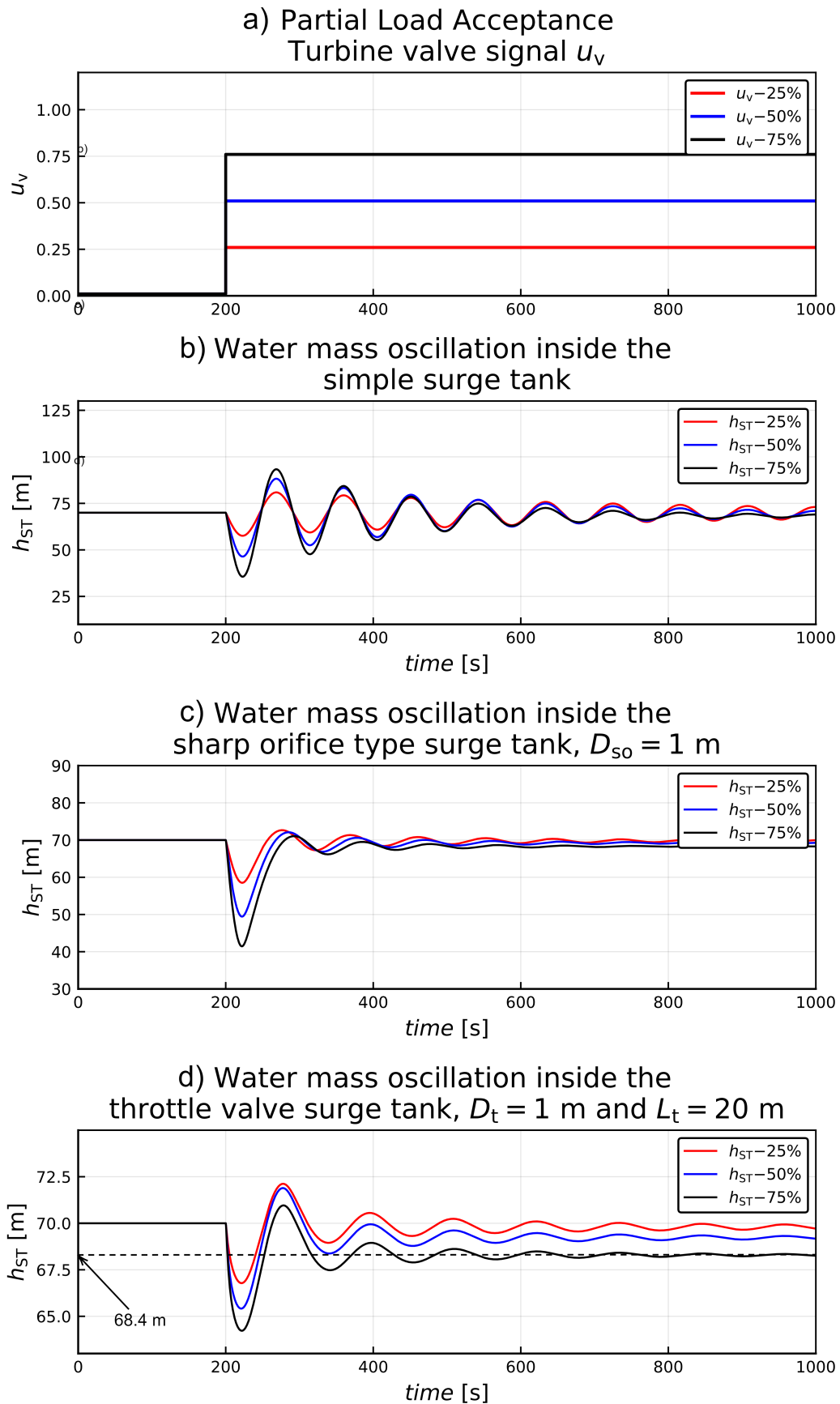


Figure 3.8: Water mass oscillation inside the surge tanks for PLA. In the figure,  $u_v - 25\%$  represents the gate signal for a partial load acceptance of 25% of the total load capacity of the plant. Similarly,  $h_{ST} - 25\%$  represents water mass oscillation for a load acceptance of 25% from a no-load condition.

### 3.1.2.6 Partial Load Rejection (PLR)

Partial load rejections study can be created at  $t = 200$ s by changing the turbine's gate signal as

$$u_v = \begin{cases} 1 & 0 < t \leq 200 \text{ s} \\ u_{vr} & 200 < t \leq 1000 \text{ s} \end{cases}$$

where  $u_{vr} \in \{0.75, 0.5, 0.25\}$  for load rejections of 25%, 50%, and 75%, respectively.

Figure 3.7 shows the water mass oscillation inside the simple, the sharp orifice type, and the throttle valve type surge tanks during the partial load rejection studies.

In Figure 3.7 d), the steady-state water level inside the surge tank increases after the PLRs in the case of a throttle valve type surge tank. This is also self-evident in other types of surge tanks. The steady-state water level within the tank is 67.2m while the plant is operated at full load; however, after a 25% rejection of the full load at  $t = 200$ s, the water level reaches a steady-state level of 67.25m. The steady-state water level under no-load conditions is the sum of the height differences between the reservoir's inlet and exit, as well as the intake, i.e,  $h_{ST}^{NL} = H_r + H_{in} = 70$ m. However, during the operation at full load conditions the steady-state water level is given as  $h_{ST}^{FL} = H_r + H_{in} + h_{in}^{FL}$  where  $h_{in}^{FL}$  is the head loss in the intake for the steady-state operation at full load condition. As the load rejection lowers from full load to no load, the steady-state head loss in the intake diminishes. At full load, the head loss in the intake is  $\approx 2.8$ m.

### 3.1.2.7 Partial Load Acceptance (PLA)

Partial load rejections can be studied at  $t = 200$ s by changing the turbine's gate signal as

$$u_v = \begin{cases} 0 & 0 < t \leq 200 \text{ s} \\ u_{va} & 200 < t \leq 1000 \text{ s} \end{cases}$$

where  $u_{va} \in \{0.25, 0.5, 0.75\}$  for partial load acceptance studies of 25%, 50%, and 75%, respectively. Figure 3.8 shows the water mass oscillation inside the simple, the sharp orifice type, and the throttle valve type surge tanks during the partial load acceptances.

In Figure 3.7 d), the steady-state water level inside the surge tank decreases after the PLAs as shown in the case of a throttle valve type surge tank. The steady-state water level within the tank is 70m while the plant is operated at no load, i.e,  $h_{ST}^{NL} = H_r + H_{in}$ ; however, after a 75% acceptance of the full load at  $t = 200$ s, the water level reaches a steady-state level of 68.4m. As the load acceptance increases from no load to full load, the steady-state head loss in the intake increases.

### 3.1.2.8 PLR, PLA, and turbine pressure

Figure 3.9 shows the turbine pressure for Trollheim HPP compared with the simple, the sharp orifice type, and the throttle valve type surge tanks during partial load rejection studies.

Figure 3.10 shows the turbine pressure for Trollheim HPP compared with the simple, the sharp orifice type, and the throttle valve type surge tanks during partial load acceptance studies.

### 3.1.3 Air-cushion surge tank (ACST)

In the paper presented in Appendix A, an air-cushion surge tank has been modeled without the inclusion of the access tunnel to the air chamber. In the case of the hydropower plant with ACST having an access tunnel, the ACST can be modeled by the inclusion of the friction factor due to the access tunnel, similarly, as in the case of the throttle valve type surge tank. The paper presented in Appendix B provides the detailed modeling of the ACST. It is of interest to:

1. validate the developed model of the ACST with the experimental data from the 130MW Torpa HPP from [7]
2. study the hydraulic behavior of the ACST during various load acceptances and rejections.

Figure 3.11 (a) shows the layout diagram of Torpa HPP. Similarly, Figure 3.11 (b) shows the simulation model of Torpa HPP created in OpenHPL.

Figure 3.12 shows the simulated versus real measurement for Torpa HPP. As shown in Figure 3.11 (b),  $u_{v1}$  and  $u_{v2}$  are the turbine valve signals for the turbine Unit-1 and the turbine Unit-2, respectively, for controlling the volumetric discharge through the turbines.

The input turbine valve signal for Unit-1 is given by

$$u_{v1} = \begin{cases} 0.68 & 0 < t \leq 500 \text{ s} \\ \frac{0.68}{50}(t - 550) + 0.98 & 500 \text{ s} < t \leq 550 \text{ s} \\ 0.98 & 550 \text{ s} < t \leq 1200 \text{ s} \end{cases},$$

and the input turbine valve signal for Unit-2 is given by,

$$u_{v2} = \begin{cases} 0.55 & 0 < t \leq 500 \text{ s} \\ \frac{0.55}{50}(t - 550) + 0.93 & 500 \text{ s} < t \leq 550 \text{ s} \\ 0.93 & 550 \text{ s} < t \leq 1200 \text{ s} \end{cases}.$$

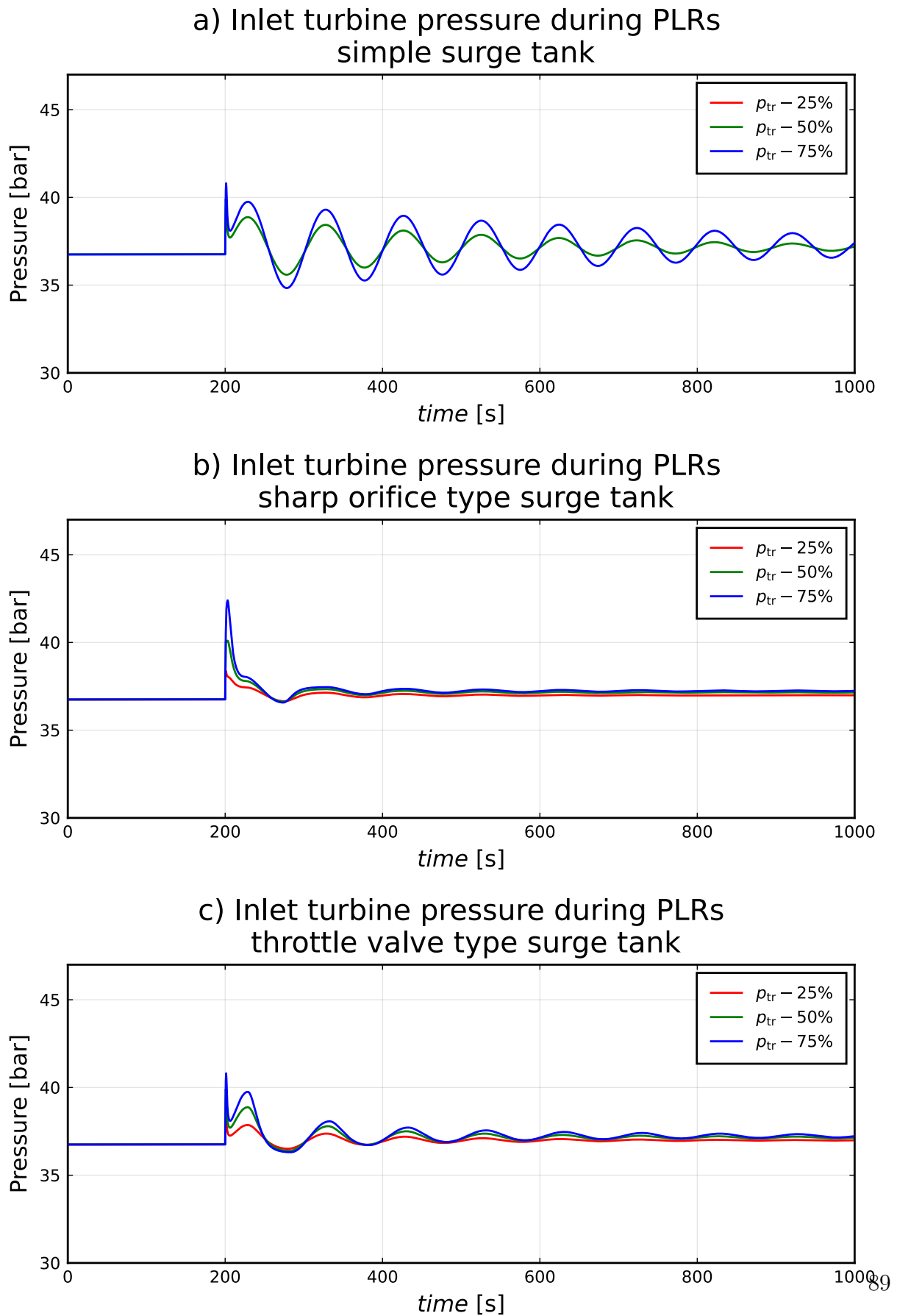
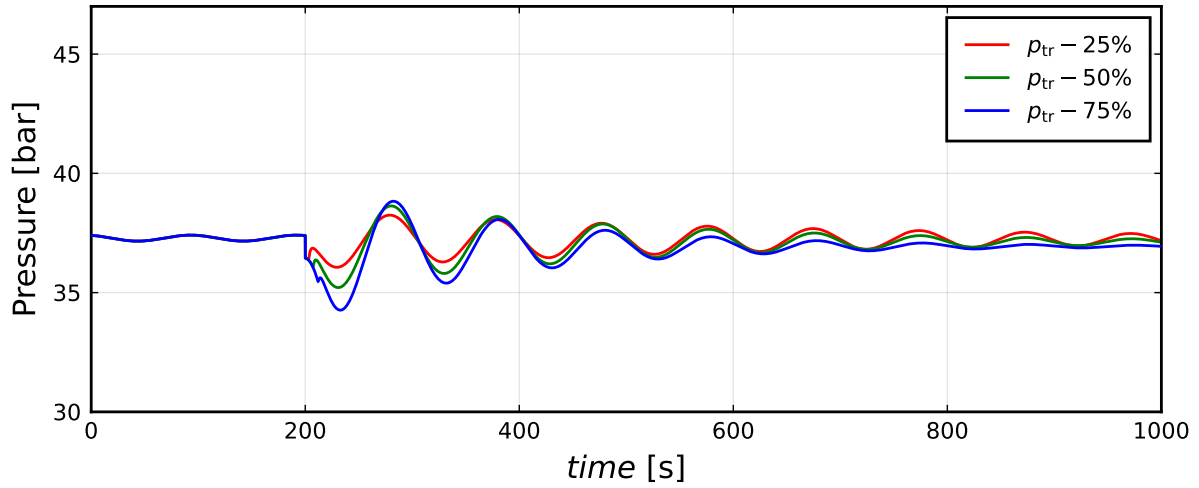
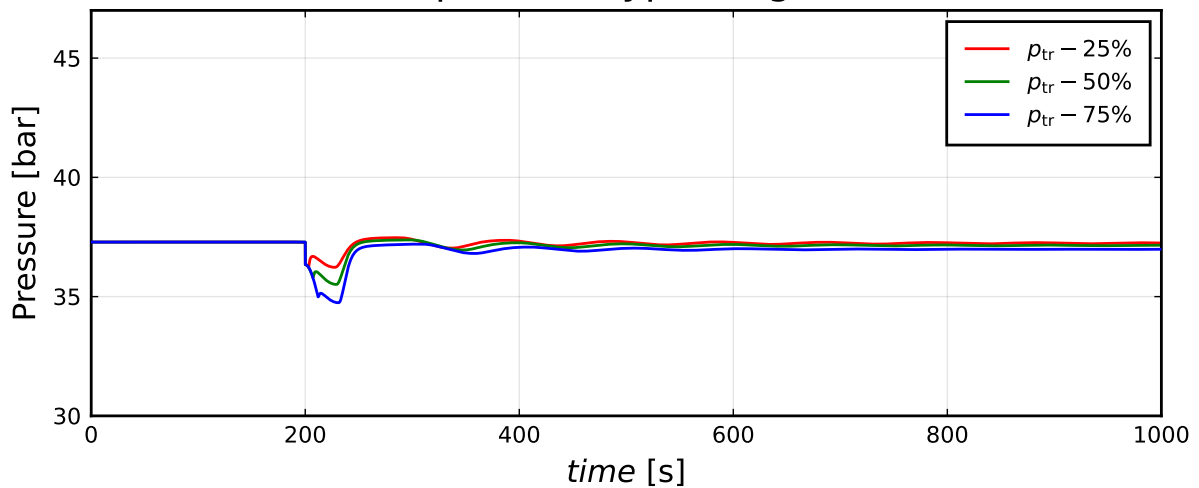


Figure 3.9: Turbine pressure for various partial load rejections (PLRs) for surge tanks.

a) Inlet turbine pressure during PLAs  
simple surge tank



b) Inlet turbine pressure during PLAs  
sharp orifice type surge tank



c) Inlet turbine pressure during PLAs  
throttle valve type surge tank

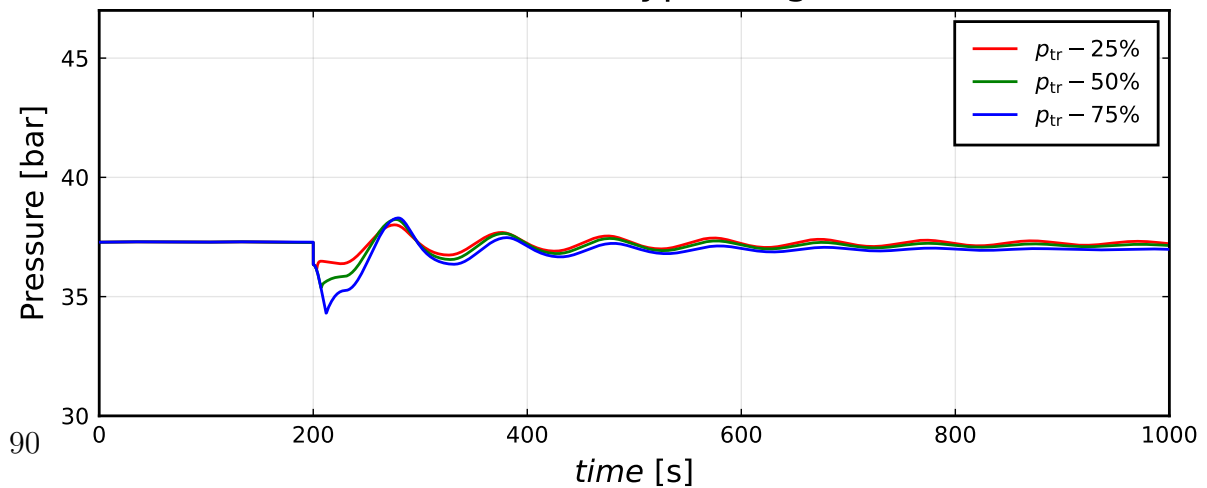


Figure 3.10: Turbine pressure for various partial load acceptances (PLAs) for surge tanks.

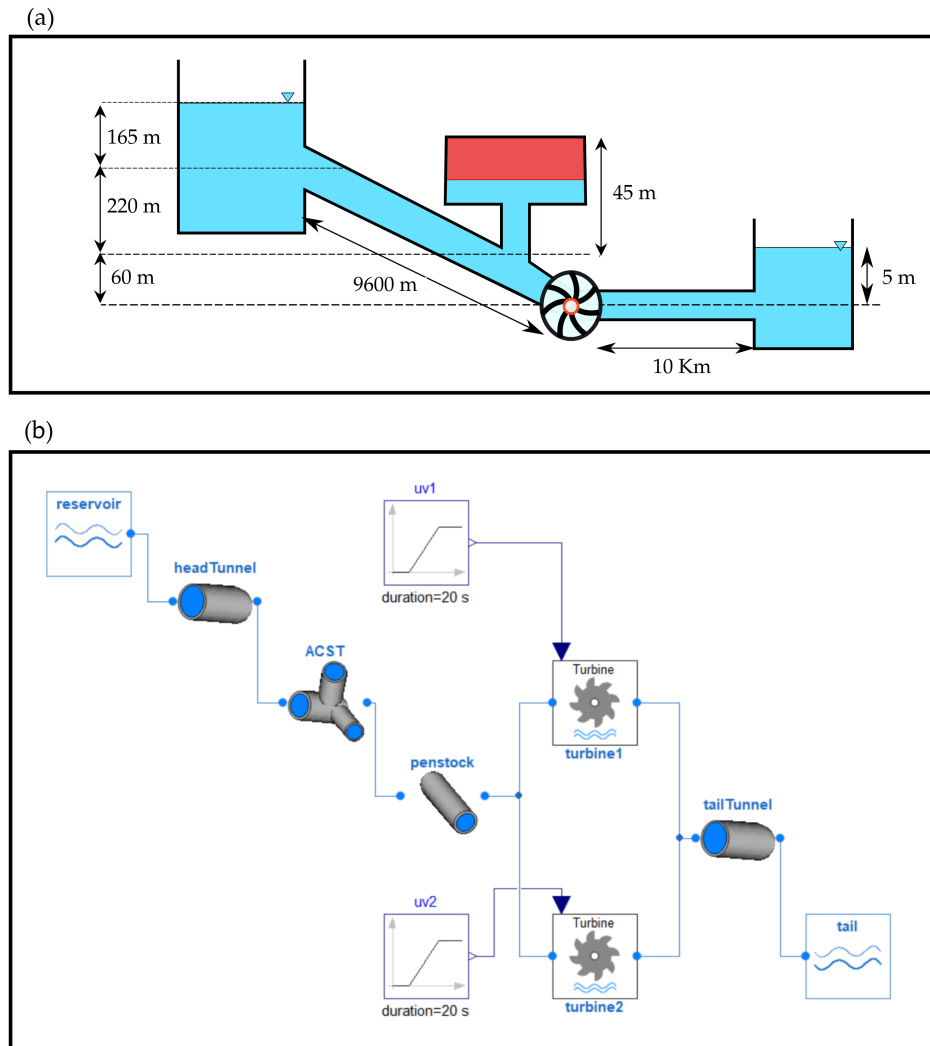


Figure 3.11: (a) Layout diagram for Torpa HPP. Nominal head, nominal discharge, and nominal power output are 445 m,  $40\text{m}^3/\text{s}$  and  $150\text{MW}$ , respectively. The ACST has air volume of  $1300\text{m}^3$ , initially pressurized at  $41 \cdot 10^5\text{Pa}$ . Similarly, both of the headrace and tailrace tunnels are 7 m in diameter. Torpa HPP consists of two turbine units, Unit-1 and Unit-2, each rated at  $75\text{MW}$  with rated discharge at  $20\text{m}^3/\text{s}$ . (b) Simulation model of Torpa HPP implemented in OpenHPL from the head reservoir to the tail reservoir.



### 3 Main Results

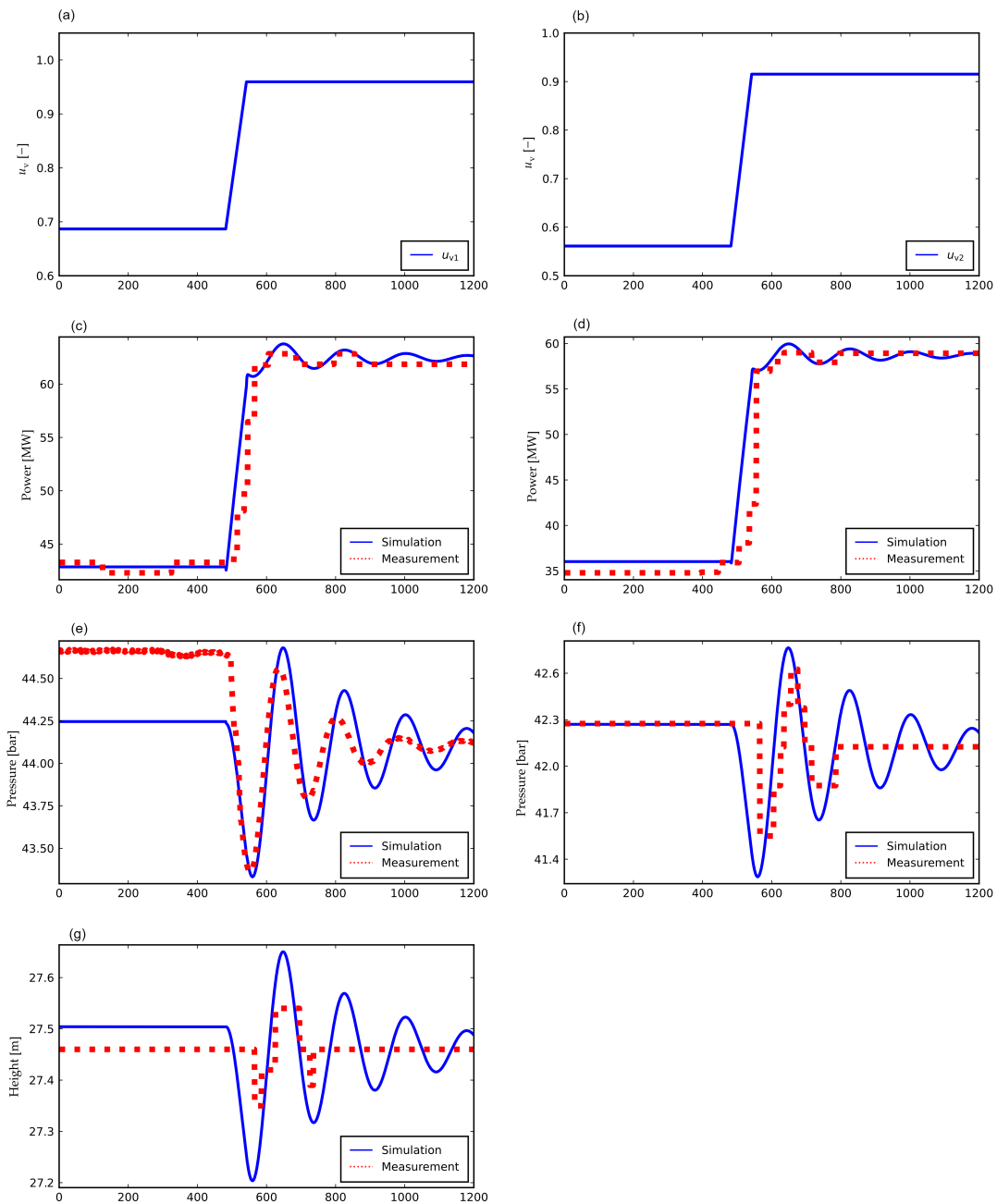


Figure 3.12: Simulation versus real measurements for Torpa HPP, (a) turbine valve signal for Unit-1, (b) turbine valve signal for Unit-2, (c) power output for Unit-1, (d) power output for Unit-2, (e) inlet pressure of the turbine units or the outlet pressure of the penstock, (f) air cushion pressure inside the ACST, and (g) height of water level inside the ACST. Experimental data are provided by [7].

For inputs  $u_{v1}$  and  $u_{v2}$ , the mechanical power outputs for turbine Unit-1 (Figure 3.12 c) and turbine Unit-2 (Figure 3.12 d), the turbine inlet pressure  $p_{tr}$  (Figure 3.12 e), and the air pressure inside the surge tank  $p_c$  (Figure 3.12 f) are recorded for 1200s with the measurement samples taken at each second. The air pressure  $p_c$  is measured using the pressure sensor PARO scientific 8DP000-S with an error of less than 0.01 % of full scale of 6Mpa, the turbine inlet pressure  $p_{tr}$  is measured using the pressure sensor PARO scientific DIQ 73K with an error of less than 0.04% of full scale of 20Mpa, and the measurements for the mechanical power outputs are provided by the plant owner from Torpa HPP. The information about Torpa HPP and its experimental procedures are taken from [7]. Figure 3.12 shows that the simulation corresponds well with the real measurements in the case of power productions from the turbines (Figure 3.12 c,d). In the case of the turbine inlet pressure  $p_{tr}$  (Figure 3.12 e) there is an steady-state error of 0.6bar for  $0 < t \leq 500$ s. In this work, the headrace tunnel is considered with a simple slanted pipe geometry as shown in Figure 3.11 a. Similar steady-state error can be seen in the case of the height of water level inside the ACST  $h$  (Figure 3.12 g) with negligible error of 0.05m. In the case of air pressure inside the ACST  $p_c$ , the simulation and the measurement data are in good agreement. The measurement sampling rate in the case of water level  $h$ , air pressure  $p_c$ , and turbine power outputs are slower and oscillatory because the data are only recorded after a minimum change in the measured value, which may be the reason for the steady-state errors and phase difference between the simulation and measurements shown in Figure 3.12 c,d,f,g. In addition, in Figure 3.12 f,g for  $800\text{s} < t \leq 1200\text{s}$ , the simulated values have poorly damped oscillation while the measurement quickly reaches a steady value. The simulated and the experimental dynamics of the variables ( $p_c$  and  $h$ ) are not captured well because of the slower sampling rate of the sensors, and the real plant has more damped responses than the simulated results. The simulation and the real measurements are matched by manual tuning of pipe roughness height of the headrace tunnel ( $\epsilon \approx 0.4\text{mm}$ ), hydraulic diameter of the access tunnel  $D_t \approx 15\text{m}$ , and hydraulic diameter of the air chamber  $D \approx 24\text{m}$ .

Figure 3.13 shows hydraulic performance of the ACST during load acceptance and rejection studies for Torpa HPP. Figure 3.13 a,c,e,g shows the turbine valve signal  $u_v$ , the air pressure  $p_c$ , the turbine inlet pressure  $p_{tr}$ , and the water level inside ACST  $h$ , respectively, for the different percentage change in the load acceptances. Similarly, Figure 3.13 b,d,f,h shows  $u_v$ ,  $p_c$ ,  $p_{tr}$  and  $h$ , respectively, for the different percentage change in the load rejections.

Figure 3.13 a shows the turbine valve signal generated for load acceptances of 25%, 50%, 75%, and 100%. Figure 3.13 c, at  $t = 500\text{s}$ , shows that from the no load operation to TLA, the difference in the air pressure  $p_c$  inside the ACST is around 4bar. Similarly, Figure 3.13 e shows that the difference in turbine inlet pressure  $p_{tr}$  is around 3bar, and Figure 3.13 g shows that the difference in the water level  $h$  inside the ACST is around 1m. In addition, Figure 3.13 c shows that the difference in  $p_c$  from no load operation to 25% load acceptance, 50% load acceptance and 75% load acceptance are around 1bar, 2bar

### 3 Main Results

and 3 bar, respectively. Similarly, results can be obtained for  $p_{tr}$  (Figure 3.13 e) and  $h$  (Figure 3.13 g). For  $p_c$ ,  $p_{tr}$  and  $h$  oscillation dies out as the time progresses for  $t > 500$ s.

Figure 3.13 b shows the turbine valve signal generated for load rejection studies of 25%, 50%, 75%, and 100%. Figure 3.13 d, at  $t = 500$ s, shows that from full load operation to TLR, the difference in  $p_c$  is around 4 bar as similar in the case of TLA. Similarly, the difference is around 3 bar in the case of  $p_{tr}$ , as shown in Figure 3.13 f. The difference in  $h$  from full load operation to TLR is also 1 m, as in the case of TLA. Similarly, from Figure 3.13 d, the difference in  $p_c$  from full load operation to load rejection studies of 25% , 50% and 75% are around 1 bar, 2 bar and 3 bar, respectively. Similar results can be obtained for  $p_{tr}$  (Figure 3.13 f) and  $h$  (Figure 3.13 h). For  $p_c$ ,  $p_{tr}$  and  $h$ , oscillation dies out for  $t > 500$ s, similar to the cases of load acceptance. However, the oscillation dies out quicker in the case of TLA than TLR.

#### 3.1.4 Summary

In the paper presented in Appendix A, modeling of different types of surge tanks used in hydropower systems is provided as feature extensions of OpenHPL. Unlike the simple surge tank, the sharp orifice type surge tank includes an orifice for the water-flow obstruction in the inlet of the surge tank. Likewise, the throttle valve surge tank includes an access tunnel with a smaller diameter at the inlet of the surge tank where the water flows toward the larger diameter of the tank. For modeling the sharp orifice type surge tank, and the throttle valve type surge tank, generalized fluid friction factors for the hydraulic obstructions are considered. The simple surge tank had been used previously for the modeling and validation of Trollheim HPP in [6]; however, the experimental data are validated with the model for the turbine flow rate, turbine's inlet, and outlet pressure, and the turbine generated power. Thus, the model of the simple surge tank can be used for the modeling of other hydropower plants. The model of the sharp orifice type surge tank and the throttle valve surge tank are not validated with experimental data. However, these models can be used for studying the maximum required height of the surge tank, the water mass oscillation surge inside the surge tank, and the water hammer effect at various load acceptances and rejections. The paper presented in Appendix C provides the performance of the surge tanks on the different hydropower discharge rates. Water mass oscillations inside the simple, the sharp orifice type, the throttle valve type, and the air-cushion type surge tanks are studied for various load acceptances and rejections. Results show that the maximum required height of the surge is lowest in the case of a sharp orifice type surge tank. However, the results show that mass oscillation attains a steady state quicker in the case of the throttle valve surge tank. For the sharp orifice type surge tank with a diameter of the orifice  $D_{so}$  and the simple surge tank with diameter  $D$ , the maximum required height of the surge tank decreases exponentially for  $D_{so} \leq 0.5D$ . Similarly, for the throttle valve surge tank with the diameter of the throat  $D_t$ , the maximum required

### 3.1 Surge Tanks

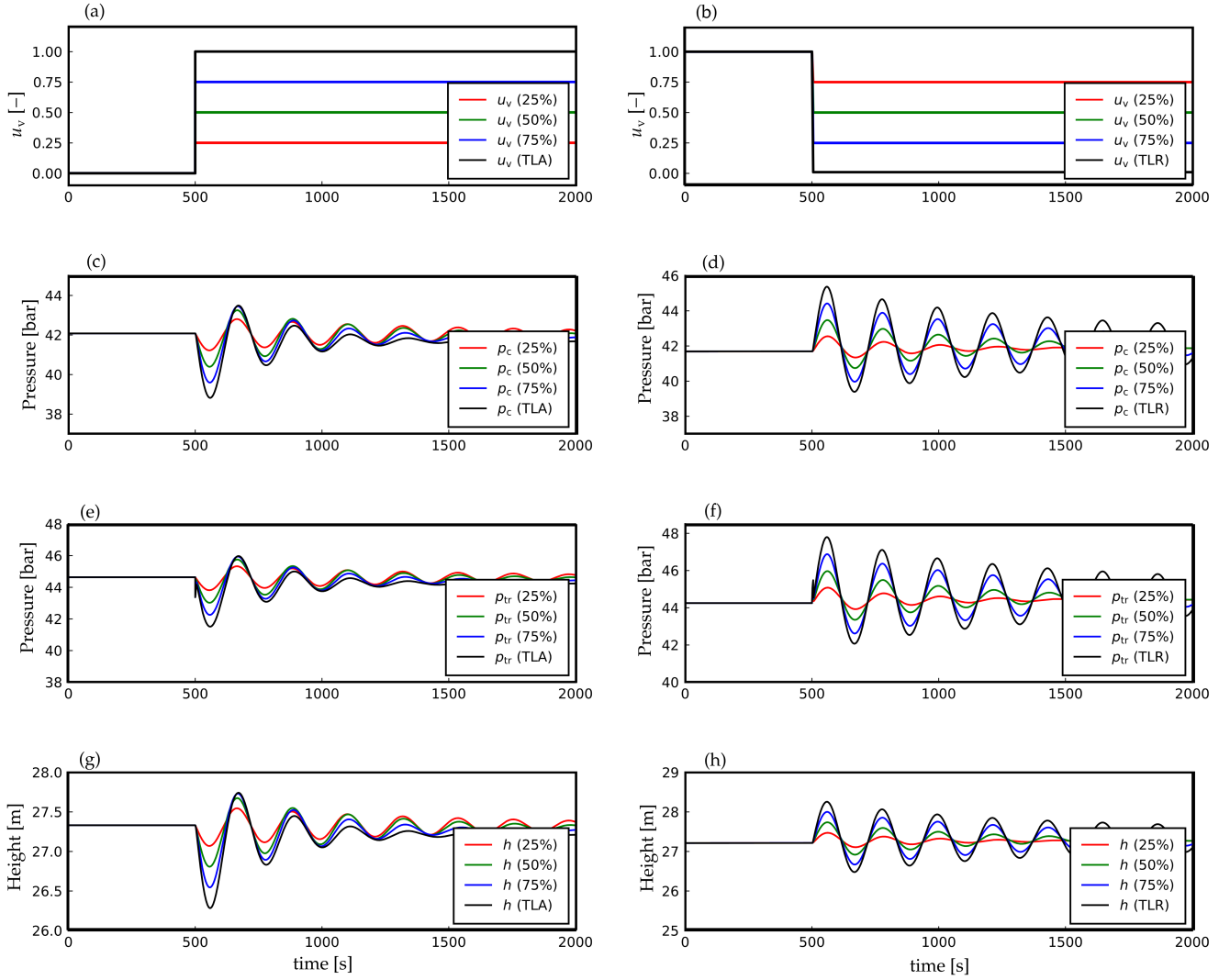


Figure 3.13: Hydraulic performance of the ACST for Torpa HPP for the different percentage change in the load acceptances and the load rejections, (a) turbine valve signal  $u_v$  as an input to the load acceptances, (b) turbine valve signal  $u_v$  as an input to the load rejections, (c) air pressure  $p_c$  for the load acceptances, (d) air pressure  $p_c$  for the load rejections, (e) turbine inlet pressure  $p_{tr}$  for the load acceptances, (f) turbine inlet pressure  $p_{tr}$  for the load rejections, (g) water level inside the ACST  $h$  for the load acceptances, and (h) water level inside the ACST for the load rejections.

### 3 Main Results

height of the surge tank decreases exponentially for  $D_t \leq 0.375D$ . The mass oscillation dies out quickest in the case of the throttle valve surge tank.

The paper in Appendix A also provides a model of the ACST without the inclusion of the access tunnel. The model of ACST is further extended with the inclusion of the access tunnel in the paper presented in Appendix B, and the model of the ACST has been validated with the experimental data from the Torpa HPP. The model is built with the consideration of an access tunnel of a smaller diameter connected to an air chamber of a larger diameter. The experimental data and the model simulation were matched by manual tuning of the pipe roughness height of the headrace tunnel, and hydraulic diameters of the access tunnel and the air chamber of the ACST. Oscillations die out much quicker for the real plant than for the model. The simulation studies carried out for load acceptance and rejection show the robust hydraulic behavior of the ACST in terms of suppressing water mass oscillation and water hammer pressure which indicates that a hydropower plant with ACST makes it a potential candidate for flexible hydropower in case of an energy-mix interconnected power grid. The model of the ACST can be further improved by considering air density for calculating frictional force due to air inside the ACST. The model can also be further improved by assuming the velocity of air inside the surge tank varies linearly between the air-water connection surface and the top of the surge tank. At the air-water connection surface, the velocity of the water equals the velocity of the air. At the top of the surge tank, the velocity of air should be considered zero.

## 3.2 Draft Tubes

For draft tubes, two types, viz., a conical diffuser and Moody spreading pipes, are modeled. In the paper presented in Appendix A, a simulation case study is performed for Trollheim HPP in Norway in the case of load rejection from the prime mover from full load to half load, and the inlet pressure at the turbine is observed for the operation of the draft tube. The model of a conical diffuser is based on a generalized fluid friction factor due to the diffusion of the draft tube from a smaller diameter to a larger diameter. For achieving maximum efficiency in the case of the conical diffuser, a diffusion angle of  $8^\circ$  is considered, Section 2.2.5. Similarly, the model of the Moody spreading pipes is developed considering the generalized friction factor based on the bifurcation angle  $\theta$  for  $15^\circ \leq \theta \leq 90^\circ$ .

Figure 3.14 shows the simulated responses for the conical diffuser and Moody spreading pipes. The influent diameter  $D_i = 4\text{ m}$  for both types of draft tubes. The effluent diameter  $D_e = 4.978\text{ m}$  for the conical diffuser with the diffusion angle of  $8^\circ$  and the effluent diameter  $D_o = 3.5\text{ m}$  for the Moody spreading pipes. The length of the main part of the Moody spreading pipes is  $L_m = 4\text{ m}$  and the length of the branches  $L_b = 3\text{ m}$ . Moody spreading pipes draft tube is simulated for branching angles of  $15^\circ$ ,  $30^\circ$ , and  $45^\circ$ .

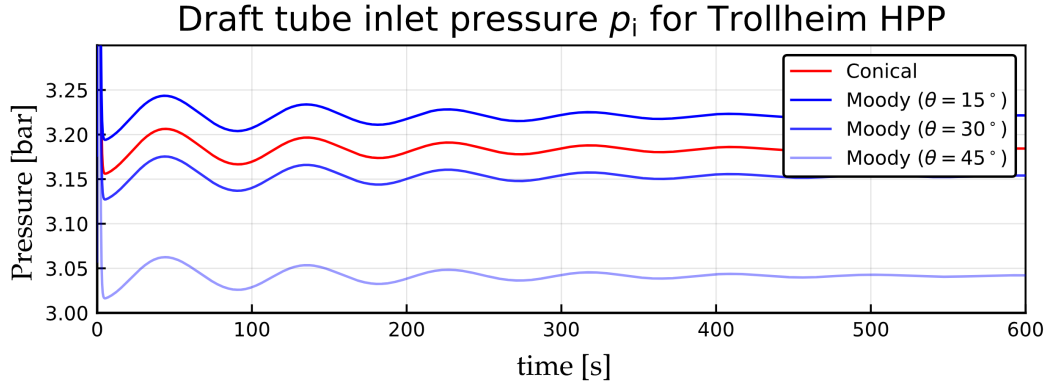


Figure 3.14: Simulated response for the inlet pressure of the conical diffuser and the Moody spreading pipes with different branching angles.

The model of the conical diffuser is only considered with a diffusion angle of  $8^\circ$ . Thus, the model of the conical diffuser can be extended further with the inclusion of the friction factor for other diffusion angles from [3]. The models of the conical diffuser and the Moody spreading pipes have not been validated with experimental data.

### 3.3 Active Power Frequency Control in OpenHPL

#### 3.3.1 Test case : Trollheim hydropower plant

For studying active power frequency control, we take as case study island operation of the Trollheim HPP. The power plant specifications are given in Table 3.1.

##### 3.3.1.1 Fitting the AGC prediction model

Section 2.3.3.2 provides an AGC prediction model (control model) which will be used for tuning the controller. The model of the turbine and the hydropower governor (with static/transient droop) in OpenHPL is given in Section 2.2.3.6 and 2.2.3.9, respectively, and these models are different from the turbine and the governor models from the per unit AGC prediction model from Section 2.3.3.2.

Thus, the parameter of the prediction model can be tuned for better fit to data generated by the OpenHPL implementation of the Trollheim HPP. Parameters  $M$ ,  $T_w$  and  $T_g$  in the grid, turbine, and governor servo mechanism models, are tuned.

In addition, the droop (regulation)  $R$  of the AGC prediction model has to be tuned to partially describe the lack of transient droop compared to the OpenHPL as well since the

### 3 Main Results

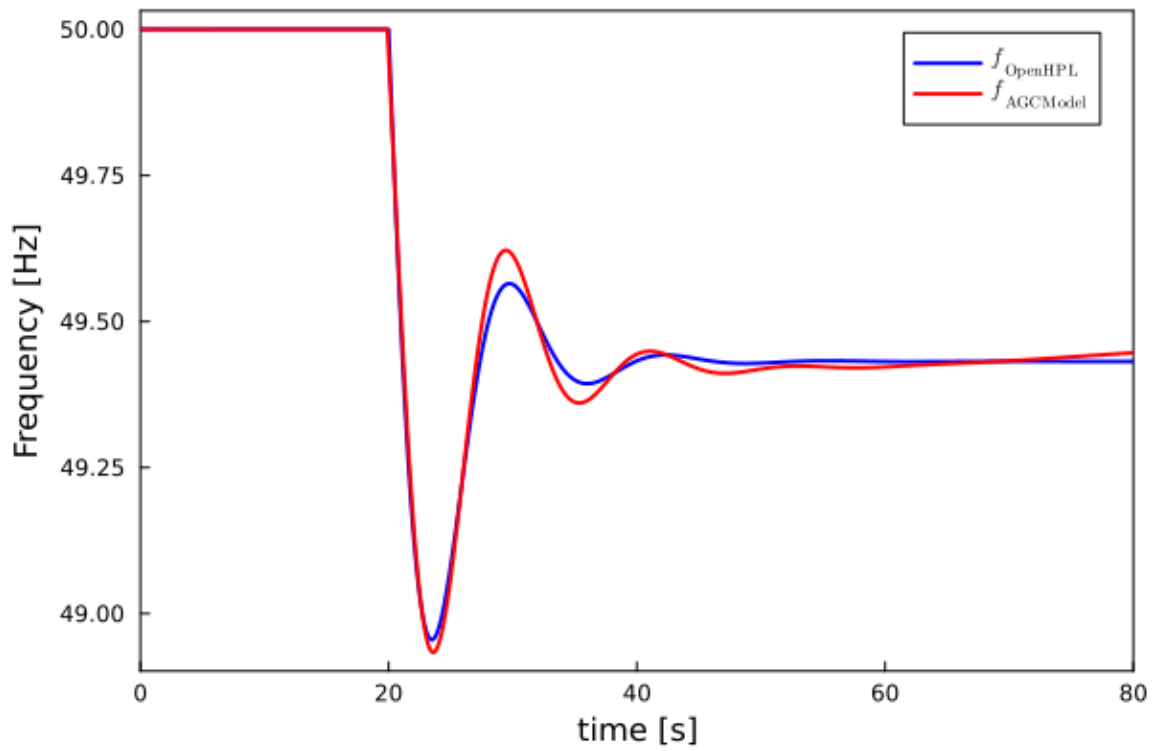


Figure 3.15: Fitting frequency step responses from the AGC prediction model and the Trollheim HPP from OpenHPL.  $M$ ,  $T_w$ ,  $T_g$  and  $R$  are the tuned parameters for the AGC prediction model with respect to the OpenHPL model.

### 3.3 Active Power Frequency Control in OpenHPL

Table 3.1: Trollheim HPP specifications.

Quantities	Symbol	Value
Nominal head	$H^n$	460m
Nominal discharge	$\dot{V}^n$	24m/s
Length of the penstock	$L_p$	500m
Cross-sectional area of the penstock	$A_p$	$4\pi\text{m}^2$
Water time constant	$T_w = \frac{L_p \dot{V}^n}{g A_p H^n}$	0.44 s
Rated power (Base power)	$P^r$	130MW
Inertia of turbine-generator aggregates	$J$	$1.5 \cdot 10^4 \text{kgm}^2$
Gate servo motor time constant	$T_{gs}$	0.2 s
Pilot servo motor time constant	$T_{ps}$	1.75 s
Dashpot's valve time constant	$T_\delta$	0.2 s
Static droop coefficient	$\sigma$	0.1
Transient droop coefficient	$\delta$	0.04
Maximum gate opening rate	$\dot{u}^{\max}$	0.05 pu/s
Maximum gate closing rate	$\dot{u}^{\min}$	0.2 pu/s

effect of the transient droop  $\delta$  has not been considered in this prediction model. The governor model for Trollheim HPP in OpenHPL given in Section 2.2.3.9 has considered the effect of the transient droop as well. The parameters can be tuned by least squares data fitting, where data = frequency step response from the OpenHPL Trollheim HPP model, and model = AGC prediction model from Section 2.3.3.2 (this was implemented in Julia). The objective function of the least squares data fitting is given as

$$\min_{\theta} J_{ls} = \sum_{i=1}^N (f_{\text{OpenHPL},i} - f_{\text{AGCModel},i})^2$$

where the parameter  $\theta$  are the parameter from the AGC prediction model that needs to be tuned for the OpenHPL Trollheim HPP model;  $M, T_w, T_g$  and  $R$ .  $f_{\text{OpenHPL}}$  is the frequency output from the OpenHPL, and can be used as measurement data, and  $f_{\text{AGCModel}}$  is the frequency output from the AGC prediction model from Section 2.3.3.2.

The parameters of the governor model of Trollheim HPP in OpenHPL are given in Table 3.1. To find the parameters of the AGC prediction model for the Trollheim HPP implemented in OpenHPL, we considered a load change  $\bar{P}^\delta = 0.1 \text{p.u.}$  at  $t = 20\text{s}$  from the steady-state operation with power output  $65\text{MW}$ , and the output frequency step response of the grid is observed for the next  $60\text{s}$ . The output frequency step response is used as data in the least squares data fitting problem.



### 3 Main Results

Table 3.2: Trollheim HPP control model parameters.

Quantities	Symbol	Value
Turbine time constant	$T_w$	0.39 s
Governor time constant	$T_g$	3.34 s
Machine constant	$M$	10.2 s
Load damping factor	$D$	0.8
Governor droop	$R$	0.14

Figure 3.15 shows the frequency step responses of Trollheim HPP in OpenHPL and the AGC prediction model with tuned parameters. The AGC prediction model can be used for control design, for example as a prediction model for MPC. The fitted parameters of the AGC prediction model are given in Table 3.2.

The parameters of the control model (AGC prediction model) in Table 3.2 are used for tuning the PI controller using SIMC PID tuning rules [56]. The AGC prediction model transfer function is developed in Figure 2.11.

#### 3.3.1.2 Active power frequency PI control

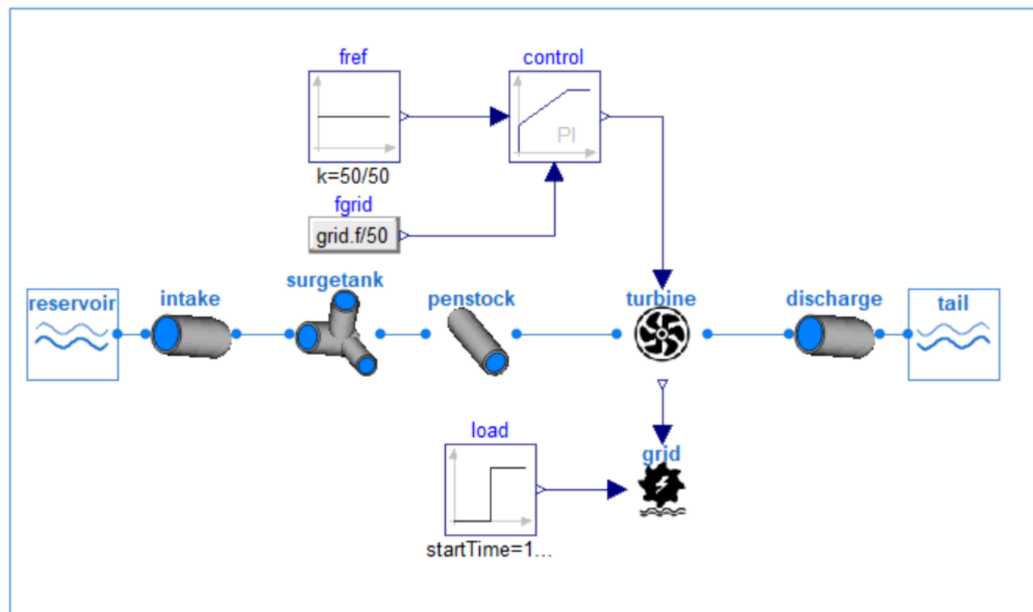
It is of interest to implement active power frequency control of Trollheim HPP in OpenHPL for three cases:

1. Isochronous governor control
2. Droop governor control, and
3. Automatic generation control.

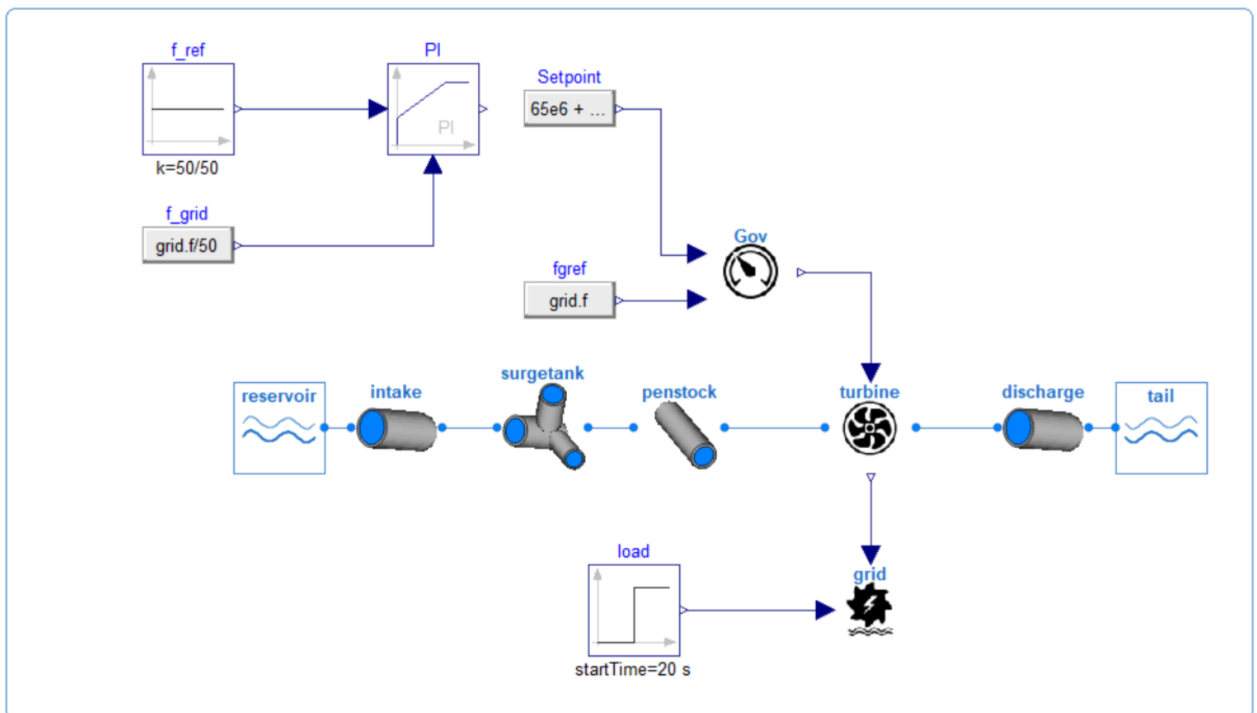
Figure 3.16 shows the active power frequency control of Trollheim HPP implemented in OpenHPL in island operation. Figure 3.16 a) shows the isochronous governor control where a PI controller drives the per unit frequency deviation of the grid to zero after the load disturbance. Figure 3.16 b) shows the case where the AGC prediction model has been used to tune a PI controller, and this PI controller has been implemented in OpenHPL as part of the Trollheim HPP model.

Figure 3.17 shows the frequencies, load, and generations of Trollheim HPP when operated in isochronous governor mode, droop governor control mode, and AGC mode. Droop governor control mode is used in multi-generators hydropower plants either in island operation or in the interconnected networks. Here, all the active power frequency control modes are given for frequency step responses comparisons. The PI controller parameters in the case of isochronous governor mode are  $K_{IG} = 7$  and  $T_{IG} = 5$  s. The parameters for the

### 3.3 Active Power Frequency Control in OpenHPL



a) Isochronous Governor Control of a Trollheim HPP.



b) Automatic Generation Control of Trollheim HPP.

Figure 3.16: Active power frequency control of Trollheim HPP implemented in OpenHPL.

3 Main Results

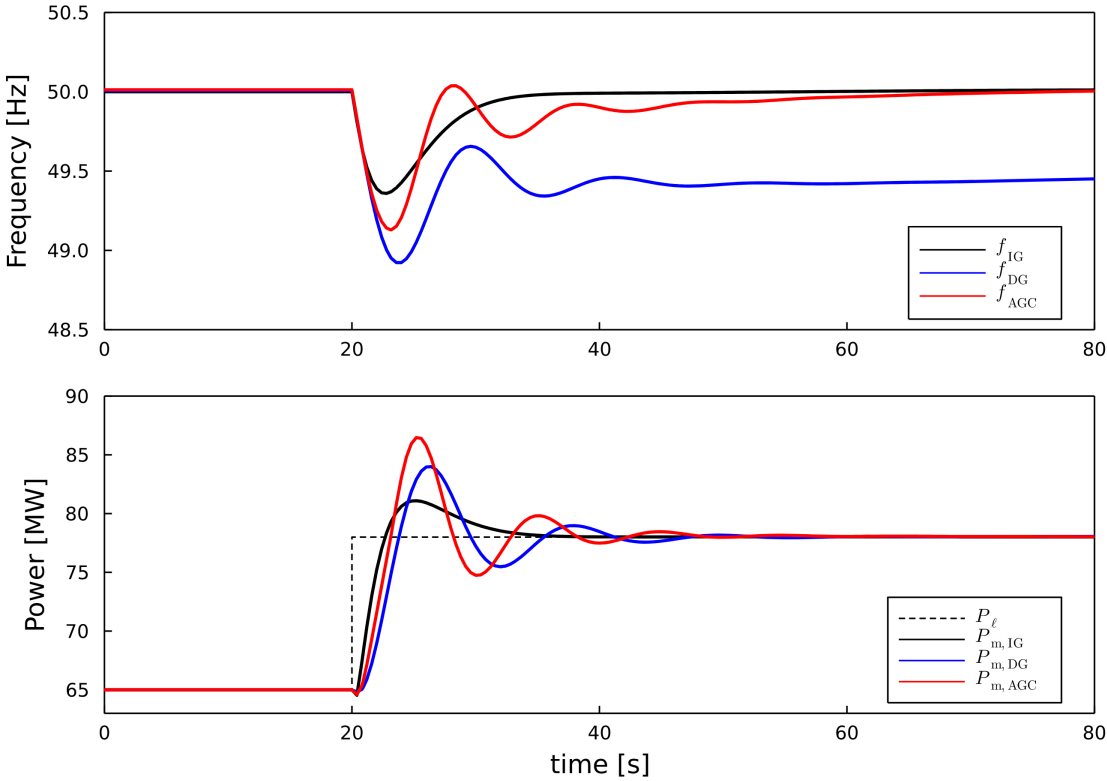


Figure 3.17: Power frequency control of Trollheim HPP.

### 3.3 Active Power Frequency Control in OpenHPL

Table 3.3: Specifications of units in multi-generator system areas.

Quantities	AGC unit	Unit-1	Unit-2
Rated powers $P^r$	130MW	100MW	70MW
Inertia of turbine-generator aggregates $J$	$1.5 \cdot 10^4 \text{kgm}^2$	$1.2 \cdot 10^4 \text{kgm}^2$	$1 \cdot 10^4 \text{kgm}^2$
Droop $R$	0.1	0.1	0.2

controller are first tuned using SIMC PID tuning rules [56], and fine tuned through trial and error to get smoother responses. The PI controller parameters in the case of AGC mode are  $K_{AGC} = 2$  and  $T_{AGC} = 5$  s. The power plant is operated at 65 MW in steady-state up to 20 s. At  $t = 20$  s, a load disturbance of 10% of the rated power, i.e.,  $P_\ell^\delta = 13$  MW is injected, and the mechanical power generation and frequencies of the grid are observed in three cases. From Figure 3.17, we see that both the isochronous governor and the AGC bring the frequency of the grid back to 50 Hz. The isochronous governor restores the grid frequency  $f_G$  to 50 Hz within 15 s, i.e., at  $t \approx 35$  s after the load disturbance occurs at  $t = 20$  s. However, AGC restores the grid frequency  $f_{AGC}$  to 50 Hz within 50 s, i.e., at  $t \approx 70$  s after the load disturbance occurs at  $t = 20$  s. On the other hand, in the case of droop governor control of Trollheim HPP, the grid frequency  $f_{DG}$  achieves a new steady-state frequency with  $f_{DG} \approx 49.4$  Hz at  $t \approx 50$  s. Figure 3.17 also shows the mechanical power generation when the load disturbance is created at  $t = 20$  s.

#### 3.3.2 Multi-generator system

To study the operation of AGC in a multi-generator system, three fictitious hydropower plants were created based on the Trollheim HPP. Table 3.3 shows the ratings, inertia, and droop of the units. One unit is the AGC unit which takes part in restoring the grid frequency. The other two units are non-AGC units but take part in the primary control during load disturbances.

Figure 3.18 shows frequencies, load, and generations in the multi-generator system. The power plants are initially operated in steady state with power production of 45 MW each up to  $t = 20$  s. The total steady state production is 135 MW. At  $t = 20$  s a load disturbance  $P_\ell^\delta = 10$  MW is injected. All the units take part in primary control (with droop governor control). As a supplementary control action, the AGC unit increases its generation to restore the grid frequency at 50 Hz. During secondary control or frequency restoration control, the non-AGC units, Unit-1 and Unit-2 return to their own previous set-points producing 45 MW each. As the droop of Unit-2 is greater than that of Unit-1, Unit-2 has slower production change during the period of disturbance than Unit-1 as shown in the power productions from the units in Figure 3.18.

### 3 Main Results

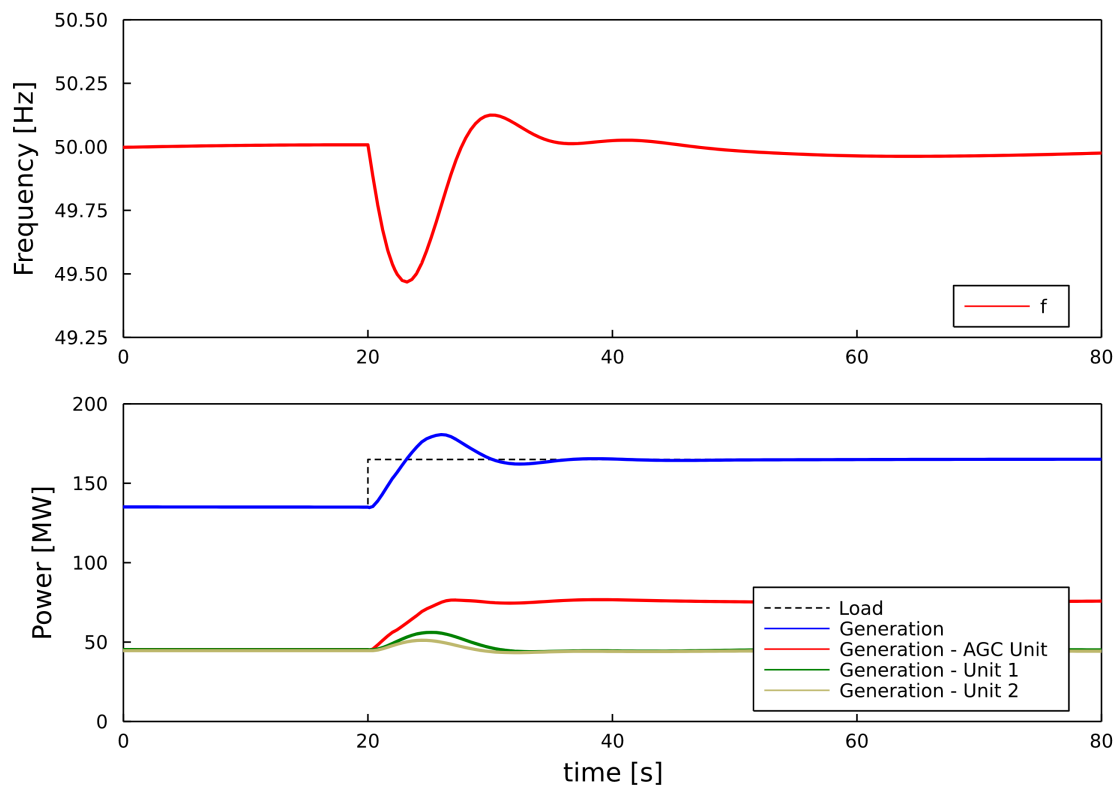


Figure 3.18: AGC in the multi-generator system. Three units: one AGC unit and two non-AGC units are operating in parallel to supply a common consumer load. A load disturbance of 10MW is created at  $t = 20$ s and the frequency of the grid, and generations from the hydropower units are observed for the next 60s.

### 3.3 Active Power Frequency Control in OpenHPL

Table 3.4: Control model parameters for two synchronous areas.

Quantities	Area-1	Area-2
Rated power	$P_1^r = 130 \text{ MW}$	$P_2^r = 130 \text{ MW}$
Turbine time constant	$T_{w1} = 0.35 \text{ s}$	$T_{w2} = 0.35 \text{ s}$
Governor time constant	$T_{g1} = 0.2 \text{ s}$	$T_{g2} = 0.4 \text{ s}$
Machine constant	$M_1 = 11.7 \text{ s}$	$M_2 = 11.7 \text{ s}$
Load damping factor	$D_1 = 0.8$	$D_2 = 0.8$
Governor droop	$R_1 = 0.1$	$R_2 = 0.2$
Frequency bias factor	$B_1 = 10.8$	$B_2 = 5.8$

#### 3.3.3 Interconnected areas

We consider two synchronous areas connected with a tie line flow between the areas. Table 3.4 shows AGC prediction model parameters (control model parameters) of the two areas. The control model parameters for both the synchronous areas are taken for the Trollheim HPP. The synchronous areas are different in terms of their governor time constant and governor droop coefficients as shown in Table 3.4. The synchronizing power coefficients  $\bar{P}_s$  for the interconnected network is set to **2p.u.** Currently, OpenHPL does not have model of tie-line power flow between the synchronous areas. Thus, the results obtained in this section are from the block diagram shown in Figure 2.14, and are presented for future reference.

Figure 3.19 shows the frequencies of synchronous areas, power generations from each area, and tieline power flow from Area-1 to Area-2. A load increase of **10MW** is created at  $t = 20\text{s}$  for Area-1, and this load increase will cause the grid frequencies of the areas to drift away from **50Hz**. Figure 3.19 shows that the frequencies of synchronous areas,  $f_1$  and  $f_2$ , are restored to **50Hz** after the load disturbance. The mechanical power generations  $P_{m,1}$  and  $P_{m,2}$  from both areas as in Figure 3.19 shows that both areas take part in the primary control from  $t = 20\text{s}$  to  $t \approx 37\text{s}$ . As a secondary control action the generations (from the AGC unit) from Area-1 should be increased to meet the change in the load demand of **10MW** and the AGC unit of Area-2 should return to its own set-point. In the figure, the generation from Area-1 is increased from **65MW** to **75MW** while generation from Area-2 remains at its own set-point. The new steady state in power production is reached around  $t = 60\text{s}$ . As the AGC control of two synchronous areas should also maintain the tie line power at the scheduled level, the figure also shows that tie line power is re-scheduled at **50MW** after the load disturbance at Area-1.

### 3 Main Results

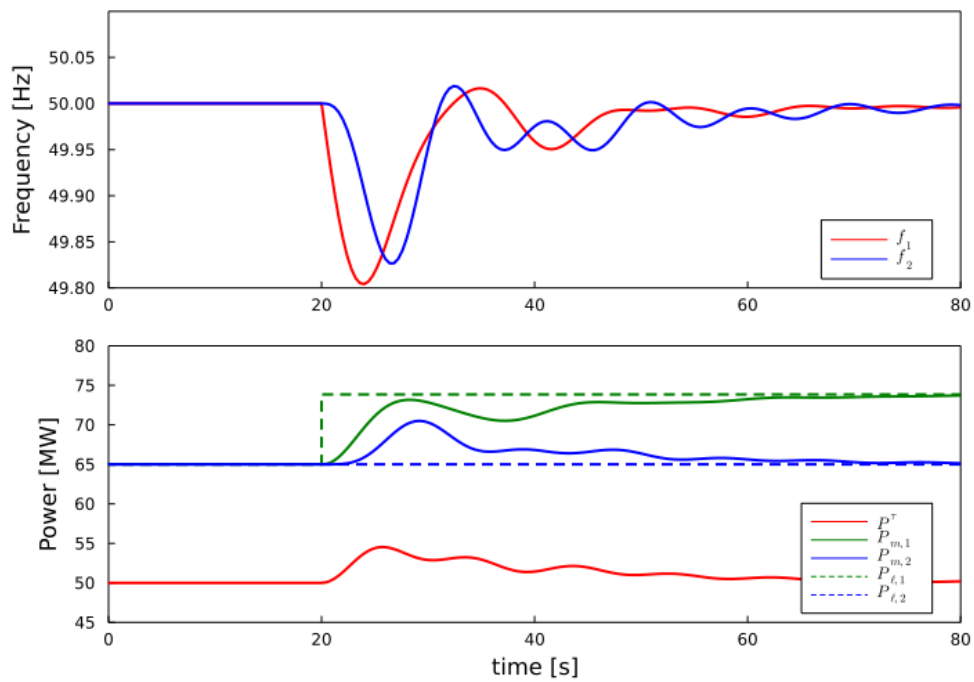


Figure 3.19: Frequencies, load, and generations plot for two synchronous areas after a load disturbance of 10MW in Area-1. In the figure, load disturbance of 10MW is created at  $t = 20$ s and the frequencies of the grids, generations from the hydropower units, and tie line flow from Area-1 to Area-2 are observed for next 60s.

### 3.3 Active Power Frequency Control in OpenHPL

Table 3.5: Operating conditions for linearization of Trollheim HPP.

Quantities	Symbol	Value
Governor reference power	$P_{\text{ref},o}$	65 MW
Frequency	$f_o$	50 Hz
Load	$P_{\ell,o}$	65 MW
Turbine flow rate	$\dot{V}_{\text{tr}}(t=0)$	14.81 m/s
Water level in surge tank	$h_{\text{st}}(t=0)$	70.34 m

#### 3.3.4 MPC for AGC

##### 3.3.4.1 System

We consider Trollheim HPP shown in Figure 3.16 b) as a system/plant for studying active power frequency control using MPC. The model developed in OpenHPL is linearized as in [31]. The power plant is linearized around the operating point shown in Table 3.5 where subscript "o" in  $f_o$  represents the operating point, and so on. We have used OMJulia<sup>1</sup>, the OpenModelica Julia API, for linearization of the Trollheim HPP model. In AGC, the change in load disturbance should be balanced by acting on mechanical power output of the turbine by changing the governor's power set point. Thus, for linearization of Trollheim HPP we consider two inputs, viz., deviation in the governor set point  $P_{\text{ref}}^\delta$  and the load disturbance  $P_\ell^\delta$ . Furthermore, we also consider three outputs: frequency of the grid  $f$ , turbine gate signal  $u_v$ , and mechanical power out of the turbine  $P_m$ .

The implementation of linearization of OpenHPL model using OMJulia in Julia is done as

```

1 using OMJulia
2 HPP = OMJulia.OMCSession()# object instantiation
3 HPP.ModelicaSystem("OpenHPL.mo", "LinearizationTrollheimHPP")
4 HPP.setLinearizationOptions(["stepSize = 0.1e-6", "stopTime = 1e-6"])
5 As, Bs, Cs, Ds = HPP.linearize()

```

After linearization of Trollheim HPP using OMJulia, we find the state space model of Trollheim HPP with system matrices given as

<sup>1</sup><https://openmodelica.org/doc/OpenModelicaUsersGuide/latest/omjulia.html>



### 3 Main Results

$$\begin{aligned}
 A_s &= \begin{bmatrix} -1.71 \cdot 10^{-7} & -7.37 & \dots & 0 \\ 0 & 0 & \ddots & 0 \\ \vdots & \vdots & \ddots & \vdots \\ 0 & -142.27 & \ddots & -8.1 \cdot 10^{-6} \\ 0 & 0 & \dots & 0 \end{bmatrix} \in \mathbb{R}^{7 \times 7} \\
 B_s &= \begin{bmatrix} 0 & -3.41 \cdot 10^{-8} \\ 0 & 0 \\ \vdots & \vdots \\ 0 & 0 \\ 0 & 0 \end{bmatrix} \in \mathbb{R}^{7 \times 2} \\
 C_s &= \begin{bmatrix} 0 & -2.1 \cdot 10^8 & \dots & 0 & 0 \\ 1 & 0 & \dots & 0 & 0 \\ 0 & 1 & \dots & 0 & 0 \end{bmatrix} \in \mathbb{R}^{2 \times 7} \\
 D_s &= \begin{bmatrix} 0 & 0 \\ 0 & 0 \\ 0 & 0 \end{bmatrix}.
 \end{aligned}$$

Some of the matrix elements above may contain non-zero values. Information about the state, input and output variables for Trollheim HPP, and their order for the linearized model can be found using following commands:

- 1 HPP.getLinearStates() #gives states
- 2 HPP.getLinearInputs()
- 3 HPP.getLinearOutputs()

The linearization algorithm from OMJulia for Trollheim HPP gives state  $x$ , input  $u$  and output  $y$  as in the following order

$$\begin{aligned}
 x &= (f, u_v, x_d, x_g, \dot{V}_p, \dot{V}_{st}, m_{st}) \\
 u &= (P_{ref}, P_\ell) \\
 y &= (P_m, f, u_v)
 \end{aligned}$$

where  $u_v$  is the turbine gate signal,  $x_d$  is the internal state for transient droop of the governor,  $x_g$  is the internal state for the pilot servo of the governor,  $\dot{V}_p$  is the volumetric flow rate through the penstock,  $\dot{V}_{st}$  is the volumetric flow rate through the penstock, and  $m_{st}$  is the water mass in the surge tank. Actually, the linearization algorithm has also considered two more states: the mass of the reservoir and the mass of the tailrace. However, due to the assumption of the constant water level in the reservoir and the tailrace, their rows in the  $A$  matrix are zero vectors and can be neglected for further analysis.

### System in deviation variable form

The model of Trollheim HPP can now be represented in deviation variable form in state  $x^\delta$ , input  $u^\delta$ , and output  $y^\delta$  around the operating conditions given in Table 3.5 using system matrices  $A_s, B_s, C_s$  and  $D_s$  as

$$\frac{dx^\delta}{dt} = A_s x^\delta + B_s u^\delta \quad (3.3)$$

$$y^\delta = C_s x^\delta + D_s u^\delta \quad (3.4)$$

where  $x^\delta \triangleq x - x_0$  is the deviation of variable  $x$  from the operating point  $x_0$ , and so on;  $u^\delta \triangleq u - u_0$  and  $y^\delta \triangleq y - y_0$ . Since all the elements of  $D_s$  matrix is zero we can write  $y^\delta = C_s x^\delta$  neglecting matrix  $D_s$ .

The input deviation around the operating point is  $u^\delta = (P_{\text{ref}}^\delta, P_\ell^\delta)$ . We can split the input  $u^\delta$  into deviation form of governor power set point  $P_{\text{ref}}^\delta$  and deviation form of load disturbance  $P_\ell^\delta$ , i.e,  $u^\delta \rightarrow (u^\delta, w^\delta)$  where, now, the notation  $u^\delta$  represents the deviation in governor power set point, i.e,  $u^\delta = P_{\text{ref}}^\delta$  and  $w^\delta$  represents the load disturbance, i.e.,  $w^\delta = P_\ell^\delta$ . Furthermore, we also need to split the input matrix  $B_s$  column-wise, i.e,  $B_s \rightarrow [B_s \ G_s]$  where, now,  $B_s$  is the input matrix and  $G_s$  is the disturbance matrix.

Equations 3.3 and 3.4 can then be written in the form of control input  $u^\delta$  and disturbance  $w^\delta$  as

$$\frac{dx^\delta}{dt} = A_s x^\delta + B_s u^\delta + G_s w^\delta \quad (3.5)$$

$$y^\delta = C_s x^\delta \quad (3.6)$$

where

$$x^\delta = (f^\delta, u_v^\delta, x_d^\delta, x_g^\delta, \dot{V}_p^\delta, \dot{V}_{st}^\delta, m_{st}^\delta)$$

$$u^\delta = P_{\text{ref}}^\delta$$

$$w^\delta = P_\ell^\delta$$

$$y^\delta = (P_m^\delta, f^\delta, u_v^\delta).$$

### System in discrete time domain

We will be using discrete time domain equations for both models inside MPC and the system using sampling time  $\Delta t$ . For this Eqs. 3.5 and 3.6 can be written in the discrete

### 3 Main Results

time domain as

$$x_{k+1}^{\delta} = A_{sd}x_k^{\delta} + B_{sd}u_k^{\delta} + G_{sd}w_k^{\delta} \quad (3.7)$$

$$y_k^{\delta} = C_{sd}x_k \quad (3.8)$$

where the discrete time domain can be obtain using *exact discretization*<sup>2</sup>.

#### 3.3.4.2 Objective function

Our objective is to minimize the generation input while returning the frequency of the grid to reference value, i.e, at 50Hz after the load disturbance.

The prediction model for MPC can be formulated in several ways. For instance,

1. a discrete time *per unit* AGC prediction model for MPC from Section 2.3.3.2 where the model parameters from Table 3.2 for Trollheim HPP can be used. However, the discrete time system in Section 3.3.4.1 to be controlled should be converted from SI unit to per unit using an expression from Eq. 2.16. Here, the MPC prediction model has the lower order than the system model
2. a discrete time linearized model of the Trollheim HPP from Section 3.3.4.1, i.e., the MPC prediction model is same as the linearized system model.

Consider a discrete time per unit AGC prediction model for MPC taken from Section 2.3.3.2 with the model parameters taken from Table 3.2. The objective function is constructed as in Eq. 2.19 with AGC as a SISO system as

$$\min_{\bar{P}_{ref}^{\delta}} J = \sum_{k=0}^{N_p-1} \left[ q \cdot \left( \bar{f}_k^{\delta} - \bar{f}_{ref,k}^{\delta} \right)^2 + p \cdot \left( \bar{P}_{ref,k}^{\delta} - \bar{P}_{ref,k-1}^{\delta} \right)^2 \right] + s \cdot \left( \bar{f}_{N_p}^{\delta} - \bar{f}_{ref,N_p}^{\delta} \right)^2 \quad (3.9)$$

s.t.

$$0.0017 \text{ p.u./s} \leq \dot{\bar{P}}_{m,k}^{\delta} \leq 0.0017 \text{ p.u./s} \quad (3.10)$$

$$-0.002 \text{ p.u.} \leq \bar{f}_k^{\delta} \leq 0.002 \text{ p.u.} \quad (3.11)$$

$$\bar{x}_{k+1}^{\delta} = \bar{A}_{md}\bar{x}_k^{\delta} + \bar{B}_{md}\bar{u}_k^{\delta} + \bar{G}_{md}\bar{w}_k^{\delta} \quad (3.12)$$

$$\bar{y}_k^{\delta} = \bar{C}_{md}\bar{x}_k^{\delta} \quad (3.13)$$

$$\bar{x}_0^{\delta} = \text{given} \quad (3.14)$$

where  $\bar{A}_{md}$ ,  $\bar{B}_{md}$ ,  $\bar{G}_{md}$  and  $\bar{C}_{md}$  are the discrete time system matrices for the AGC prediction model for MPC calculated as in Section 2.3.3.2 where  $\bar{x}^{\delta} = \left( \bar{f}_k^{\delta}, \bar{P}_m^{\delta}, \bar{P}_v^{\delta} \right)$ ,  $\bar{u}^{\delta} = \bar{P}_{ref}^{\delta}$ ,  $\bar{w}^{\delta} = \bar{P}_l^{\delta}$ ,

<sup>2</sup><https://en.wikipedia.org/wiki/Discretization>

and  $\bar{y}^\delta = \bar{f}^\delta$ .  $q$ ,  $p$  and  $s$  are the used as tuning factors for giving weights to the change in frequency over the horizon, change in governor reference horizon, and change in frequency at the end point of the horizon.

In Eq. 3.10, the hydropower generation rate constraint (GRC) is considered 10% of the total generation per minute<sup>3</sup>, i.e.,  $|\dot{\bar{P}}_{m,k}^\delta| \leq 0.0017 \text{ p.u./s}$  [57], and the generation rate constraint at time step  $k$  is expressed in terms of sampling time  $\Delta t$  as

$$\dot{\bar{P}}_{m,k}^\delta = \frac{\bar{P}_{m,k}^\delta - \bar{P}_{m,k-1}^\delta}{\Delta t}.$$

where  $q$ ,  $p$  and  $s$  are the used as tuning factors for giving weights to the change in frequency over the horizon, change in governor reference horizon, and change in frequency at the end point of the horizon. In Eq. 3.10, the hydropower generation rate constraint is considered 10% of the total generation per minute, i.e.,  $|\dot{\bar{P}}_{m,k}^\delta| \leq 0.0017 \text{ p.u./s}$  [57], and the generation rate constraint at time step  $k$  is expressed in terms of sampling time  $\Delta t$  as

$$\dot{\bar{P}}_{m,k}^\delta = \frac{\bar{P}_{m,k}^\delta - \bar{P}_{m,k-1}^\delta}{\Delta t}.$$

It is a requirement that the grid must satisfy the boundary  $50 \pm 0.1 \text{ Hz}$  which can be written in the form of frequency constraint in *per unit* as  $-0.002 \text{ p.u.} \leq \bar{f}_k^\delta \leq 0.002 \text{ p.u.}$  as represented in Eq. 3.11 [58].

#### 3.3.4.3 State estimation

At each time step  $k$ , MPC requires knowledge of all the states in the prediction model. A linear Kalman filter can be implemented as in Section 2.3.3.4 for estimating current state with the inclusion of measurement noise in the output. For simplicity reasons, it has been assumed that states of the MPC prediction model are known perfectly. The reported results in the sequel give an upper bound for the achievable performance; if a state estimator such as UKF, etc., see Section 2.4.4, had been included, the performance might deteriorate.

The system simulation model outputs represented by Eq. 3.8 should be converted from SI unit to per unit before using the outputs as estimated states for the prediction model. The outputs from Trollheim HPP, with base frequency 50Hz and base power 130MW, at each time step  $k$  is  $y_k^\delta = (P_{m,k}^\delta, f_k^\delta, u_{g,k}^\delta)$ . The estimated states for the prediction model at time step  $k$  is then given by  $\hat{x}_k^\delta = \left( \frac{f_k^\delta}{50}, \frac{P_{m,k}^\delta}{130 \cdot 10^6}, u_{g,k}^\delta \right)$ .

<sup>3</sup>Note that 10% p.u./min GRC =  $\frac{0.1}{60} \text{ p.u./s}$ .

### 3 Main Results

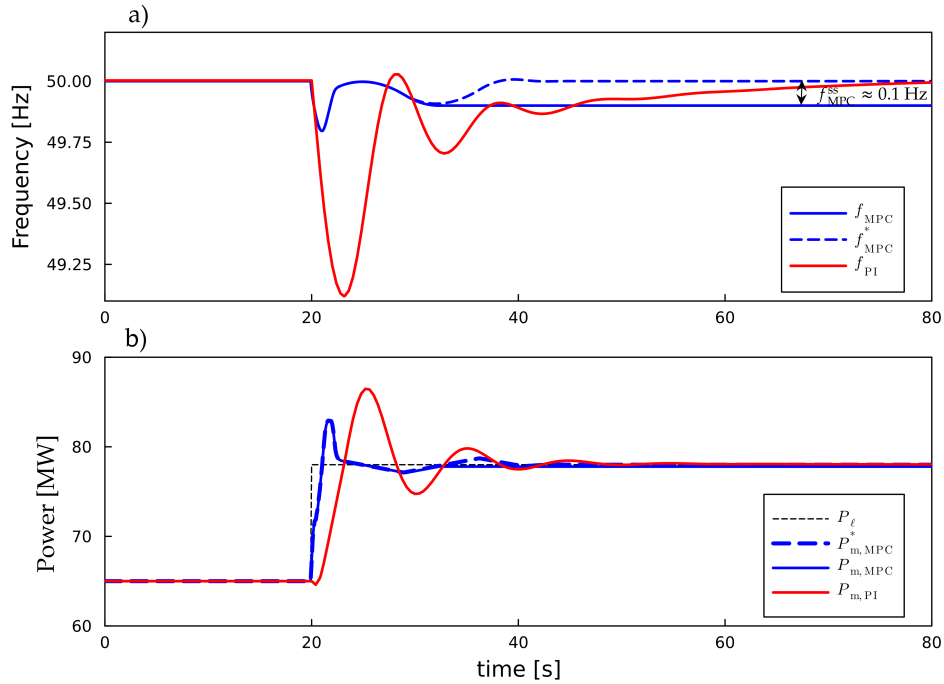


Figure 3.20: Frequency, load and generation responses using PI and MPC for AGC of Trollheim HPP. In the blue dashed lines, integral action has been added to MPC.

#### 3.3.4.4 Solving MPC formulation

The objective function represented by Eq. 3.9 has a quadratic cost and linear constraints. The objective function can be formulated as a quadratic programming (QP) problem to be solved at each time step  $k$ . Several solvers are available for solving QP problems using many scripting languages<sup>4</sup>. Here, JuMP.jl [59], a Julia package for modeling, optimization and solving problems, has been used. We have compared results from the solvers: a) Ipopt<sup>5</sup>, and b) COSMO<sup>6</sup>[60].

#### 3.3.5 Comparing frequency step response from MPC and PI controller

In Figure 3.20 a),  $f_{\text{MPC}}$  (solid blue line) is the frequency of the grid when “MPC model = AGC prediction model for MPC”, and “system = model from OpenHPL of the Trollheim HPP”. Similarly, in Figure 3.20 b),  $P_{m,\text{MPC}}$  (solid blue line) is the mechanical power output. Due to the differences in the model structures, there will be an off-set in the steady state as shown in the Figure 3.20 a). The frequency is offset by  $\approx 0.1\text{ Hz}$ . At  $t = 20\text{ s}$ , a load

<sup>4</sup>[https://en.wikipedia.org/wiki/Quadratic\\_programming](https://en.wikipedia.org/wiki/Quadratic_programming)

<sup>5</sup><https://github.com/jump-dev/Ipopt.jl>

<sup>6</sup><https://oxfordcontrol.github.io/COSMO.jl/stable/>

### 3.3 Active Power Frequency Control in OpenHPL

disturbance of 10% of the rated power, i.e.,  $P_\ell = 13\text{MW}$  is created, and the frequencies of the grid are observed. For MPC, the parameters  $q$  and  $s$  are both set to unity, and the tuning parameter  $p$  is set to be 0.1 after some trial and error. The prediction horizon is  $N_p = 200$  which equals to 20s for  $\Delta t = 0.1\text{s}$ . The total time of the prediction horizon is chosen to be more than the difference in the time between the load disturbance event and the time it takes for the droop governor control to achieve the steady state frequency deviation, i.e, as in Figure 3.17,  $N_p > \frac{20}{\Delta t}$ .  $f_{\text{PI}}$  is the frequency step response from the PI controller.

The steady state deviation error  $f_{\text{MPC}}^{\text{ss}} = 0.1\text{Hz}$  can be removed using integral actions. One of the ways to achieve integral action is by augmenting the prediction model with an integrating/slowly varying mean disturbance model which also influences the output, see the following subsection.

#### 3.3.5.1 Integral action

Consider a case when there is no load disturbance in the grid. As mentioned, we assume that the disturbance is a slowly changing ‘‘constant’’,

$$\bar{w}_{k+1}^\delta = \bar{w}_k^\delta. \quad (3.15)$$

Furthermore, we assume that this disturbance directly influences the output via a matrix (disturbance-to-output)  $\bar{C}_w$ ,

$$\bar{y}_k^\delta = \bar{C}_{\text{md}}\bar{x}_k^\delta + \bar{C}_w\bar{w}_k^\delta. \quad (3.16)$$

The model now consists of Eqs. 3.12, 3.15, and 3.16. By augmenting the state vector, we can write the model as

$$\tilde{x}_{k+1}^\delta = \tilde{A}_{\text{md}}\tilde{x}_k^\delta + \tilde{B}_{\text{md}}\tilde{u}_k^\delta \quad (3.17)$$

$$\tilde{y}_k^\delta = \tilde{C}_{\text{md}}\tilde{x}_k^\delta \quad (3.18)$$

with

$$\begin{aligned} \tilde{x}_k^\delta &= \begin{bmatrix} \bar{x}_k^\delta \\ \bar{w}_k^\delta \end{bmatrix} \\ \tilde{A}_{\text{md}} &= \begin{bmatrix} \bar{A}_{\text{md}} & \bar{G}_{\text{md}} \\ 0 & I \end{bmatrix} \\ \tilde{B}_{\text{md}} &= \begin{bmatrix} \bar{B}_{\text{md}} \\ 0 \end{bmatrix} \\ \tilde{C}_{\text{md}} &= \begin{bmatrix} \bar{C}_{\text{md}} & \bar{C}_w \end{bmatrix}. \end{aligned}$$

### 3 Main Results

The disturbance-to-output matrix  $\bar{C}_w$  should be chosen in such a way that

$$\text{rank} \begin{bmatrix} \bar{A}_{\text{md}} - I & \bar{G}_{\text{md}} \\ \bar{C}_{\text{md}} & \bar{C}_w \end{bmatrix} = n_x + n_y$$

holds true for *observability* [61].

In Figure 3.20 a),  $f_{\text{MPC}}^*$  (dash blue line) is the frequency of the grid after the AGC prediction model is augmented using disturbance-to-output matrix  $\bar{C}_w \approx [-0.024]^7$ . It can be seen from Figure 3.20 that both PI controller and MPC with integral action restore the grid frequency to 50Hz. The frequency step response from MPC is much smoother than the frequency step response from the PI controller. This is because of the fact that MPC uses more model information than the PI controller. In the PI controller only measurement of the frequency deviation  $\bar{f}^\delta$  is used to generate the governor set-point. However, in MPC, the AGC prediction model requires estimated values of  $\bar{P}_m^\delta$  and  $\bar{P}_v^\delta$  using measurement of the frequency deviation  $\bar{f}^\delta$ . The controller is able to achieve better control action when it knows the knowledge of the entire states. The estimated states provides more model information to the controller while solving optimal control problem.

#### 3.3.6 Using linearized OpenHPL Trollheim HPP model as MPC prediction model

Using constraints as in Eqs. 3.10,3.11, Fig. 3.21 shows frequency step responses, load, and generations in two cases. They are:

1. Case-1: the MPC prediction model = the AGC prediction model, and plant = the linearized OpenHPL Trollheim HPP model. Since, the prediction model and the plant model are different, we need integral action for this case. The disturbance-to-output matrix is set to  $\bar{C}_w = [-0.024]$ .
2. Case-2: the MPC prediction model is identical to the plant model; the plant = the linearized OpenHPL Trollheim HPP model. Because of equality, no integral action is required in this case. In reality, integral action is always required as there is always a mismatch between the model and the plant in real life situations.

The frequency step response for Case-2 is somewhat better than for Case-1. This is natural, since Case-2 uses perfect model knowledge.

---

<sup>7</sup>This “matrix” value ensures that the observability condition is satisfied, and that integral action is achieved.

### 3.3 Active Power Frequency Control in OpenHPL

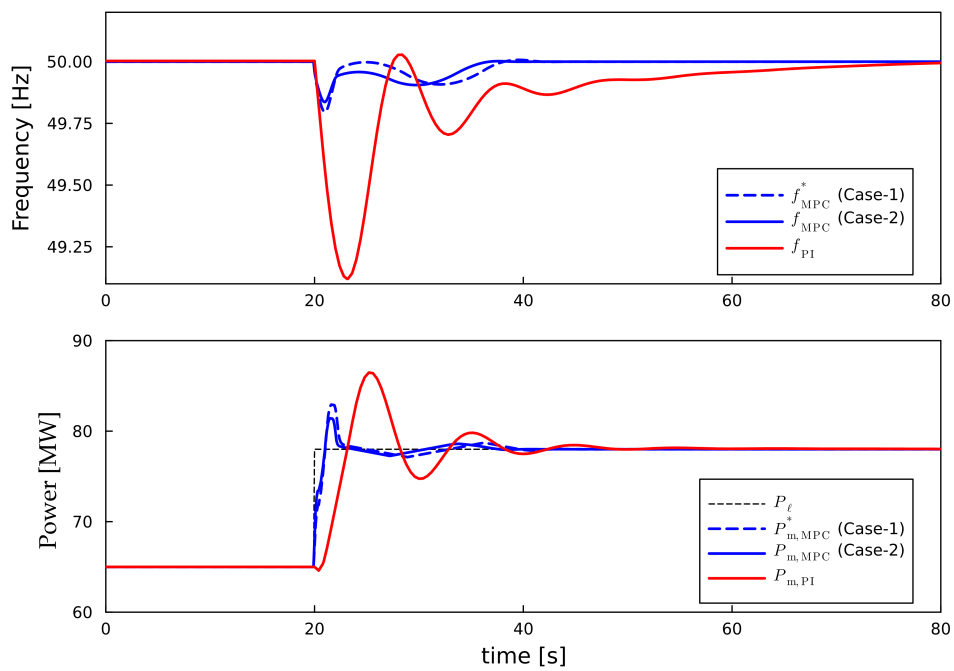


Figure 3.21: Responses for frequency, load and generation. Case-1: when “MPC model = the AGC prediction model”, “plant = linearized OpenHPL model”. Case-2: when “MPC model + plant = linearized OpenHPL model”.



### 3.3.7 Output frequency constraint violation

It is a requirement that the output frequency must be constrained. Ideally, we want  $-0.01\text{ Hz} \leq \bar{f}_k^\delta \leq 0.01\text{ Hz}$ , i.e., the grid frequency should lie between 49.90 Hz and 50.01 Hz.

The results in Figure 3.21 are based on hard constraints on frequency ( $-0.01\text{ Hz} \leq \bar{f}_k^\delta \leq 0.01\text{ Hz}$ ) and rate of change of power ( $0.0017\text{ p.u./s} \leq \dot{\bar{P}}_{m,k}^\delta \leq 0.0017\text{ p.u./s}$ ; the generation rate constraint, GRC) In Sub-figure a) (also shown in Figure 3.22 a), 10% GRC), we see that the frequency constraint is violated in the interval  $t = 21\text{ s}$  to  $t = 22.5\text{ s}$ : the frequency reaches a minimum of 48.84 Hz which breaks the constraint by 0.06 Hz. All responses shown in Figures 3.20 and 3.21 are obtained using the Ipopt solver.

It is of interest to check why the hard constraints are violated. The reason could be a) it is not possible to simultaneously satisfy both hard constraint, and the solvers have a fall-back algorithm to handle constraint violation, or b) inaccuracies in the solvers. To check this, the hard constraint on the rate of change of power (GRC) is removed leaving a hard constraint only on the frequency. In Figures 3.22 a) and b), results are found using the Ipopt solver, while Figures 3.22 c) and d) are found using the COSMO solver.

Figure 3.22 demonstrates that both solvers satisfy the constraint on frequency when the GRC is removed. Ipopt is known to have a default algorithm for handling conflicting constraints, so the constraint violation in Figure 3.21 can be explained by Ipopt's fall-back algorithm. For COSMO, there is no such fall-back algorithm; the applied cone splitting algorithm is known to relax on accuracy to increase speed [60]. The accuracy can, however, be tuned.

For AGC, removing the constraint on the power generation rate (GRC) is problematic because breaking this constraint leads to excessive water hammer effect. We are thus left with balancing two evils: increased water hammer effect and/or increased frequency deviation. In practice, this should be addressed more systematically than leaving it to a fall-back algorithm such as in Ipopt. The problem is not pursued further here.

### 3.3.8 Computation time

It is of interest to see the computation time for Case-1 and Case-2. The computational time was calculated using *Processor: Intel(R) Core(TM) i7-9750H CPU @ 2.60GHz with Installed RAM: 32 GB*. The average computational time for solving the optimal control problem for a time step  $k$  for Case-1 is 5 ms (using only Ipopt solver). The average computational time for solving optimal control problem for a time step  $k$  for Case-2 is 70 ms. The linearized model of OpenHPL can be used for real time MPC application with discretization time  $\Delta t = 0.1\text{ s}$ . These computational times provided here are only for the case of Trollheim HPP, however, for a hydropower system with more number of hydropower

### 3.3 Active Power Frequency Control in OpenHPL

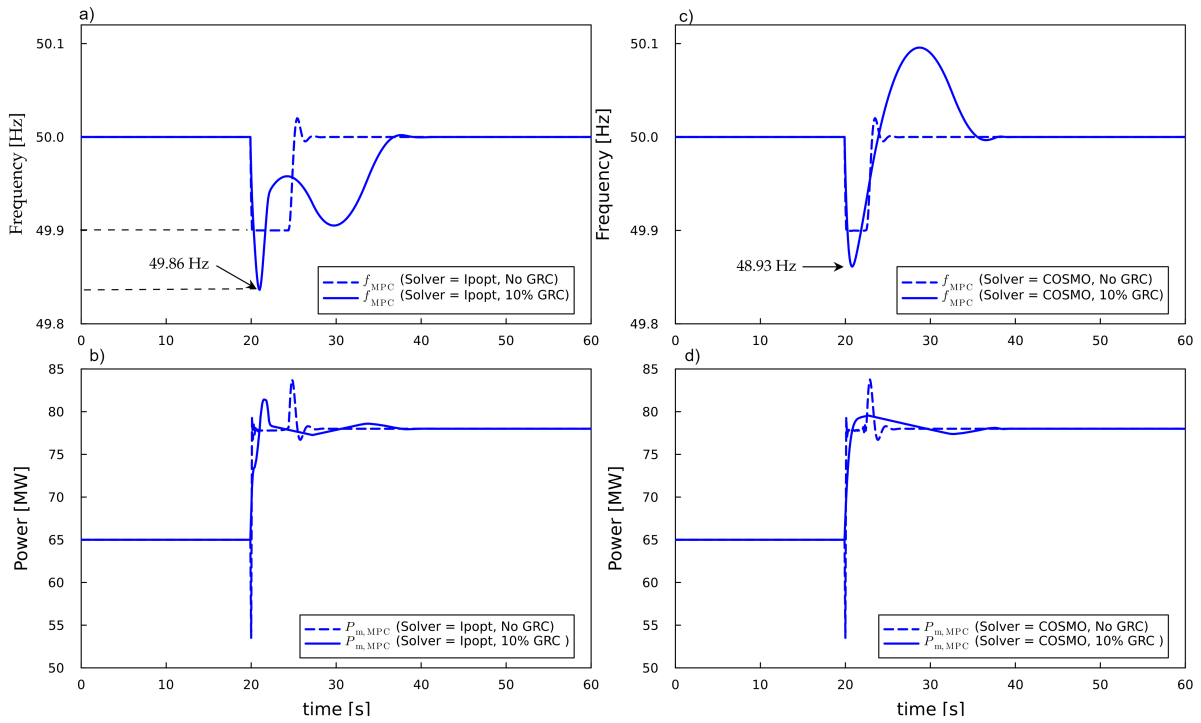


Figure 3.22: Responses for frequency and generation using Ipopt and COSMO solvers.

units and synchronous generating units there will be increment in the computational time.

#### 3.3.9 Summary

In this section, an application of the OpenHPL library is given, in the form of active power frequency control. Three types of power grid control are studied, viz., isochronous governor control, droop governor control, and automatic generation control (AGC) for an isolated power system. The use of AGC in a multi-generation system is also studied. Furthermore, the use of AGC with PI controller and MPC has been compared. Operation of the MPC is better than the PI controller. The control performance of the MPC improves when improved prediction models are used compared to the standard AGC prediction model used in the literature. The average computational time for solving the optimal control problem using a linearized model of the OpenHPL Trollheim HPP as the prediction model inside MPC is 70% of the sample time on a specific laptop. To further consider the use of MPC, it is further necessary to analyze the delay and possibly reduce it.

### 3.4 State Estimation of Thermal Model using Bayesian Inference

Two papers were published in relation to state and parameter estimation of the thermal model using Bayesian inference. These papers are:

- Paper 1: M. Pandey and B. Lie, “Bayesian Inference for Thermal Model of Synchronous Generator Part I : Parameter Estimation,” *IEEE Access*. 2022, 10: 103529-103537.
- Paper 2: M. Pandey and B. Lie, “Bayesian Inference for Thermal Model of Synchronous Generator Part II : State Estimation,” *IEEE Access*, 2022, 10: 105612-105620.

The posterior parameter distributions presented in Paper 1 are unrealistically narrow. The distributions have been corrected in the following paper:

- A. Jayamanne, Z. Ban, M. Pandey, A. Ghaderi and B. Lie, Markov Chain Monte Carlo Methods Applied to a Synchronous Generator Model, Under review, *IEEE Access*. 2023.

The modifications were essentially a) use of a much longer burn-in period in the MCMC algorithm, b) subsampling the data to make the parameters more data sensitive. Although Paper 1 contains some incorrect results, it demonstrates interesting methods, and is therefore included in the thesis, Appendix D. The improved paper has another main author, and is not included.

In this section, the main results from Paper 2 are presented. Paper 2 is also attached in Appendix E.

#### 3.4.1 Metal and air temperature estimation

Figure 3.23 shows air and metal temperature estimation using particle filter with number of particles  $N_p = 200$  using Ris04 resampling. From the figure,  $\hat{T}_{r,k|k}$  is the estimated rotor copper temperature where the mean (red), standard deviation (dark gray), and the ensemble of the mean (light gray) are plotted together. Figure 3.23 also shows the *a posteriori* estimates of the mean and the standard deviation, and the evolution of each particle (the ensemble) plotted together for  $T_s$ ,  $T_{Fe}$ ,  $T_a^c$ ,  $T_a^\delta$  and  $T_a^h$ . In the figure,  $T_s^m$ ,  $T_{Fe}^m$ ,  $T_a^{c,m}$  and  $T_a^{h,m}$  are the measurements available for the stator copper temperature, the stator iron temperature, the cooled air temperature and the hot air temperature, respectively. These measurements are used for estimating unmeasured  $T_r$  and  $T_a^\delta$ .

### 3.4 State Estimation of Thermal Model using Bayesian Inference

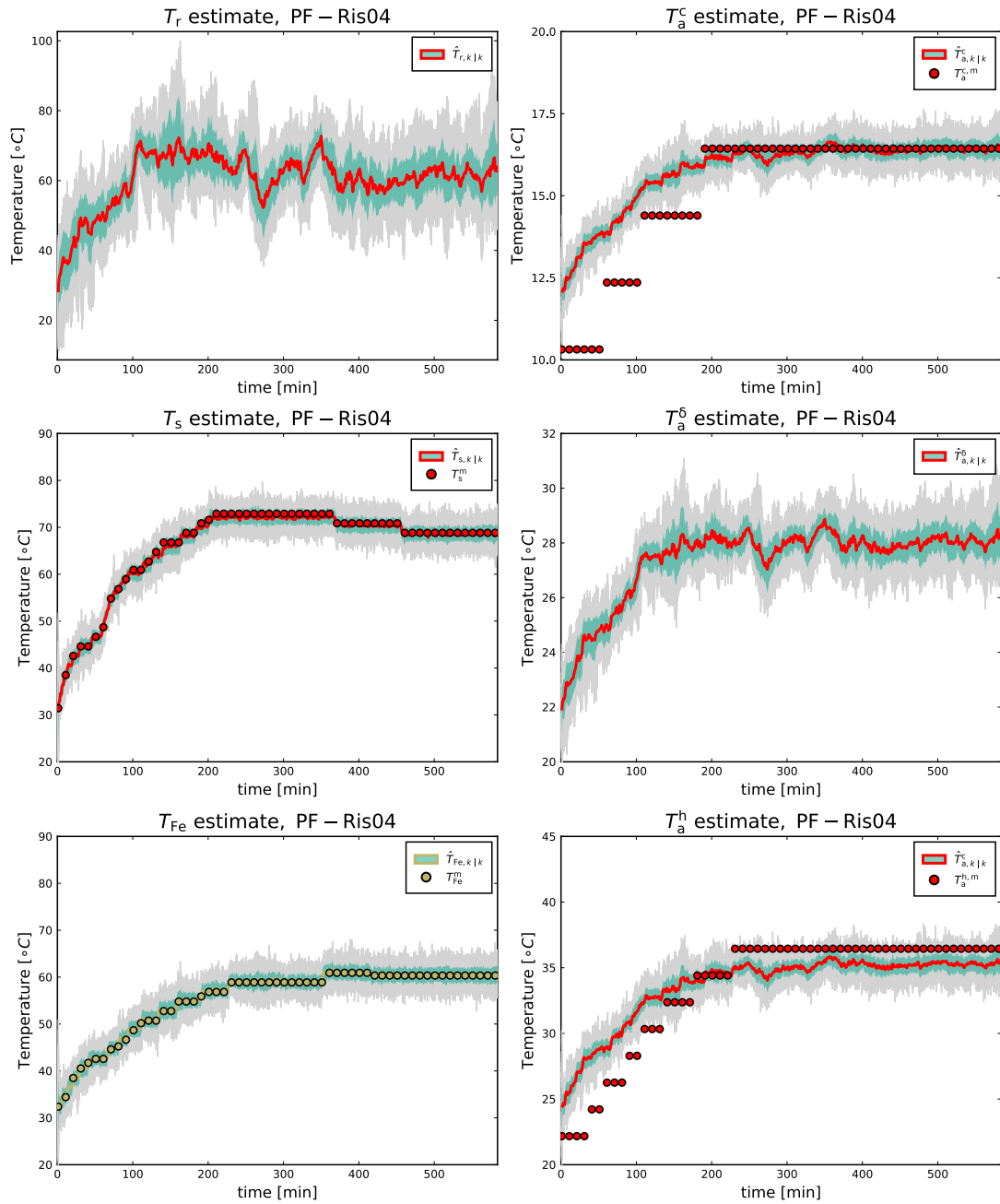


Figure 3.23: Metal and air temperatures estimation using particle filter with  $N_p = 200$  and Ris04 resampling.

### 3 Main Results

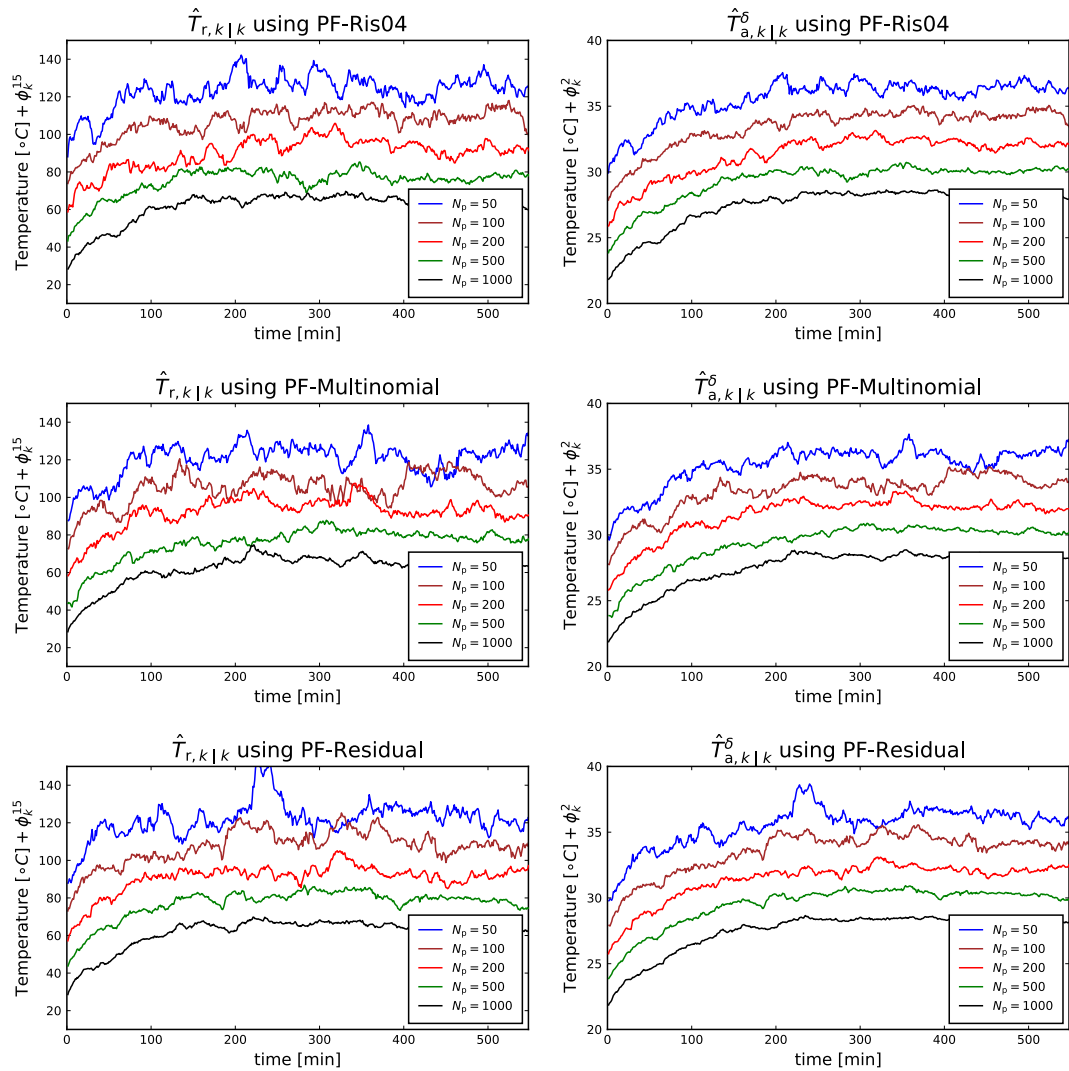


Figure 3.24: Metal and air temperatures estimation using particle filter with different number of particles for RisO4, multinomial, and residual resampling. In the figure, the temperature curves have been vertically shifted (represented by  $\phi_k^{15}$  and  $\phi_k^2$ ) for clarity of presentation. In reality they start at same temperature.

### 3.4 State Estimation of Thermal Model using Bayesian Inference

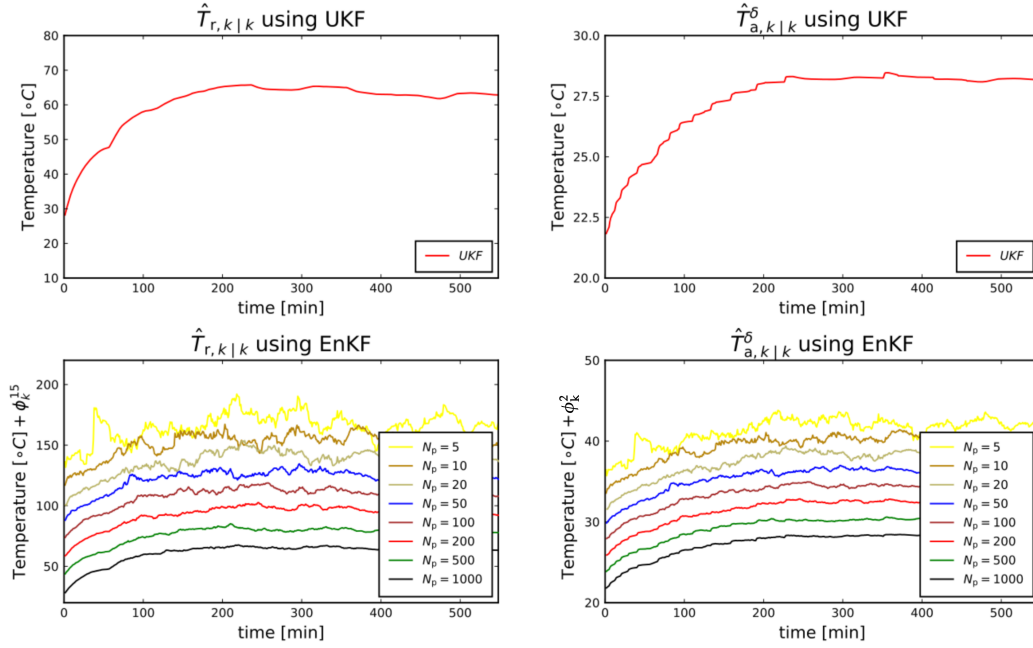


Figure 3.25: Metal and air temperatures estimation using UKF and EnKF with different number of particles. In the figure, the some of the temperature curves have been vertically shifted (represented by  $\phi_k^{15}$  and  $\phi_k^2$ ) for clarity of presentation. In reality they start at same temperature.

#### 3.4.2 Estimation with different resampling algorithms

It is of interest to compare the estimation of unmeasured temperatures  $T_r$  and  $T_a^\delta$  using a different number of particles and different kinds of sampling algorithms. Figure 3.24 shows the *a posteriori* estimate for  $T_r$  and  $T_a^\delta$  with different number of particles using the Ris04, multinomial, and residual resampling. For  $\hat{T}_{r,k|k}$  using Ris04 we see that as the number of particles increases from  $N_p = 50$  toward  $N_p = 1000$ , the estimation gets improved. Similar results can be seen from Figure 3.24 for both  $\hat{T}_{r,k|k}$  and  $\hat{T}_{a,k|k}^\delta$  using multinomial and residual resamplings. The estimate  $\hat{T}_{a,k|k}^\delta$  is much better than the estimate  $\hat{T}_{r,k|k}$ . This means that for the same estimation accuracy, a higher number particles  $N_p$  is needed for the rotor metal temperature than for air temperatures. Similar, results were obtained in the case of *a posteriori* estimates of  $T_r$  and  $T_a^\delta$  using stratified and systematic resamplings. However, the *a posteriori* estimates are much better with Regularized Particle Filter (RPF) and Auxiliary Particle Filter (APF).

### 3.4.3 Estimation using UKF and EnKF

The estimated  $T_r$  and  $T_a^\delta$  using both UKF and EnKF with different number of particles are shown in Figure 3.25. In the figure, the estimation of  $T_r$  and  $T_a^\delta$  using EnKF shows that as the number of particles in the ensemble increases the estimation improves. The estimation using UKF and EnKF with  $N_p$  above 200 gives comparable results. Comparing EnKF from Figure 3.25 with PFs with different resamplings from Figure 3.24, we see that particle filters with  $N_p = 50$  gives similar results as EnKF with  $N_p = 5$ .

### 3.4.4 Estimation innovation and computation time

It is of interest to see the estimation innovation  $\varepsilon$  versus the number of particles  $N_p$  for different estimation algorithms. It is also of interest to see the computational time  $\tau$  for each of the estimation algorithms. The estimators were implemented in the Julia language and the computational time was calculated using *Processor: Intel(R) Core(TM) i7-9750H CPU @ 2.60GHz* with *Installed RAM: 32 GB*. All the state estimators' computational times are presented relative to the time of UKF. The absolute mean time for UKF is 0.26ms. Since, the sampling time of the measurement data is 1 min, UKF can be used for real-time state estimation for the thermal model of the synchronous generator.

Table 3.6 shows  $\varepsilon$  and  $\tau$  for EnKF and particle filters compared relative to UKF for different number of particles. This shows that as the number of particles increases, the RMSE of innovation residuals  $\varepsilon$  decreases. However, the computational time  $\tau$  increases. From Table 3.6 for EnKF we see that as  $N_p$  increases, the RMSE of  $\varepsilon$  converges to 0.9°C. Similar, results can be seen for PF-Ris04, PF-Multinomial, PF-Residual, PF-stratified, and PF-systematic with different  $N_p$ . Furthermore, from Table 3.6 for EnKF the computational time  $\tau$  for  $N_p = 1000$  is 290 times the computational time for UKF whereas to obtain the similar estimation error with  $N_p = 1000$  for PF-Ris04, PF-Multinomial, PF-Residual, PF-stratified, and PF-systematic the computational time for these filters are 400 times that of computational time for UKF. However, from Table 3.6, we see that both PF-RPF and PF-APF suffers from estimation accuracy and computational time.

### 3.4.5 Summary

In this section, an application use of the particle filter, the state estimation in the case of the thermal model of synchronous generator is studied. The paper presented in Appendix E is Part II of two papers on parameter and state estimation using Bayesian inference for a thermal model of a synchronous generator. The paper presents state estimation of the thermal model of a synchronous generator. State estimation of rotor copper and air-gap temperatures are performed using Bayesian inference. Estimators such as Unscented Kalman Filter (UKF), Ensemble Kalman Filter (EnKF), and Particle Filters (PFs) with

### 3.4 State Estimation of Thermal Model using Bayesian Inference

Table 3.6: Estimation algorithms, estimation innovation  $\varepsilon$ , and computational time  $\tau$ . PF-Stratified, PF-Systematic, PF-RPF and PF-APF are compared relative to UKF.

Filters	RMSE of $\varepsilon$	$\tau$ for $\Delta t = 1$ min
UKF	1	1(0.26ms)
EnKF ( $N_p = 5$ )	1.23	1.95
EnKF ( $N_p = 20$ )	0.98	5.91
EnKF ( $N_p = 50$ )	0.93	13.68
EnKF ( $N_p = 200$ )	0.91	55.68
EnKF ( $N_p = 500$ )	0.90	141.37
PF-Ris04 ( $N_p = 5$ )	1.72	2.47
PF-Ris04 ( $N_p = 20$ )	1.08	7.85
PF-Ris04 ( $N_p = 50$ )	0.99	19.86
PF-Ris04 ( $N_p = 200$ )	0.96	82.34
PF-Ris04 ( $N_p = 500$ )	0.95	199.71
PF-Multinomial ( $N_p = 5$ )	1.71	2.50
PF-Multinomial ( $N_p = 20$ )	1.12	7.86
PF-Multinomial ( $N_p = 50$ )	1.00	19.21
PF-Multinomial ( $N_p = 200$ )	0.96	82.00
PF-Multinomial ( $N_p = 500$ )	0.96	197.48
PF-Residual ( $N_p = 5$ )	1.68	2.50
PF-Residual ( $N_p = 20$ )	2.066	7.88
PF-Residual ( $N_p = 50$ )	1.07	19.04
PF-Residual ( $N_p = 200$ )	1.04	82.09
PF-Residual ( $N_p = 500$ )	1.02	197.23
PF-Stratified ( $N_p = 5$ )	1.71	2.49
PF-Stratified ( $N_p = 20$ )	1.11	7.85
PF-Stratified ( $N_p = 50$ )	0.99	18.85
PF-Stratified ( $N_p = 200$ )	0.960	78.86
PF-Stratified ( $N_p = 500$ )	0.952	199.07
PF-Systematic ( $N_p = 5$ )	1.67	2.49
PF-Systematic ( $N_p = 20$ )	1.08	7.85
PF-Systematic ( $N_p = 50$ )	0.99	18.85
PF-Systematic ( $N_p = 200$ )	0.963	78.86
PF-Systematic ( $N_p = 500$ )	0.960	199.07
PF-RPF ( $N_p = 5$ )	38.09	3.19
PF-RPF ( $N_p = 20$ )	1.76	20.20
PF-RPF ( $N_p = 50$ )	1.55	80.44
PF-RPF ( $N_p = 200$ )	1.45	1022.6
PF-RPF ( $N_p = 500$ )	1.42	6599.65
PF-APF ( $N_p = 5$ )	11.36	2.50
PF-APF ( $N_p = 20$ )	4.14	7.87
PF-APF ( $N_p = 50$ )	1.96	20.32
PF-APF ( $N_p = 200$ )	1.56	82.06



### 3 Main Results

different sampling algorithms, are compared based on the estimation accuracy and computational time. Inferences are drawn for the posterior distributions of the state, error convergence and particle realizations of the state estimator, choice, and computational effort of the estimators. Results show that the UKF has fair estimation accuracy with the fastest computational time as compared to other estimators. PFs are formulated based on five different resampling algorithms: Ris04, multinomial, residual, stratified, and systematic resamplings. Results show that the problem of sample impoverishment in PFs can be ordered from worst to best as stratified, systematic, multinomial, Ris04, and residual resamplings, respectively. We also showed that regardless of the computational time, UKF estimation is comparable with EnKF with the number of particles  $N_p = 200$ . In the case of estimation accuracy, PFs with  $N_p = 50$  give comparable estimation accuracy with EnKF with  $N_p = 5$ . For the air-cooled synchronous generator, UKF and EnKF are better estimators than PFs. As a final concluding remark, we choose UKF based on the fair estimation accuracy and the fastest computational time with temperature estimation under standard deviation of  $\sigma \approx 0.2^\circ\text{C}$ .

## 4 Conclusion and Future Perspectives

This chapter presents conclusions in terms of work carried out for the feature extension of OpenHPL and the thermal model of synchronous generator. The chapter ends by providing future perspectives of the work.

### 4.1 Feature Extension of OpenHPL

Models of different types of surge tanks and draft tubes are developed as features extensions to the existing open-source hydropower library — OpenHPL. In additions, a standard active power frequency control is implemented in OpenHPL.

- A simple surge tank model is compared with a sharp orifice type surge tank, a throttle valve surge tank, and an ACST in terms of water mass oscillation and water hammer. The model of ACST is validated with experimental data from the Torpa HPP. The influence of diameters of the sharp orifice and the throttle valve surge tank in terms of the maximum required height and suppression of water mass oscillations are studied for different percentage changes in load acceptance and rejection.
- Mechanistic model of a conical diffuser and Moody spreading pipes (or hydraucone) are developed as features extensions to OpenHPL.

### 4.2 Other Results

- A standard active power frequency control method is studied using PI controller and MPC. The performance of the MPC is better than the PI controller. The effect of hard constraints in MPC were looked into. The studied methods bring little new in themselves, but it is demonstrated how these methods can be used in combination with OpenHPL.
- Various state estimation algorithms are implemented for temperature monitoring of a thermal model of a hydro generator. Such monitoring is important to allow for more flexible operation of hydropower systems with intermittent power injected into

## 4 Conclusion and Future Perspectives

the grid. Comparing various state estimators (UKF, EnKF, and PFs), the overall conclusion was that UKF is the most suitable choice among the estimators for this particular problem. This work is independent of OpenHPL, but the estimators can be made to work in combination with OpenHPL.

### 4.3 Future Work

Based on the experience of the author regarding modeling, simulation, and control, the following future work is worth considering:

#### **Cavitation prediction**

An initial study by the author on cavitation prediction using OpenHPL showed two of the main problems regarding the modeling of a draft tube and a reaction turbine (Francis or Kaplan). First, modeling of the draft tube requires the inclusion of accurate dimensions (height differences and cross-sections) and the friction factor due to diffusion from a smaller inlet diameter to a larger outlet diameter of the draft tube. Second, it is difficult to model a reaction turbine with the inclusion of the friction coefficients for shock, whirl, and pipe friction while computing the overall efficiency of the turbine. Furthermore, for the accurate prediction of cavitation inception inside the turbine-draft tube system, it is important to consider both types of water velocities, viz., radial and tangential velocities.

The effect of the radial velocity of the flow inside most hydropower units (intake, surge tank, penstock, etc.), is negligible. We have only considered average tangential velocity for the models in OpenHPL. However, for an accurate model of the velocities inside the turbine-draft tube unit, the effect of swirl due to radial velocity should be taken into consideration. This directs us to a more accurate 2D modeling of the turbine-draft tube unit. Modern methods for developing surrogate models should be studied to simplify such 2D models.

#### **Draft tube**

A draft tube in a reaction turbine is a combination of three parts (a) a cone, (b) an elbow, and (c) a rectangular diffuser. The performance of the rectangular diffuser is similar to the cone and can be represented by the same model based on the hydraulic cross-sections. The modeling of the cone and the rectangular diffuser is straightforward as in Appendix A. However, the model is further refined if we discretize the length of the cone into several segments, and apply the friction factors due to diffusion for each segment. The modeling

of the elbow is challenging to accurately predict the flow rate through the elbow. The author believes that an improved result can be seen if the length and diameter of the elbow are discretized into several fine segments, but finer discretization will be a trade-off against the computational effort.

### **Turbine models**

OpenHPL already has a Francis turbine model. A Pelton turbine model has been implemented, but has not been validated. It is, however, lacking a Kaplan turbine model. Implementation and validation of Pelton and Kaplan models would be very useful. Kaplan turbines can be modeled with the inclusion of friction factors for shock, whirl, and pipe friction loss as in [62].

### **Run-Of-River models**

OpenHPL already has a draft open channel unit. This should be improved and validated to allow for run-of-river hydropower plants.

### **IEEE 30 bus test system**

Models of hydropower plants can be implemented with OpenHPL. Similarly, models of synchronous generators to end users can be modeled from OpenIPSL for example as in [63]. Furthermore, models of solar and wind power plants can be implemented from PhotoVoltaics and WindPowerPlants, respectively, as in [64]. A study on the integration of both intermittent and dispatchable sources can be implemented for an IEEE 30 bus test<sup>1</sup> system.

### **Control of generator temperature**

Inclusion of intermittent energy in the grid requires more flexible generator operation. State estimation of generator temperature is important, but it needs to be combined with advanced control algorithms such as MPC. This was discussed in [5]. Combination of such a possibility with OpenHPL allows for extensive advance testing.

---

<sup>1</sup><http://labs.ece.uw.edu/pstca/>

### **The two-language-problem**

Some advance control algorithms (MPC, etc. ) and state estimation algorithms (Moving Horizon Estimator, MHE) require model simulation for each time steps in the system simulator. For simplicity, if Euler integration is used, this implies a loop within a loop. The Modelica language does not currently support this. Implementation of MPC and MHE therefore currently requires combination of Modelica with a scripting language. It would be of interest to eliminate this two-language-problem and combine Modelica with other languages.

# Bibliography

- [1] B. Lie, *Project, FM1015 Modelling of Dynamic Systems*, University of South-Eastern Norway, Sep. 2018, Group Project Task.
- [2] G. Tiwari, J. Kumar, V. Prasad, and V. K. Patel, “Utility of cfd in the design and performance analysis of hydraulic turbines—a review,” *Energy Reports*, vol. 6, pp. 2410–2429, 2020.
- [3] A. L. Gerhart, J. I. Hochstein, and P. M. Gerhart, *Munson, Young and Okiishi’s Fundamentals of Fluid Mechanics*. John Wiley & Sons, 2020.
- [4] I. E. Idelchik, “Handbook of hydraulic resistance,” *Washington*, 1986.
- [5] T. Øyvang, “Enhanced power capability of generator units for increased operational security,” Ph.D. dissertation, University of South-Eastern Norway, 2018.
- [6] L. Vytvytskyi and B. Lie, “OpenHPL for Modelling the Trollheim Hydropower Plant,” *Energies*, vol. 12, no. 12, p. 2303, 2019.
- [7] K. V. Vereide, “Hydraulics and Thermodynamics of Closed Surge Tanks for Hydropower Plants,” Ph.D. dissertation, Norwegian University of Science and Technology, 2016.
- [8] “Sustainable development goals,” *Wikipedia*, Oct 2019. [Online]. Available: [https://en.wikipedia.org/wiki/Sustainable\\_Development\\_Goals#Goal\\_7:\\_Affordable\\_and\\_clean\\_energy](https://en.wikipedia.org/wiki/Sustainable_Development_Goals#Goal_7:_Affordable_and_clean_energy)
- [9] “Solar power in germany,” *Wikipedia*, Sep 2019. [Online]. Available: [https://en.wikipedia.org/wiki/Solar\\_power\\_in\\_Germany](https://en.wikipedia.org/wiki/Solar_power_in_Germany)
- [10] L. Vytvytskyi, “Dynamics and model analysis of hydropower systems,” Ph.D. dissertation, University of South-Eastern Norway, 2019.
- [11] Y. Ma, S. Gowda, R. Anantharaman, C. Laughman, V. Shah, and C. Rackauckas, “Modelingtoolkit: A composable graph transformation system for equation-based modeling,” *arXiv preprint arXiv:2103.05244*, 2021.
- [12] “Overview of modelica libraries,” *Overview of Modelica Libraries - Modelica Association*. [Online]. Available: <https://www.modelica.org/libraries/ModelicaLibrariesOverview>

## Bibliography

- [13] R. Fitzgerald and V. L. Van Blaricum, “Water hammer and mass oscillation (whamo) 3.0 user’s manual,” CONSTRUCTION ENGINEERING RESEARCH LAB (ARMY) CHAMPAIGN IL, Tech. Rep., 1998.
- [14] W. Yang, J. Yang, W. Guo, W. Zeng, C. Wang, L. Saarinen, and P. Norrlund, “A mathematical model and its application for hydro power units under different operating conditions,” *Energies*, vol. 8, no. 9, pp. 10 260–10 275, 2015.
- [15] C. Nicolet, “Hydroacoustic modelling and numerical simulation of unsteady operation of hydroelectric systems,” EPFL, Tech. Rep., 2007.
- [16] B. R. Sharefi, “Modeling for control of hydropower systems,” Master’s thesis, Telemark University College, Porsgrunn, Norway, 2011.
- [17] W. Zhou, “Modeling, Control and Optimization of a Hydropower Plant,” Ph.D. dissertation, University College of Southeast Norway, 2017.
- [18] V. Splavska, “Simulation and control of hydro power plants,” Master’s thesis, University College of South-Eastern Norway, 2017.
- [19] A. Kurganov and G. Petrova, “A second-order well-balanced positivity preserving central-upwind scheme for the saint-venant system,” *Communications in Mathematical Sciences*, vol. 5, no. 1, pp. 133–160, 2007.
- [20] B. Lie, *Modeling of Dynamic Systems*, University of South-Eastern Norway, 2017, Lecture Notes.
- [21] J. Machowski, Z. Lubosny, J. W. Bialek, and J. R. Bumby, *Power system dynamics: stability and control*. John Wiley & Sons, 2020.
- [22] P. Pourbeik *et al.*, “Dynamic models for turbine-governors in power system studies,” *IEEE Task Force on Turbine-Governor Modeling*, vol. 1, 2013.
- [23] E. Mosonyi, *Water power development: high-head power plants*. Akadémiai kiadó, 1965, vol. 2.
- [24] J. Pickford, *Analysis of water surge*. Taylor & Francis, 1969.
- [25] C. Jaeger, “Present trends in surge tank design,” *Proceedings of the Institution of Mechanical Engineers*, vol. 168, no. 1, pp. 91–124, 1954.
- [26] J. Guo, K. Woldeyesus, J. Zhang, and X. Ju, “Time evolution of water surface oscillations in surge tanks,” *Journal of Hydraulic Research*, vol. 55, no. 5, pp. 657–667, 2017.
- [27] A. Lydersen, *Fluid flow and heat transfer*. John Wiley & Sons Incorporated, 1979.
- [28] H. Saadat, *Power system analysis*. McGraw-hill, 1999.

- [29] P. S. Kundur and O. P. Malik, *Power system stability and control*. McGraw-Hill Education, 2022.
- [30] D. Simon, *Optimal state estimation: Kalman, H infinity, and nonlinear approaches*. John Wiley & Sons, 2006.
- [31] L. Vytvytskyi and B. Lie, “Linearization for analysis of a hydropower model using python api for openmodelica,” pp. 216–221, 2018.
- [32] I. Graabak and M. Korpås, “Balancing of variable wind and solar production in Continental Europe with Nordic hydropower A review of simulation studies,” *Energy Procedia*, vol. 87, no. 1876, pp. 91–99, 2016.
- [33] I. Graabak, S. Jaehnert, M. Korpås, and B. Mo, “Norway as a Battery for the Future European Power System Impacts on the Hydropower System,” *Energies*, vol. 10, no. 12, p. 2054, 2017.
- [34] I. Graabak, M. Korpås, S. Jaehnert, and M. Belsnes, “Balancing future variable wind and solar power production in central-west europe with norwegian hydropower,” *Energy*, vol. 168, pp. 870–882, 2019.
- [35] P. Khadka, D. Winkler, and T. Øyvang, “Online monitoring of a synchronous generator’s capability with matlab,” in *Proceedings of The 60th SIMS Conference on Simulation and Modelling SIMS 2019, August 12-16, Västerås, Sweden*, no. 170. Linköping University Electronic Press, 2020, pp. 198–205.
- [36] T. Øyvang, J. K. Nøland, R. Sharma, G. J. Hegglid, and B. Lie, “Enhanced power capability of generator units for increased operational security using nmpe,” *IEEE Transactions on Power Systems*, vol. 35, no. 2, pp. 1562–1571, 2019.
- [37] A. Boglietti, A. Cavagnino, D. Staton, M. Shanel, M. Mueller, and C. Mejuto, “Evolution and modern approaches for thermal analysis of electrical machines,” *IEEE Transactions on Industrial Electronics*, vol. 56, no. 3, pp. 871–882, March 2009.
- [38] A. M. EL-Refaeie, N. C. Harris, T. M. Jahns, and K. M. Rahman, “Thermal analysis of multibarrier interior PM synchronous Machine using lumped parameter model,” *IEEE Transactions on Energy Conversion*, vol. 19, no. 2, pp. 303–309, June 2004.
- [39] S. Nategh, O. Wallmark, M. Leksell, and S. Zhao, “Thermal Analysis of a PMSRM Using Partial FEA and Lumped Parameter Modeling,” *IEEE Transactions on Energy Conversion*, vol. 27, no. 2, pp. 477–488, June 2012.
- [40] Y.-K. R. Chin, E. Nordlund, and A. Staton, “Thermal analysis-lumped-circuit model and finite element analysis,” in *IPEC 2003: 6th International Power Engineering Conference*. NANYANG TECHNOLOGICAL UNIV, 2003, pp. 952–957.



## Bibliography

- [41] T. Øyvang, J. K. Nøland, G. J. Hegglid, and B. Lie, “Online model-based thermal prediction for flexible control of an air-cooled hydrogenerator,” *IEEE Transactions on Industrial Electronics*, 2018.
- [42] K. Aleikish, “Hybrid Machine Learning and Mechanistic Thermal Model of Synchronous Generator,” Master’s thesis, University of South-Eastern Norway, 2020.
- [43] E. Melfald, “Thermal model parameter estimation of a hydroelectric generator using machine learning,” Master’s thesis, University of South-Eastern Norway, 2020.
- [44] M. Pandey, “Model Fitting and State Estimation for Thermal Model of Synchronous Generator,” Master’s thesis, University of South-Eastern Norway, 2019.
- [45] N. Gordon, “Beyond the kalman filter: Particle filters for tracking applications,” in *Fusion 2004: Seventh International Conference on Information Fusion*, 2004.
- [46] F. Gustafsson, “Particle filter theory and practice with positioning applications,” *IEEE Aerospace and Electronic Systems Magazine*, vol. 25, no. 7, pp. 53–82, 2010.
- [47] T. Li, M. Bolic, and P. M. Djuric, “Resampling methods for particle filtering: classification, implementation, and strategies,” *IEEE Signal processing magazine*, vol. 32, no. 3, pp. 70–86, 2015.
- [48] J. M. Giron-Sierra, *Digital Signal Processing with Matlab Examples, Volume 3*. Springer, 2017.
- [49] R. E. Kalman, “A new approach to linear filtering and prediction problems,” *Journal of basic Engineering*, vol. 82, no. 1, pp. 35–45, 1960.
- [50] S. J. Julier and J. K. Uhlmann, “New extension of the kalman filter to nonlinear systems,” in *Signal processing, sensor fusion, and target recognition VI*, vol. 3068. International Society for Optics and Photonics, 1997, pp. 182–194.
- [51] G. Evensen, “The ensemble kalman filter: Theoretical formulation and practical implementation,” *Ocean dynamics*, vol. 53, no. 4, pp. 343–367, 2003.
- [52] D. Alspach and H. Sorenson, “Nonlinear bayesian estimation using gaussian sum approximations,” *IEEE transactions on automatic control*, vol. 17, no. 4, pp. 439–448, 1972.
- [53] K. K. Kottakki, M. Bhushan, and S. Bhartiya, “An improved gaussian sum unscented kalman filter,” *IFAC Proceedings Volumes*, vol. 47, no. 1, pp. 355–362, 2014.
- [54] C. Campestrini, T. Heil, S. Kosch, and A. Jossen, “A comparative study and review of different Kalman filters by applying an enhanced validation method,” *Journal of Energy Storage*, vol. 8, pp. 142–159, 2016.

- [55] J. Keller, H.-J. Hendricks Franssen, and G. Marquart, “Comparing seven variants of the ensemble kalman filter: How many synthetic experiments are needed?” *Water Resources Research*, vol. 54, no. 9, pp. 6299–6318, 2018.
- [56] S. Skogestad and C. Grimholt, “The simc method for smooth pid controller tuning,” in *PID control in the third millennium*. Springer, 2012, pp. 147–175.
- [57] T. Mohamed, H. Bevrani, A. Hassan, and T. Hiyama, “Decentralized model predictive based load frequency control in an interconnected power system,” *Energy Conversion and Management*, vol. 52, no. 2, pp. 1208–1214, 2011.
- [58] N. Modig, R. Eriksson, P. Ruokolainen, J. N. Ødegård, S. Weizenegger, and T. D. Fechtenburg, “Overview of frequency control in the nordic power system,” *Nordic Analysis Group*, 2022.
- [59] I. Dunning, J. Huchette, and M. Lubin, “JuMP: A Modeling Language for Mathematical Optimization,” *SIAM Review*, vol. 59, no. 2, pp. 295–320, 2017.
- [60] M. Garstka, M. Cannon, and P. Goulart, “Cosmo: A conic operator splitting method for convex conic problems,” *Journal of Optimization Theory and Applications*, vol. 190, no. 3, pp. 779–810, 2021.
- [61] U. Maeder, F. Borrelli, and M. Morari, “Linear offset-free model predictive control,” *Automatica*, vol. 45, no. 10, pp. 2214–2222, 2009.
- [62] L. Vytvytskyi and B. Lie, “Mechanistic model for Francis turbines in OpenModelica,” *IFAC-PapersOnLine*, vol. 51, no. 2, pp. 103–108, 2018.
- [63] M. Baudette, M. Castro, T. Rabuzin, J. Lavenius, T. Bogodorova, and L. Vanfretti, “OpenIPSL: Open-instance power system library—update 1.5 to “iTesla power systems library (iPSL): A modelica library for phasor time-domain simulations”,” *SoftwareX*, vol. 7, pp. 34–36, 2018.
- [64] M. Pandey, D. Winkler, R. Sharma, and B. Lie, “Using MPC to Balance Intermittent Wind and Solar Power with Hydro Power in Microgrids,” *Energies*, vol. 14, no. 4, p. 874, 2021.



# **Part II**

## **Publications**



## Appendix A

# Mechanistic modeling of different types of surge tanks and draft tubes for hydropower plants

Madhusudhan Pandey (M.P.) and Bernt Lie (B.L.)

Published in: *Proceedings of SIMS 2020 Virtual, Finland, 22-24 September 2020*. Linköping University Electronic Press, 2020, pp. 131-138.

<https://doi.org/10.3384/ecp20176131>

Author Contributions: Conceptualization, M.P.; initial studies, all authors; methodology, M.P.; software, M.P.; validation, all authors; formal analysis, all authors; writing—original draft preparation, M.P.; visualization, B.L., M.P.; supervision, B.L.



# Mechanistic modeling of different types of surge tanks and draft tubes for hydropower plants

Madhusudhan Pandey, Bernt Lie

TMCC, University of South-Eastern Norway, Bernt.Lie@usn.no

## Abstract

OpenHPL is an open-source hydropower library consisting of models for hydropower components that are developed based on mass and 1D momentum balance. It consists of mechanistic models for the flow of water in filled pipes (inelastic and elastic walls, incompressible and compressible water), a mechanistic model of a Francis turbine (including design of turbine parameters), friction models, etc. This paper includes an extension of OpenHPL with mechanistic models of different types of surge tanks (sharp orifice type, throttle valve surge tank, air-cushion surge tank) and draft tubes (conical diffusers and Moody spreading pipes). The simulated response of the models is presented using a case study of real hydro power plants.

*Keywords:* surge tanks, draft tubes, air-cushion surge tank, throttle valve surge tank, conical diffuser, Moody spreading pipes

## 1 Introduction

### 1.1 Background

The electricity generation from renewables has increased because of the rise in coal prices, oil insecurity, climatic concern (Brown, 2012), and the nuclear power debate (Wikipedia, 2019). There is a demand for renewable-sources economy over the coal-fired economy (Brown, 2012). The renewable energy sources are a combination of intermittent and dispatchable energy sources. Intermittent sources like solar, wind, and tidal power plants exhibit fluctuating power production that creates an imbalance between generation and load. In this regard, renewable dispatchable sources like hydro power plants play a significant role in balancing out the variability caused by intermittent sources. Current hydropower modeling, design, and analysis tools are limited and available commercially. Freely available tools include CASiMiR-Hydropower<sup>1</sup>, LVTrans<sup>2</sup>, and OpenHPL<sup>3</sup>, while commercial tools include Alab<sup>4</sup> and Modelon Hydro Power Library (HPL)<sup>5</sup>. In this regards, it drives motivation for open-source hydro power library development for modeling, design, and

analysis.

### 1.2 Previous studies

A mechanistic model of hydropower systems has been developed in (Splavska et al., 2017) using mass and 1D linear momentum balance which leads to a Modelica<sup>6</sup> based open-source hydropower library OpenHPL, and was initiated in a PhD study (Vytvytskyi, 2019). OpenHPL is under development at the University of South-Eastern Norway. Currently, OpenHPL has units for flow of water in filled pipes (inelastic and elastic walls, incompressible and compressible water) (Vytvytsky and Lie, 2017), a mechanistic model of a Francis turbine (including design of turbine parameters), friction models, etc (Vytvytskyi and Lie, 2018). The library also has draft models for a Pelton turbine, Francis turbine friction model, surge shaft, open channel flow, and a hydrology model. In addition, some accompanying work on analysis tools has been developed in scripting languages (Python, Julia) related to state estimation, structural analysis, etc (Vytvytskyi and Lie, 2019b). The library has been tested on real power plant data (Vytvytskyi and Lie, 2019a). The library is designed to interface to other Modelica libraries, e.g., libraries with generator models, electric grid, etc., for example, OpenHPL can be integrated with PVSystems<sup>7</sup> for photovoltaics as in (Pandey and Lie, 2020).

In this regard it is of interest to further develop units for OpenHPL. This paper primarily focuses on mechanistic models of surge tanks and draft tubes. The simple surge tank mechanistic model developed in (Splavska et al., 2017) is further enhanced by a sharp orifice type surge tank and a throttle valve surge tank considering hydraulic resistance in the inlet to the surge tank. The surge tank model is also further enhanced using air-cushion surge tank as a closed surge tank mechanistic model. A further extension to the library includes mechanistic models of draft tubes: conical diffuser and moody spreading pipes.

### 1.3 Outline of the paper

The paper is organized as follows. Model developments for surge tanks and draft tubes are provided in Section 2. The simulated response for the developed mechanistic model for surge tanks and draft tubes are presented in Section 3. Conclusions and future work are sketched in

<sup>1</sup>[http://www.casimir-software.de/save\\_download.php?language=2](http://www.casimir-software.de/save_download.php?language=2)

<sup>2</sup><http://svingentech.no/about%20lvtrans.html>

<sup>3</sup><https://github.com/simulatino/OpenHPL>

<sup>4</sup><http://www.alab.no/Alab-Hydropower-Software/Functionality-Alab-Hydropower-Software/Operation-simulation-with-waterway>

<sup>5</sup><https://www.modelon.com/library/hydro-power-library/>

<sup>6</sup><https://www.modelica.org/>

<sup>7</sup><https://github.com/raulpearson/PVSystems>



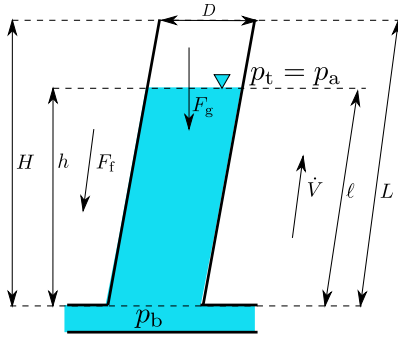


**Figure 1.** Simple surge tank with geometrical dimensions of height  $H$ , length  $L$ , and diameter  $D$ . The height of liquid level inside the surge tank is  $h$  with slanted length to be  $\ell$ . The volumetric flow rate inside the surge tank is  $\dot{V}$  with  $F_f$  as fluid friction.  $F_g$  is the gravitational force due to fluid mass  $m$  inside the surge tank.  $p_b$  is the bottom pressure and  $p_t$  is the top pressure equivalent to atmospheric pressure  $p_a$  for a free-fluid surface. For a hydropower system, we considered fluid inside the surge tank to be water with color as blue.

Section 4.

## 2 Model Development

Two main assumptions were made while developing models for hydro power units. First, we consider incompressible water flow inside the units. Second, we consider the inelastic pipe for modeling all types of surge tanks and draft tubes.

### 2.1 Surge tanks

A surge tank is usually placed between an intake and a penstock pipe in a hydro power system. The prime benefit of a surge tank is to provide a low-pressure region to dissipates pressure energy released during the sudden opening and closing of the turbine valve. Depending on the location and head, the surge tank can be of open type (water surface at atmospheric pressure) or closed type (water surface in contact with pressurized gas/air).

#### 2.1.1 Simple surge tank

A simple surge tank is shown in Fig. 1.

The mass and momentum balance for a dynamical system can be expressed as in (Lie, 2017a, p. 87-88, 226-227),

$$\begin{aligned}\frac{dm}{dt} &= \dot{m}_i - \dot{m}_e \\ \frac{d\mathcal{M}}{dt} &= \dot{\mathcal{M}}_i - \dot{\mathcal{M}}_e + F,\end{aligned}$$

where subscript i and e refers to influent and effluent properties, respectively.  $m$ ,  $\mathcal{M}$  and  $F$  represents mass, linear momentum and force acted-upon in a dynamical system. If  $\dot{m}$  and  $\dot{\mathcal{M}}$  are mass flow rate and momentum flow rate for a system with single entry and single exit, it is commonly written as  $\dot{m}_i - \dot{m}_e = \dot{m}$  and  $\dot{\mathcal{M}}_i - \dot{\mathcal{M}}_e = \dot{\mathcal{M}}$ .

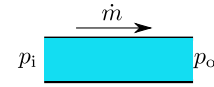


**Figure 2.** A hydropower unit, for example a simple rigid pipe, with ideal fluid (water) flow from a inlet pressure point  $p_i$  to outlet pressure  $p_o$  with  $\dot{m}$  as a flow variable. The pressure point inside the pipe is considered to be a across variable.

For surge tanks, if  $\dot{m}$  and  $\dot{\mathcal{M}}$  represents water mass flow rate and momentum flow rate of water inside the surge tank, respectively, then,

$$\frac{dm}{dt} = \dot{m} \quad (1)$$

$$\frac{d\mathcal{M}}{dt} = \dot{\mathcal{M}} + F. \quad (2)$$

The modeling of hydropower units in OpenHPL is considered using  $\dot{m}$  as a flow variable and pressure  $p$  at any point in a unit as a across variable<sup>8</sup>.

Figure 2 shows a connector for a hydropower unit created for OpenHPL. While developing a unit, for example a surge tank in our case, mathematical terms in mass and momentum balances as expressed in Eq. 1 and Eq. 2 should be reduced using algebraic variables to  $\dot{m}$ ,  $p_b$ , and  $p_t$ . For the surge tank we have  $p_i = p_b$  and  $p_o = p_t$  for a volumetric flow  $\dot{V}$  sign convention to be positive in the upward direction as in Fig. 1.

The mass balance equation represented in Eq. 1 can be represented by series of algebraic equations. The mass of water inside the surge tank leads to,

$$m = \rho A \ell \quad (3)$$

$$\ell = \frac{h}{\cos \theta} \quad (4)$$

$$A = \frac{\pi D^2}{4}, \quad (5)$$

and the mass flow rate leads to,

$$\dot{m} = \rho \dot{V}, \quad (6)$$

where  $A$  and  $\theta$  represents cross-sectional area and slant angle of a cylindrical surge tank with diameter  $D$ .  $\rho$  represents density of the fluid.  $h$  and  $\dot{V}$  are differential variable with initial height of water level inside the surge tank as  $h_o$  and initial discharge to the surge tank as  $\dot{V}_o$ . Similarly, the momentum balance equation in Eq. 2 can be represented by a series of algebraic equations as,

$$\mathcal{M} = mv \quad (7)$$

$$v = \frac{\dot{V}}{A} \quad (8)$$

$$\dot{\mathcal{M}} = \dot{m}v \quad (9)$$

$$F = F_p - F_f - F_g, \quad (10)$$

<sup>8</sup>The across and flow variables are used for creating a connectors in Modelica language. For more details, please see <https://mbe.modelica.university/components/connectors/>.

where  $v$  is the velocity of water inside the surge tank in the direction of  $\dot{V}$  and  $F$  is the total force acting inside the surge tank in the direction of  $v$ .  $F_p$  is the force exerted due to pressure difference  $p_b - p_t$ .  $F_f$  is the fluid friction acting opposite in the direction of  $v$ , and  $F_g$  is directed downward due to gravity.

The pressure force exerted in the normal direction of  $A$  is given by,

$$F_p = (p_b - p_t)A. \quad (11)$$

Furthermore, the fluid friction  $F_f$  is calculated as,

$$F_f = \frac{K''' A_w f_D}{4} \quad (12)$$

$$A_w = \pi D \ell \quad (13)$$

$$K''' = \frac{\rho \dot{V} |\dot{V}|}{2A^2}, \quad (14)$$

where  $K'''$  is the kinetic energy of the fluid per volume which is proportional to the quadratic variation of  $\dot{V}$  and  $v$ . The expression for  $K'''$  is  $\frac{\rho v |v|}{2}$ . The absolute value for  $v$  and  $\dot{V}$  allow for reversing direction of water flow.  $A_w$  represent the wetted area due to water flow inside the surge tank given by an expression  $A_w = \pi D \ell$ . In Eq. 12,  $f_D$  represents Darcy's friction factor given by an *implicit* expression in the Colebrook–White equation (Colebrook and White, 1937; Colebrook et al., 1939) for *transient* full-fluid flow in the conduit. There exists several *explicit* approximation for  $f_D$  that requires less computation as listed in (Lie, 2017a, p. 239). For OpenHPL, we are using the explicit approximation of Colebrook–White equation from (Swanee and Jain, 1976),

$$\frac{1}{\sqrt{f_D}} = -2 \log_{10} \left( \frac{\varepsilon/D}{3.7} + \frac{5.7}{N_{Re}^{0.9}} \right), \quad (15)$$

for  $N_{Re} = (2300 - 10^8)$  and  $\varepsilon/D = (10^{-5} - 0.005)$ , where  $\varepsilon$  is a conduit roughness height and  $N_{Re}$  is the Reynolds number expressed by  $N_{Re} = \frac{\rho |v| D}{\mu}$ . Here,  $\mu$  represents kinematic viscosity of the fluid.

For *laminar* flow,  $f_D = \frac{64}{N_{Re}}$  with  $N_{Re} < 2100$ . The region for the fluid with  $2100 \leq N_{Re} < 2300$  is a *transition* flow interpolated with a 4<sup>th</sup> order polynomial equation.

The expression for force due to gravity is given as,

$$F_g = mg \cos \theta. \quad (16)$$

Equation 1 to 16 represents Differential Algebraic Equations (DAEs) for the mechanistic modeling of simple surge tank represented in Fig. 1 and can be solved using equation based modeling language like Modelica.

### 2.1.2 Sharp orifice type surge tank

The model of the simple surge tank can be further modified using a sharp orifice hydraulic obstruction inside the surge tank as represented in Fig. 3.

To model the sharp orifice type surge tank we employ the *generalized friction factor* for sharp orifice fitting as

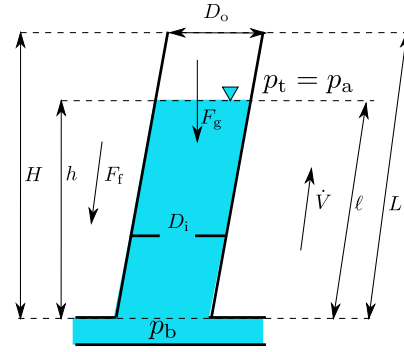


**Figure 3.** Sharp orifice type surge tank with a sharp orifice of diameter  $D_i$  as shown by horizontal perturbation bars inside the surge tank. The sharp orifice acts as a hydraulic obstruction for water flowing inside the surge tank.

given in (Lie, 2017a, p. 246). The expression for fluid friction force represented by Eq. 12 needs a correction term due to the sharp orifice. The frictional force exerted due to sharp orifice can be calculated using an expression for a pressure drop expression as given in (Lie, 2017a, p. 244). The overall frictional force for the sharp orifice type surge tank is now calculated by the expression as,

$$F_f = \frac{K''' A_w f_D}{4} + \frac{1}{2} \rho v |v| A \phi_{so}, \quad (17)$$

where  $A$  is the cross-sectional area of the sharp orifice type surge tank with diameter  $D_o$  which is equivalent to the simple surge tank with diameter noted with symbol  $D$ , and  $\phi_{so}$  is a generalized friction factor.  $\phi_{so}$  depends on  $N_{Re}$ , and the diameter of the surge tank and the orifice.

For  $N_{Re} < 2500$ :

$$\phi_{so} = \left[ 2.72 + \left( \frac{D_i}{D_o} \right)^2 \left( \frac{120}{N_{Re}} - 1 \right) \right] \cdot \phi_{so}^0$$

For  $N_{Re} \geq 2500$ :

$$\phi_{so} = \left[ 2.72 + \left( \frac{D_i}{D_o} \right)^2 \cdot \frac{4000}{N_{Re}} \right] \cdot \phi_{so}^0$$

where,

$$\phi_{so}^0 = \left[ 1 - \left( \frac{D_i}{D_o} \right)^2 \right] \left[ \left( \frac{D_i}{D_o} \right)^4 - 1 \right].$$

Equation 1 to 11, Eq.17, and Eq.13 to 16 represent DAEs for the mechanistic model of the sharp orifice type surge tank.

### 2.1.3 Throttle valve surge tank

To model a throttle valve surge tank we employ a similar method for correction of fluid frictional force as in the case of a sharp orifice type surge tank. A schematic diagram for throttle valve surge tank is given in Fig. 4.

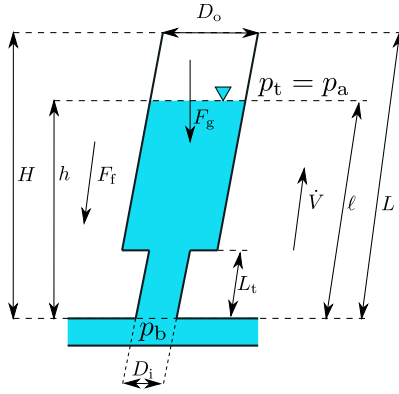


**Figure 4.** Throttle valve surge tank with the diameter and the length of throat as  $D_i$  and  $L_t$ , respectively. The throat in the figure acts as a hydraulic obstruction for the water flow inside the surge tank.

The water mass, velocity, momentum, and the fluid friction force for a throttle valve surge tank varies depending upon the water level inside the surge tank as above or below the throat.

1. **For  $\ell \leq L_t$ :** When the water level is at the throat or below the throat, we have,

$$m = \rho A_t \ell \quad (18)$$

$$F_f = \frac{K''' A_{w,t} f_D}{4}, \quad (19)$$

where  $A_t$  is the area of throat,  $A_{w,t}$  is wetted area for the throat given by expression  $A_{w,t} = \pi D_t \ell$ . The average velocity for this case is calculated using  $v = \frac{\dot{V}}{A_t}$  and  $K'''$  is given by expression  $K''' = \frac{1}{2} \rho v |v|$

2. **For  $\ell > L_t$ :** When water level inside the surge tank is above the throat of the surge tank, the frictional factor due to the throat should be considered.

The mass of the water inside the surge tank in this case is given as,

$$m = \rho (A_t L_t + A (\ell - L_t)), \quad (20)$$

where  $A = \frac{\pi D_o^2}{4}$ . Similarly, the average velocity, water momentum, and pressure force are given as,

$$v = \frac{\dot{V}}{2} \left( \frac{1}{A_t} + \frac{1}{A} \right)$$

$$\mathcal{M} = \rho \dot{V} \ell$$

$$F_p = (p_b - (p_t + \rho g (\ell - L_t))) A_t + \rho g (\ell - L_t) A.$$

Observe that while considering the frictional force correction factor for  $\ell > L_t$  the velocity direction is important.

**a). For  $v \geq 0$ :** The friction factor is calculated considering a *square expansion* type pipe fitting and the generalized friction factor is given as (Lie, 2017a, p. 245)

For  $N_{Re} < 4000$ :

$$\phi_{se} = 2 \left[ 1 - \left( \frac{D_o}{D_i} \right)^4 \right]$$

For  $N_{Re} \geq 4000$ :

$$\phi_{se} = (1 + 0.8 f_D) \left[ 1 - \left( \frac{D_o}{D_i} \right)^2 \right]^2.$$

This gives the total frictional force for this case,

$$F_f = \frac{K''' A_w f_D}{4} + \frac{1}{2} \rho v_e |v_e| A_t \phi_{se}, \quad (21)$$

where  $\phi_{se}$  represents the generalized friction factor for the square expansion type fitting. The *entrance velocity* for square expansion type fitting is expressed as  $v_e = \frac{\dot{V}}{A_t}$  and the *entrance area* is  $A_t$ . The wetted area is calculated using  $A_w = \pi D (\ell - L_t)$ .

**b). For  $v < 0$ :** The flow of water in this case is considered to be from the top of the surge tank to the bottom direction. The friction factor is calculated considering *square reduction* type pipe fitting and the generalized friction factor is given as,

for  $N_{Re} < 2500$ :

$$\phi_{sr} = \left( 1.2 + \frac{160}{N_{Re}} \right) \left[ \left( \frac{D_i}{D_o} \right)^4 - 1 \right]$$

and for  $N_{Re} \geq 2500$ :

$$\phi_{sr} = (0.6 + 0.48 f_D) \left( \frac{D_i}{D_o} \right)^2 \left[ \left( \frac{D_i}{D_o} \right)^2 - 1 \right].$$

This gives the total frictional force for this case to be,

$$F_f = \frac{K''' A_w f_D}{4} + \frac{1}{2} \rho v_e |v_e| A \phi_{sr}, \quad (22)$$

where  $\phi_{sr}$  represents the generalized friction factor for the square reduction type fitting. The *entrance velocity* is expressed as  $v_e = \frac{\dot{V}}{A}$  and the *entrance area* is  $A$ .

#### 2.1.4 Air-cushion surge tank

The general schematic of air-cushion surge tank is shown in Fig. 5. The free water surface inside the surge tank is filled with pressurized air making it as a closed type surge tank.

The pressure wave during a *load rejection* traveled from *high pressure region* (at the end of penstock) to the *low pressure region* (near free water surface, i.e., through the surge tank in hydro power systems). During this period, water mass inside the surge tank oscillates, dissipating pressure. The more the amplitude of water mass oscillation the higher should be the physical height of the surge tank. For reducing the amplitude of water oscillation inside the surge tank, pressurized air is placed inside the surge tank making a closed surge tank. This will cause the air to compress and expand adiabatically (Vereide et al., 2016; Zhang et al., 2009), and the energy due to high pressure is released as a form of work done for compression and rarefaction. For an adiabatic process we have,

$$pV^\gamma = \text{constant}, \quad (23)$$

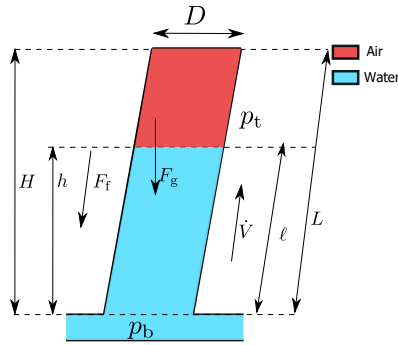


**Figure 5.** Air-cushion surge tank with initial air pressure of  $p_t$  which is normally tens of atmospheric pressure.

where  $p$ ,  $V$ , and  $\gamma$  is the pressure, volume, and ratio of specific heats at constant pressure and at constant volume, respectively, for air. The mechanistic model of air cushion surge tank is similar to that of simple surge tank, however with correction term for  $m$  and  $p_t$  for a simple surge tank.

The mass of water and air inside surge tank is given as,

$$m = \rho A \ell + m_a, \tag{24}$$

and the air pressure inside the surge tank is given by,

$$p_t = p_c \left( \frac{L - \ell_o}{L - \ell} \right)^\gamma, \tag{25}$$

where  $m_a$  is the mass of air inside the surge tank given by expression,

$$m_a = \frac{p_c A (L - \ell_o) M_a}{RT^o}. \tag{26}$$

In Eq. 25,  $p_c$  is the initial air cushion pressure when initial slant height of liquid level inside the surge tank is  $\ell_o$ . The expression shown in Eq. 25 is derive from Eq. 23 equalizing the *initial* and *final* expression. In Eq. 26,  $M_a$  represents molar mass of air,  $R$  is the universal gas constant, and  $T^o$  is the temperature of air inside the surge tank.

## 2.2 Draft tube

A draft tube is a hydraulic device used in reaction turbines in a hydro power systems for utilizing the available kinetic energy at the exit of the runner of the turbine. One of the prime benefits of a draft tube is to increase the turbine pressure head by decreasing the exit velocity out of the runner which will improves the overall efficiency of hydropower systems. And the other benefit is that the back flow of water from a *tailrace* to the turbine is restricted due to higher pressure region at the turbine’s outlet due to draft tube (Gubin, 1973). There are various types of draft tubes; the most common type is a conical diffuser and others are variants of the conical diffuser (Arasu, 2008). In this paper, we will derive a mechanistic model for a conical diffuser and a hydracone or a Moody spreading pipes (White, 1921).

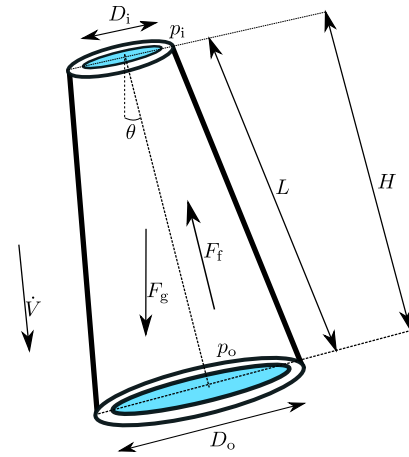


**Figure 6.** Conical diffuser inclined at angle  $\theta$  with input diameter  $D_i$  and output diameter  $D_o$ .  $p_i$  and  $p_o$  are input and output pressure of the conical diffuser with  $p_i > p_o$ .

### 2.2.1 Conical diffuser

A general schematic of the conical diffuser is shown in Fig. 6.

The influent and effluent mass flow of water through the conical diffuser is same. This gives  $\frac{dm}{dt} = 0$  from Eq. 1. Thus, the mechanistic model is derived from the momentum balance given by Eq. 2 with series of DAEs. First, we consider the model of the conical diffuser considering it be a cylinder of average diameter  $D = \frac{D_i + D_o}{2}$ . Second, we will add a frictional force correction factor for the conical diffuser expanded from  $D_i$  to  $D_o$  (with a *diffusion angle* normally in the range of  $(5^\circ - 20^\circ)$ ).

$$\frac{dM}{dt} = \dot{M} + F \tag{27}$$

$$M = mv \tag{28}$$

$$v = \frac{\dot{V}}{A} \tag{29}$$

$$\dot{M} = \dot{m}v \tag{30}$$

$$F = F_p - F_g - F_f, \tag{31}$$

where  $F_p = p_i A_i - p_o A_o$ ,  $A_i = \frac{\pi D_i^2}{4}$ ,  $A_o = \frac{\pi D_o^2}{4}$ ,  $A = \frac{\pi D^2}{4}$ , and  $F_g = mg \cos \theta$ . The mass of water inside the diffuser is given by,

$$m = \rho V,$$

where  $V$  is the volume of water. The expression for  $V$  can be calculated as<sup>9</sup>,

$$V = \frac{\pi H}{12} (D_i^2 + D_o^2 + D_i D_o).$$

The overall frictional force is calculated using expression

$$F_f = \frac{K''' A_w f_D}{4} + \frac{1}{2} \rho v |v| A_i \phi_d, \tag{32}$$

<sup>9</sup><https://mathworld.wolfram.com/ConicalFrustum.html>

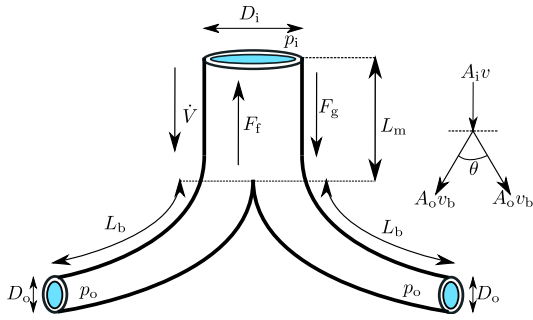


**Figure 7.** Moody spreading pipes with length of *main part*  $L_m$  with both the *branch* length of  $L_b$ .  $v$  and  $v_b$  are velocity through the main part and the branch part, respectively. The continuity equation for the pipe branching is  $A_i v = A_o v_b + A_o v_b$ . The pipe contracts from the point of branching to the outlet of the branch in the real case of hydracone as explain in (White, 1921, p. 276). However, we are considering a constant cross-section throughout the branch pipe.  $\theta$  is a branching angle or a bifurcation angle.

where  $\phi_d$  is the generalized friction factor due to the diffusion.

The *head loss* for a conical diffuser, diffused from  $D_i$  to  $D_o$ , is minimum at a diffusion angle of  $8^\circ$  for a fixed value of  $\frac{D_o}{D_i}$ . For a *pair value* of diffusion angle and the ratio  $\frac{D_o}{D_i}$ ,  $\phi_d$  can be calculated from (Munson et al., 2009, p. 420). For our case, for a maximum efficiency conical diffuser, we will consider a diffusion angle of  $8^\circ$  which gives

$$\phi_d \approx 0.23 \left(1 - \frac{D_i}{D_o}\right)^2. \quad (33)$$

The mechanistic model of a conical diffuser can be represented by using DAEs from Eq. 27 to 33.

### 2.2.2 Moody spreading pipes

The schematic diagram of a moody spreading pipes or a hydracone is shown in Fig. 7.

For Moody spreading pipes,  $\frac{dm}{dt} = 0$ , and the mechanistic model is developed from the momentum balance. We take the momentum balance considering verticle direction i.e.,  $y$ -axis momentum conservation. The series of DAEs are,

$$\frac{d\mathcal{M}}{dt} = \dot{\mathcal{M}} + F \quad (34)$$

$$\mathcal{M} = m_m v_m + 2m_b v_b \cos \frac{\theta}{2} \quad (35)$$

$$\dot{\mathcal{M}} = \dot{m}_m v_m + 2\dot{m}_b \cos \frac{\theta}{2} \quad (36)$$

$$F = F_p - F_f - F_g, \quad (37)$$

where  $m_m$  and  $m_b$  are mass of water in the main part and the branching part, respectively given by expressions  $m_m = \rho A_i L_m$  and  $m_b = \rho A_o L_b$ . Similarly,  $v_m$  and  $v_b$  are the velocity in the main and the branching part, respectively.  $v_m = \frac{\dot{V}}{A_i}$  and  $v_b$  are calculated using continuity equation

**Table 1.**  $\phi_d^o$  for different value of  $\theta$  for Moody spreading pipes friction factor correction

$\theta$	15	30	45	60	90
$\phi_d^o$	0.04	0.16	0.36	0.64	1

for branching pipes using expression as,

$$A_i v_m = A_o v_b + A_o v_b$$

$$A_i v_m = 2A_o v_b$$

$$v_b = \frac{A_i}{2A_o} v_m.$$

Furthermore, expressions for  $\dot{m}_m$  and  $\dot{m}_b$  are given as,

$$\dot{m}_m = \rho \dot{V}$$

$$\dot{m}_b = \rho \dot{V}_b$$

$$\dot{V}_b = A_o v_b,$$

where  $\dot{V}_b$  is the volumetric flow rate in the brach.

The components in Eq. 37 are expressed as,

$$F_p = p_i A_i - 2p_o A_o \cos \frac{\theta}{2} \quad (38)$$

$$F_g = m_m g + 2m_b g \cos \frac{\theta}{2}. \quad (39)$$

The fluid frictional force  $F_f$  is calculated considering fluid friction in the main and the brach pipe with addition of a generalized frictional force correction factor for branching. The overall frictional force is then,

$$F_f = F_{f,m} + 2F_{f,b} \cos \frac{\theta}{2} + 2 \cdot \frac{1}{2} \rho v_m |v_m| A_i \phi_d, \quad (40)$$

where  $\phi_d$  is the generalized friction factor for a single branch in case of branching and taken from (Idelcik, 1966, p. 281, 301), given as,

$$\phi_d = 1 + \left(\frac{v_b}{v_m}\right)^2 - 2\frac{v_b}{v_m} \cos \theta - \phi_d^o \left(\frac{v_b}{v_m}\right)^2, \quad (41)$$

where  $\phi_d^o$  depends on  $\theta$  and calculated from Table 1.

$F_{f,m}$  and  $F_{f,b}$  are fluid frictional force, calculated using Eq. 12, for main and the branch pipe for Moody spreading pipes.

Equation 34 to 41 represent DAEs for mechanistic modeling of Moody spreading pipes or Hydracone.

## 3 Simulated Responses and Results

For the simulated responses from the mechanistic models of surge tank and draft tubes we take a case study from a real hydropower plant. For simulating open surge tanks and draft tubes we are using the layout of the Trollheim hydro power plant and for simulating air-cushion surge tank we are using the layout of the Torpa hydropower plant.

The layout diagram of Trollheim and Torpa hydro power plants are shown in Fig. 8.



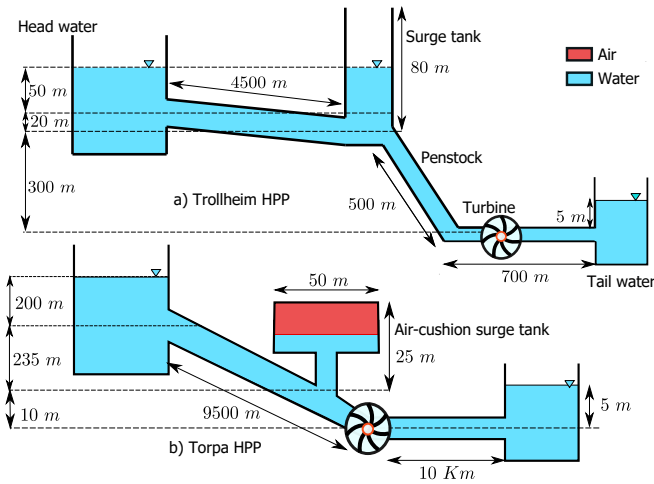


**Figure 8.** Layout diagram for the Trollheim (Vytyvtskyi and Lie, 2019a) and the Torpa Hydro Power Plant (HPP) (Vereide et al., 2016). Nominal head, nominal discharge, and nominal power output are 370 m, 40 m<sup>3</sup>/s and 130 MW for the Trollheim HPP, and 445 m, 35 m<sup>3</sup>/s and 150 MW for Torpa HPP. Torpa HPP has two turbine units each having nominal power output of 75 MW. The air-cushion surge tank for the Torpa HPP has air volume of 13,000 m<sup>3</sup> initially pressurized at 4.1 Mpa. For the Trollheim HPP, the diameter for both of the penstock and the surge tank is 4 m while for both of the headrace and the tailrace tunnel is 6 m. Similarly, for the Torpa HPP, the diameter of both of the headrace and the tailrace tunnel is 7 m.

### 3.1 Responses for surge tanks

Figure 9 shows the simulated response for different surge tanks for the Trollheim HPP and the Torpa HPP.

In case of the Trollheim HPP, the manifold pressure surge during load acceptance<sup>10</sup> in case of a simple surge tank has higher amplitude than that for sharp orifice and throttle valve surge tank. Furthermore, the pressure surge dies out soon in case of both sharp orifice and throttle valve surge tank. Also, the diameter of sharp orifice and throttle valve affects the manifold pressure surge oscillation. For example, when  $D_t = 1$  m for a throttle valve surge tank the manifold pressure  $p_b$  settles after 20 s while for sharp orifice type with  $D_{so} = 1$  m,  $p_t$  settles around 300 s.

In case of the Torpa HPP, the dynamics of both manifold pressure and air-cushion pressure is the same with a difference of almost 2 bars.

### 3.2 Responses for draft tubes

Figure 9 shows the simulated response for a conical diffuser and Moody spreading pipes for the the Trollheim HPP.

For a Moody spreading pipes draft tube, the inlet pressure  $p_i$  decreases as the branching angle decreases.

<sup>10</sup>It is the condition when the load at prime mover is added suddenly. For instance, in case of turbine running an electrical generator the sudden industrial operation like electrical motors, etc., can be considered as a load acceptance.

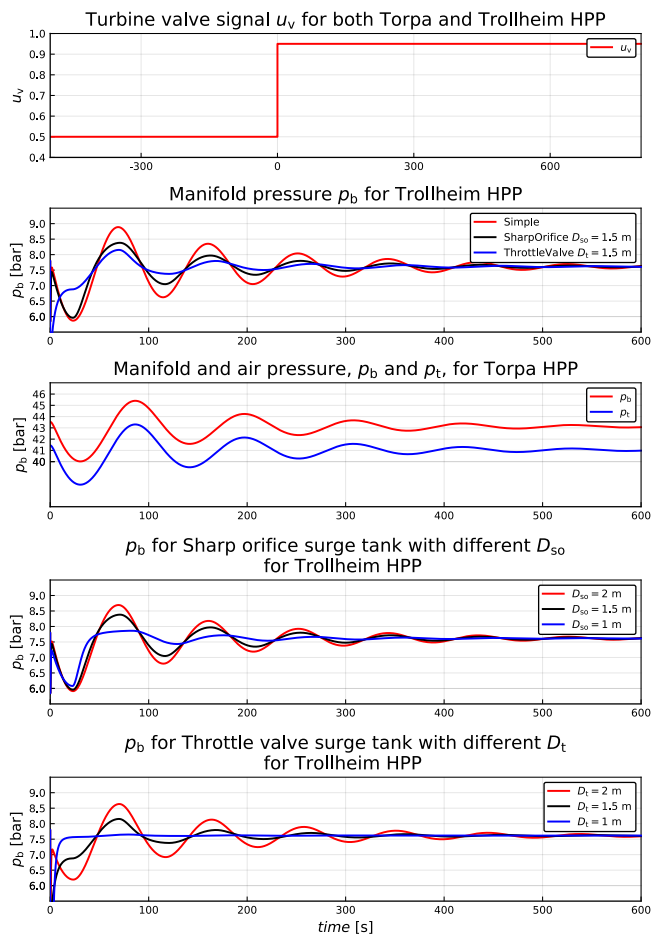


**Figure 9.** Simulated response for different surge tanks with step change of 0.45 to turbine’s valve signal. The turbine’s valve signal starts at  $t = -500$  s to show that simulation is performed in steady-state for  $-500$  s and at  $t = 0$  s the valve signal is change from 0.5 to 0.95 to see the dynamics of other variables.

## 4 Conclusions and Future Work

This paper consists of mechanistic models for different types of surge tanks and draft tubes. Result shows that the pressure surge during load acceptance dies out soon for the throttle valve surge tank when the diameter of throat is decreased successively. Similar operations can be obtained for a sharp orifice type surge tank, however, pressure surge amplitude decays soon in case of a throttle valve surge tank. For an air-cushion surge tank, the dynamics of both manifold pressure and air-cushion pressure are the same. For a Moody spreading pipes, the inlet pressure decreases when the braching angle is decreased.

Future work includes testing of the surge tank and draft tube mechanistic models with experimental data. The dynamics of sharp orifice type surge tank and throttle valve surge tank can be validated with simulated results from (Bhattarai et al., 2019). The air-cushion surge tank model can be validated with experimental results obtained from (Vereide et al., 2016). Similarly, model validation for the conical diffusers can be done with experimental data from

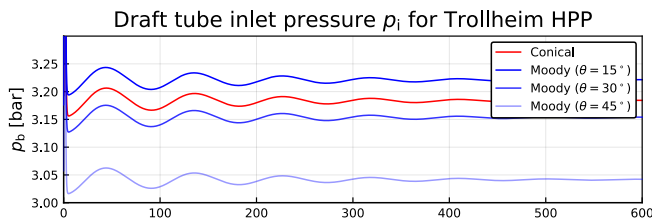


**Figure 10.** Simulated response for conical diffuser and Moody spreading pipes for different branching angle.  $D_i = 4$  m for both types of draft tubes.  $D_o = 4.978$  m for conical diffuser with diffusion angle of  $8^\circ$  and  $D_o = 3.5$  m for Moody spreading pipes.  $L_m = 4$  m and  $L_b = 3$  m for Moody spreading pipes. Moody spreading pipes draft tube is simulated for different branching angle of  $15^\circ$ ,  $30^\circ$ , and  $45^\circ$ .

(Vytvytskyi and Lie, 2019a). For Moody spreading pipes, prior model judgement is required from experts.

## References

- A Valan Arasu. *Turbo Machines*. Vikas Publishing House, 2008.
- Khem Prasad Bhattarai, Jianxu Zhou, Sunit Palikhe, Kamal Prasad Pandey, and Naresh Suwal. Numerical modeling and hydraulic optimization of a surge tank using particle swarm optimization. *Water*, 11(4):715, 2019.
- R. Lester Brown. Plan B Updates - 107: The Great Transition, Part I: From Fossil Fuels to Renewable Energy | EPI, Aug 2012. [http://www.earth-policy.org/plan\\_b\\_updates/2012/update107](http://www.earth-policy.org/plan_b_updates/2012/update107).
- CF Colebrook and CM White. Experiments with fluid friction in roughened pipes. *Proceedings of the Royal Society of London. Series A-Mathematical and Physical Sciences*, 161(906):367–381, 1937.
- Cyril Frank Colebrook, T Blench, H Chatley, EH Essex, JR Finnicome, G Lacey, J Williamson, and GG Macdonald. Correspondence. turbulent flow in pipes, with particular reference to the transition region between the smooth and rough pipe laws.(includes plates). *Journal of the Institution of Civil engineers*, 12(8):393–422, 1939.
- Maksimillian Fedorovich Gubin. *Draft tubes of hydro-electric stations*. Published for the Bureau of Reclamation, US Dept. of the Interior and ÅS, 1973.
- IE Idelcik. Handbook of hydraulic resistance: coefficients of local resistance and of friction. Technical report, ERDA Div. Phys. Res., 1966.
- Bernt Lie. Modeling of Dynamic Systems, August 2017a. Lecture notes, Version of August 8.
- BR Munson, DF Young, and TH Okiishi. *Fundamentals of Fluid Mechanics*, 2009.
- Madhusudhan Pandey and Bernt Lie. *The Role of Hydropower Simulation in Smart Energy Systems*. 2020.
- Valentyna Splavska, Liubomyr Vytvytskyi, and Bernt Lie. Hydropower systems: comparison of mechanistic and table look-up turbine models. In *Proceedings of the 58th Conference on Simulation and Modelling (SIMS 58) Reykjavik, Iceland, September 25th–27th, 2017*, number 138, pages 368–373. Linköping University Electronic Press, 2017.
- PK Swanee and Akalank K Jain. Explicit equations for pipeflow problems. *Journal of the hydraulics division*, 102(5), 1976.
- Kaspar Vereide, Bjørnar Svingen, Torbjørn Kristian Nielsen, and Leif Lia. The effect of surge tank throttling on governor stability, power control, and hydraulic transients in hydropower plants. *IEEE Transactions on Energy Conversion*, 32(1):91–98, 2016.
- Liubomyr Vytvytskyi and Bernt Lie. Comparison of elastic vs. inelastic penstock model using OpenModelica. In *Proceedings of the 58th Conference on Simulation and Modelling (SIMS 58) Reykjavik, Iceland, September 25th–27th, 2017*, number 138, pages 20–28. Linköping University Electronic Press, 2017. doi:<http://dx.doi.org/10.3384/ecp1713820>.
- Liubomyr Vytvytskyi. *Dynamics and model analysis of hydropower systems*. PhD thesis, University of South-Eastern Norway, 2019. URL <http://hdl.handle.net/11250/2608105>.
- Liubomyr Vytvytskyi and Bernt Lie. Mechanistic model for Francis turbines in OpenModelica. *IFAC-PapersOnLine*, 51(2):103–108, 2018. doi:<https://doi.org/10.1016/j.ifacol.2018.03.018>.
- Liubomyr Vytvytskyi and Bernt Lie. OpenHPL for Modelling the Trollheim Hydropower Plant. *Energies*, 12(12):2303, 2019a.
- Liubomyr Vytvytskyi and Bernt Lie. Combining measurements with models for superior information in hydropower plants. *Flow Measurement and Instrumentation*, 69:101582, 2019b.
- William M White. *The Hydraucone Regainer, Its Development and Applications in Hydro-electric Plants*. 1921.
- Wikipedia. Nuclear power debate, Oct 2019. [https://en.wikipedia.org/wiki/Nuclear\\_power\\_debate](https://en.wikipedia.org/wiki/Nuclear_power_debate).
- Xiaohong Zhang, Zhengfei Zhao, and Yanhang Zhang. Study on wave calculation of an air cushion surge chamber. In *2009 International e-Conference on Advanced Science and Technology*, pages 70–73. IEEE, 2009.

## Appendix B

# Mechanistic Model of an Air Cushion Surge Tank for Hydro Power Plants

Madhusudhan Pandey (M.P.), Dietmar Winkler (D.W.), Kaspar Vereide (K.V.), Roshan Sharma (R.S.) and Bernt Lie (B.L.)

Published in: *Energies* 2022, 15(8), 2824.

<https://doi.org/10.3390/en14040874>

Author Contributions: Conceptualization, M.P., K.V., R.S. and B.L.; methodology, M.P., R.S. and B.L.; software, M.P. and D.W.; validation, M.P., K.V. and B.L.; formal analysis, M.P.; investigation, M.P.; resources, M.P., D.W. and K.V.; writing—original draft preparation, M.P.; writing—review and editing, M.P.; visualization, M.P. and B.L.; supervision, D.W., K.V. and B.L.





## Article

# Mechanistic Model of an Air Cushion Surge Tank for Hydro Power Plants

Madhusudhan Pandey <sup>1</sup>, Dietmar Winkler <sup>1</sup>, Kaspar Vereide <sup>2</sup>, Roshan Sharma <sup>1</sup> and Bernt Lie <sup>1,\*</sup>

<sup>1</sup> Telemark Modeling and Control Center (TMCC), University of South-Eastern Norway (USN), 3918 Porsgrunn, Norway; madhusudhan.pandey@usn.no (M.P.); dietmar.winkler@usn.no (D.W.); roshan.sharma@usn.no (R.S.)

<sup>2</sup> Department of Civil and Environmental Engineering, Norwegian University of Science and Technology, 7034 Trondheim, Norway; kaspar.veraide@ntnu.no

\* Correspondence: bernt.lie@usn.no

**Abstract:** Due to the increasing use of renewable energy sources, and to counter the effects of fossil fuels, renewable dispatchable hydro power can be used for balancing load and generation from intermittent sources (solar and wind). During higher percentage change in load acceptance or rejection in the intermittent grid, the operations of surge tanks are crucial in terms of water mass oscillation and water hammer pressure, and to avoid wear and tear in actuators and other equipment, such as hydro turbines. Surge tanks are broadly classified as open types, with access to open air, and closed types, with a closed volume of pressurized air. Closed surge tanks are considered to have a more flexible operation in terms of suppressing water mass oscillation and water hammer pressure. In this paper, a mechanistic model of an air cushion surge tank (ACST) for hydro power plants is developed based on the ordinary differential equations (ODEs) for mass and momentum balances. The developed mechanistic model of the ACST is a feature extension to an existing open-source hydro power library—OpenHPL. The developed model is validated with experimental data from the Torpa hydro power plant (HPP) in Norway. Results show that the air friction inside the ACST is negligible as compared to the water friction. The results also indicate that a hydro power plant with an ACST is a potential candidate as a flexible hydro power in an interconnected power system grid supplied with intermittent energy sources. Conclusions are drawn based on the simulation results from hydraulic performance of the ACST.

**Keywords:** air cushion surge tank (ACST); air friction model; flexible hydro power plants; mechanistic model; OpenHPL



**Citation:** Pandey, M.; Winkler, D.; Vereide, K.; Sharma, R.; Lie, B. Mechanistic Model of an Air Cushion Surge Tank for Hydro Power Plants. *Energies* **2022**, *15*, 2824. <https://doi.org/10.3390/en15082824>

Academic Editors: Adam Adamkowski and Anton Bergant

Received: 17 March 2022

Accepted: 11 April 2022

Published: 13 April 2022

**Publisher's Note:** MDPI stays neutral with regard to jurisdictional claims in published maps and institutional affiliations.



**Copyright:** © 2022 by the authors. Licensee MDPI, Basel, Switzerland. This article is an open access article distributed under the terms and conditions of the Creative Commons Attribution (CC BY) license (<https://creativecommons.org/licenses/by/4.0/>).

## 1. Introduction

### 1.1. Background

Electricity generation from renewable energy is increasing because of oil insecurity, climatic concern, the nuclear power debate, and carbon emission prices. In a growing trend of renewable energy, today's power systems are a combination of intermittent and dispatchable renewable sources in a common interconnected grid. Intermittent sources include sources like solar power plants and wind power plants, whose variability can be balanced using a dispatchable renewable source like a hydro power plant, as discussed in [1,2]. In an interconnected power grid with both intermittent and dispatchable sources, a sudden loss in generation from the intermittent sources, for example, shadowing a large number of solar panels as in the case of solar power plants, a shutdown of the wind generators for unacceptable wind velocity as in the case of wind power plants, hydro power plants must be able to operate with a higher percentage of load acceptance to cope with the loss in generation, and to protect the power grid from a blackout. Similarly, when there is a sudden increase in production from the intermittent generation, hydro power plants must be able to operate with a higher percentage of load rejection to cope with grid

instability and blackout. This indicates the need for flexible operation of dispatchable hydro power plants. In [3,4], the concept of *flexible hydro power* is coined for the interconnected power grid. Similarly, in [5] cascaded hydro power plants are considered as one of the candidates for flexible hydro power plants. In relation to the concept of flexible hydro power, hydro power plants with open surge tanks are relatively less able to tackle a higher percentage of load acceptance and rejection. However, power plants with ACST are more likely to tackle a higher percentage of load acceptance and rejection as ACST can be placed very near to the turbine. Hydraulic behavior of the open surge tanks studied in [6] outlines their operational limits in terms of their design heights and water hammer effects. As the percentage of load acceptance and rejection increases in the case of the open surge tanks, water mass oscillation inside the surge tanks may exceed the maximum allowed height and the operational limit of the power plant equipment due to an excessive water hammer effect. Similarly, in [7,8] the benefits of ACST with respect to open surge tanks are given.

In this regard, it is of interest to study the hydraulic behavior of an ACST (closed surge tank) with respect to open surge tanks. A simple mechanistic model of an ACST was developed and studied previously in [9] as a feature extension to an open-source hydro power library—OpenHPL. OpenHPL is based on an equation-based language—Modelica. OpenHPL is under development at the University of South-Eastern Norway. This paper primarily focuses on the model improvements from [9], validation of the improved model with experimental data from [10], and hydraulic behavior of an ACST in relation to flexible hydro power plants.

### 1.2. Previous Work and Contributions

The model of hydraulic transients inside the surge tank is a well-established theory using Newton's second law [11,12]. The use of hydraulic resistances in the inlet of the surge tank helps to reduce water hammer effects. Different types of surge tanks designed with respect to the hydraulic resistances are presented in [13]. The time evolution equations for developing a mechanistic model of the surge tank are given in [14]. The hydraulic resistance at the inlet of different kinds of surge tanks can be studied from [14,15]. Closed surge tanks or ACST are important in terms of suppressing water mass oscillation due to the cushioning of air during hydraulic transients [16]. A hydraulic scale model of an ACST was studied in [10] based on 1D mass and momentum balances. In [17], a simulation study was carried out considering 1D mass and momentum equations for both water and air inside the ACST. In the paper, it is shown that the mass and momentum balances for air inside the ACST can be further simplified with an ideal gas relation. Other studies include the gas seepage theory for air loss through the ACST chamber in [18], a monitoring method for the hydraulic behavior of the ACST in [19], stability analysis of the ACST in [20], etc. The model developed in most of the previous work assumes an adiabatic process for the cushioning of air inside the ACST. The polytropic constant for air  $\gamma$  is considered around 1.4 for almost all the models of the ACST. However, previous work lacks modeling of the ACST with a possible consideration of friction due to air flow inside the ACST during its operation. The following research contributions are provided in this paper:

- a mechanistic model of an ACST, and
- a comparison between the ACST models with and without air friction.

### 1.3. Outline

Section 2 provides a mechanistic model of an ACST based on mass and momentum balances. In Section 3, model fitting and simulation results are outlined through a case study of the ACST used in Torpa Hydro Power Plant (HPP). Section 4 provides conclusions and future work.

## 2. Mechanistic Model of ACST

A general schematic and a flow diagram of an ACST is shown in Figure 1. The free water surface inside the surge tank is filled with pressurized air. Figure 1a shows the general

schematic of an ACST where the water with volumetric flow rate  $\dot{V}$  flows towards the air chamber through the access tunnel with length  $L_t$  and diameter  $D_t$ . The intake-penstock manifold pressure at the bottom of the tank is represented by  $p_m$ , and the air pressure at the air chamber due to the cushioning of the air is represented by  $p_c$ . The diameter of the air chamber is  $D$ .  $H$  is the total height of the surge tank and  $L$  is the total vertical slant length of the surge tank. In the figure,  $h$  represents the water level inside the tank during the operation of the ACST, and the dotted line in Figure 1a indicates that  $h$  is a variable quantity. Figure 1b shows a flow diagram inside the surge tank where  $F_f$  is the fluid friction against  $\dot{V}$ ,  $F_g$  is the force due to gravity in the downward direction, and  $F_g^{\dot{V}}$  is the projection of  $F_g$  in the alignment of the flow.

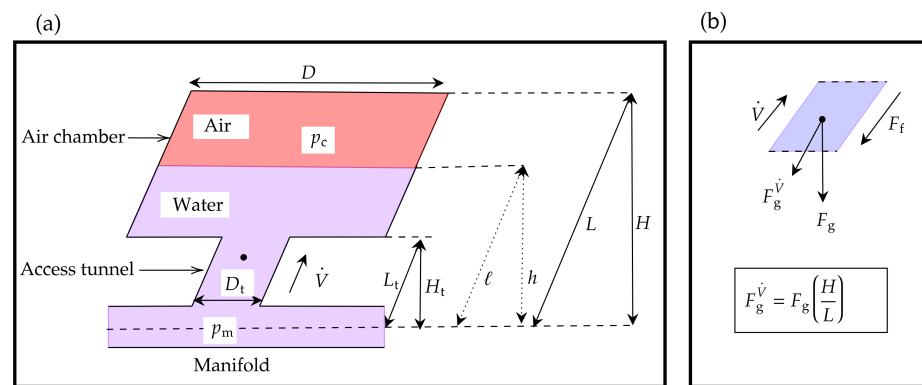


**Figure 1.** ACST with an access tunnel and an air chamber. (a) general schematic of ACST and (b) flow diagram.

Models developed in OpenHPL are based on a semi-explicit DAE formulation with a differential equation for the mass and the momentum balances as described in [21] and given by

$$\frac{dm}{dt} = \dot{m} \tag{1}$$

$$\frac{d\mathcal{M}}{dt} = \dot{\mathcal{M}} + F \tag{2}$$

where  $\dot{m}$  and  $\dot{\mathcal{M}}$  represent the mass flow rate and the momentum flow rate, respectively.

Equations (1) and (2) are expressed with a series of algebraic equations as

$$\dot{m} = \rho \dot{V} \tag{3}$$

$$\mathcal{M} = mv \tag{4}$$

$$\dot{\mathcal{M}} = \dot{m}v \tag{5}$$

$$F = F_p - F_g^{\dot{V}} - F_f \tag{6}$$

where  $\rho$  is the density of the water,  $m$  is the mass of air and water inside the ACST,  $v$  is the average velocity of the flow,  $V$  is the volume of the ACST,  $F$  is the total force acting in the surge tank,  $F_p$  is the pressure force, and  $F_f$  is the fluid frictional force. The expressions for all the variables are given in the sequel. A general idea regarding mathematical formulations of these variables is taken from [9].

The total mass inside the surge tank is expressed as

$$m = m_w + m_a \tag{7}$$

where  $m_w$  and  $m_a$  are the masses of the water and the air inside the surge tank, respectively.  $m_a$  is constant inside the chamber and is determined based on the initial air cushion pressure  $p_{c0}$  which is considered to be a design parameter for the hydraulic performance

of the surge tank. If  $h_{c0}$  is the initial water level inside the surge tank for the initial air cushion pressure  $p_{c0}$ , then the expression for the mass of the air inside the surge tank is found from an adiabatic compression and rarefaction of the air inside the surge tank during operation. It is found that for an ACST with a larger diameter, the heat transfer between air and water, air to the walls of the ACST, etc., can be neglected, and an adiabatic process of compression and rarefaction of the air inside the ACST can be assumed [16]. For an adiabatic process with pressure  $p$ , volume  $V$ , and  $\gamma$  of the air inside the ACST, considering standard temperature and pressure (STP), the relation  $pV^\gamma = \text{constant}$  is assumed where  $\gamma$  is the ratio of specific heats at constant pressure and at constant volume. The mass of the air is then calculated formulating an ideal gas relation with the initial air pressure  $p_{c0}$  and the initial volume  $A\left(L - h_{c0}\frac{L}{H}\right)$  given by

$$m_a = \frac{p_{c0}A\left(L - h_{c0}\frac{L}{H}\right)M_a}{RT^\circ} \quad (8)$$

where  $M_a$  is the molar mass of air,  $R$  is the universal gas constant and  $T^\circ$  is the temperature taken at STP. Similarly,  $A$  is the area of the air chamber expressed as  $A = \pi\frac{D^2}{4}$ .

From Equation (2) formulating  $p_{c0}V_0^\gamma = p_cV^\gamma$ , the air cushion pressure during the operation of the surge tank is given by

$$p_c = p_{c0}\left(\frac{L - h_{c0}\frac{L}{H}}{L - \ell}\right)^\gamma \quad (9)$$

where  $p_c$  depends on the length  $\ell$  inside the ACST.

During the operation of the surge tank, the mass of the water inside the surge tank  $m_w$  varies according to the variation in  $h$ . Thus, the expression for  $m_w$  is formulated considering two different scenarios inside the surge tank based on the variation of the water level  $h$ . First we consider (i)  $h \leq H_t$  and second we consider (ii)  $h > H_t$ . Furthermore, we also formulate expressions for  $F_p$  and  $F_f$  for both of the scenarios of the water level  $h$ .

### 2.1. Case $h \leq H_t$

When the water level is up to the tip of the access tunnel or below the tip of the access tunnel,  $m_w$  is given by  $m_w = \rho A_t \ell$  where  $\ell$  is the slant height for  $h$  as shown in Figure 1a.  $m_w$  is further expressed as

$$m_w = \rho A_t h \frac{L}{H}. \quad (10)$$

The pressure force  $F_p$  is formulated based on the pressure difference at the manifold and the air pressure with an expression

$$F_p = (p_m - p_c)A_t. \quad (11)$$

The frictional force  $F_f$  is expressed as

$$F_f = F_{D,w} + F_{D,a} \quad (12)$$

where  $F_{D,w}$  is the frictional force formulated for water flow inside the surge tank based on Darcy's friction factor for water,  $f_{D,w}$ . Similarly,  $F_{D,a}$  is the frictional force formulated for air flow inside the surge tank based on Darcy's friction factor for air,  $f_{D,a}$ . Both  $f_{D,w}$  and  $f_{D,a}$  are calculated as in [9]. The general expression for Darcy's friction factor  $f_D$  is based on Reynolds' number  $N_{Re} = \frac{\rho|v|D}{\mu}$  and expressed as

$$f_D = \begin{cases} \frac{64}{N_{Re}} & N_{Re} < 2100 \\ aN_{Re}^3 + bN_{Re}^2 + cN_{Re} + d & 2100 \leq N_{Re} \leq 2300 \\ \frac{1}{\left(2 \log_{10} \left(\frac{\varepsilon}{3.7D} + \frac{5.7}{N_{Re}^{0.9}}\right)\right)^2} & N_{Re} > 2300 \end{cases}$$

where  $\mu$  is the dynamic viscosity of the fluid,  $\varepsilon$  is the pipe roughness height. For the region  $2100 \leq N_{Re} \leq 2300$ ,  $f_D$  is calculated from a cubic interpolation, with the coefficients  $a$ ,  $b$ ,  $c$ , and  $d$ , differentiable at the boundaries. The final expression for  $F_f$  is calculated as in [9] given as

$$F_f = \frac{1}{2} \rho v |v| \left( A_{w,w} \frac{f_{D,w}}{4} + A_{w,a} \frac{f_{D,a}}{4} \right) \quad (13)$$

where  $|v|$  preserves the fluid frictional force against both directions of flow; flow induced from the access tunnel towards the air chamber, and vice-versa.  $A_{w,w}$  is the wetted area due to water flow inside the surge tank given by

$$A_{w,w} = \pi D_t \ell \quad (14)$$

and  $A_{w,a}$  is the wetted area due to the air during adiabatic compression and rarefaction inside the surge tank, and expressed as

$$A_{w,a} = \pi [D(L - L_t) + D_t(L_t - \ell)]. \quad (15)$$

## 2.2. Case $h > H_t$

When the water level inside the surge tank is above the access tunnel expression for  $m_w$  is formulated by summing the mass of water inside the access tunnel and the mass of water inside the air chamber, and is expressed as

$$m_w = \rho [A_t L_t + A(\ell - L_t)]. \quad (16)$$

For  $\ell > L_t$  we consider Figure 2 for finding the total pressure force  $F_p$  in the direction of the flow. The calculation of the fluid frictional force is given in Figure 3. From Figure 2, the pressure force  $F_p$  is calculated based on the junction pressure  $p_j$  between the junction of the access tunnel and the air chamber.  $p_j$  is expressed as the sum of the air pressure  $p_c$  and the hydrostatic pressure due to the difference in liquid-level  $h - H_t$ . The junction pressure is then expressed as

$$p_j = p_c + \rho g (\ell - L_t) \frac{H}{L} \quad (17)$$

which relates in the final expression for  $F_f$  as

$$F_p = (p_m - p_j) A_t + (p_j - p_c) A. \quad (18)$$

From Figure 2, the overall fluid frictional force  $F_f$  is calculated with an expression given as

$$F_f = F_{D,w} + F_\phi + F_{D,a} \quad (19)$$

where  $F_{D,w} + F_{D,a}$  is given as

$$F_{D,w} + F_{D,a} = \frac{1}{2} \rho v |v| \left( A_{w,w} \frac{f_{D,w}}{4} + A_{w,a} \frac{f_{D,a}}{4} \right)$$

where  $A_{w,w} = \pi [D_t L_t + D(\ell - L_t)]$  and  $A_{w,a} = \pi D(L - \ell)$ ; the calculations were similarly performed as in Equations (14) and (15).

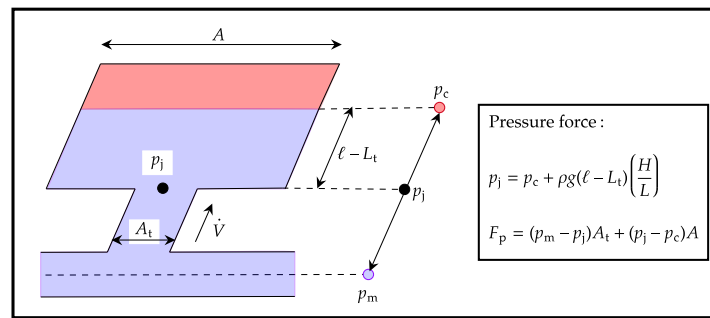


**Figure 2.** Considering junction pressure  $p_j$  for evaluating the overall pressure force  $F_p$  in the direction of flow.  $p_j$  is the pressure calculated based on the sum of air pressure  $p_c$  and hydrostatic pressure due to liquid-level  $h - H_t$ .

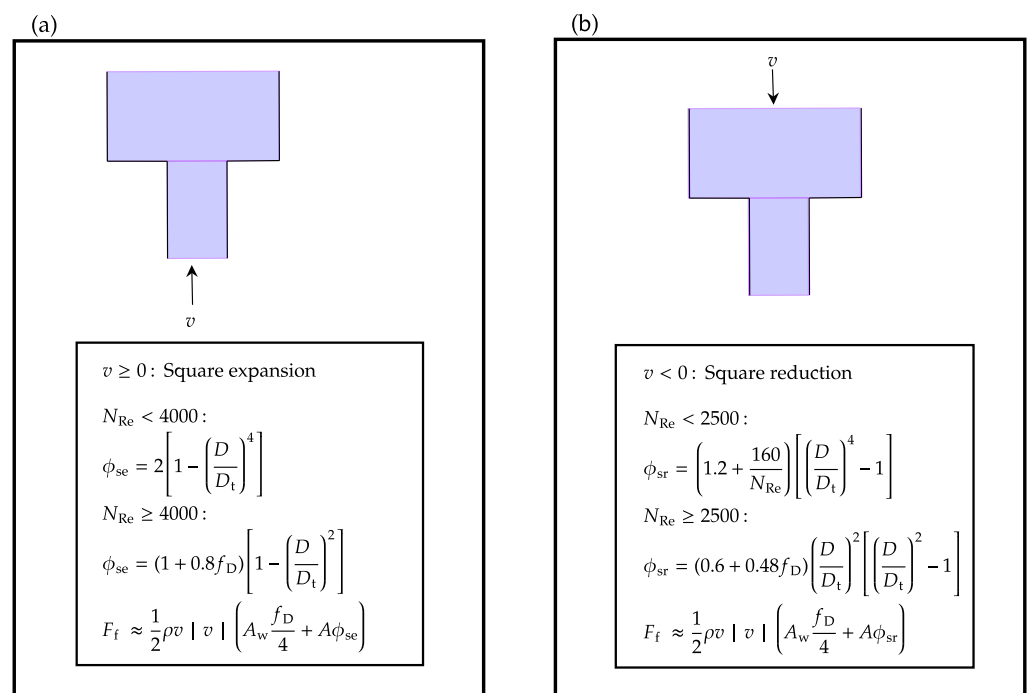


**Figure 3.** Expressions for fluid frictional force  $F_f$  considering (a) the square expansion type fitting for the flow towards the chamber through the access tunnel and (b) the square reduction type fitting for the flow through the chamber to the access tunnel. In the figures,  $\phi_{se}$  and  $\phi_{sr}$  are the generalized friction factors for the square expansion and the square reduction type fittings, respectively, taken from [15].

In Equation (19),  $F_\phi$  is the fluid frictional force due to water flow from the access tunnel towards the air chamber, and vice-versa.  $F_\phi$  can be expressed in terms of the pressure drop (alternatively can be expressed in terms of the head loss). When the water is flowing from the access tunnel towards the air chamber, we consider the pressure drop due to the square expansion type of fitting as shown in Figure 3a, and when the water is flowing from the air chamber towards the access tunnel, we consider the pressure drop due to the square reduction type of fitting as shown in Figure 3b. Thus,  $F_\phi$  is calculated based on the generalized friction factors  $\phi_{se}$  for the square expansion type of fitting and  $\phi_{sr}$  for the square reduction type of fitting. Additionally, for both types of flows as shown in Figure 3, we assume an average cross-sectional area

$$\bar{A} = \frac{A + A_t}{2}.$$

If  $\Delta p_\phi$  is the pressure drop due to the fittings, there exists a relationship between  $\Delta p_\phi$ , the average kinetic energy of the fluid per volume  $K''' = \frac{1}{2}\rho v |v|$  and the friction factor  $\phi = \{\phi_{se}, \phi_{sr}\}$ . The relationship between  $\Delta p_\phi$ ,  $K'''$ , and  $\phi$  is given by

$$\Delta p_\phi = \phi K'''.$$

The pressure drop  $\Delta p_\phi$  is related to  $F_\phi$  through the average cross-sectional area  $\bar{A}$  and given as

$$F_\phi \approx \Delta p_\phi \bar{A}$$

which can be further expressed as

$$F_\phi \approx \frac{1}{2}\rho v |v| \bar{A} \phi, \quad \phi = \{\phi_{se}, \phi_{sr}\}.$$

The final expression for overall fluid frictional force  $F_f$  is then given as

$$F_f \approx \frac{1}{2}\rho v |v| \left( A_{w,w} \frac{f_{D,w}}{4} + A_{w,a} \frac{f_{D,a}}{4} + \bar{A} \phi \right) \quad \phi = \{\phi_{se}, \phi_{sr}\}. \quad (20)$$

This completes the expressions for variables  $m$ ,  $F_p$  and  $F_f$  for the two scenarios of the liquid level inside the surge tank, viz.,  $h \leq H_t$  and  $h > H_t$ . To further complete the information of variables in Equation (6), the expression for  $F_g^{\dot{V}}$  is calculated as

$$F_g^{\dot{V}} = mg \frac{H}{L}, \quad (21)$$

as shown in the flow diagram of Figure 1a. Finally, the mechanistic model of the ACST needs an expression for the average velocity  $v$  expressed as

$$v = \frac{\dot{V}}{\bar{A}}. \quad (22)$$

Equations (1)–(6), in addition to other associated algebraic relations from Equations (7)–(22), represent a semi-explicit DAEs formulation for the ACST, and can be modeled in an equation-based modeling language like Modelica. The developed mechanistic model of the ACST is implemented in OpenHPL as a feature extension, and the case study was carried out for Torpa HPP.

### 3. Case Study

Figure 4a shows the layout diagram of Torpa HPP. Similarly, Figure 4b shows the simulation model of Torpa HPP created in OpenHPL. In Figure 4b, the reservoir model, the intake tunnel model, the penstock model, and the discharge model are developed as in [21]. A detailed model of the penstock considering water compressibility and pipe elasticity can be formulated from [22]. However, we consider the penstock model as a simple pipe model. Similarly, the Francis turbine mechanistic model for the case study is modeled as in [23]. The mechanistic model for the tailrace is taken as an exact mirror replica of the reservoir model.

The dimensions of the ACST shown in Figure 4a are found based on the piezometric diagram for Torpa HPP from [10]. The model developed in Section 2 is based on a cylindrical access tunnel and a cylindrical air chamber. Thus, the hydraulic diameters for the access tunnel  $D_t$  and the air chamber  $D$  are evaluated based on the volume of air inside the chamber using the operating conditions. Table 1 shows the parameters and the operating conditions of the ACST for Torpa HPP.



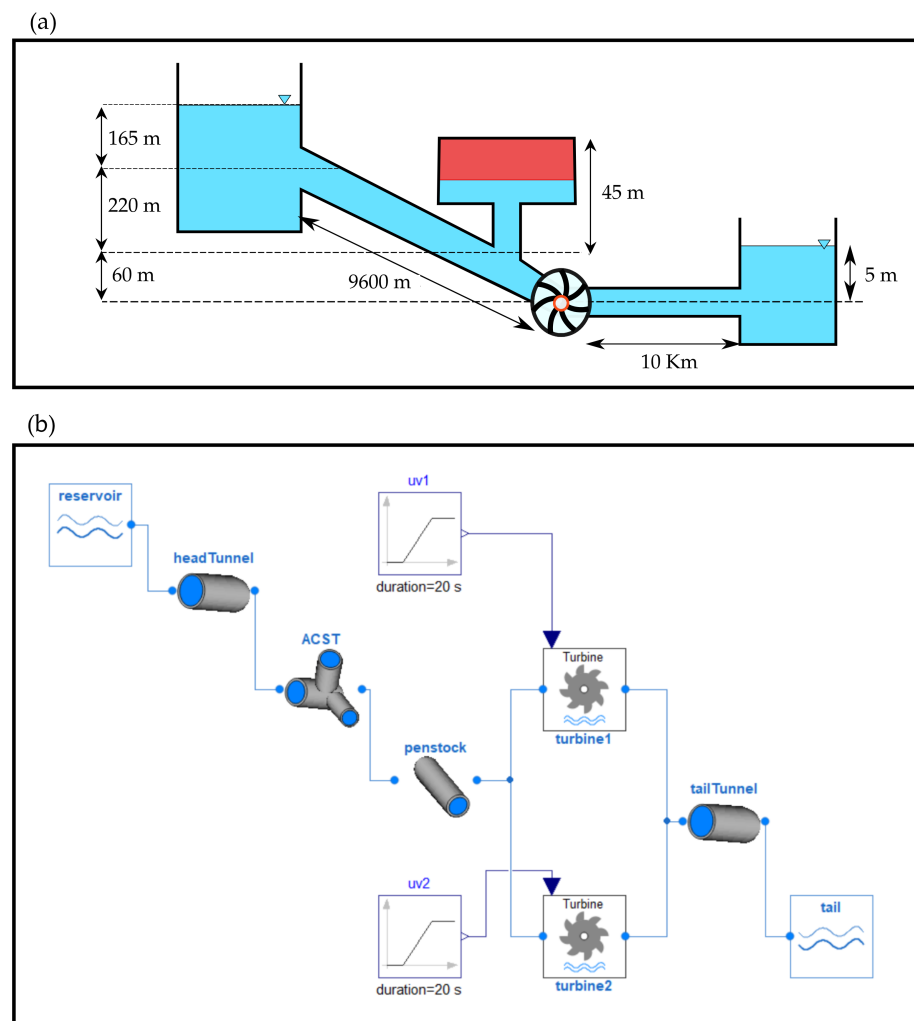


**Figure 4.** (a) Layout diagram for Torpa HPP. Nominal head, nominal discharge, and nominal power output are 445 m,  $40 \text{ m}^3/\text{s}$  and 150 MW, respectively. The ACST has air volume of  $13,000 \text{ m}^3$ , initially pressurized at  $41 \cdot 10^5 \text{ Pa}$ . Similarly, both of the headrace and tailrace tunnels are 7 m in diameter. Torpa HPP consists of two turbine units each rated at 75 MW with rated discharge at  $20 \text{ m}^3/\text{s}$ . Torpa HPP also consists of a tailrace surge tank not shown in the figure. (b) Simulation model of Torpa HPP implemented in OpenHPL from the head reservoir to the tail reservoir.

For the model created in Figure 4b, it is of interest to:

1. validate the model with the experimental data from [10],
2. simulate the model considering air friction inside the ACST, and
3. study the hydraulic behavior of the ACST at different load acceptances and rejections.

### 3.1. Simulation Versus Real Measurements

Figure 5 shows the simulated versus real measurement for Torpa HPP. As shown in Figure 4b,  $u_{v1}$  and  $u_{v2}$  are the turbine valve signals for the turbine unit-1 and the turbine unit-2, respectively, for controlling the volumetric discharge through the turbines. The input turbine valve signal for unit-1 is given by

$$u_{v1} = \begin{cases} 0.68 & 0 < t \leq 500 \text{ s} \\ \frac{0.68}{50}(t - 550) + 0.98 & 500 \text{ s} < t \leq 550 \text{ s} \\ 0.98 & 550 \text{ s} < t \leq 1200 \text{ s} \end{cases},$$

and the input turbine valve signal for unit-2 is given by,

$$u_{v2} = \begin{cases} 0.55 & 0 < t \leq 500 \text{ s} \\ \frac{0.55}{50}(t - 550) + 0.93 & 500 \text{ s} < t \leq 550 \text{ s} \\ 0.93 & 550 \text{ s} < t \leq 1200 \text{ s}. \end{cases}$$

For inputs  $u_{v1}$  and  $u_{v2}$ , the mechanical power outputs for the turbine unit-1 (Figure 5c) and the turbine unit-2 (Figure 5d), the turbines inlet pressure  $p_{tr}$  (Figure 5e), and the air pressure inside the surge tank  $p_c$  (Figure 5f) are recorded for 1200 s with the measurement samples taken at each second. The air pressure  $p_c$  is measured using the pressure sensor PARO scientific 8DP000-S with an error of less than 0.01% of full scale of 6 Mpa, the turbine inlet pressure  $p_{tr}$  is measured using the pressure sensor PARO scientific DIQ 73K with an error of less than 0.04% of full scale of 20 Mpa, and the measurements for the mechanical power outputs are provided by the plant owner from Torpa HPP. The information about Torpa HPP and its experimental procedures are taken from [24]. Figure 5 shows that the simulation corresponds well with the real measurements in the case of power productions from the turbines (Figure 5c,d). In the case of the turbine inlet pressure  $p_{tr}$  (Figure 5e) there is an steady-state error of 0.6 bar for  $0 < t \leq 500$  s. We believe that the steady-state error in  $p_{tr}$  for  $0 < t \leq 500$  s can be eradicated by the inclusion of detailed geometrical dimensions for the headrace tunnel. In this paper, the headrace tunnel is considered with a simple slanted pipe geometry as shown in Figure 4a. Similar steady-state error can be seen in the case of the height of water level inside the ACST  $h$  (Figure 5g) with negligible error of 0.05 m. In the case of air pressure inside the ACST  $p_c$ , the simulation and the measurement data are in good agreement. The measurement sampling rate in the case of water level  $h$ , air pressure  $p_c$ , and turbine power outputs are slower and oscillatory because the data are only recorded after a minimum change in the measured value, which may be the reason for the steady-state errors and phase difference between the simulation and measurements shown in Figure 5c,d,f,g. In addition, in Figure 5f,g for  $800 \text{ s} < t \leq 1200 \text{ s}$ , the simulated values have poorly damped oscillation while the measurement quickly reaches a steady value. The simulated and the experimental dynamics of the variables ( $p_c$  and  $h$ ) are not captured well because of the slower and oscillatory sampling rate of the sensors. The simulation and the real measurements are matched by manual tuning of pipe roughness height of the headrace tunnel ( $\varepsilon \approx 0.4 \text{ mm}$ ), hydraulic diameter of the access tunnel  $D_t \approx 15 \text{ m}$ , and hydraulic diameter of the air chamber  $D \approx 24 \text{ m}$ .

**Table 1.** Parameters and operating conditions of the ACST for Torpa HPP.

Quantity	Symbol	Value
Hydraulic diameter of the throat	$D_t$	15 m
Hydraulic diameter of the chamber	$D$	24 m
Length of the throat	$L_t$	29 m
Total height	$H$	50 m
Total length	$L$	58 m
Pipe roughness height	$\varepsilon$	0.9 mm
Total volume	—	$17 \cdot 10^3 \text{ m}^3$
Operating temperature	$T^\circ$	293 K
Adiabatic exponent for air at STP	$\gamma$	1.4
Molar mass of air at STP	$M_a$	$29 \cdot 10^{-3} \text{ kg mol}^{-1}$
Universal gas constant	$R$	$8.314 \text{ JK}^{-1} \text{ mol}^{-1}$
Initial pressure of air	$p_c(0) = p_{c0}$	$41 \cdot 10^5 \text{ Pa}$
Initial water level	$h(0) = h_{c0}$	27 m
Initial volume of air	$V_0$	$13 \cdot 10^3 \text{ m}^3$

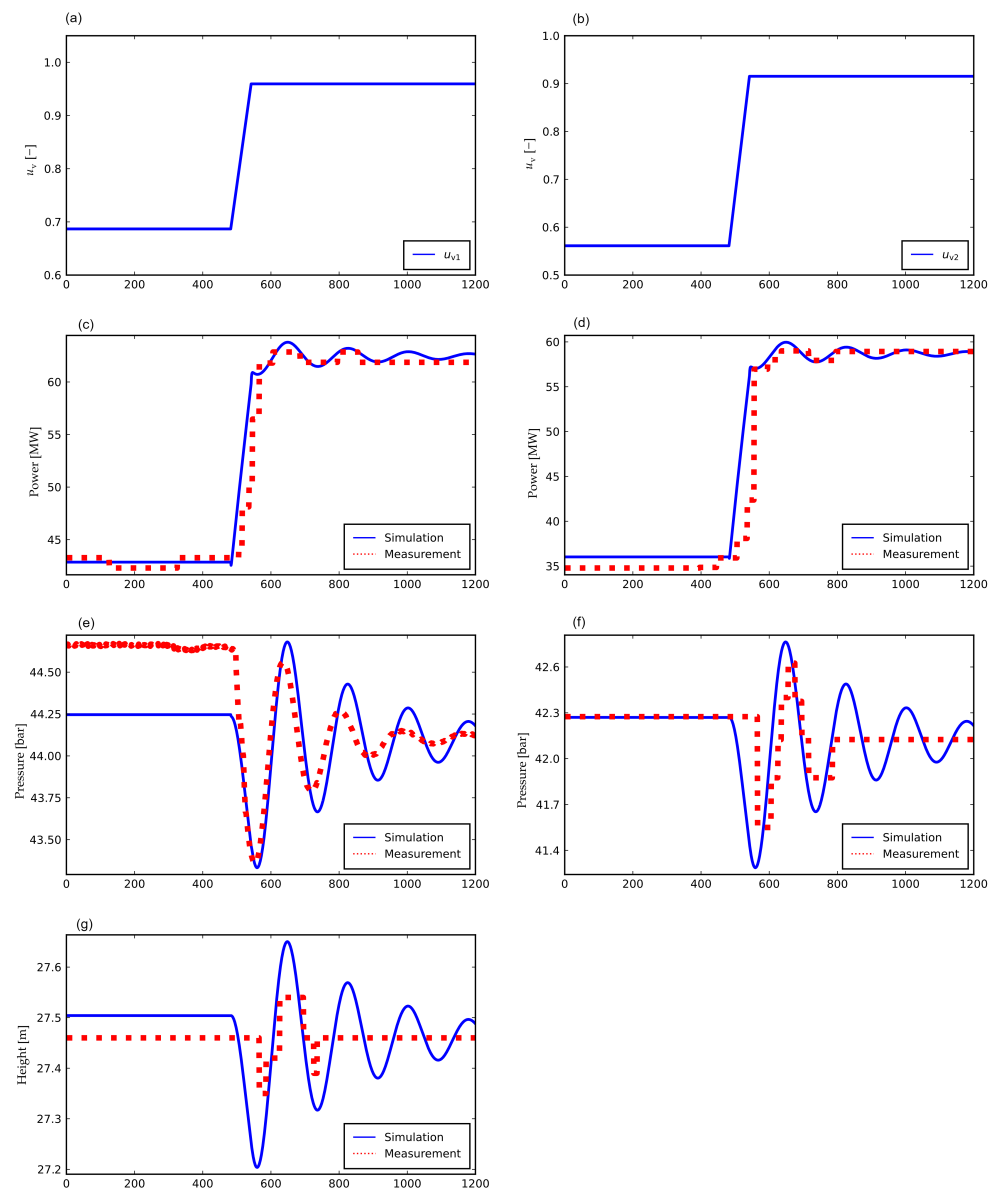


**Figure 5.** Simulation versus real measurements for Torpa HPP, (a) turbine valve signal for unit-1, (b) turbine valve signal for unit-2, (c) power output for unit-1, (d) power output for unit-2, (e) inlet pressure of the turbine units or the outlet pressure of the penstock, (f) air cushion pressure inside the ACST, and (g) height of water level inside the ACST.

### 3.2. Effect of Air Friction Inside ACST

We now consider Torpa HPP with each of the turbine units rated at 75 MW as a single entity, for simplification, with 150 MW with input  $u_v$  as the turbine valve signal. This simplification is made for studying the hydraulic behavior of the ACST in terms of the air friction inside the ACST, and the operation of Torpa HPP with respect to load acceptance and rejection (Section 3.3). Only simulated results will be presented in the sequel.

The air friction force  $F_{D,a}$  modeled using Darcy's friction factor  $f_D$  inside the ACST of Torpa HPP is considered using Equation (12) for the case of water level  $h \leq H_t$ , and using Equation (19) for the case of water level  $h > H_t$ . The input to the turbine with valve signal  $u_v$  for the simulation purpose is given by

$$u_v = \begin{cases} 0.5 & 0 < t \leq 500 \text{ s} \\ 0.95 & 500 \text{ s} < t \leq 1500 \text{ s} \end{cases}$$

where the hydro-turbine is loaded from half-load to nominal load at time  $t = 500$  s.

Figure 6 shows hydraulic behavior of the ACST for the turbine loading from 50% to 95%. Figure 6b–d show the water level  $h$  inside the ACST, the air cushion pressure  $p_c$ , and the inlet turbine pressure  $p_{tr}$ , respectively, for the ACST modeled with and without the air friction consideration. From Figure 6c, we see that the differences in air cushion pressure  $p_c$  for the ACST modeled with and without the air friction consideration is in the order of  $10^{-5}$  bar = 1 Pa, even for the turbine loaded from half load to the nominal operation. This is because of the fact that fluid frictional force  $F_f$  depends on Darcy's friction factor  $f_D$ , and  $f_D$  depends on Reynolds' number  $N_{Re} = \frac{\rho|v|D}{\mu}$  where  $\mu$  is the dynamic viscosity of the fluid. At STP,  $\mu_{air} = 1.81 \cdot 10^{-5}$  Pa · s and  $\mu_{water} = 8.90 \cdot 10^{-4}$  Pa · s which can be approximated as  $\mu_{water} \approx 100 \mu_{air}$ .

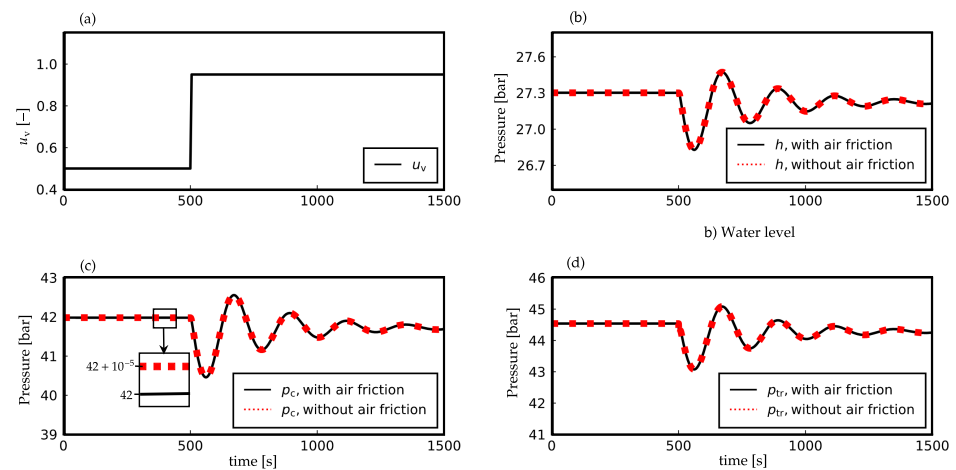


**Figure 6.** ACST model with and without frictional force due to the air inside ACST for Torpa HPP, (a) turbine valve signal  $u_v$ , (b) water level  $h$  inside ACST, (c) air cushion pressure  $p_c$ , and (d) turbine inlet pressure  $p_{tr}$ .

### 3.3. Operations of ACST in Load Acceptance and Rejection

Load acceptance and rejection are created by changing the turbine valve signal  $u_v$  from one operating condition to another operating condition, and are described in the sequel.

#### 3.3.1. Load Acceptances

We consider Torpa HPP running at *no load* condition for a time period of 500 s. At  $t = 500$  s, a different load acceptance condition is created by changing the turbine valve signal  $u_v$ , and the hydraulic behavior of the ACST is observed for the next 1500 s. The turbine valve signal  $u_v$  is generated as

$$u_v = \begin{cases} 0 & 0 < t \leq 500 \text{ s} \\ u_{va} & 500 \text{ s} < t \leq 2000 \text{ s} \end{cases}$$

where  $u_{va} \in \{0.25, 0.5, 0.75, 1.0\}$  for load acceptances of 25%, 50%, 75%, and 100%, respectively. For a total load acceptance (TLA) the load acceptance is 100%.

#### 3.3.2. Load Rejections

In contrast to the load acceptances, we now consider Torpa HPP running at *full load* condition for a time period of 500 s. At  $t = 500$  s, a different load rejection condition is

created by changing the turbine valve signal  $u_v$ , and the hydraulic behavior of the ACST is observed for the next 1500 s. The turbine valve signal  $u_v$  is generated as

$$u_v = \begin{cases} 1.0 & 0 < t \leq 500 \text{ s} \\ u_{vtr} & 500 \text{ s} < t \leq 2000 \text{ s} \end{cases}$$

where  $u_{vtr} \in \{0.75, 0.5, 0.25, 0.0\}$  for load rejections of 25%, 50%, 75%, and 100%, respectively. For a total load rejection (TLR), the load rejection is 100%.

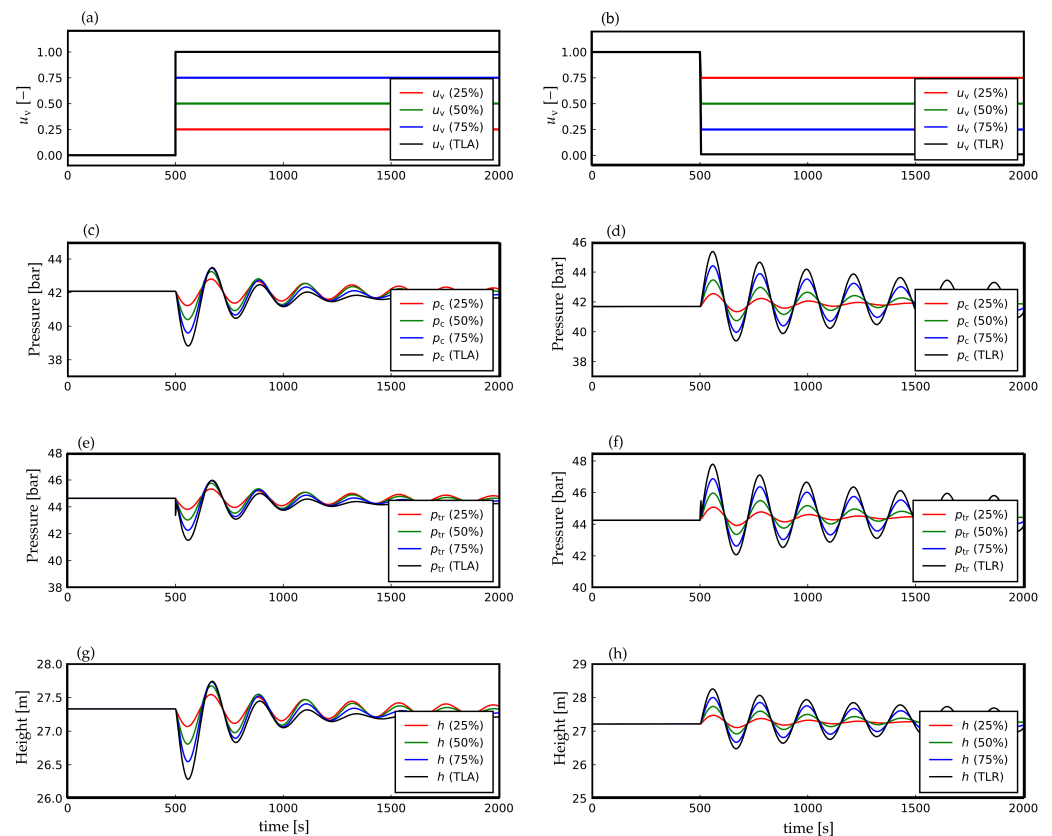
Figure 7 shows hydraulic performance of the ACST during load acceptances and rejections for Torpa HPP. Figure 7a,c,e,g shows the turbine valve signal  $u_v$ , the air pressure  $p_c$ , the turbine inlet pressure  $p_{tr}$  and the water level inside ACST  $h$ , respectively, for the different percentage change in the load acceptances. Similarly, Figure 7b,d,f,h shows  $u_v$ ,  $p_c$ ,  $p_{tr}$  and  $h$ , respectively, for the different percentage change in the load rejections.

Figure 7a shows the turbine valve signal generated for load acceptances of 25%, 50%, 75%, and 100%. Figure 7c, at  $t = 500$  s, shows that from the no load operation to TLA, the difference in the air pressure  $p_c$  inside the ACST is around 4 bar. Similarly, Figure 7e shows that the difference in turbine inlet pressure  $p_{tr}$  is around 3 bar, and Figure 7e shows that the difference in the water level  $h$  inside the ACST is around 1 m. In addition, Figure 7c shows that the difference in  $p_c$  from no load operation to 25% load acceptance, 50% load acceptance and 75% load acceptance are around 1 bar, 2 bar and 3 bar, respectively. Similarly, results can be obtained for  $p_{tr}$  (Figure 7e) and  $h$  (Figure 7g). For  $p_c$ ,  $p_{tr}$  and  $h$  oscillation dies out as the time progresses for  $t > 500$  s.

Figure 7b shows the turbine valve signal generated for load rejections of 25%, 50%, 75%, and 100%. Figure 7d, at  $t = 500$  s, shows that from full load operation to TLR, the difference in  $p_c$  is around 4 bar as similar in the case of TLA. Similarly, the difference is around 3 bar in the case of  $p_{tr}$ , as shown in Figure 7f. The difference in  $h$  from full load operation to TLR is also 1 m, as in the case of TLA. Similarly, from Figure 7d, the difference in  $p_c$  from full load operation to load rejections of 25%, 50% and 75% are around 1 bar, 2 bar and 3 bar, respectively. Similar results can be obtained for  $p_{tr}$  (Figure 7f) and  $h$  (Figure 7h). For  $p_c$ ,  $p_{tr}$  and  $h$ , oscillation dies out for  $t > 500$  s, similar to the case of load acceptances. However, the oscillation dies out sooner in the case of TLA than TLR.

### 3.3.3. ACST as a Flexible Hydro Power

The results for Figure 7 show hydraulic behavior of the ACST in the case of load acceptance and rejection. The difference in the water level is around 1 m for both TLA and TLR. Similarly, the difference in the air pressure is around 4 bar for both TLA and TLR. Referring to the results on the hydraulic performance of the ACST from Section 3.3 and the study carried out for different types of open surge tanks in [6] clearly indicates that ACST has a robust performance on suppressing water mass oscillation and water hammer pressure during a higher percentage of load acceptances and rejections, unlike different types of open surge tanks. Since one of the prominent requirements of a flexible hydro power plant is to have a robust operation under various load acceptances and rejections, a hydro power plant operated with ACST makes it a potential candidate for participating in the concept of flexible hydro power.



**Figure 7.** Hydraulic performance of the ACST for Torpa HPP for the different percentage change in the load acceptances and the load rejections, (a) turbine valve signal  $u_v$  as an input to the load acceptances, (b) turbine valve signal  $u_v$  as an input to the load rejections, (c) air pressure  $p_c$  for the load acceptances, (d) air pressure  $p_c$  for the load rejections, (e) turbine inlet pressure  $p_{tr}$  for the load acceptances, (f) turbine inlet pressure  $p_{tr}$  for the load rejections, (g) water level inside the ACST  $h$  for the load acceptances, and (h) water level inside the ACST for the load rejections.

#### 4. Conclusions and Future Work

A mechanistic model of an ACST has been developed considering an access tunnel connected to an air chamber. The difference in diameters of the access tunnel and the air chamber has been taken into consideration. The model is further enhanced with the inclusion of Darcy's friction force for air inside the ACST. Model fitting is done for the 150 MW Torpa HPP. The experimental data and the model simulation were matched by manual tuning of pipe roughness height of the headrace tunnel, and hydraulic diameters of the access tunnel and the air chamber of the ACST. Apart from the model fitting, simulation results show that the effect of air friction inside the ACST is negligible as compared to water friction. The simulation studies carried out for load acceptance and rejection show the robust hydraulic behaviors of the ACST in terms of suppressing water mass oscillation and water hammer pressure, which indicate that a hydro power plant with ACST makes it a potential candidate for flexible hydro power in case of an energy-mix (intermittent and dispatchable sources) interconnected power grid.

Future work includes the study of the hydraulic behavior of ACST in interconnected grids supplied with intermittent generation. In addition, the model for ACST can be improved using Lagrangian computational fluid dynamics. For the Lagrangian approach, the meshless discretization technique smoothed particle hydrodynamics (SPH) can be used to handle coupling between the free water surface and air inside the ACST [25,26].

**Author Contributions:** Conceptualization, M.P., K.V., R.S. and B.L.; methodology, M.P., R.S. and B.L.; software, M.P. and D.W.; validation, M.P., K.V. and B.L.; formal analysis, M.P.; investigation, M.P.; resources, M.P., D.W. and K.V.; writing—original draft preparation, M.P.; writing—review and editing, M.P.; visualization, M.P. and B.L.; supervision, D.W., K.V. and B.L. All authors have read and agreed to the published version of the manuscript.

**Funding:** This research received no external funding.

**Institutional Review Board Statement:** Not applicable.

**Informed Consent Statement:** Not applicable.

**Data Availability Statement:** Not applicable.

**Acknowledgments:** Help and discussions with Liubomyr Vytvytsky, ABB Oslo, regarding model tuning is gratefully acknowledged.

**Conflicts of Interest:** The authors declare no conflict of interest.

## References

- Pandey, M.; Winkler, D.; Sharma, R.; Lie, B. Using MPC to Balance Intermittent Wind and Solar Power with Hydro Power in Microgrids. *Energies* **2021**, *14*, 874. [[CrossRef](#)]
- Pandey, M.; Lie, B. The Role of Hydropower Simulation in Smart Energy Systems. In Proceedings of the 2020 IEEE 7th International Conference on Energy Smart Systems (ESS), Kyiv, Ukraine, 12–14 May 2020; pp. 392–397.
- Charmasson, J.; Belsnes, M.; Andersen, O.; Eloranta, A.; Graabak, I.; Korpås, M.; Helland, I.; Sundt, H.; Wolfgang, O. *Roadmap for Large-Scale Balancing and Energy Storage from Norwegian Hydropower: Opportunities, Challenges and Needs until 2050*; SINTEF Energi AS: Trondheim, Norway, 2018.
- Huertas-Hernando, D.; Farahmand, H.; Holttinen, H.; Kiviluoma, J.; Rinne, E.; Söder, L.; Milligan, M.; Ibanez, E.; Martínez, S.M.; Gomez-Lazaro, E.; et al. Hydro power flexibility for power systems with variable renewable energy sources: An IEA Task 25 collaboration. *Wiley Interdiscip. Rev. Energy Environ.* **2017**, *6*, e220. [[CrossRef](#)]
- Graabak, I.; Korpås, M.; Jaehnert, S.; Belsnes, M. Balancing future variable wind and solar power production in Central-West Europe with Norwegian hydropower. *Energy* **2019**, *168*, 870–882. [[CrossRef](#)]
- Pandey, M.; Lie, B. The influence of surge tanks on the water hammer effect at different hydro power discharge rates. In Proceedings of the SIMS 2020, Oulu, Finland, 22–24 September 2020; Linköping University Electronic Press: Linköping, Sweden, 2020; pp. 125–130.
- Vereide, K.; Richter, W.; Zenz, G.; Lia, L. Surge Tank Research in Austria and Norway. *Wasserwirtschaft* **2015**, *1*, 58–62. [[CrossRef](#)]
- Vereide, K.; Lia, L.; Nielsen, T. Physical modelling of hydropower waterway with air cushion surge chamber. In Proceedings of the 5th International Symposium on Hydraulic Structures, Brisbane, Australia, 25–27 June 2014.
- Pandey, M.; Lie, B. Mechanistic modeling of different types of surge tanks and draft tubes for hydropower plants. In Proceedings of the SIMS 2020, Oulu, Finland, 22–24 September 2020; Linköping University Electronic Press: Linköping, Sweden, 2020; pp. 131–138.
- Vereide, K.; Lia, L.; Nielsen, T.K. Hydraulic scale modelling and thermodynamics of mass oscillations in closed surge tanks. *J. Hydraul. Res.* **2015**, *53*, 519–524. [[CrossRef](#)]
- Mosonyi, E. *Water Power Development: High-Head Power Plants*; Akadémiai kiadó: Budapest, Hungary, 1965; Volume 2.
- Pickford, J. *Analysis of Water Surge*; Taylor & Francis: Abingdon, UK, 1969.
- Jaeger, C. Present trends in surge tank design. *Proc. Inst. Mech. Eng.* **1954**, *168*, 91–124. [[CrossRef](#)]
- Guo, J.; Woldeyesus, K.; Zhang, J.; Ju, X. Time evolution of water surface oscillations in surge tanks. *J. Hydraul. Res.* **2017**, *55*, 657–667. [[CrossRef](#)]
- Lydersen, A. *Fluid Flow and Heat Transfer*; John Wiley & Sons Incorporated: Hoboken, NJ, USA, 1979.
- Vereide, K.V. *Hydraulics and Thermodynamics of Closed Surge Tanks for Hydropower Plants*. Ph.D. Thesis, NTNU, Trondheim, Norway, 2016.
- Wang, C.; Yang, J.; Nilsson, H. Simulation of water level fluctuations in a hydraulic system using a coupled liquid-gas model. *Water* **2015**, *7*, 4446–4476. [[CrossRef](#)]
- Yulong, L. Studies on gas loss of air cushion surge chamber based on gas seepage theory. In Proceedings of the 2011 International Conference on Electric Technology and Civil Engineering (ICETCE), Lushan, China, 22–24 April 2011; pp. 723–725.
- Ou, C.; Liu, D.; Li, L. Research on dynamic properties of long pipeline monitoring system of air cushion surge chamber. In Proceedings of the 2009 Asia-Pacific Power and Energy Engineering Conference, Wuhan, China, 27–31 March 2009; pp. 1–4.
- Yang, X.L.; Kung, C.S. Stability of air-cushion surge tanks with throttling. *J. Hydraul. Res.* **1992**, *30*, 835–850. [[CrossRef](#)]
- Vytvytskyi, L. *User's Guide for the Open Hydropower Library (OpenHPL)*; University of South-Eastern Norway, Porsgrunn, Norway, 2019.



22. Vytvytsky, L.; Lie, B. Comparison of elastic vs. inelastic penstock model using OpenModelica. In Proceedings of the 58th Conference on Simulation and Modelling (SIMS 58), Reykjavik, Iceland, 25–27 September 2017; Linköping University Electronic Press: Linköping, Sweden, 2017; Volume 138, pp. 20–28. [[CrossRef](#)]
23. Vytvytskyi, L.; Lie, B. Mechanistic model for Francis turbines in OpenModelica. *IFAC-PapersOnLine* **2018**, *51*, 103–108. [[CrossRef](#)]
24. Vereide, K.; Svingen, B.; Nielsen, T.K.; Lia, L. The effect of surge tank throttling on governor stability, power control, and hydraulic transients in hydropower plants. *IEEE Trans. Energy Convers.* **2016**, *32*, 91–98. [[CrossRef](#)]
25. Rakhsha, M.; Kees, C.E.; Negrut, D. Lagrangian vs. Eulerian: An analysis of two solution methods for free-surface flows and fluid solid interaction problems. *Fluids* **2021**, *6*, 460. [[CrossRef](#)]
26. Bimbato, A.M.; Alcântara Pereira, L.A.; Hirata, M.H. Study of surface roughness effect on a bluff body—The formation of asymmetric separation bubbles. *Energies* **2020**, *13*, 6094. [[CrossRef](#)]





## Appendix C

# The influence of surge tanks on the water hammer effect at different hydro power discharge rates

Madhusudhan Pandey (M.P.) and Bernt Lie (B.L.)

Published in: *Proceedings of SIMS 2020 Virtual, Finland, 22-24 September 2020*. Linköping University Electronic Press, 2020, pp. 125-130.

<https://doi.org/10.3384/ecp20176125>

Author Contributions: Conceptualization, M.P.; methodology, M.P. and B.L.; software, M.P.; validation, M.P. and B.L.; formal analysis, M.P.; investigation, M.P.; resources, M.P. and B.L.; writing—original draft preparation, M.P.; writing—review and editing, M.P.; visualization, M.P. and B.L.; supervision, B.L.



# The influence of surge tanks on the water hammer effect at different hydro power discharge rates

Madhusudhan Pandey, Bernt Lie

TMCC, University of South-Eastern Norway, Bernt.Lie@usn.no

## Abstract

This paper provides an overview of different types of surge tanks used in hydropower systems. The water mass oscillation inside the simple, sharp orifice type, throttle valve, and air-cushion surge tanks are studied. It is found that the diameter of the sharp orifice and the throat plays an important role in obstructing water mass flowing inside the surge tank which consequences to reduce the effect of water hammer over times in the pressure tunnels. Sharp orifice type surge tanks are more efficient to reduce the allowed maximum height of surge tank for avoiding water spilling out of the surge tank during the total load rejection from the prime movers. However, throttle valve surge tanks are more efficient for decaying of pressure surges sooner. It is also found that the difference-amplitude of water mass oscillation inside the air-cushion surge tank is insignificant. Conclusions are drawn based on the case study of Trollheim and Torpa hydroelectric plants in Norway.

*Keywords: water mass oscillation, surge tanks throttling, sharp orifice type surge tank, air-cushion surge tank, throttle valve surge tank, water hammer*

## 1 Introduction

### 1.1 Background

A high-head reaction-turbine hydro power system basically consists of an intake tunnel via a high-pressure steep penstock tunnel to the reaction turbines (eg., Francis turbine). A surge tank is usually placed between the intake pressure tunnel and the penstock. In case of a load rejection<sup>1</sup>, the turbine valve is rapidly positioned for a required volumetric flow (discharge) of water through the turbine. During rapid closing of the turbine valve, the water masses flowing in the intake tunnel and in the penstock are suddenly decelerated. A high-pressure region is created at the lower end of the penstock because of the obstructed water-inertia<sup>2</sup> which causes pressure waves to travel in the up-

<sup>1</sup>Load rejection is simply a phenomenon where load connected to a prime mover, for eg., Francis turbine, is suddenly disconnected or decreased. However, in case of a load acceptance, a load is connected to the prime mover. A load is anything which is operated with the help of prime mover. For a hydroelectric plant, loads are electrical units connected through the grid in an interconnected electrical network.

<sup>2</sup>The obstructed water mass flowing through the pressure tunnel is generally called as water inertia.

ward direction<sup>3</sup>. The magnitude of the travelled pressure wave after sudden closure of the turbine valve is termed as a *water hammer*. The energy of the pressure wave is released at the nearest low-pressure free water surface, i.e., at the surge tank placed between the intake tunnel and penstock (Mosonyi, 1991, p. 129).

In this regard, it is of interest to see the effect of the water hammer at different discharges through the turbine during the load acceptance or rejection. The water inside the surge tank oscillates after the energy from the pressure wave is released at the free water surface inside the surge tank. The oscillation of water mass lasts until the pressure wave energy is fully dissipated. The design height and length of the surge tank should thus depend on the amplitude of the pressure wave, i.e., the water hammer. The amplitude of water mass oscillation inside the surge tank can be decreased using water flow-obstruction in the inlet of the surge tank, eg., in case of throttle valve surge tank and sharp orifice type surge tank (Aronovich et al., 1970). Similarly, energy from the pressure wave can be dissipated using pressurized air inside a closed surge tank, usually referred to as an air-cushion surge tank (Vereide et al., 2014). This paper will mainly focus on the simulated response at different discharge for *manifold pressure*<sup>4</sup>, velocity, mass flow rate and water mass oscillation inside the different kinds of surge tanks.

### 1.2 Previous studies

A detailed overview of the time evolution of water mass oscillation inside a surge tank is given in (Guo et al., 2017) with differential equations governing the oscillation phenomenon. Similarly, a law governing oscillation phenomenon inside the simple surge tank is explored in (Travaš, 2014). The water mass oscillation control analysis using a self-adaptive auxiliary control system in the surge tank has been done in (Wan et al., 2019). The solution of water mass oscillation mathematical equations has been done using the finite element method in (Wan et al., 2019).

<sup>3</sup>The pressure wave traveled from higher pressure to lower pressure region and dissipated near to free water surface.

<sup>4</sup>It is a bottom pressure point of the surge tank where the outlet of the intake tunnel and inlet of a steep penstock meet.

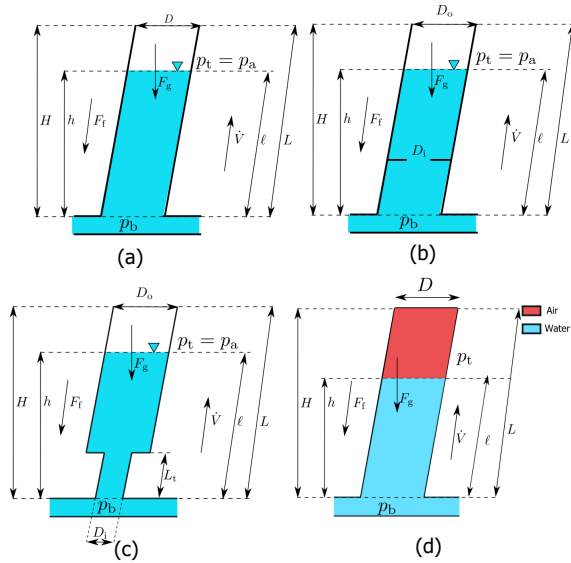


**Figure 1.** Different types of surge tanks. (a) Simple surge tank without hydraulic resistance. (b) Sharp orifice type surge tank with hydraulic resistance of horizontal bars forming an orifice of a diameter  $D_i$ . (c) Throttle valve surge tank with hydraulic resistance of diameter  $D_i$  at the entry of surge tank with square expansion from diameter  $D_i$  to diameter  $D_o$ . The length of the throat is  $L_t$ . (d) Air-cushion surge tank filled with air at pressure  $p_t$  and diameter  $D$ .

### 1.3 Outline of the paper

The paper is organized by providing a brief introduction to different types of surge tanks and their operation in Section 2. Section 3 provides the simulated responses for Trollheim and Torpa hydro power plants with different types of surge tanks at different discharges. Results and discussions are provided in Section 4 while conclusions and future works are explained in Section 5.

## 2 Surge tanks and their operation

A detailed mechanistic model of simple, sharp orifice type, throttle valve, and air-cushion surge tank are articulated in (Pandey and Lie, 2020, Submitted) for a Modelica<sup>5</sup> based hydro power library- OpenHPL<sup>6</sup>. OpenHPL is an open-source hydropower library consisting of models for hydropower components that are developed based on mass and 1D momentum balance. It consists of mechanistic models for the flow of water in filled pipes (inelastic and elastic walls, incompressible and compressible water), a mechanistic model of a Francis turbine (including design of turbine parameters), friction models, etc.

The different types of surge tanks are shown in Figure 1. For a simple surge tank shown in Figure 1 (a), during the load acceptance/rejection, a high-pressure region is created at the end of the penstock and at the end of the turbine. The high pressure region thus creates pressure wave which traveled through the penstock releasing pres-

sure wave energy by the means of water mass oscillation inside the surge tank. The height and length of surge tank thus depends on the water mass oscillation inside the surge tank. For a simple surge tank, the maximum height of surge tank would be sum of piezometric height from surge tank bottom to reservoir surface and the highest amplitude of water mass oscillation during a *total load rejection*<sup>7</sup>.

If the height of surge tank is not practically possible then other surge tanks with hydraulic resistances like horizontal bars forming a sharp orifice as in sharp orifice type surge tank or a throat in the entry of surge tank as in throttle valve surge tank can be used. Figure 1 (b) shows a sharp orifice type surge tank with orifice diameter  $D_i$  which obstructs water mass moving from the base of surge tank towards the free water surface inside the surge tank. This will cause the oscillation of water mass to dies out sooner than in the simple case. Similarly, the highest amplitude of water mass oscillation is decreased which decreases the practical height of the surge tank. The throat with diameter  $D_t$  and length  $L_t$ , in case of the throttle valve surge tank as shown in Figure 1 (c), has the same operation as that of sharp orifice type surge tank. Figure 1 (d) shows air-cushion surge tank.

## 3 Simulated Responses

### 3.1 Case study: Trollheim HPP

The case study for the simulated responses for different types of surge tanks at different discharge rates is studied for Trollheim and Torpa hydro power plant. The general layout diagram is shown in Figure 2.

#### 3.1.1 Total Load Rejection (TLR)

First, we consider a case of a simple surge tank for Trollheim Hydro Power Plant (HPP) for a layout shown in Figure 2 (a) Trollheim HPP for a total load rejection. Assuming frictionless intake pressure tunnel and ideal gate valve for turbine (i.e., time of opening and closure of the gate valve is *zero*), the maximum allowable height of a simple surge tank for restriction of water-spilling from surge tank is given by the expression as in Eq. 1,

$$H_{ST} = H_{res} + H_{in} + Y_{max}, \quad (1)$$

where  $Y_{max}$  is the maximum surge or maximum water mass oscillation height during total load rejection (Mosonyi, 1991, p. 162) given as in 2,

$$Y_{max} = \frac{\dot{V}_n}{A_{in}} \sqrt{\frac{L_{in}}{g} \left( \frac{A_{in}}{A_{ST}} \right)}, \quad (2)$$

where  $H_{ST}$ ,  $H_{in}$ , and  $H_{res}$  are height difference for surge tank, intake and reservoir, respectively.  $A_{in}$  and  $L_{in}$  are

<sup>7</sup>A total load rejection is a phenomenon where a hydroelectric plant running with full discharge through the turbine is completely shutdown. The turbine valve signal is instantaneously changed from full opening to full closed.

<sup>5</sup><https://www.modelica.org>

<sup>6</sup><https://github.com/simulatio/OpenHPL>

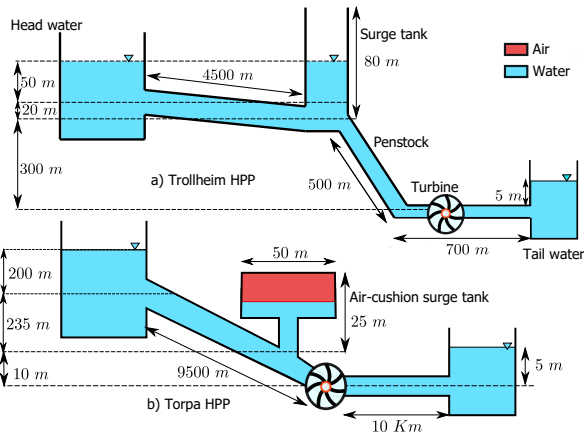


**Figure 2.** Layout diagram for Trollheim (Vytyvtskiy and Lie, 2019) and Torpa Hydro Power Plant (HPP) (Vereide et al., 2014). Nominal head, nominal discharge, and nominal power output are 370m, 40m<sup>3</sup>/s and 130MW for Trollheim HPP, and 445m, 35m<sup>3</sup>/s and 150MW for Torpa HPP. Torpa HPP has two turbine units each having nominal power output of 75MW. The air-cushion surge tank for Torpa HPP has air volume of 13,000m<sup>3</sup> initially pressurized at 4.1Mpa. For Trollheim HPP, the diameter for both of the penstock and the surge tank is 4m while for both of the headrace and the tailrace tunnel is 6m. Similarly, for Torpa HPP, the diameter of both of the headrace and the tailrace tunnel is 7m.

cross-sectional area and length of intake pressure tunnel, respectively.  $\dot{V}_n$  is the nominal discharge with  $g$  as the acceleration due to gravity. From Figure 2 (a) Trollheim HPP we have  $H_{res} = 50m$ ,  $H_{in} = 20m$  and  $Y_{max}$  is calculated using expression Eq. 2 as 45m. Thus, the height of surge tank for avoiding water spilling out for a simple surge tank for Trollheim HPP during total load rejection is 115m.

Figure 3 shows the turbine valve signal creating a total load rejection at 1500s and plots of water mass oscillation for simple, sharp orifice type and throttle valve surge tank. It shows that hydraulic resistances in case of sharp orifice type and throttle valve surge tank dampens out the mass oscillation sooner than that of the simple surge tank and the maximum allowed height of surge tank  $H_{ST}$  for avoiding water spilling out of surge tank is less for sharp orifice type surge tank during TLR.

**3.1.2 Effect of diameter of orifice and throat for TLR**

The maximum allowed height of sharp orifice type and throttle valve surge tank for avoiding water spilling through the surge tank can be decreased based on decreasing diameter of orifice and throat as shown in Figure 4.

**3.1.3 Total Load Acceptance (TLA)**

A case of a total load acceptance is created using turbine guide valve control signal  $u_v = \begin{cases} 0.01 & 0 < t \leq 200 \text{ s} \\ 1 & t > 200 \text{ s} \end{cases}$  at time 200s for Trollheim HPP. The simulated response for water mass oscillation for simple, sharp orifice and throttle

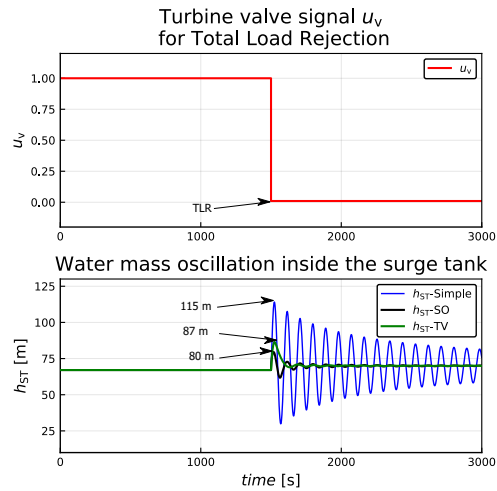


**Figure 3.** Water mass oscillation inside the surge tank for Trollheim HPP. A total load rejection is created using control signal  $u_v = \begin{cases} 1 & 0 < t \leq 1500 \text{ s} \\ 0.01 & t > 1500 \text{ s} \end{cases}$  at time 1500s. In the figure, TLR represents total load rejection, SO and TV depicts sharp orifice type and throttle valve surge tank. The maximum amplitude of water mass oscillation  $h_{ST}$  is 115m at around 1500s for simple surge tank. While for sharp orifice type and throttle valve surge tank it is 80m and 87m, respectively. The diameter of orifice for sharp orifice type surge tank  $D_{so}$  and that of throat for throttle valve surge tank  $D_t$  are both 1m. The length of throat for throttle valve surge tank is 20m.

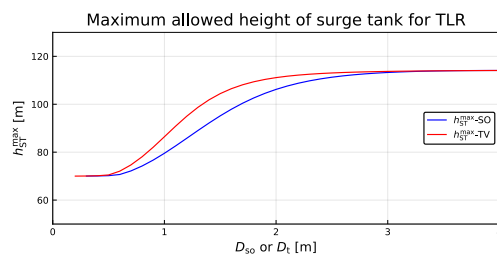


**Figure 4.** Maximum allowed height of surge tank for different diameter of sharp orifice (SO) type and throttle valve (TV) surge tank.  $h_{ST}^{max}$  represent the maximum amplitude of water mass oscillation during TLR. As the diameter of hydraulic resistances like sharp orifice or throat at the entry of the surge tank is decreased the maximum height of water mass oscillation decreased. For example when  $D_t$  and  $D_{so}$  both are 1m,  $h_{ST}^{max}$  for sharp orifice type surge tank is 80m and for throttle valve surge tank is 87m.

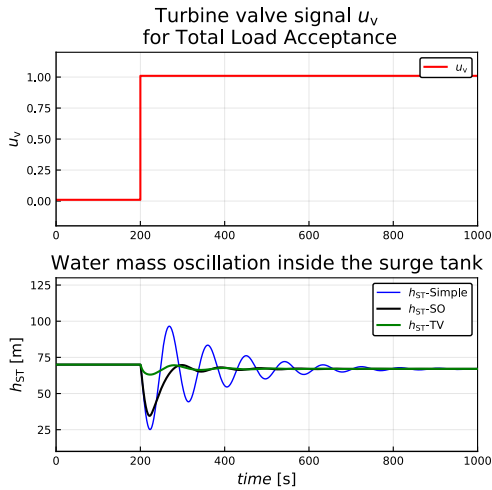


**Figure 5.** Water mass oscillation inside the surge tanks for TLA. The oscillation dies out soon in case of both sharp orifice and throttle valve surge tank.

valve surge tank is shown in Figure 5.

**3.1.4 Partial Load Rejection (PLR)**

Partial load rejections and acceptances can be created by changing the turbine’s gate signal.

For a 25 % load rejections while the hydropower plant is running at total load the turbine gate signal is generated as,

$$u_v = \begin{cases} 1 & 0 < t \leq 200 \text{ s} \\ 0.75 & t > 200 \text{ s} \end{cases},$$

where the plant is running at total load up to 200 s and with partial load (75 %) after 200 s.

Similarly, for a 50 % load rejection the turbine’s gate signal is generated as,

$$u_v = \begin{cases} 1 & 0 < t \leq 200 \text{ s} \\ 0.50 & t > 200 \text{ s} \end{cases},$$

and for for a 75 % load rejection,

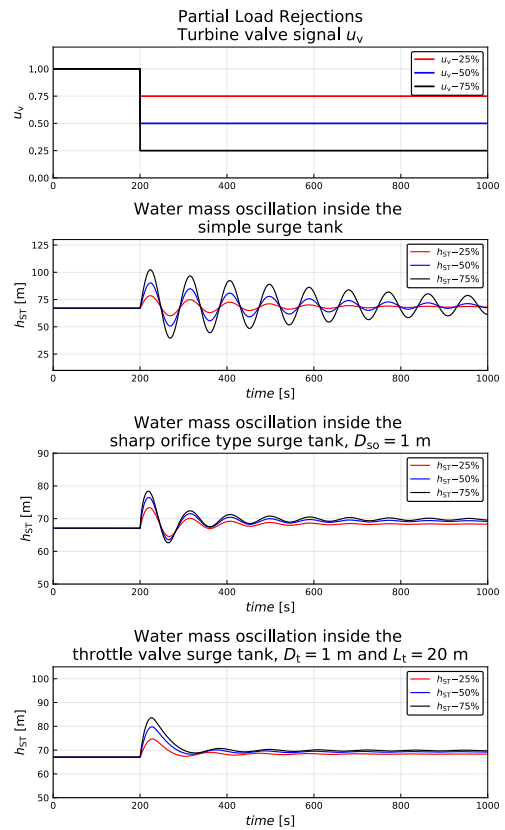
$$u_v = \begin{cases} 1 & 0 < t \leq 200 \text{ s} \\ 0.25 & t > 200 \text{ s} \end{cases}.$$

Figure 6 shows water mass oscillation inside the simple, sharp orifice and throttle valve surge tank during the partial load rejections.

**3.1.5 Partial Load Acceptance (PLA)**

For a 25 % load acceptance while the hydropower plant is running at no load condition, the turbine gate signal is generated as,

$$u_v = \begin{cases} 0 & 0 < t \leq 200 \text{ s} \\ 0.25 & t > 200 \text{ s} \end{cases},$$



**Figure 6.** Water mass oscillation inside the surge tanks for PLR. In the figure,  $u_v - 25\%$  represents the gate signal for a partial load rejection of 25% of the total load capacity of the plant. Similarly,  $h_{ST} - 25\%$  represents water mass oscillation for a load rejection of 25%.

where as for a 50 % load acceptance,

$$u_v = \begin{cases} 0 & 0 < t \leq 200 \text{ s} \\ 0.50 & t > 200 \text{ s} \end{cases},$$

and for a 75 % load acceptance,

$$u_v = \begin{cases} 0 & 0 < t \leq 200 \text{ s} \\ 0.75 & t > 200 \text{ s} \end{cases}.$$

Figure 7 shows water mass oscillation inside the simple, sharp orifice and throttle valve surge tank during the partial load rejections.

**3.2 Case study: Torpa HPP**

The water mass oscillation and the air pressure inside the air-cushion surge tank during load rejections and acceptance for Torpa HPP is shown in Figure 8 and 9, respectively.

**4 Results, and Discussions**

For Trollheim HPP, from Figure 3 in case of a TLR, the maximum allowed height of the surge tank for restriction of water spilling out of a simple surge tank is 115 m. Similarly, for sharp orifice type surge tank it is 80mand for

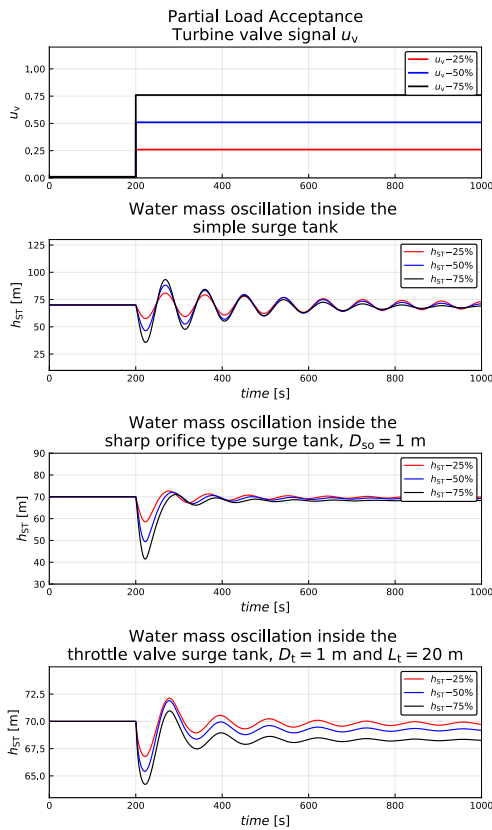


**Figure 7.** Water mass oscillation inside the surge tanks for PLA. In the figure,  $u_v - 25\%$  represents the gate signal for a partial load acceptance of 25% of the total load capacity of the plant. Similarly,  $h_{ST} - 25\%$  represents water mass oscillation for a load acceptance of 25% from a no load condition.

throttle valve surge tank it is 87 m. From Figure 4 it can be seen that the maximum allowed height of surge tank in case of a total load rejection is decreased as the diameter of sharp orifice and diameter of the throat is decreased. For a surge tank of diameter 4 m, in case of Trollheim HPP, the maximum allowed height of the simple surge tank,  $h_{ST}^{\max}$  during TLR is same for sharp orifice type surge tank with  $D_{so} \in [3, 4]$ , however,  $h_{ST}^{\max}$  decreases as  $D_{so} \in [0.5, 3)$ . Similarly, in case of throttle valve surge tank  $h_{ST}^{\max}$  is same for  $D_t \in [2, 4]$  and simple surge tank, however,  $h_{ST}^{\max}$  decreases as  $D_t \in [0.1, 2)$ .

For Torpa HPP, from Figure 8 and 9 in case of load rejections and acceptance, respectively, manifold pressure inside the surge tank does not vary much in case of load acceptance than in case of rejections.

## 5 Conclusions

The maximum allowed height of a simple surge tank, considering the TLR operation of the plant, can be decreased using a suitable diameter of the sharp orifice in case of a sharp orifice type surge tank and with a throttle valve surge tank with suitable diameter of the throat. The maximum allowed height of the surge tank is lowest in case of sharp orifice type surge tank, however, the mass oscillation dies

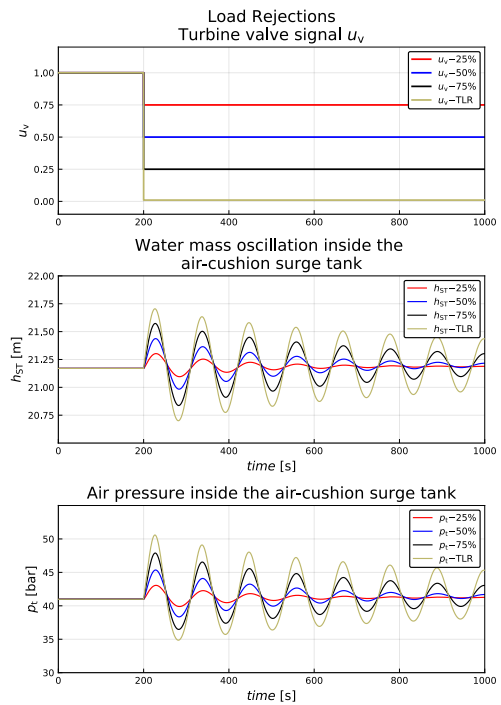


**Figure 8.** Water mass oscillation and air pressure inside the air cushion surge tank for load rejections. In figure, TLR represents a total load rejection.

out soon in case of throttle valve surge tank with an inference that impact of water hammer in the pressure tunnel is less in case of throttle valve surge tank.

In the case of a sharp orifice type surge tank, the maximum allowed height of the surge tank in comparison with a simple surge tank decreases exponentially for  $D_{so} \leq 0.5 \cdot D$  where  $D$  and  $D_{so}$  are the diameter of the simple surge tank and the diameter of the sharp orifice. Similarly, for throttle valve surge tank  $D_t \leq 0.375 \cdot D$  where  $D_t$  is the diameter of the throat. Both for load rejections and acceptance, mass oscillation inside the surge tank dies sooner in case of a throttle valve surge tank. The frequency of water mass oscillation in the case of a simple surge tank is the same for both load rejections and acceptance.

For the air-cushion surge tank, water mass oscillation inside the surge tank is insignificant for both load acceptance and rejections. The varying of air pressure inside the surge tank for partial load rejections is greater than that for the partial load acceptance.

## References

- Grigorii Vladimirovich Aronovich, Nikolai Archilovich Kartvelishvili, and Ya K Lyubimtsev. Water hammer and surge tanks. Technical report, Israel program for scientific translations, 1970.
- Junke Guo, Kokob Woldeyesus, Jianmin Zhang, and Xiaoming Ju. Time evolution of water surface oscillations in surge tanks. *Journal of Hydraulic Research*, 55(5):657–667, 2017.



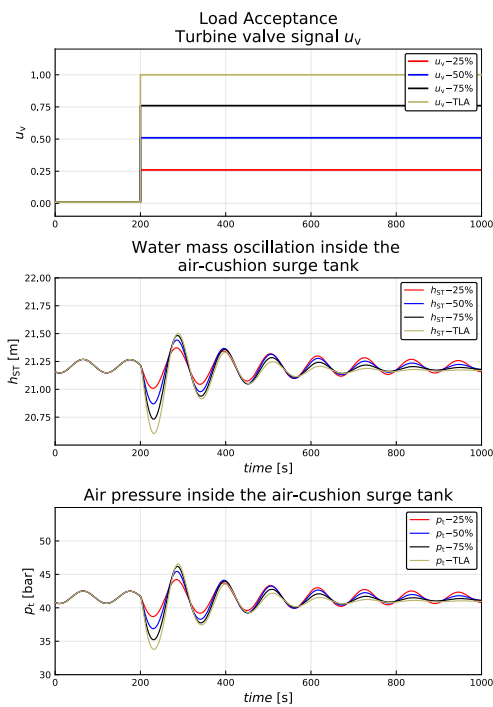


**Figure 9.** Water mass oscillation and air pressure inside the air cushion surge tank for load acceptance. In figure, TLA represents a total load rejection.

Emil Mosonyi. *Water power development*, volume 2A. Publishing house of the Hungarian Academy of Sciences, 1991.

Madhusudhan Pandey and Bernt Lie. Mechanistic modeling of different types of surge tanks and draft tubes for hydropower plants. In *Proceedings of The 61th SIMS Conference on Simulation and Modelling SIMS 2020, September 22-24, Oulu, Finland*. Linköping University Electronic Press, 2020, Submitted.

Vanja Travaš. Water mass oscillations in a generic surge chamber. *Građevinar*, 66(04.):323–334, 2014.

K Vereide, L Lia, T Nielsen, et al. Physical modelling of hydropower waterway with air cushion surge chamber. In *11th National Conference on Hydraulics in Civil Engineering & 5th International Symposium on Hydraulic Structures: Hydraulic Structures and Society-Engineering Challenges and Extremes*, page 134. Engineers Australia, 2014.

Liubomyr Vytvytskyi and Bernt Lie. OpenHPL for Modelling the Trollheim Hydropower Plant. *Energies*, 12(12):2303, 2019.

Wuyi Wan, Boran Zhang, Xiaoyi Chen, and Jijian Lian. Water hammer control analysis of an intelligent surge tank with spring self-adaptive auxiliary control system. *Energies*, 12(13):2527, 2019.

## Appendix D

# Bayesian Inference for Thermal Model of Synchronous Generator Part I : Parameter Estimation

Madhusudhan Pandey (M.P.) and Bernt Lie (B.L.)

Published in: *IEEE Access*

<https://doi.org/10.1109/ACCESS.2022.3209232>

Author Contributions: Conceptualization, B.L. and M.P.; initial studies, all authors; methodology, all authors; software, B.L. and M.P.; validation, B.L. and M.P.; formal analysis, B.L. and M.P.; writing—original draft preparation, M.P.; visualization, B.L. and M.P.; supervision, B.L.

## APPLIED RESEARCH

# Bayesian Inference for Thermal Model of Synchronous Generator—Part I: Parameter Estimation

**MADHUSUDHAN PANDEY AND BERNT LIE**<sup>1</sup>, (Member, IEEE)

Telemark Modeling and Control Center (TMCC), 3901 Porsgrunn, Norway

Corresponding author: Bernt Lie (bernt.lie@usn.no)

**ABSTRACT** Due to the increasing injection of intermittent power sources (solar+wind) into a common grid, dispatchable sources such as hydro power should be able to help reduce the variability in load and the variability in generation caused by the intermittent sources. A hydro generator should be able to operate short-term beyond its thermal capability limit. This requires the monitoring of internal temperatures in the hydro generator. In this paper, a thermal model of an air-cooled synchronous generator is presented, emphasizing the various aspects of parameter estimation and identifiability using Bayesian inference. Inferences are drawn from the posterior distributions of the parameters and initial conditions, dispersion (spreading) of particles and sampling efficiency, practical parameter identifiability, and model mismatch with experiments. Results show extremely narrow parameter distributions. It is early to generalize about the posterior distribution of air-related and metal-related parameters of the air-cooled synchronous generator based on the single experimental data presented here.

**INDEX TERMS** Bayesian inference, model fitting, parameter estimation, parameter identifiability, synchronous generator, thermal model.

## I. INTRODUCTION

Electricity generation from intermittent sources such as solar power, wind power, tidal power, etc., is rapidly increasing in modern electric power system networks. The intermittency in these sources causes the power system networks to operate in different operating conditions. Dispatchable sources such as hydro power can be used for removing the variability in the system's power production caused by the intermittent sources [1], [2], [3], [4]. Thus, in a modern power system, the hydro generators play a significant role in the flexible operation of the intermittent grid. A concept of flexible hydro power is coined in [5] for modern intermittent power system networks. This adheres to a new research requirement in the case of a synchronous hydro generator operating in tandem with the intermittent sources. The performance of the synchronous generator depends on its capability diagram [6]. The capability diagram provides information about the oper-

ating regimes of the synchronous generator in case of the various operational limits, viz., armature current limit, field current limit, and under-excitation [7]. In [6], an instance of exploiting more active power from the hydro generator is studied by controlling the internal temperature of the machine. The control of the armature current limit and the field current limit will result in a decrease in resistance of the armature and the field winding due to temperature monitoring of the rotor copper, stator copper, and stator iron. Furthermore, because of an increase in the active current through the synchronous generator, more active power can be exploited. The temperature is controlled by cooled air circulation through the generator's internal surfaces. The cooled air is supplied through a heat exchanger, in a closed loop. Previous work includes a brief review of thermal analysis of electrical machines [8]. Lumped-parameter thermal network (LPTN) models of the thermal machines are provided in [9], [10], and [11]. Finite element analysis (FEM), and computational fluid dynamics (CFD) models were studied in [12] and [13]. A totally enclosed water-cooled thermal model

The associate editor coordinating the review of this manuscript and approving it for publication was Bo Shen<sup>1</sup>.

of synchronous machines for an electric vehicle has been proposed in [14]. More recently, a totally enclosed thermal model of an air-cooled hydro generator has been developed in [15] using a closed-loop heat exchanger model for cooling heated air from the outlet of the generator. The thermal model of the air-cooled generator is further extended in [16] with the inclusion of temperature-dependent electrical resistances, temperature-dependent specific heat capacities of the metals, and fluids (air+water) inside the air-cooled hydro generator. The model of the air-cooled hydro generator is represented by a computationally cheap online solution of the non-linear model of the heat exchanger in [17], where a hybrid model (mechanistic+data-driven) is proposed using linear and non-linear regression.

In Section II, materials and methods are outlined. Section III provides the mathematical governing equations for the air-cooled hydro generator. In Section IV, results from parameter estimation and parameter identifiability using Bayesian inference are discussed. Conclusions are drawn in Section V with future work suggested in Section VI.

II. MATERIALS AND METHODS

A. SYSTEM DESCRIPTION

Figure 1 shows the working principle of a thermal model of an air-cooled synchronous hydro generator. The cold air out of the heat exchanger is blown by a fan into the rotor/stator air gap. The air is heated by heat flow from the rotor, air gap windage, and bearing friction. Furthermore, the air is forced into the iron cores and then gets heated by the heat flow from the iron cores. The heated air is now collected at the stator’s outlet and passed through a counter current heat exchanger. The heated air is cooled using continuous cold water circulation in the heat exchanger and then fed again into the air gap as a closed loop process. The heat exchanger is provided with cold water, with mass flow rate  $\dot{m}_w$ , at temperature  $T_w^c$ . The air mass flow rate is  $\dot{m}_a$  with temperature  $T_a^h$  at stator outlet and heat exchanger entry. The rotor copper heat source,  $\dot{Q}_r^\sigma$ , is due to eddy currents caused by  $I_f$ . Similarly, the stator copper heat source,  $\dot{Q}_s^\sigma$ , is due to stator terminal current  $I_t$ .  $\dot{Q}_{Fe}^\sigma$  is stator iron heat source, and  $\dot{Q}_f^\sigma$  is heat generated due to friction in the stator/rotor air gap. The thermal operation of the air-cooled synchronous generator is mainly influenced by  $\dot{m}_w$ ,  $\dot{m}_a$ ,  $T_w^c$ ,  $\dot{Q}_{Fe}^\sigma$ ,  $\dot{Q}_f^\sigma$ ,  $I_t$ , and  $I_f$ . It is of interest to consider evolution of temperature in the rotor, stator, and iron core indicated by  $T_r$ ,  $T_s$  and  $T_{Fe}$ , respectively. Monitoring of these temperatures allows for optimal exploitation of active power production by enhancing the capability diagram to a new regime of operation [6].

Figure 2 shows the Bayesian framework for inference about parameters of a dynamical system. In the figure,  $x, u, z, \theta$ , and  $y$  are the states, inputs, algebraic variables, parameters, and outputs, respectively. In the figure,  $p(\theta)$  is the prior probability distribution of  $\theta$ ,  $p(y|\theta)$  is the likelihood function, and  $p(\theta|y)$  is the estimated posterior distribution of  $\theta$ . Section IV provides detailed explanation about

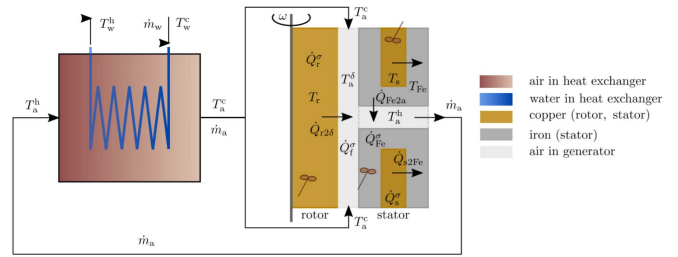


FIGURE 1. Thermal model of the synchronous generator taken from [16].

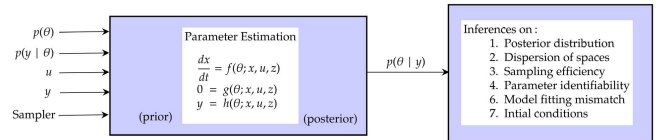


FIGURE 2. Bayesian inference for the parameter estimation.

priors and likelihood. In Fig. 2, we also see that the posterior distribution of parameters allows for various inferences about the parameters of a dynamical system. The inferences include (i) finding statistical moments from the posterior distribution of the parameters, (ii) finding the relative dispersion of the parameter space and the relative sampling efficiency between the parameters, (iii) model mismatch with experiment and (iv) inferences related to the posterior distribution of the initial conditions while working with the model and the experimental data offline.

B. EXPERIMENTAL DATA

A heat-run test, of the synchronous machine, was performed for 600 min [15] with sampling rate = [1] min. Only data from  $t = 16$  min to  $t = 600$  min, i.e., 584 data points, will be used for model fit. For each minute, for a supplied field current, starting from a cold-start, measurements for different quantities are recorded. The cold-run last up to 53 min, where the terminal voltage is built-up due to residual flux in rotor windings. The measurements are available for both electrical quantities and temperatures related to the air-cooled synchronous generator. After the cold-run, the field current is increased which increases the temperature of the stator copper and the stator iron. The measured quantities are summarized in Table 1, and the experimental data are plotted in Fig. 3. The expression for terminal current  $I_t$  as shown in Table 1, indicates that it is not measured using a sensor, however calculated from a mathematical expression relating power and voltage.

III. MATHEMATICAL MODEL

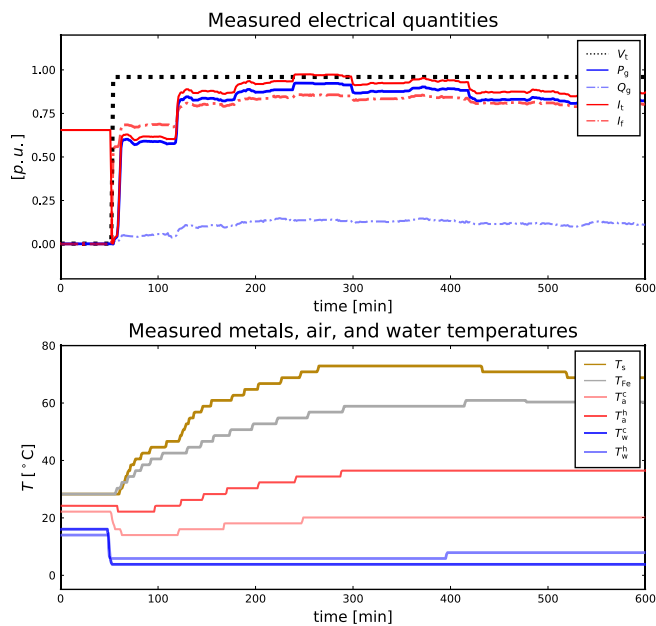
The mathematical equations governing generator metal temperatures taken from [16] and [18] are

$$m_r \hat{c}_{p,Cu} \frac{dT_r}{dt} = 1.1R_r I_f^2 - \mathcal{U}A_{r2s}(T_r - T_a^\delta) \quad (1)$$

$$m_s \hat{c}_{p,Cu} \frac{dT_s}{dt} = 3R_s I_t^2 - \mathcal{U}A_{s2Fe}(T_s - T_{Fe}) \quad (2)$$

**TABLE 1. Measured quantities from a 600 min heat-run test.**

Quantity	Symbol	Units	Sensor
Generator terminal voltage	$V_t$	kV	-
Active power of generator	$P_g$	MW	-
Reactive power of generator	$Q_g$	MVar.	-
Rotor field current	$I_f$	A	-
Temperature of stator copper	$T_s$	°C	PT 100
Temperature of stator iron	$T_{Fe}$	°C	PT 100
Hot air temperature	$T_a^h$	°C	Pt 100/CTD
Cold air temperature	$T_a^c$	°C	Pt 100/CTD
Cold water temperature	$T_w^c$	°C	Analog
Hot water temperature	$T_w^h$	°C	Analog
Terminal current	$I_t = \frac{P_g^2 + Q_g^2}{\sqrt{3}V_t}$	A	-


**FIGURE 3. Experimental data for generator model from a 600 min heat-run test taken from [15].**

$$m_{Fe} \hat{c}_{p,Fe} \frac{dT_{Fe}}{dt} = \mathcal{U}A_{s2Fe}(T_s - T_{Fe}) - \mathcal{U}A_{Fe2a}(T_{Fe} - T_a^h) + \dot{Q}_{Fe}^\sigma. \quad (3)$$

Similarly, the dynamical equations for air inside the generator are

$$0 = \dot{m}_a \hat{c}_{p,a}(T_a^c - T_a^\delta) + \mathcal{U}A_{r2\delta}(T_r - T_a^\delta) + \dot{Q}_f^\sigma \quad (4)$$

$$0 = \dot{m}_a \hat{c}_{p,a}(T_a^\delta - T_a^h) + \mathcal{U}A_{Fe2a}(T_{Fe} - T_a^h), \quad (5)$$

and the heat exchanger is model as

$$(N_{St}^w - N_{St}^a e^{-N_{St}^\Delta}) T_a^c = N_{St}^\Delta T_a^h + N_{St}^a (1 - e^{-N_{St}^\Delta}) T_w^c. \quad (6)$$

In Eq. 6  $N_{St}^i$  for  $i \in \{w, a, \Delta\}$  are dimensionless Stanton numbers relating heat transfer coefficient, density, heat capacity, and velocity.

Equations 1-6 can be written in Differential Algebraic Equations (DAEs) form as

$$\frac{dx}{dt} = f(x, z, u; \theta)$$

$$0 = g(x, z, u; \theta)$$

$$y = h(x, z, u; \theta) \quad (7)$$

where  $x = (T_r, T_s, T_{Fe})$ ,  $z = (T_a^c, T_a^\delta, T_a^h)$ ,  $u = (I_f, I_t, T_w^c)$ ,

$$\theta = (m_r, m_s, m_{Fe}, R_r, R_s, \hat{c}_{p,Cu}, \hat{c}_{p,Fe}, \hat{c}_{p,a}, \dot{m}_a, \mathcal{U}A_{r2\delta}, \mathcal{U}A_{s2Fe}, \mathcal{U}A_{Fe2a}, \dot{Q}_{Fe}^\sigma, \dot{Q}_f^\sigma, N_{St}^a, N_{St}^w, N_{St}^\Delta).$$

The parameters and operating conditions are given in Table 2.

Out of the three states,  $T_s$  and  $T_{Fe}$  are measured, while it is of interest to estimate the temperature of rotating rotor copper  $T_r$ . Similarly, out of three algebraic variables,  $T_a^c$  and  $T_a^h$  are measured, and it is also of interest to estimate air gap temperature  $T_a^\delta$ . The measured inputs, states and algebraic variables are shown in Fig. 3.

## IV. PARAMETER ESTIMATION

### A. PROBLEM FORMULATION

It is of interest to estimate the thermal parameters and initial conditions of the air-cooled hydro generator using Bayesian inference.

The expected value of parameter  $\hat{\theta}$  is calculated as

$$\hat{\theta} = \arg \max_{\theta} p(\theta | y),$$

where  $p(\theta | y)$  is the ‘‘posterior probability distribution of parameter  $\theta$  for the given data  $y$ ’’.  $p(\theta | y)$  is expressed in terms of likelihood  $p(y | \theta)$  and prior  $p(\theta)$ ,

$$p(\theta | y) = \frac{p(y | \theta) p(\theta)}{p(y)} \quad (8)$$

where  $p(y)$  is independent of  $\theta$ , and is used as a normalization constant for  $p(\theta | y)$ .  $p(y)$  is also known as the evidence or the marginal likelihood. The prior  $p(\theta)$  is our prior beliefs about the probability density function for the parameter  $\theta$  without seeing the data. Similarly, the likelihood  $p(y | \theta)$  is a model representing the distribution of the data given a fixed parameter  $\theta$  and calculated as

$$p(y | \theta) = \prod_{i=1}^N p(y_i | \theta).$$

The evidence  $p(y)$  used for normalization is calculated as the joint probability distribution of  $p(\theta | y)$  and  $p(y)$

$$p(y) = \int p(\theta | y) p(y) d\theta. \quad (9)$$

The analytical solution to Eq. (9) is only available for simple cases, and in real-life Bayesian inference, numerical solutions are used. The Bayesian parameter estimation method is applied to the system given by Eqs. (1-6).

### B. FORMULATION USING TURING.JL

Turing.jl is a Julia package for probabilistic programming [19]. Turing.jl is also composable with DifferentialEquations.jl [20], a Julia package for differential equations, facilitating Bayesian inference in the parameter of the system

TABLE 2. Parameters and initial operating conditions.

Quantities	Symbols	Values
Mass of rotor copper, stator copper and stator iron	$m_r, m_s, m_{Fe}$	9260 kg, 6827 kg, 71200 kg
Ohmic resistances of rotor copper and stator copper	$R_r, R_s$	0.127 $\Omega$ , 1.95 m $\Omega$
Specific heat capacities of copper and iron	$\hat{c}_{p,Cu}, \hat{c}_{p,Fe}$	0.385 kJ/kg/K, 0.465 kJ/kg/K
Specific heat capacities of air and water	$\hat{c}_{p,a}, \hat{c}_{p,w}$	1.15 kJ/kg/K, 4.2 kJ/kg/K
Air and water mass flow rates	$\dot{m}_a, \dot{m}_w$	49.2 kg/s, 53.9 kg/s
Heat transfer, rotor to air gap, stator copper to iron, and stator iron to air	$\mathcal{U}A_{r2\delta}, \mathcal{U}A_{s2Fe}, \mathcal{U}A_{Fe2a}$	2.7 kW/K, 20 kW/K, 14.3 kW/K
Stator iron generated heat	$\dot{Q}_{Fe}^\sigma$	212 kW
Friction heating	$\dot{Q}_f^\sigma = 0.8 \cdot \dot{W}_f$	422.4 kW
Friction work	$\dot{W}_f$	528 kW
Stanton number, air	$N_{St}^a = \frac{\mathcal{U}A_x}{\hat{c}_{p,a}\dot{m}_a}$	0.785
Stanton number, water	$N_{St}^w = \frac{\mathcal{U}A_x}{\hat{c}_{p,w}\dot{m}_w}$	0.196
Stanton number, difference	$N_{St}^\Delta = N_{St}^w - N_{St}^a$	-0.589
Heat transfer, air to water	$\mathcal{U}A_x = 1 / \left( \frac{1}{h_a A_x} + \frac{1}{h_w A_x} \right)$	44.46 kW/K
Heat transfer, solid to air	$h_a A_x$	55.6 kW/K
Heat transfer, solid to water	$h_w A_x$	222 kW/K
Initial value of rotor copper, stator copper, and stator iron temperatures	$T_a^c(t=0), T_s(t=0), T_{Fe}(t=0)$	28°C, 28°C, 28°C
Initial value of cooled air, air-gap, and hot air temperatures, stator copper, and stator iron temperatures	$T_a^c(t=0), T_a^\delta(t=0), T_a^h(t=0)$	14°C, 18°C, 22°C

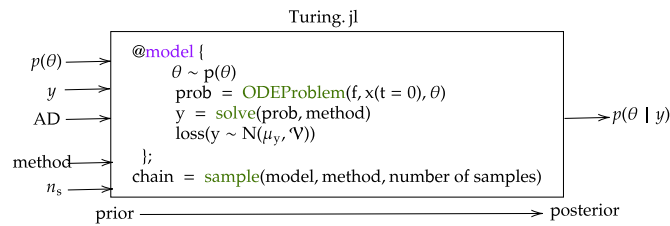


FIGURE 4. Bayesian inference implemented in Turing.jl in the Julia language.

represented by differential equations. The problem is formulated as shown in Fig. 4.

For the differential equations represented by Eqs. (1-6) we want to estimate posterior distributions of:

- initial states  $T_r(t=0)$ ,  $T_s(t=0)$ , and  $T_{Fe}(t=0)$
- heat transfer coefficients  $\mathcal{U}A_{r2\delta}$ ,  $\mathcal{U}A_{s2Fe}$ ,  $\mathcal{U}A_{Fe2a}$ , and  $\mathcal{U}A_x$
- heat sources  $\dot{Q}_{Fe}^\sigma$  and  $\dot{Q}_f^\sigma$ .

Table 3 shows the priors and the data for the estimation of the selected parameters. In the table,  $\mathcal{V}$ , usually chosen as an inverse gamma function mostly for measurement sequence in Bayesian inference [21], is the prior to the variance of the measurement noise where we assume  $\mathcal{V} \sim \Gamma^{-1}(2, 3)$ . We have assumed that all measurements have the same noise variance since all temperatures are of similar size. The measurement vector is  $y = (T_s \ T_{Fe} \ T_a^c \ T_a^h)$ . A loss function is formulated using Turing.jl. The priors for the initial rotor copper temperature are truncated normal distributions. For parameters  $\theta$  such as initial descriptor (differential and algebraic variables) as well as model constants, it is common to

assume a normal distribution, e.g.,  $\theta \sim \mathcal{N}(\mu, \sigma)$ . Because we normally want to limit the distribution to lie within a range  $\theta \in [\theta_{min}, \theta_{max}]$ , e.g., to avoid negative values, it is quite common to use a truncated normal distribution for the prior of  $\theta$ ,

$$\theta \sim \mathcal{T}(\mathcal{N}(\mu, \sigma), \theta_{min}, \theta_{max})$$

where  $\mathcal{T}$  represents truncated normal distribution for  $\theta$ . The prior to the initial rotor copper temperature is chosen as  $T_r(t=0) \sim \mathcal{T}(\mathcal{N}(30, 3), 25, 35)$  where the mean  $\mu_{T_r(t=0)} = 30^\circ\text{C}$  and is taken from Table 2 and the standard deviation  $\sigma_{T_r(t=0)} = 3$  is the initial deviation that is assumed. Similarly, the prior for  $T_r(t=0)$  is truncated between  $25^\circ\text{C}$  and  $35^\circ\text{C}$ . The priors of  $T_s(t=0)$  and  $T_{Fe}(t=0)$  are also set accordingly with variance = 3 and the mean value taken from Table 2 within some relevant values of  $\theta_{min}$  and  $\theta_{max}$  for the parameters. Priors of other parameters to be found are also set accordingly from Table 2. It is important to note that the posterior distributions are approximated based on the numerical solution of Eq. (9) using different sampling methods. It is out of the scope of this paper to detail sampling methods. Some of the available sampling methods are listed in Table 3 and usage of these sampling algorithms can be found in [19]. We have chosen the NUTS sampler with the number of particles in the sampling as  $N_s = 1000$  to estimate the parameters.

### C. ESTIMATED PARAMETERS

The posterior distributions of the estimated heat transfer parameters are shown in Fig. 5. Figure 5 (a) shows the distribution of the variance  $\mathcal{V}$  of the measurement noises.



TABLE 3. Priors, data and sampling methods.

Prior distributions	Data	Sampling
$\mathcal{V} \sim \Gamma^{-1}(2, 3)$ $T_r(t=0) \sim \mathcal{T}(\mathcal{N}(30, 3), 25, 35)$ , $\mathcal{U}A_{r2\delta} \sim \mathcal{T}(\mathcal{N}(2.7, 1), 0.2, 5)$ , $\dot{Q}_{Fe}^\sigma \sim \mathcal{T}(\mathcal{N}(212, 40), 20, 400)$ , etc.	$y = [y_1 \ y_2 \ \dots \ y_N]$ $u = [u_1 \ u_2 \ \dots \ u_N]$	1. Importance sampling (IS) 2. Sequential Monte Carlo (SMC) 3. Metropolis-Hastings (MH) 4. Hamiltonian Monte Carlo (HMC) 5. No-U-Turn Sampler (NUTS) 6. Particle Gibbs sampling (PG)

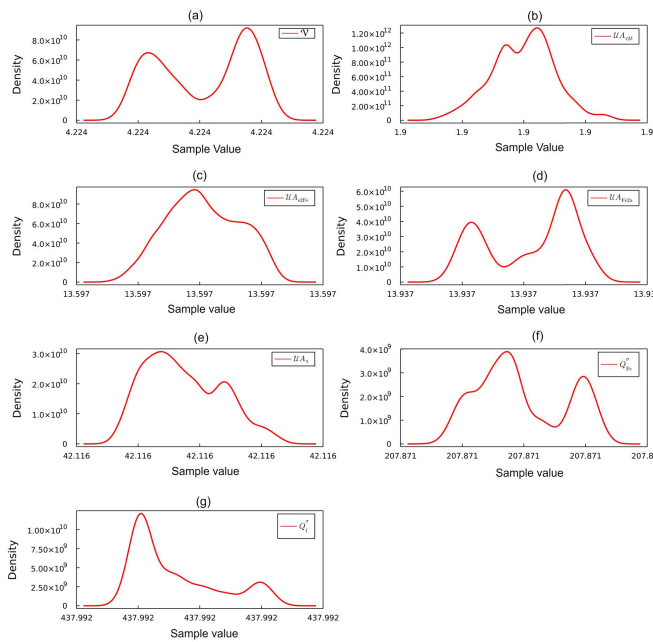


FIGURE 5. Posterior distribution of heat transfer parameters for the thermal model of the air-cooled synchronous generator.

Figures 5 (b-g) show the posterior distributions of heat transfer parameters with mean and variance as shown in Table 4. The expected value of these distributions are used as the estimated parameters. Similarly, Fig. 6 shows the estimated initial conditions for the metal temperatures of the air-cooled generators.

**D. ANALYSIS OF ESTIMATED PARAMETERS**

The estimated parameters are analyzed based on mean and standard deviation as well as naive standard error (Naive SE) [22], and effective sample size (ESS) [23] as shown in Table 4.

**1) NAIVE STANDARD ERROR (NAIVE SE)**

Naive SE is a term defined for inferential statistics similarly to the mean and the standard deviation defined for descriptive statistics. Naive SE is computed as in [22]. Naive SE provides a measure of the potential error in the estimate while parameter inference is done through Bayes’ theorem. Naive SE

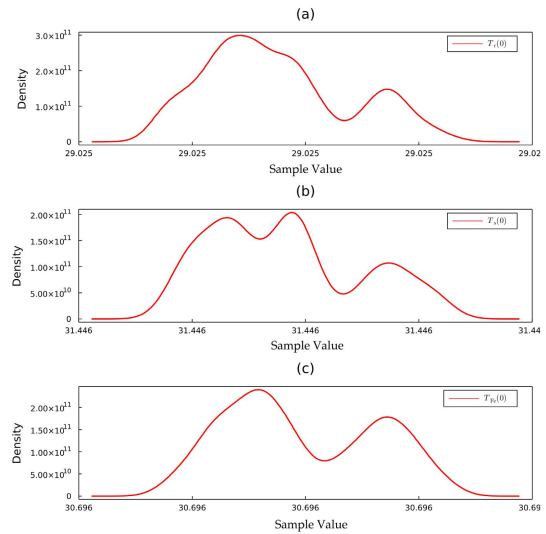


FIGURE 6. Posterior distribution of initial values for the thermal model of the air-cooled synchronous generator.

TABLE 4. Analysis of the Bayesian inference using NUTS sampler for the estimation of initial values, heat transfers and heat sources parameters for air-cooled generator.

Parameter	Mean	Std.	Naive SE $\hat{\sigma}_\theta$	ESS
$\mathcal{V}$	4.22	$5.87 \cdot 10^{-12}$	$1.85 \cdot 10^{-13}$	2.16
$T_r(t=0)$	29.02	$1.49 \cdot 10^{-12}$	$4.74 \cdot 10^{-14}$	4.92
$T_s(t=0)$	31.44	$2.08 \cdot 10^{-12}$	$6.48 \cdot 10^{-14}$	2.61
$T_{Fe}(t=0)$	30.69	$1.83 \cdot 10^{-12}$	$6.12 \cdot 10^{-14}$	2.36
$\mathcal{U}A_{r2\delta}$	1.90	$3.35 \cdot 10^{-13}$	$1.06 \cdot 10^{-14}$	12.70
$\mathcal{U}A_{s2Fe}$	13.59	$3.98 \cdot 10^{-12}$	$1.25 \cdot 10^{-13}$	10.77
$\mathcal{U}A_{Fe2a}$	13.92	$1.01 \cdot 10^{-11}$	$3.20 \cdot 10^{-13}$	2.24
$\mathcal{U}A_x$	42.11	$1.26 \cdot 10^{-11}$	$4.00 \cdot 10^{-13}$	4.35
$\dot{Q}_{Fe}^\sigma$	207.87	$1.29 \cdot 10^{-10}$	$4.08 \cdot 10^{-12}$	2.57
$\dot{Q}_f^\sigma$	437.99	$6.31 \cdot 10^{-11}$	$1.99 \cdot 10^{-12}$	2.65

calculates the width of sample means around the population mean. The lower the value of naive SE, the lower is the dispersion. Naive SE can also be used to find the upper and lower limit for the 95% confidence interval of the parameter given by  $\bar{\theta} \pm \hat{\sigma}_\theta$  where  $\bar{\theta}$  is the mean value of the parameter and  $\hat{\sigma}_\theta$  is the naive SE.

From Table 4 we see that Naive SE measuring the dispersion of sample means around the population mean, in the case of initial conditions lies between  $4.74 \cdot 10^{-14}$  to  $6.48 \cdot 10^{-14}$ .

The ratios of Naive SE for initial values is  $\hat{\sigma}_{T_r} : \hat{\sigma}_{T_s} : \hat{\sigma}_{T_{Fe}} = 4.74 : 6.48 : 6.12$ . Since  $T_r(t=0)$  has lower Naive SE, the posterior distributions of  $T_s(t=0)$  and  $T_{Fe}(t=0)$  are wider than the posterior distribution of  $T_r(t=0)$ . This shows that the posterior distribution of the temperature of the initial states related to the rotating copper inside the hydro generator is less wider than that of stationary copper and iron.

From Table 4 we see that the naive SE in the case of heat transfer from rotor copper to the air-gap  $\mathcal{U}_{A_{r2\delta}}$  is smaller as compared to the heat transfer from the stator copper to stator iron  $\mathcal{U}_{A_{s2Fe}}$  and the heat transfer from iron to air  $\mathcal{U}_{A_{Fe2a}}$ . Thus, the posterior distribution of the heat transfer parameter related to the air is more narrower than the heat transfer parameter related to the metal inside the hydro generator. From the values of the naive SE from Table 4 in the case of heat sources parameters of the hydro generator, the dispersion in the posterior distribution of the iron heat source parameter  $\dot{Q}_{Fe}^o$  is higher than that of the friction heat source parameter  $\dot{Q}_f^o$  indicating that the heat source parameter related to air is less wider than the metals.

## 2) EFFECTIVE SAMPLE SIZE (ESS)

ESS describes the correlation between observations in the sample [23]. The calculation of ESS in Turing.jl is performed as in [24]. The higher the value of ESS, the higher is the correlation between the observations in the sample. ESS also helps to determine the relative sampling efficiency of the estimates based on the correlation between the observations in the sample. The relative sampling efficiency of the parameters from the estimated ESS can be calculated as

$$\hat{\eta}_\theta = 1 - \frac{ESS_{\theta_j}}{\sum ESS_{\theta_j}} \quad (10)$$

The smaller the value of ESS, the higher is the sampling efficiency. From Table 4, the relative sampling efficiency  $\hat{\eta}$  among the initial conditions  $T_r(t=0)$ ,  $T_s(t=0)$ , and  $T_{Fe}(t=0)$ , the relative sampling efficiency of stator iron temperature  $T_{Fe}(t=0)$  is higher as compared to the relative sampling efficiency of  $T_r(t=0)$  and  $T_s(t=0)$ . In addition comparing all the temperatures, the rotor copper temperature  $T_r(t=0)$  has the lowest sampling efficiency. This shows that the temperature related to the rotating part of the hydro generator has lower sampling efficiency than the stationary part of the hydro generators. The sampling efficiency of the temperatures can be calculated using Eq. (10). The sampling efficiency for rotor copper temperature is given as  $\hat{\eta}_{T_r} = 1 - \frac{4.92}{4.92+2.61+2.36} \approx 0.5$ . The ratios of sampling efficiency for temperatures is  $\hat{\eta}_{T_r} : \hat{\eta}_{T_s} : \hat{\eta}_{T_{Fe}} \approx 0.5 : 0.73 : 0.76$ . Similarly from Table 4 using the estimated ESS for the heat transfer parameters, the relative sampling efficiency of heat transfer from rotating rotor copper to air-gap  $\mathcal{U}_{A_{r2\delta}}$  is lower as compared to heat transfer between stationary copper to stationary iron  $\mathcal{U}_{A_{s2Fe}}$  or heat transfer from stationary iron to air  $\mathcal{U}_{A_{Fe2a}}$ . Similarly from Table 4, we can see that both heat source parameters have the same sampling efficiency.

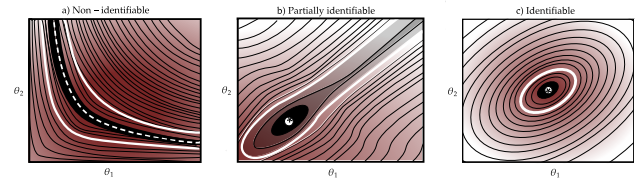


FIGURE 7. Parameters identifiability based on the joint posterior probability distribution of the parameters based on [27].

## E. PARAMETER IDENTIFIABILITY

Parameter identifiability tells whether a parameter can be computed uniquely from the given model structure and observations. For complex systems, the number observed quantities is much smaller than the number of states + algebraic variables. It is therefore of interest to estimate the distribution of parameters that can explain the experimental data well. In inferential statistics, the joint posterior distribution of parameters found in Section IV using the Bayesian method can be used for parameter identifiability analysis. In frequentist statistics, profile likelihood projections are used for parameter identifiability [25], [26], [27]. Parameter non-identifiability occurs due to (i) indistinguishability of parameters in the model structure, and (ii) insufficiency in the experimental data. Identifiability analysis considering model structure is termed structural identifiability and identifiability analysis considering the amount and quality of experimental data is termed practical identifiability. Structural identifiability is out of the scope of the paper and our focus is on practical identifiability analysis. Figure 7 shows three cases of the joint posterior probability distribution of parameters  $\theta_1$  and  $\theta_2$  where Fig. 7 (a) illustrates that both parameters are structurally non-identifiable since the parameters do not converge to a point. The white lines show the posterior high density interval (HDI) within which an unobserved parameter value falls with a particular probability. The white dashed line indicates that the parameters diverge to infinity. The non-identifiability in parameters can only be resolved after the model structure is distinguishable with parameters. In Fig. 7 (b), the parameters are partially identifiable only at the lower density interval. The partially identifiable parameters are denoted as practically non-identifiable parameters. Identifiability of practically non-identifiable parameters can be improved by increasing the amount and the quality of the experimental data. Finally, Fig. 7 (c) shows that parameters converge to a point and are identifiable.

Figure 8 shows the posterior joint probability distribution or the marginal kernel density estimate of heat transfer parameter  $\mathcal{U}_{A_{r2\delta}}$  with other heat transfer and heat source parameters. The central region in the marginal posterior distribution shows the HDI for the parameter space with a higher confidence region for the estimated parameters. Since the joint density plot of other heat transfer and heat source parameters bounded within a region, all the heat transfer and heat source parameters are identifiable. The joint points in the central region bounded with distorted ellipses in the figure show the



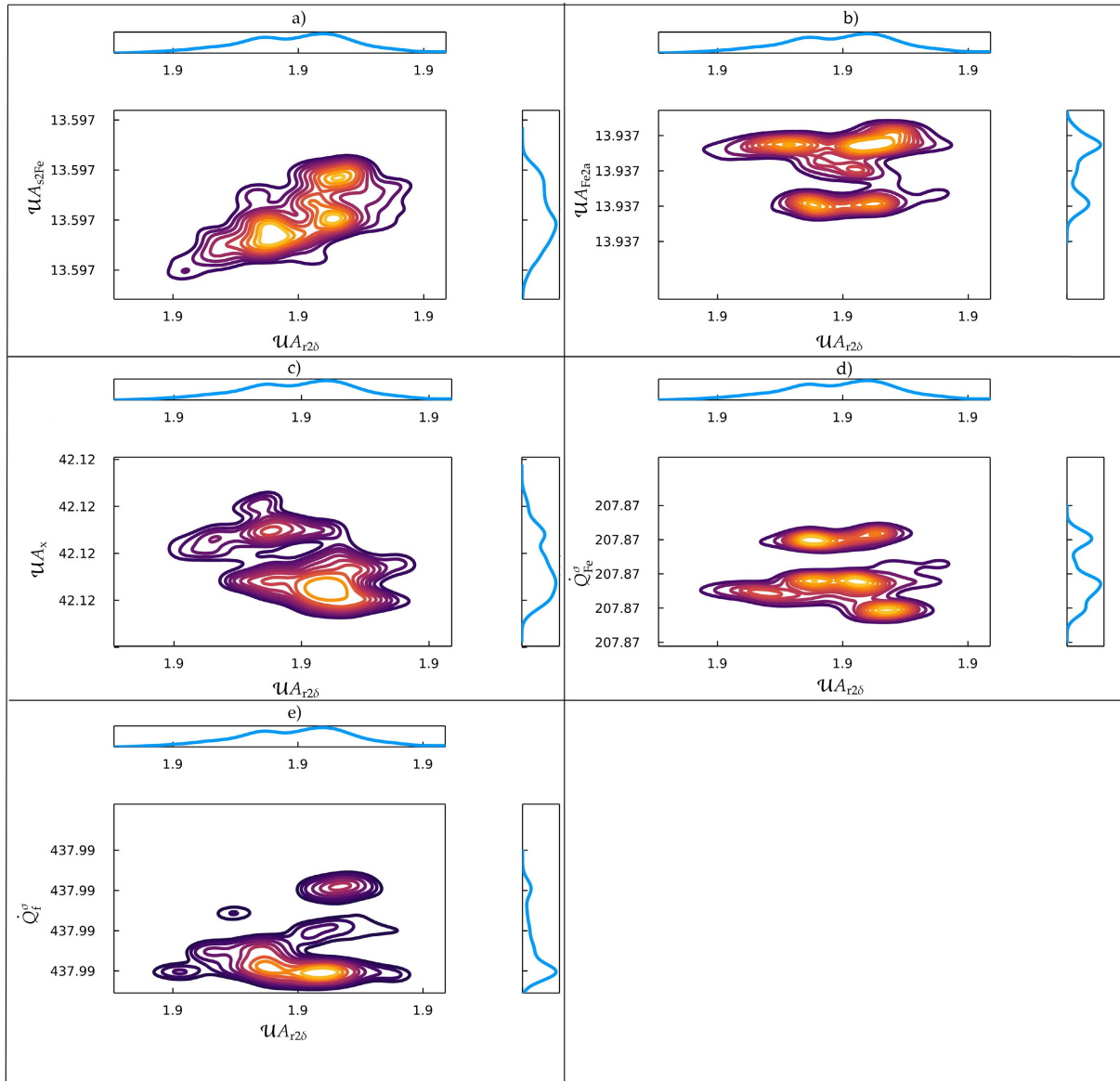


FIGURE 8. Marginal kernel density plot of  $UA_{r2\delta}$  with other heat transfer and heat sources parameters.

modal values of the parameters. The joint posterior probability distribution of  $UA_{s2Fe}$  with other heat transfer and heat sources parameters, and so on, are not shown in the figure. The identifiability of all the parameters and initial conditions can also be inferred directly from the posterior distribution of the parameters shown in Figs. 5 and 6, respectively.

**F. MODEL FITTING**

It is of interest to see how well the mathematical model fits with the experimental data. The estimated initial conditions and parameters are used to compare the fitted model with the experimental data.

Figure 9 shows the simulation versus experiment using the estimated parameters for the simulation. The model represents the experimental data well. In the figure, experimental data are well-matched with the simulation in the case of the

stator copper temperature  $T_s$  and cold air temperature  $T_a^c$ . The experimental data and the simulation are less well matched for the lower temperature region before  $t \approx 300$  s in the case of stator iron temperature  $T_{Fe}$  and hot air temperature  $T_a^h$ .

In the case of  $T_{Fe}$ , the mismatch between the experiment and the simulation prior to  $t \approx 300$  s as shown in Fig. 9 is caused by the influence of the heat transfer parameter. The posterior distributions of the heat transfer parameter  $UA_{Fe2a}$  and  $UA_{s2Fe}$  related to stationary parts are more wider than the heat transfer parameter  $UA_{r2\delta}$  related to rotating parts.  $UA_{r2\delta}$  is the heat transfer related to the rotating copper,  $UA_{s2Fe}$  is the heat transfer related to stationary copper, and  $UA_{Fe2a}$  is the heat transfer related to stationary iron. From this result, we can infer the dispersion characteristics of the posterior distribution of the stationary copper, stationary iron, and rotating copper in the case of the air-cooled

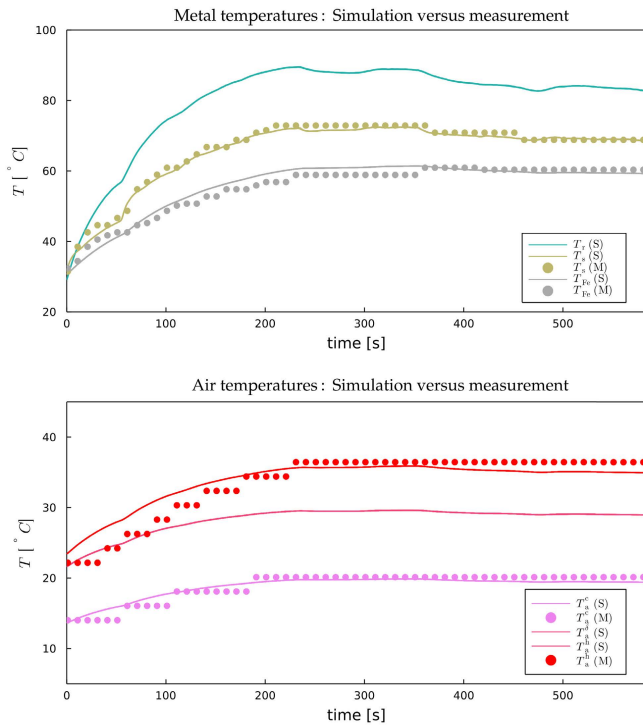


**FIGURE 9. Model fit of simulation versus experimental measurements. In the figure,  $T_r$  (S), and  $T_r$  (M) represent simulated and measured rotor copper temperature, respectively.**

synchronous generator. The posterior distribution of the heat transfer parameters related to the stationary parts is more wider than the posterior distribution of the heat transfer parameters related to the rotating parts. The stationary iron receives heat from the heated stator copper at temperature  $T_s$  because of terminal current  $I_t$  flowing through the stator copper. Thus, the posterior distribution of heat transfer parameter related to stationary iron is more wider. This is because of the result from Section IV-D that the posterior distribution of the heat transfer parameter related to iron receiving heat from the stationary copper  $\mathcal{U}_{A_{s2Fe}}$  and the heat transfer from heated stationary iron to air  $\mathcal{U}_{A_{s2Fe}}$  are more wider. Thus, the simulation results of the stator iron  $T_{Fe}$  is not matched with the experimental data for lower temperature region before  $t \approx 300$  s for the air-cooled synchronous generator. In the real operation of the air-cooled hydro generator at Åbjøra, Norway [15], for a period with the average time constant of 53 min the machine was in the state of the cold-run as described in Section II-B. The stationary iron takes time to get heated from the stationary copper heated from the terminal current  $I_t$ .

Similarly, in the case of hot air temperature  $T_a^h$ , the mismatch between the experiment and the simulation before  $t \approx 300$  s as shown in Fig. 9 is because of the influence of the heat transfer parameter related to the stationary iron;  $\mathcal{U}_{A_{Fe2a}}$  and  $\mathcal{U}_{A_{s2Fe}}$ . From Fig. 1 the iron heat source  $\dot{Q}_{Fe2a} = \mathcal{U}_{A_{Fe2a}}(T_{Fe} - T_a^h)$  [16] which indicates that the non-homogeneous heating of iron during the cold-run of the hydro generator cause heat transfer parameter related to stationary

iron  $\mathcal{U}_{A_{Fe2a}}$  to attain different modal values as shown in Fig. 5 (c). In addition, this non-homogeneous heating of the iron also affect the iron heat source parameter  $Q_{Fe}^\sigma$  as shown in Fig. 5 (e). This means that during the cold-run of the air-cooled synchronous generator the air inside the hydro generator at temperature  $T_a^h$  is heated intermittently or non-homogeneously as indicated by the experimental data during the cold-run prior to  $t \approx 300$  s. Similar, intermittency can be seen in the case of experimental data for cold air temperature  $T_a^c$  and stationary iron temperature  $T_{Fe}$ . As the air temperatures  $T_a^c$ ,  $T_a^\delta$  and  $T_a^h$  inside the machine are inter-related through governing Eqs. (3), (4), and (5), it can be predicted that the experimental data during the cold-run of the hydro generator for air-gap temperature  $T_a^\delta$  should also be intermittent. The governing equations for the metal and air temperatures formulating a dynamic model for the air-cooled machines with stationary iron parts need intermittent correction for its heat transfer parameter related to iron during the cold-run of the machine.

**V. CONCLUSION**

For the air-cooled synchronous generator as described in Section II-A, results from the analysis of the estimated parameters as described in Section IV-D show that the posterior distribution of temperatures of the stationary parts inside the air-cooled synchronous generator is more wider than the rotating parts. In the case of the heat transfer parameters, the posterior distribution of the heat transfer parameters related to metals is more wider than the posterior distribution of the air-related parameters. Furthermore results also indicate that the posterior distribution of the heat sources parameters related to iron is also more dispersed than other heat sources parameters like heat source due to friction, etc.

From Section IV-E, results indicate that all the parameters estimated are practically identifiable. From Section IV-F, results indicate that the mismatch between the experimental data and the simulation results for the iron temperature and hot air temperature during the cold-run of the hydro generator is due to the higher dispersion characteristics in the posterior distribution of the stationary parts of the generator. The stationary iron takes time to get heated from the stationary copper. The stationary copper gets heated from the terminal current flowing through the stator copper. Thus, the posterior distribution of parameters for the air-cooled synchronous generator affects the mismatch between experimental data and the simulation results. Results also indicate that the heat transfer parameter related to iron attains an intermittent value during the cold-run of the air-cooled synchronous generator.

**VI. FUTURE WORK**

The governing equations for the air-cooled hydro generator, represented by Eqs. (1-6), are considered with constant metal resistances and constant specific heat capacities. Future work includes parameter estimation and identifiability in the case of temperature dependent resistances and specific heat capacities. From Figs. 5 and 6, we see extremely narrower

parameter distribution. It would be interesting to see the relationship between the measurement data available for the descriptor and the width of parameter distribution.

## REFERENCES

- [1] M. Pandey and B. Lie, "The role of hydropower simulation in smart energy systems," in *Proc. IEEE 7th Int. Conf. Energy Smart Syst. (ESS)*, May 2020, pp. 392–397.
- [2] M. Pandey, D. Winkler, R. Sharma, and B. Lie, "Using MPC to balance intermittent wind and solar power with hydro power in microgrids," *Energies*, vol. 14, no. 4, p. 874, Feb. 2021.
- [3] I. Graabak and M. Korpás, "Balancing of variable wind and solar production in continental Europe with Nordic hydropower—A review of simulation studies," *Energy Proc.*, vol. 87, pp. 91–99, Jan. 2016.
- [4] I. Graabak, S. Jaehnert, M. Korpás, and B. Mo, "Norway as a battery for the future European power system—Impacts on the hydropower system," *Energies*, vol. 10, no. 12, p. 2054, Dec. 2017.
- [5] I. Graabak, M. Korpás, S. Jaehnert, and M. Belsnes, "Balancing future variable wind and solar power production in Central-West Europe with Norwegian hydropower," *Energy*, vol. 168, pp. 870–882, Feb. 2019.
- [6] T. Øyvang, J. K. Noland, R. Sharma, G. J. Hegglid, and B. Lie, "Enhanced power capability of generator units for increased operational security using NMPC," *IEEE Trans. Power Syst.*, vol. 35, no. 2, pp. 1562–1571, Mar. 2019.
- [7] P. Khadka, D. Winkler, and T. Øyvang, "Online monitoring of a synchronous generator's capability with MATLAB," in *Proc. Linköping Electron. Conf., Västerås, Sweden*, Jan. 2020, pp. 198–205.
- [8] A. Boglietti, A. Cavagnino, D. Staton, M. Shanel, M. Mueller, and C. Mejuto, "Evolution and modern approaches for thermal analysis of electrical machines," *IEEE Trans. Ind. Electron.*, vol. 56, no. 3, pp. 871–882, Mar. 2009.
- [9] A. M. El-Refaie, N. C. Harris, T. M. Jahns, and K. M. Rahman, "Thermal analysis of multibarrier interior PM synchronous machine using lumped parameter model," *IEEE Trans. Energy Convers.*, vol. 19, no. 2, pp. 303–309, Jun. 2004.
- [10] S. Nategh, O. Wallmark, M. Leksell, and S. Zhao, "Thermal analysis of a PMSRM using partial FEA and lumped parameter modeling," *IEEE Trans. Energy Convers.*, vol. 27, no. 2, pp. 477–488, Jun. 2012.
- [11] N. Rostami, M. R. Feyzi, J. Pyrhönen, A. Parviainen, and M. Niemelä, "Lumped-parameter thermal model for axial flux permanent magnet machines," *IEEE Trans. Magn.*, vol. 49, no. 3, pp. 1178–1184, Mar. 2013.
- [12] F. Marignetti, V. D. Colli, and Y. Coia, "Design of axial flux PM synchronous machines through 3-D coupled electromagnetic thermal and fluid-dynamical finite-element analysis," *IEEE Trans. Ind. Electron.*, vol. 55, no. 10, pp. 3591–3601, Oct. 2008.
- [13] Y.-K. R. Chin, E. Nordlund, and A. Staton, "Thermal analysis-lumped-circuit model and finite element analysis," in *Proc. 6th Int. Power Eng. Conf.*, 2003, pp. 952–957.
- [14] B. Zhang, R. Qu, W. Xu, J. Wang, and Y. Chen, "Thermal model of totally enclosed water-cooled permanent magnet synchronous machines for electric vehicle applications," in *Proc. Int. Conf. Electr. Mach. (ICEM)*, Sep. 2014, pp. 2205–2211.
- [15] T. Øyvang, J. K. Noland, G. J. Hegglid, and B. Lie, "Online model-based thermal prediction for flexible control of an air-cooled hydrogenerator," *IEEE Trans. Ind. Electron.*, vol. 66, no. 8, pp. 6311–6320, Aug. 2018.
- [16] M. Pandey, "Model fitting and state estimation for thermal model of synchronous generator," M.S. thesis, Dept. Technol., Natural Sci. Marine Sci., Univ. South-Eastern Norway, Notodden, Norway, 2019.
- [17] K. Aleikish, "Hybrid machine learning and mechanistic thermal model of synchronous generator," M.S. thesis, Dept. Sci. Elect. Power Eng., Univ. South-Eastern Norway, Notodden, Norway, 2020.
- [18] T. Øyvang, "Enhanced power capability of generator units for increased operational security," Ph.D. dissertation, Univ. South-Eastern Norway, 2018.
- [19] H. Ge, K. Xu, and Z. Ghahramani, "Turing: A language for flexible probabilistic inference," in *Proc. Int. Conf. Artif. Intell. Statist. (AISTATS)*, Playa Blanca, Spain, Apr. 2018, pp. 1682–1690. [Online]. Available: <http://proceedings.mlr.press/v84/ge18b.html>
- [20] C. Rackauckas and Q. Nie, "DifferentialEquations.jl—A performant and feature-rich ecosystem for solving differential equations in Julia," *J. Open Res. Softw.*, vol. 5, no. 1, p. 15, May 2017.
- [21] Wikipedia. (2020). *Inverse-Gamma Distribution*. Accessed: Oct. 10, 2021. [Online]. Available: [https://en.wikipedia.org/wiki/Inverse-gamma\\_distribution/](https://en.wikipedia.org/wiki/Inverse-gamma_distribution/)
- [22] Stack Exchange. (2020). *Naive SE vs Time Series SE: Which Statistics Should I Report After Bayesian Estimation?* Accessed: Oct. 10, 2021. [Online]. Available: <https://stats.stackexchange.com/questions/74450/naive-se-vs-time-series-se-which-statistics-should-i-report-after-bayesian-esti>
- [23] Wikipedia. (2020). *Effective Sample Size*. Accessed: Oct. 10, 2021. [Online]. Available: [https://en.wikipedia.org/wiki/Effective\\_sample\\_size](https://en.wikipedia.org/wiki/Effective_sample_size)
- [24] K. Xu, "Probabilistic programming in Julia new inference algorithms," M.S. thesis, Univ. Cambridge, Cambridge, U.K., 2016.
- [25] N. R. Kristensen, H. Madsen, and S. B. Jørgensen, "Parameter estimation in stochastic grey-box models," *Automatica*, vol. 40, no. 2, pp. 225–237, Feb. 2004.
- [26] O. M. Brastein, A. Ghaderi, C. F. Pfeiffer, and N.-O. Skeie, "Analysing uncertainty in parameter estimation and prediction for grey-box building thermal behaviour models," *Energy Buildings*, vol. 224, Oct. 2020, Art. no. 110236.
- [27] A. Raue, C. Kreutz, T. Maiwald, J. Bachmann, M. Schilling, U. Klingmüller, and J. Timmer, "Structural and practical identifiability analysis of partially observed dynamical models by exploiting the profile likelihood," *Bioinformatics*, vol. 25, no. 15, pp. 1923–1929, 2009.



**MADHUSUDHAN PANDEY** received the M.Sc. degree in electrical power engineering from the University of South-Eastern Norway (USN), Norway, in 2019. Since 2019, he has been a Ph.D. Researcher with TMCC, USN, Porsgrunn, Norway. His research interests include modeling, control, and optimization of dynamic systems and integration of dispatchable renewable energy sources with variable renewable energy sources.



**BERNT LIE** (Member, IEEE) received the Ph.D. degree in engineering cybernetics from the Norwegian University of Science and Technology (NTNU), Norway, in 1990. From 1987 to 1991, he was an Assistant and an Associate Professor at NTNU. In 1992, he joined at the University of South-Eastern Norway, where he is currently a Professor in informatics and the Leader of the Telemark Modeling and Control Center. His research interests include control relevant modeling and advanced control, with applications mainly within the process and energy industries.

...

## Appendix E

# Bayesian Inference for Thermal Model of Synchronous Generator Part II : State Estimation

Madhusudhan Pandey (M.P.) and Bernt Lie (B.L.)

Published in: *IEEE Access*

<https://doi.org/10.1109/ACCESS.2022.3209695>

Author Contributions: Conceptualization, B.L. and M.P.; initial studies, all authors; methodology, all authors; software, B.L. and M.P.; validation, B.L. and M.P.; formal analysis, B.L. and M.P.; writing—original draft preparation, M.P.; visualization, B.L. and M.P.; supervision, B.L.

APPLIED RESEARCH

# Bayesian Inference for Thermal Model of Synchronous Generator Part–II: State Estimation

MADHUSUDHAN PANDEY AND BERNT LIE<sup>1</sup>, (Member, IEEE)

Telemark Modeling and Control Center (TMCC), 3901 Porsgrunn, Norway

Corresponding author: Bernt Lie (bernt.lie@usn.no)

**ABSTRACT** This paper is the Part II of the series on parameter and state estimation using the Bayesian inference for a thermal model of a synchronous generator. Part I is about Parameter Estimation. In this paper, state estimation of rotor copper and air-gap temperatures of the synchronous generator are performed using Bayesian inference. Estimators such as Unscented Kalman Filter (UKF), Ensemble Kalman Filter (EnKF), and Particle Filters (PFs) with different sampling algorithms, are compared based on the estimation accuracy and computational time. The inferences are drawn for the posterior distributions of the state, dispersion of particles, error convergence and particle realizations of the state estimator, choice, and the computational effort of the estimators. Results show that UKF has fair estimation accuracy with the fastest computational time as compared to other estimators.

**INDEX TERMS** Bayesian method, EnKF, particle filters, state estimation, synchronous generator, thermal model, UKF.

## I. INTRODUCTION

Because of the growing usage of intermittent power sources, such as solar and wind power, in a shared electrical grid, dispatchable sources such as hydro power should be able to eliminate the unpredictability in load and generation induced by the intermittent sources. As a result, for best active power utilization, hydro generators should be able to run beyond their thermal capability limit. This necessitates the monitoring of the hydro generator’s interior temperatures. In Part I of this paper titled “Bayesian Inference for Thermal Model of Synchronous Generator Part I : Parameter Estimation”, various aspects of parameter estimation and parameter identifiability for the thermal model of the synchronous generator is emphasized. In this paper, for the same thermal model of synchronous generator, various aspects of state estimation using Bayesian inference is emphasized. It is requested to follow Part I for the governing equations, and experimental data of the thermal model of the air-cooled synchronous generator.

Section II outlines materials and methods. Section III provides state estimation using Bayesian inference. In Section IV, particle filters are initialized and implemented. Furthermore,

The associate editor coordinating the review of this manuscript and approving it for publication was Bo Shen<sup>2</sup>.

PFs and Kalman filters are compared in Section V. Section VI provides estimation versus computational time of the estimators. Conclusions are drawn in Section VII.

## II. MATERIALS AND METHODS

### A. SYSTEM DESCRIPTION

Figure 1 shows the Bayesian framework for the inferences about the states of a dynamical system. In the figure,  $x$ ,  $u$ ,  $z$ ,  $\theta$  and  $y$  are the states, inputs, algebraic variables, parameters and outputs, respectively. For the state estimation shown in Fig. 1,  $x$  and  $z$  are estimated when  $u$ ,  $\theta$  and  $y$  are given.  $p(x_1)$  is the prior distribution of the initial conditions of the states,  $p(Y_1 | x_1)$  is the initial likelihood and  $p(x_k | Y_k)$  is the estimated posterior distribution of states by formulating a recursive relation considering measurement available at each instance of measurement data for outputs where  $Y_k = [y_1, y_2, \dots, y_k]$ . In the figure, we see that the Bayesian state estimation allows posterior distribution of the state, dispersion analysis of the state, particles realization needed in the state estimation, relationship between the parameters with the multimodal posterior distribution and the choice of particle or ensemble type filters, inference on particles realization with error convergence and computational effort, and sub-optimality comparison between different estimators.



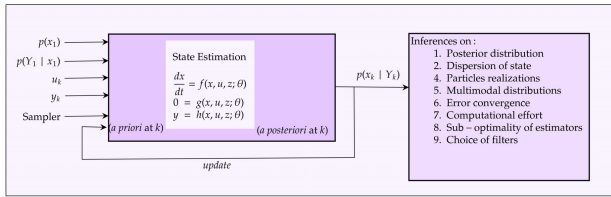


FIGURE 1. Bayesian inference for the state estimation.

## B. MODEL AND EXPERIMENTAL DATA

The mathematical equations governing the generator's metal and air temperatures, measurement data, parameters, and operating conditions are taken from [1] and [2], and also well-presented in Part I. The governing equations contain 3 differential equations representing time evolution for the metal temperatures, and 3 algebraic equations relating the metal temperatures with the air temperatures.

## III. STATE ESTIMATION

### A. RECURSIVE BAYESIAN FILTER

The Bayesian formulation of the parameter estimation problem as in Part I can also be used for state estimation by replacing parameter  $\theta$  with state  $x$ . However, states are quantities that change with time unlike parameters, the state estimation is only done at the point where the time is specified, let's say at time instant  $k$ . This estimate is usually a point estimate though the posterior density distribution of state is also available at each instance of time.

Furthermore, the measurement  $y$  as in the parameter estimation problem (Part I) is replaced with the measurement available  $Y_k = [y_1, y_2, \dots, y_k]$ . The Bayesian formulation at time instant  $k$  conditioned with measurement up to  $Y_k$  is done as

$$p(x_k | Y_k) = \frac{p(y_k | x_k) p(x_k | Y_{k-1})}{p(y_k | Y_{k-1})} \quad (1)$$

where  $p(y_k | x_k)$  and  $p(y_k | Y_{k-1})$  are the likelihood and the evidence known from the information of the measurement noise density.  $p(x_k | Y_{k-1})$  is the prior and calculated as

$$p(x_k | Y_{k-1}) = \int p(x_k | x_{k-1}) p(x_{k-1} | Y_{k-1}) dx_{k-1}. \quad (2)$$

For a state estimation for measurement  $y = [y_1, y_2, \dots, y_k, \dots, y_N]$  with the initial state density function given as

$$p(x_1 | Y_1) = \frac{p(Y_1 | x_1) p(x_1 | Y_0)}{p(Y_1)}, \quad (3)$$

a recursive state estimation problem can be formulated. In practice, the analytical solution for the posterior density function  $p(x_k | Y_k)$  given by Eq. (1) exists for only few special cases. The analytical derivation considering a linear system with additive Gaussian noise leads to the optimal linear *Kalman* filter. Further information about the Kalman filter and its derivatives for state estimation can be found in [3]. However, for a non-linear system and systems where analytical solutions are impossible, we formulate a numerical

solution considering a sample drawn from the known initial states' density function and recursively obtain the numerical solution using Eqs. (1-3) for the posterior distribution.

### B. PARTICLE FILTER

The numerical implementation of the recursive Bayesian filter acquired drawing of random values from a known initial density function for the state ( $p(x_1)$ ). Each random value is considered a *particle*. Using these particles for the numerical approximation of the posterior of the Bayesian estimator is often termed particle filters. It is interesting to note that the estimation accuracy increases as the number of particles increases. Hence, there is always a trade-off between computational speed and estimation accuracy.

The particle filter algorithm taken from [3] is given in Table 1.  $p(x_1)$ ,  $p(w_1)$ , and  $p(v_1)$  are the initial prior densities of the states, process noise, and the measurement noise. For  $i = 1 : N_p$ ,  $x_{k|k-1}^i$  are *a priori* particles obtained by propagating the prior particles through the process equations. Similarly,  $y_{k|k-1}^i$  are the predicted measurements used for calculating the innovation  $\varepsilon_i$ . The innovation is used for calculating the likelihood  $q_i$ . A simple expression for the likelihood is found considering measurement noise as  $v_k \sim \mathcal{N}(0, \mathcal{V})$  i.e. with zero-mean  $\bar{v} = 0$  and co-variance  $\mathcal{V}$ . After then the likelihood is normalized. The normalized likelihoods are then resampled to obtain the posterior density. There are several particle methods for resampling. The particles drawn from the posterior distribution are called as *a posteriori* estimates and considered as the sub-optimal estimates. The optimality of the estimates increases as the number of particles are increased.

The *a priori* particles are distributed with *uneven weights*. The unevenly weighted particles produce degeneracy which will eventually cause estimation with larger variance. Particle degeneracy is actually a situation where a few particles having lower/higher weights dominate other particles. This gives rise to resampling and is done to make sure all particles have equal weights to minimize the estimation variance. To eradicate the problem of degeneracy, particles with lower weights are replaced with higher weights to evenly distribute particles on the basis of their weights. This process of distribution of particles evenly on the basis of weights is often termed as resampling. The resampling is done based on the resampling quality, computational cost, and easy implementation. The resampled particles are called as *a posteriori* particles from which any statistical moments, like mean and standard deviation, is updated to recursively run the filter.

### C. RESAMPLING

A simple resampling algorithm is taken from [4], given in Table 1, and this algorithm is named as *Ris04* for distinguishing it from other algorithms. In *Ris04* algorithm we first generate a uniformly distributed random number  $r$  as  $r \sim \mathcal{U}(0, 1]$ . Then we find the cumulative sum of the likelihood  $q^+$  in each iteration. If  $q^+$  is greater than equal to the generated random number we then set the *a priori* particles as

TABLE 1. Generalized particle filter.

<p><b>Initialization, <math>k = 1</math> :</b>          Draw <math>N_p</math> particles for states, process and measurement noise from initial probability distribution <math>p(x_1)</math>, <math>p(w_1)</math> and <math>p(v_1)</math>.  <math>x_{i 1}^i \sim p(x_1)</math>, <math>i \in \{1, 2, \dots, N_p\}</math>  <math>w_{i 1}^i \sim p(w_1)</math> <math>i \in \{1, 2, \dots, N_p\}</math>  <math>v_{i 1}^i \sim p(v_1)</math> <math>i \in \{1, 2, \dots, N_p\}</math>          for <math>k = 2, 3, \dots</math></p>
<p><b>Propagation step:</b>          Propagate particles through process model (<i>a priori</i> particles)  <math>x_{k k-1}^i = f(x_{k-1 k-1}^i, u_{k-1}, w_{k-1}^i)</math> <math>i \in \{1, 2, \dots, N_p\}</math></p>
<p><b>Information update:</b>          1. Propagate <i>a priori</i> particles through measurement model (predicted measurement particles)  <math>y_{k k-1}^i = h(x_{k k-1}^i, u_{k-1}, v_{k-1}^i)</math> <math>i \in \{1, 2, \dots, N_p\}</math>          2. Calculate relative likelihood <math>q_i</math> i.e. <math>p(y_k   x_{k k-1})</math> from innovation  <math>\epsilon_i = y_k - y_{k k-1}^i</math>  <math>q_i \sim \frac{1}{(2\pi)^{\frac{m}{2}}  \mathcal{V} ^{\frac{1}{2}}} e^{-\left(\frac{\epsilon_i^T \mathcal{V}^{-1} \epsilon_i}{2}\right)}</math>, <math>m</math> is dimension of the measurement equation and <math>\mathcal{V}</math> is measurement co-variance          3. Normalize <math>q_i</math>  <math>q_i = \frac{q_i}{\sum_{j=1}^{N_p} q_j}</math>          4. Resampling for <i>a posteriori</i> estimate          Pseudo code for a simple ‘‘Ris04’’ resampling:  <b>loop</b> <math>i = 1 : N_p</math>              <math>r \sim \mathcal{U}(0, 1)</math>              <math>q^+ \leftarrow 0</math>              <b>loop</b> <math>j = 1 : N_p</math>                  <math>q^+ \leftarrow q^+ + q_j</math>                  <b>if</b> (<math>q^+ &lt; r</math>)                      <math>x_{k k}^i \leftarrow x_{k k-1}^j</math>                  <b>end</b>              <b>end</b>          5. <i>A posteriori</i> update  <math>\hat{x}_{k k} = \frac{1}{n_p} \sum_{i=1}^{N_p} x_{k k}^i</math></p>

the *a posteriori* particles as shown in Table 2. Ris04 algorithm is not much efficient [3] to distribute particles evenly based on their weights. Several other more efficient resampling algorithms are available. In this paper, we focus on multinomial resampling, stratified resampling, residual resampling, and systematic resampling. These resampling algorithms are taken from [5], [6], and [7].

1) MULTINOMIAL RESAMPLING

For multinomial resampling, we first generate an ordered  $N_p$  uniform random number in  $\mathcal{U}(0, 1]$  and use it to select the *a priori* particles with higher weights based on the index of ordered random numbers. The multinomial resampling algorithm is similar to Ris04 resampling, however, the selection of particles are based on the ordered sequence of random numbers. The multinomial resampling algorithm is given in Table 2 1). In the algorithm,  $q^+$  represents the cumulative summation of the likelihood  $q_i$ , **cumsum** (.) represents the cumulative summation and **sort** (.) represents the sorting

TABLE 2. Different resamplings pseudocodes.

<p>1) Multinomial  <math>q^+ = \text{cumsum}(q_i)</math>  <math>r_i \sim \text{sort}(\mathcal{U}(0, 1]), i \in 1 : N_p</math>  <math>j = 1</math>  <b>loop</b> <math>i = 1 : N_p</math>              <b>while</b> <math>q_j^+ &lt; r_j</math>                  <math>j = j + 1</math>              <b>end</b>              <math>x_{k k}^i \leftarrow x_{k k-1}^j</math>  <b>end</b></p>	<p>2) Residual  <math>q_i^* = \frac{N_p q_i - \lfloor N_p q_i \rfloor}{N_p - \sum_{i=1}^{N_p} \lfloor N_p q_i \rfloor}</math>  <math>q^+ = \text{cumsum}(q_i^*)</math>  <math>r_i \sim \text{sort}(\mathcal{U}(0, 1]), i \in 1 : N_p</math>  <math>j = 1</math>  <b>loop</b> <math>i = 1 : N_p</math>              <b>while</b> <math>q_j^+ &lt; r_j</math>                  <math>j = j + 1</math>              <b>end</b>              <math>x_{k k}^i \leftarrow x_{k k-1}^j</math>  <b>end</b></p>
<p>3) Stratified  <math>q^+ = \text{cumsum}(q_i)</math>  <math>s_i \sim \mathcal{U}\left(\frac{i-1}{N_p}, \frac{i}{N_p}\right]</math>  <math>s_{N_p+1} = 1</math>  <math>i = 1; j = 1</math>  <b>while</b>              <b>if</b> <math>s_i &lt; q_j^+</math>                  <math>x_{k k}^i \leftarrow x_{k k-1}^j</math>                  <math>i = i + 1</math>              <b>else</b>                  <math>j = j + 1</math>              <b>end</b>  <b>end</b></p>	<p>4) Systematic  <math>q^+ = \text{cumsum}(q_i)</math>  <math>r \sim \mathcal{U}\left(0, \frac{1}{N_p}\right]</math>  <math>s_j = r + \frac{j-1}{N_p}, j \in 1 : N_p</math>  <math>s_{N_p+1} = 1</math>  <math>i = 1; j = 1</math>  <b>while</b>              <b>if</b> <math>s_i &lt; q_j^+</math>                  <math>x_{k k}^i \leftarrow x_{k k-1}^j</math>                  <math>i = i + 1</math>              <b>else</b>                  <math>j = j + 1</math>              <b>end</b>  <b>end</b></p>

function for creating an ordered sequence. Both **cumsum** (.) and **sort** (.) are available as a built-in functions in high level programming language for computation.

2) RESIDUAL RESAMPLING

The residual resampling technique works based on modification of normalized likelihoods. The modified likelihood  $q_i^*$  captures the residual from the normalized likelihood  $q_i$  based on the *floor* function of the product of  $N_p$  and  $q_i$ , i.e.,  $\lfloor N_p q_i \rfloor$ . The modified likelihood is then given as

$$q_i^* = \frac{N_p q_i - \lfloor N_p q_i \rfloor}{N_p - \sum_{i=1}^{N_p} \lfloor N_p q_i \rfloor}.$$

The modified likelihood can then be used for resampling through the Ris04 or the multinomial resampling. Pseudo code for residual resampling is given in Table 2 2).

3) STRATIFIED RESAMPLING

The stratified resampling algorithm differs from Ris04 and multinomial resampling in that the procedure for generating the sequence of random numbers is different. The algorithm for the stratified resampling algorithm is given in Table 2 3). For  $i \in 1 : N_p$  we generate the random number as  $s_i \sim \mathcal{U}\left[\frac{i-1}{N_p}, \frac{i}{N_p}\right)$  and each of these generated numbers  $s_i$  are called *strata*. These strata divides the interval  $[0, 1)$  into  $N_p$  disjoint sub-intervals  $\left(0, \frac{1}{N_p}\right] \cup \left(\frac{1}{N_p}, \frac{2}{N_p}\right] \cup \left(\frac{2}{N_p}, \frac{3}{N_p}\right] \cup \dots \cup \left(\frac{N_p-1}{N_p}, 1\right]$  [6].

#### 4) SYSTEMATIC RESAMPLING

Systematic resampling is a modified and computationally more robust algorithm than the stratified resampling algorithm. The random number is generated as  $r \sim \mathbb{U}\left(0, \frac{1}{N_p}\right]$  and the strata are calculated deterministically using the index as

$$s_j = r + \frac{j-1}{N_p}, j \in 1 : N_p.$$

Note that the random number is only generated once in the systematic resampling algorithm. This reduces the computational cost as compared to the other resampling algorithms. Pseudo code for the systematic resampling is given in Table 2 4).

#### D. SAMPLE IMPOVERISHMENT IN PARTICLE FILTER

The *a priori* particles are distributed according to the distribution function  $p(x_k | y_{k-1})$ . These particles are resampled using the posterior density function  $p(y_k | x_k)$ . In practice, if the high particles density region of the state space of the posterior density  $p(y_k | x_k)$  does not overlap with the high-density state-space region of the prior density  $p(x_k | y_{k-1})$  then only a few *a priori* particles with higher weights are selected to become the *a posteriori* particles during resampling. This process in which there is a significant decrement in the volume of the *a priori* particles to become *a posteriori* particles after the resampling is called *sample impoverishment*. If the sample impoverishment persisted with a fewer number of the *a priori* particles becoming the *a posteriori* particles, eventually, all the particles would collapse to the same value. This phenomenon is called *a black hole* in particle filtering. One way of eradicating this phenomenon is using a large number of particles, however, this increases computational cost. Several solutions are provided to deal with sample impoverishment. Roughening, prior editing, regularized particle filter (RPF), Markov chain Monte Carlo resampling, and auxiliary particle filter (APF) are some of the common methods explained in [3]. This paper will mainly focus on roughening, RPF, and APF.

#### 1) ROUGHENING

Roughening or *jittering* is a procedure where random noise is added to the *a posteriori* particles after they are resampled. This increases the volume of the distinct *a posteriori* particles and the problem of sample impoverishment is improved. Roughening creates diversification in resampled particles which are distributed evenly based on their weights. For the *a posteriori* estimates roughening can be done as

$$x_{k|k}^i \leftarrow x_{k|k}^i + w_r^i,$$

where  $w_r$  is random noise drawn from a Gaussian distribution with zero-mean and given as

$$w_r \sim \left(0, K \cdot M \cdot N_p^{-\left(\frac{1}{n_x}\right)}\right),$$

where  $n_x$  is the number of dimensions of the state space.  $K$  is a scalar tuning factor usually set to 0.2 and  $M$  is the vector containing differences between the maximum and the minimum values of the particles before roughening for the given as,

$$M = \max(x_{k|k-1}) - \min(x_{k|k-1}).$$

The roughening procedure will diversify the resampled particles by clustering. Roughening also improves statistical moments that we draw from the *a posteriori* particles.

#### 2) REGULARIZED PARTICLE FILTER (RPF)

The sampling algorithms presented in Table 2 are discrete. However, RPF assumes a probability density function using a continuous distribution. The algorithm for regularized particle filter is taken from [3].

#### 3) AUXILIARY PARTICLE FILTER (APF)

For an auxiliary particle filter (APF) we modify the likelihood obtained in Table 1 by using the following formula,

$$q_i \leftarrow \frac{(\alpha - 1)q_i + \bar{q}}{\alpha} \quad (4)$$

where  $\alpha$  is a tuning parameter for increasing the diversity in the likelihood. A typical value of  $\alpha$  for APF is 1.1 [3]. During resampling, particles that are outliers having a lower likelihood in the region of the state space are replaced with particles having a higher likelihood. The eradication of these lower weight particles will lose the diversity of distribution of the particles. APF addresses this issue by assigning outliers with the higher likelihood and this is done with Eq. (4). APF is used mostly with highly non-linear systems to address the issues of outliers in the estimation of the posterior distribution.

## IV. IMPLEMENTATION OF THE PARTICLE FILTERS

### A. INITIALIZATION

The temperature evolution equations of thermal model of the hydro generator can be written in Differential Algebraic Equations (DAEs) form as

$$\begin{aligned} \frac{dx}{dt} &= f(x, z, u; \theta) \\ 0 &= g(x, z, u; \theta) \\ y &= h(x, z, u; \theta) \end{aligned} \quad (5)$$

where  $x = (T_r, T_s, T_{Fe})$ ,  $z = (T_a^c, T_a^\delta, T_a^h)$ ,  $u = (I_f, I_t, T_w^c)$ ,

$$\theta = (m_r, m_s, m_{Fe}, R_r, R_s, \hat{c}_{p,Cu}, \hat{c}_{p,Fe}, \hat{c}_{p,a}, \dot{m}_a, \mathcal{U}_{Ar2\delta}, \mathcal{U}_{As2Fe}, \mathcal{U}_{AFe2a}, \dot{Q}_{Fe}^\sigma, \dot{Q}_f^\sigma, N_{St}^a, N_{St}^w, N_{St}^\Delta).$$

Out of the three states,  $T_s$  and  $T_{Fe}$  are measured, while it is of interest to estimate the temperature of rotating rotor copper  $T_r$ . Similarly, out of three algebraic variables,  $T_a^c$  and  $T_a^h$  are measured, and it is also of interest to estimate air gap temperature  $T_a^\delta$ .

The initialization of the particle filter is done as in Table 3.



TABLE 3. Initialization of the particle filter.

Quantity	Symbol	Value
Process co-variance	$\mathcal{W}$	diag (4, 4, 4)
Measurement co-variance	$\mathcal{V}$	diag (1, 1)
Initial state co-variance	$\mathcal{X}_1$	$10 \cdot \mathcal{W}$
Prior distribution of states	$p(x_1)$	$\mathcal{N}(\bar{x}_1, \mathcal{X}_1)$
Process disturbance	$w_k$	$\mathcal{N}(\bar{w}, \mathcal{W})$
Measurement noise	$v_k$	$\mathcal{N}(\bar{v}, \mathcal{V})$
Scalar factor for roughening	$K$	0.2
Diversity tuning parameter for APF	$\alpha$	1.1

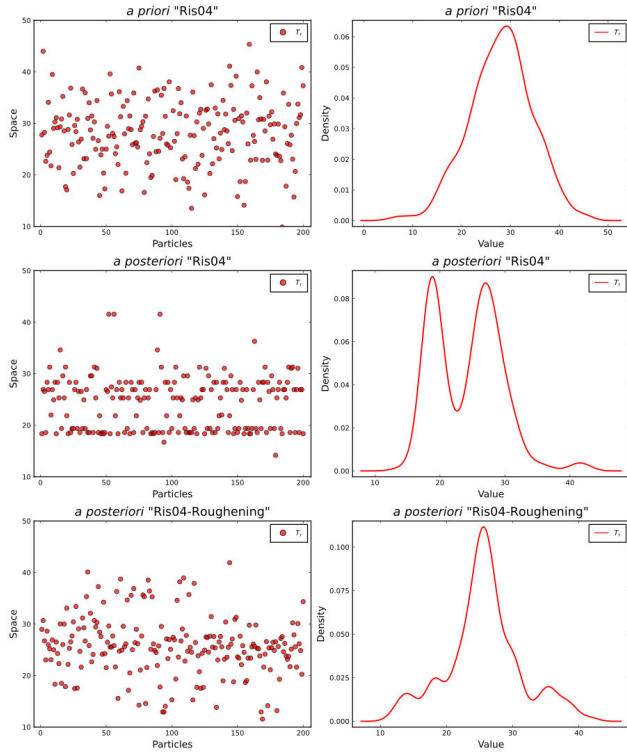


FIGURE 2. A priori and a posteriori particles and density functions for the rotor copper temperature  $T_r$  at measurement sample  $k = 2$  using particle filter with Ris04 resampling.

B. a priori AND a posteriori PARTICLES

Figure 2 shows the a priori and the a posteriori particle spaces and the density function for the rotor copper temperature  $T_r$  at measurement sample  $k = 2$  using particle filter with Ris04 resampling. The total number of particles is 200. In the figure, we see that without roughening, there is no diversity in the a posteriori particles. We see that most of the a priori particles with the lower weights which will become a posteriori particles after the resampling approach the same value as shown in the figure for particle space of the a posteriori “Ris04” without roughening. This gives rise to bi-modal density function for a posteriori particles for  $T_r$  as shown in the respective density function. On the contrary, when roughening is done with tuning parameter  $K = 0.2$ , there is the diversity in the a posteriori particles as shown in the figure for the particle space of the a posteriori “Ris04-Roughening”.

Figure 3 shows the a posteriori particle space for the rotor copper temperature  $T_r$  at measurement sample  $k = 2$  using particle filter with multinomial, residual, and stratified

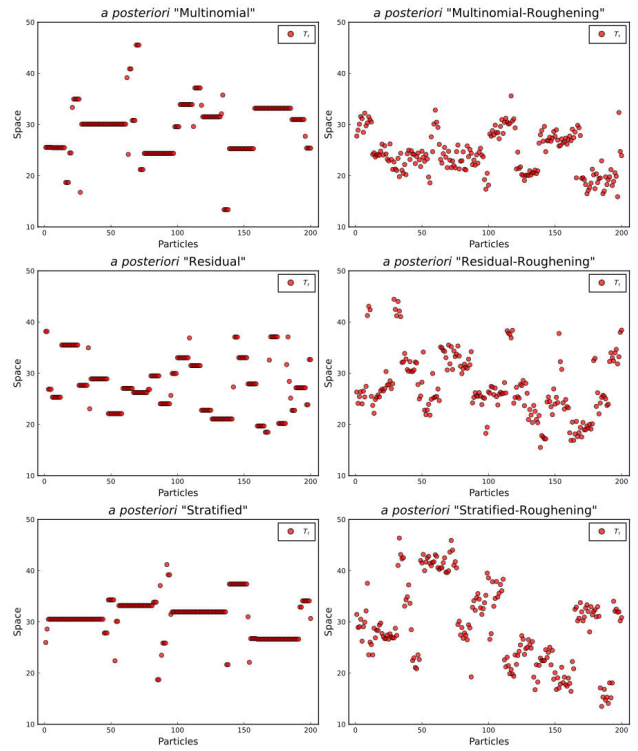


FIGURE 3. A posteriori particles for the rotor copper temperature  $T_r$  at measurement sample  $k = 2$  using particle filter with multinomial, residual and stratified resamplings.

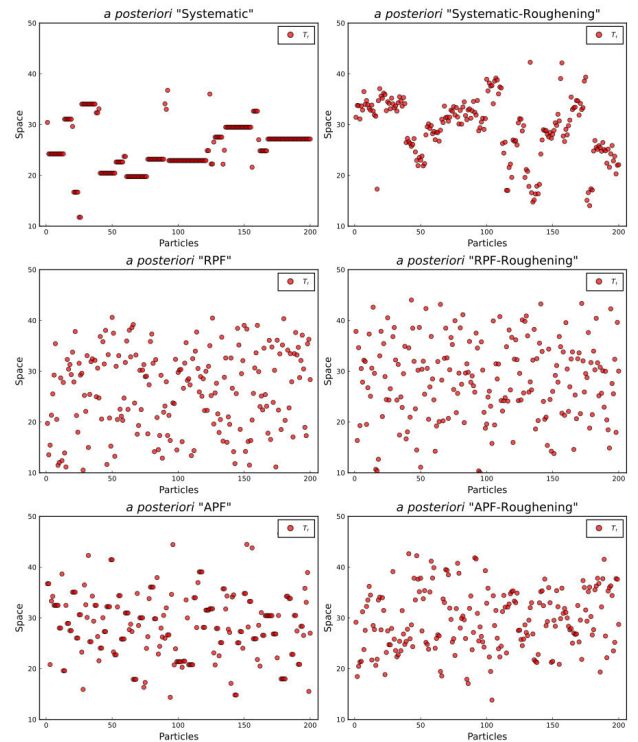
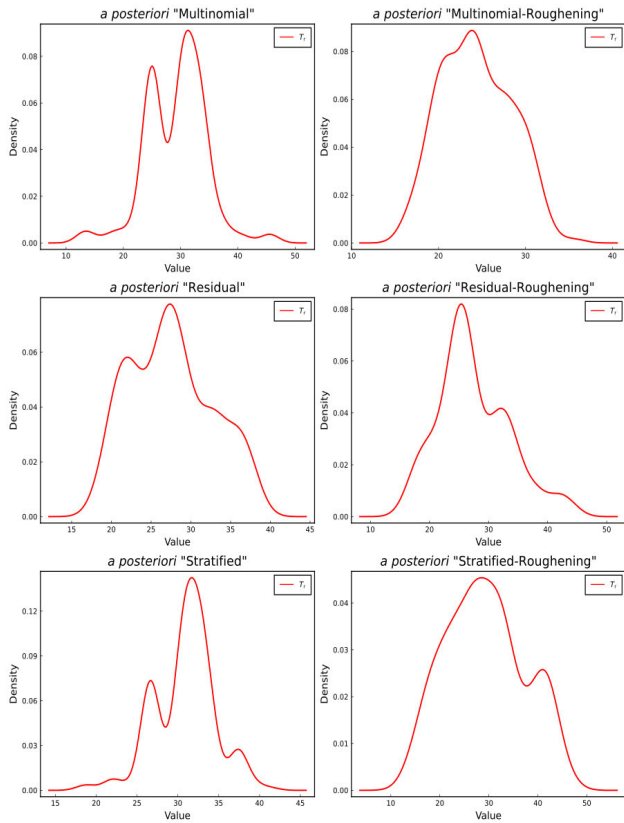


FIGURE 4. A posteriori particles for the rotor copper temperature  $T_r$  at measurement sample  $k = 2$  using particle filter with systematic, RPF and APF resamplings.

resamplings, respectively. Similarly, Fig. 4 shows the a posteriori particle space for the rotor copper temperature  $T_r$  at measurement sample  $k = 2$  using particle filter with systematic,



**FIGURE 5.** *A posteriori* density function for the rotor copper temperature  $T_r$  at measurement sample  $k = 2$  using particle filter with multinomial, residual and stratified resamplings.

RPF, and APF resamplings, respectively. Furthermore, Fig. 5 shows the *a posteriori* density functions for the rotor copper temperature  $T_r$  using particle filter with multinomial, residual, and stratified resamplings.

From Fig. 3 the *a posteriori* particles without roughening for the multinomial resampling, we see that there is the problem of sample impoverishment. The particles with lower weights get clogged into the same value and form a point where lower weights particles are sucked into like in a *black hole*. Each black hole are in fact the modal value of the *a posteriori* distribution. This creates a poor distribution of the *a posteriori* particles. As the poor distribution propagates through the time series, the error in the estimate increases. One of the solutions to solve the sample impoverishment would be to increase the number of particles. However, this process is computationally demanding. Another solution is to roughen the *a posteriori* particles with a scalar tuning parameter  $K = 0.2$ . This causes the lower weights *a posteriori* particles to cluster around the modal values preserving the volumes of particles of the *a posteriori* distribution nearly equal to that of the *a priori* and the *likelihood*. Thus, these clustered particles around the modal values diversify the *a posteriori* distribution to become a unimodal distribution as shown in Fig. 5 for the distribution of the *a posteriori* particles with multinomial roughening. Similar sample impoverishment occurs in the case of the residual resampling, stratified resampling, and systematic resampling as shown in figures

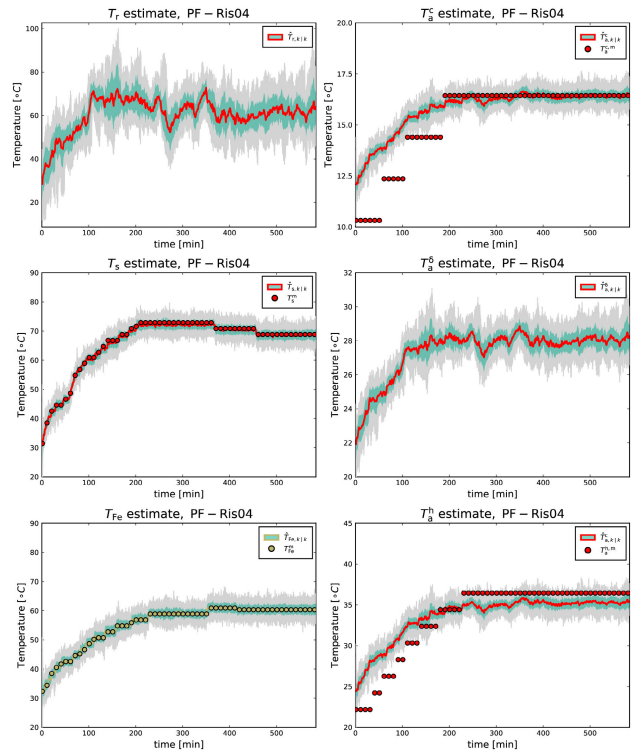


**FIGURE 6.** Metal and air temperatures estimation using particle filter with  $N_p = 200$  and Ris04 resampling.

Figs. 3 and 4. The sample impoverishment also occurs in the case of the Ris04 resampling as shown in Fig. 2. The sample impoverishment is worst in the case of the stratified resampling. By applying roughening to Ris04 and residual resampling, the *a posteriori* particles are equally weighted so that the *a posteriori* distribution is smooth than other resampling methods.

From Fig. 4 in the case of the *a posteriori* particles with RPF and APF resamplings, we see that the *a posteriori* particles are distributed evenly. There is no problem of sample impoverishment *at all* after applying these resampling algorithms. Hence, both RPF and APF are good solutions for removing the problem of sample impoverishment. In the figure, we also see that there is no need for the roughening of the particles.

### C. METAL AND AIR TEMPERATURES ESTIMATION

Figure 6 shows air and metal temperature estimation using particle filter with number of particles  $N_p = 200$  using Ris04 resampling. From the figure,  $\hat{T}_{r,k|k}$  is the estimated rotor copper temperature where the mean (red), standard deviation (dark gray), and the ensemble of the mean (light gray) are plotted together. Fig. 6 also shows the *a posteriori* estimates of the mean, the standard deviation and the ensemble of the mean plotted together for  $T_s, T_{Fe}, T_a^c, T_a^\delta$  and  $T_a^h$ . In the figure,  $T_s^m, T_{Fe}^m, T_a^{c,m}$  and  $T_a^{h,m}$  are the measurements available for the stator copper temperature, the stator iron temperature, the cooled air temperature and the hot air temperature, respectively. These measurements are used for estimating unmeasured  $T_r$  and  $T_a^\delta$ .

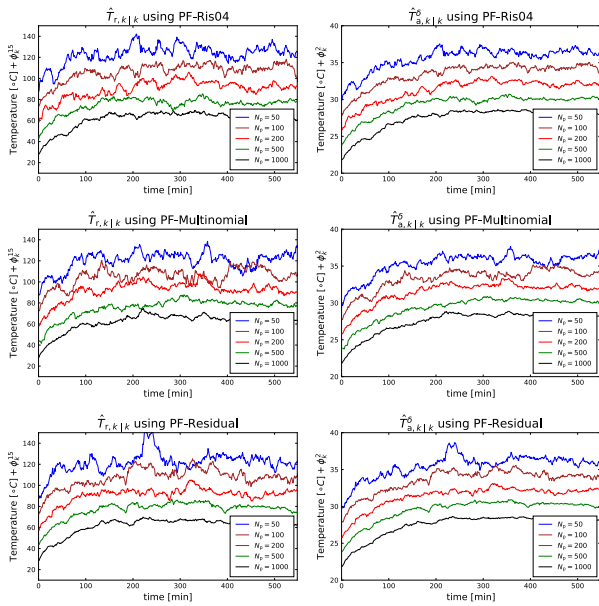


**FIGURE 7. Metal and air temperatures estimation using particle filter with different number of particles for Ris04, multinomial, and residual resampling. In the figure,  $\phi_k^{15} = 15 \cdot k$  where  $k = \{4, 3, 2, 1, 0\}$  is mapped for number of particles  $N_p = \{50, 100, 200, 500, 1000\}$  for rotor copper temperature estimate  $\hat{T}_{r,k|k}$ . Similarly,  $\phi_k^2 = 2 \cdot k$  for  $\hat{T}_{a,k|k}$ .  $\phi_k^{15}$  and  $\phi_k^2$  are introduced for greater visualization of the estimation.**

It is of interest to compare the estimation of unmeasured temperatures  $T_r$  and  $T_a^\delta$  using a different number of particles and different kinds of sampling algorithms. Fig. 7 shows the *a posteriori* estimate for  $T_r$  and  $T_a^\delta$  with different number of particles using the Ris04, multinomial, and residual resampling. For  $\hat{T}_{r,k|k}$  using Ris04 we see that as the number of particles increases from  $N_p = 50$  towards  $N_p = 1000$ , the estimation gets improved. Similar results can be seen from Fig. 7 for both  $\hat{T}_{r,k|k}$  and  $\hat{T}_{a,k|k}^\delta$  using multinomial and residual resamplings. The estimate  $\hat{T}_{a,k|k}^\delta$  is much better than the estimate  $\hat{T}_{r,k|k}$ . This adheres that for the same estimation accuracy the realization of the number of particles  $N_p$  in case of the metal temperatures is more than in the case of the air temperatures. Similar results were obtained in the case of *a posteriori* estimates of  $T_r$  and  $T_a^\delta$  with different number of particles using stratified and systematic resamplings. However, the *a posteriori* estimates are much better with RPF and APF.

**V. PARTICLE FILTER VERSUS KALMAN FILTER**

As described in Section III-A Eqs. (1-3) are solved recursively to obtain the state estimation. The analytical solution for Eq. (1) only exists for a few special cases. For instance, if we consider both the process and measurement dynamics as linear functions, and process and measurement noises as Gaussian distribution, then the analytical solution is the optimal linear Kalman filter. However, the optimal Kalman filter can not be derived from the Bayesian formulation for linear dynamical systems with non-Gaussian noises. Kalman filter can also be derived from the least-squares error method as in original KF [8] and it preserves optimality in the case of both Gaussian and non-Gaussian noises for linear systems.

**A. KALMAN FILTER AND ITS VARIANTS**

There are several variants of the original KF. As the non-linearity increases in any dynamical system, linear KF fails. For a nonlinear system with Gaussian/non-Gaussian noises, state estimation algorithms like Extended Kalman Filter (EKF), UKF [9], and EnKF [10] are employed; UKF and EnKF have several variants based on their performances. However, for a non-linear system with non-Gaussian noises, these variants of the KF can not guarantee a true estimate if the true posterior distribution is multimodal and unsymmetrical around the mean [5]. In reality, the multimodal *a posteriori* distribution can be approximated by summing up weighted Gaussian for each modal distribution as described in [11]. The Gaussian sum can also be applied to other variants of KF, for instance, Gaussian Sum-UKF (GSUKF) [12]. Several variants of the KF are compared in [13] for a case study to estimate the state of charge in lithium-ion cells. From the paper, it was shown that in addition to the selection of filter algorithm for a particular problem, the tuning of the filter also plays an important role in the estimation accuracy. Similarly, in [14] different variants of EnKF are compared and analyzed for determining the synthetic experiments required to determine the difference in RMSE between the variants.

In this paper, we are more focused on implementing and comparing UKF and EnKF with particle filters. We follow the same notations of our previous work on state estimation for the thermal model of the synchronous generator in [2] where UKF and EnKF algorithms are succinctly defined.

**B. ESTIMATION USING UKF AND EnKF**

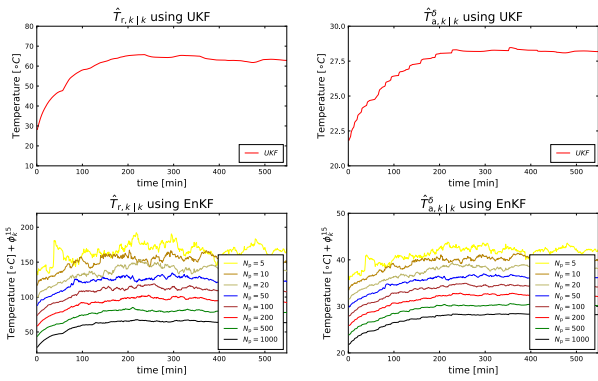
The estimated  $T_r$  and  $T_a^\delta$  using both UKF and EnKF with different number of particles are shown in Fig. 8. In the figure, the estimation of  $T_r$  and  $T_a^\delta$  using EnKF shows that as the number of particles in the ensemble increases the estimation improves. The estimation using UKF and EnKF with  $N_p$  above 200 gives comparable results. Comparing EnKF from Fig. 8 with PFs with different resamplings from Fig. 7, we see that particle filters with  $N_p = 50$  equals EnKF with  $N_p = 5$ . This shows that for a system with process and measurement noises being Gaussian distribution EnKF with a lower number of particles realization can represent particle filters with a higher number of particles realization.

**VI. ESTIMATION ACCURACY AND COMPUTATION TIME**

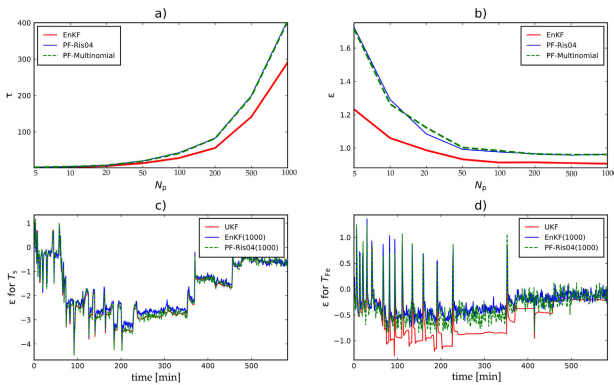
It is of interest to see the estimation accuracy  $\epsilon$  versus the number of particles  $N_p$  for different estimation algorithms. It is also of interest to see the computational effort  $\tau$  for each of the estimation algorithms. The estimators were implemented in the Julia language and the computational effort was calculated using Processor: Intel(R) Core(TM) i7-9750H CPU @ 2.60GHz with Installed RAM: 32 GB. All the state estimators' computational effort is calculated relative to UKF.

Table 4 shows the  $\epsilon$  and  $\tau$  for EnKF and particle filters compared relative to UKF for different numbers of particles.





**FIGURE 8.** Metal and air temperatures estimation using UKF and EnKF with different number of particles. In the figure,  $\phi_k^{15} = 15 \cdot k$  where  $k = \{7, 6, 5, 4, 3, 2, 1, 0\}$  is mapped for number of particles  $N_p = \{5, 10, 20, 50, 100, 200, 500, 1000\}$  for rotor copper temperature estimate  $\hat{T}_{r,k|k}$ . Similarly,  $\phi_k^2 = 2 \cdot k$  for air gap temperature estimate  $\hat{T}_{a,k|k}$ .  $\phi_k^{15}$  and  $\phi_k^2$  are introduced for greater visualization of the estimation.



**FIGURE 9.** a) Computational time  $\tau$  versus particle size  $N_p$  and b) RMSE of innovation  $\epsilon$  versus  $N_p$  for EnKF, PF-Ris04 and PF-Multinomial. c) Estimated errors for the stator copper temperature  $T_s$  and d) estimated errors for the stator iron temperature  $T_{fe}$ .

It shows that as the number of particles increases the RMSE of innovation residuals  $\epsilon$  decreases. However, the computational time  $\tau$  increases. From Table 4 for EnKF we see that as  $N_p$  increases,  $\epsilon$  converged to  $0.9^\circ\text{C}$ . Similar, results can be seen for PF-Ris04, PF-Multinomial, PF-Residual, PF-stratified, and PF-systematic with different  $N_p$ . Furthermore, from Table 4 for EnKF the computational time  $\tau$  for  $N_p = 1000$  is 290 times the computational time for UKF whereas to obtain the similar estimation error with  $N_p = 1000$  for PF-Ris04, PF-Multinomial, PF-Residual, PF-stratified, and PF-systematic the computational time for these filters are 400 times that of computational time for UKF. However, from Table 4, we see that both PF-RPF and PF-APF suffers from estimation accuracy and computational time.

Figure 9 a) shows computational time  $\tau$  versus particle size  $N_p$  for EnKF and particle filters (Ris04 and Multinomial). As the number of particle size increases, there is exponential growth in computational time. With the same particle size, EnKF performs better than particle filters. Figure 9 b) shows innovation errors  $\epsilon$  versus particle size  $N_p$  for EnKF and

**TABLE 4.** Estimation algorithms, estimation accuracy  $\epsilon$  and computational effort  $\tau$ . PF-Stratified, PF-Systematic, PF-RPF and PF-APF are compared relative to UKF.

Filters	RMSE of $\epsilon$	$\tau$ for $\Delta t = 1$ min
UKF	1	1
EnKF ( $N_p = 5$ )	1.23	1.95
EnKF ( $N_p = 20$ )	0.98	5.91
EnKF ( $N_p = 50$ )	0.93	13.68
EnKF ( $N_p = 200$ )	0.91	55.68
EnKF ( $N_p = 500$ )	0.90	141.37
EnKF ( $N_p = 1000$ )	0.90	290.88
PF-Ris04 ( $N_p = 5$ )	1.72	2.47
PF-Ris04 ( $N_p = 20$ )	1.08	7.85
PF-Ris04 ( $N_p = 50$ )	0.99	19.86
PF-Ris04 ( $N_p = 200$ )	0.96	82.34
PF-Ris04 ( $N_p = 500$ )	0.95	199.71
PF-Ris04 ( $N_p = 1000$ )	0.96	407.46
PF-Multinomial ( $N_p = 5$ )	1.71	2.50
PF-Multinomial ( $N_p = 20$ )	1.12	7.86
PF-Multinomial ( $N_p = 50$ )	1.00	19.21
PF-Multinomial ( $N_p = 200$ )	0.96	82.00
PF-Multinomial ( $N_p = 500$ )	0.96	197.48
PF-Multinomial ( $N_p = 1000$ )	0.96	403.90
PF-Residual ( $N_p = 5$ )	1.68	2.50
PF-Residual ( $N_p = 20$ )	2.066	7.88
PF-Residual ( $N_p = 50$ )	1.07	19.04
PF-Residual ( $N_p = 200$ )	1.04	82.09
PF-Residual ( $N_p = 500$ )	1.02	197.23
PF-Residual ( $N_p = 1000$ )	1.02	402.40
PF-Stratified ( $N_p = 5$ )	1.71	2.49
PF-Stratified ( $N_p = 20$ )	1.11	7.85
PF-Stratified ( $N_p = 50$ )	0.99	18.85
PF-Stratified ( $N_p = 200$ )	0.960	78.86
PF-Stratified ( $N_p = 500$ )	0.952	199.07
PF-Stratified ( $N_p = 1000$ )	0.96	413.06
PF-Systematic ( $N_p = 5$ )	1.67	2.49
PF-Systematic ( $N_p = 20$ )	1.08	7.85
PF-Systematic ( $N_p = 50$ )	0.99	18.85
PF-Systematic ( $N_p = 200$ )	0.963	78.86
PF-Systematic ( $N_p = 500$ )	0.960	199.07
PF-Systematic ( $N_p = 1000$ )	0.960	413.06
PF-RPF ( $N_p = 5$ )	38.09	3.19
PF-RPF ( $N_p = 20$ )	1.76	20.20
PF-RPF ( $N_p = 50$ )	1.55	80.44
PF-RPF ( $N_p = 200$ )	1.45	1022.6
PF-RPF ( $N_p = 500$ )	1.42	6599.65
PF-RPF ( $N_p = 1000$ )	1.43	27234.2
PF-APF ( $N_p = 5$ )	11.36	2.50
PF-APF ( $N_p = 20$ )	4.14	7.87
PF-APF ( $N_p = 50$ )	1.96	20.32
PF-APF ( $N_p = 200$ )	1.56	82.06
PF-APF ( $N_p = 1000$ )	1.44	409.80
PF-APF ( $N_p = 500$ )	1.48	200.93

particle filters (Ris04 and Multinomial). Figure 9 b) also shows that as the number of particle size increases there is an exponential decrease in the errors. With the same particle size, EnKF performs better than other particle filters.

Figure 9 c) shows the estimated time series of the innovation error  $\epsilon$  for the stator copper temperature  $T_s$  by using different estimation filters. In the figure, we see that EnKF  $N_p = 1000$  has smaller estimated errors than UKF and PF-Ris04 with  $N_p = 1000$ . Both UKF and PF-Ris04 with  $N_p = 1000$  shows *equivalent* estimation. Regardless of the computational time, EnKF estimation is better than UKF and PF-Ris04 estimations. The average estimated error difference of EnKF with other filters is about  $-0.2^\circ\text{C}$ .

Similarly, Fig. 9 c) shows the estimated time series of the innovation error  $\epsilon$  for the stator iron temperature  $T_{Fe}$  by using different estimation filters. In the figure, we see that EnKF performs better than PF-Ris04 and UKF. The performance of UKF is worst among EnKF and PF-Ris04. The average estimated error difference of UKF with other filters is about  $+0.25^\circ\text{C}$ . Estimation from UKF improves for  $t \geq [350]s$ .

## VII. CONCLUSION

From Section IV-B, results indicate that all the particle filters except PF-RPF and PF-APF suffer from the sample impoverishment. The sample impoverishment in the sampling algorithms of PFs can be ordered from worst to good as stratified, systematic, multinomial, Ris04, and residual resamplings, respectively. We *could not* draw conclusions about PF-RPF and PF-APF because both methods suffer from poor estimation accuracy. The issues with PF-RPF and PF-APF will be addressed as future work.

From Section IV-C, results from the PF estimation of the metal and the air temperatures of the generator indicate that the particles realization for the metal temperatures is higher than that of the air temperatures to obtain a similar estimation accuracy. From Section V-B we conclude that regardless of the computational time, UKF estimation is compared with EnKF with the number of particles  $N_p = 200$ . Furthermore, we also conclude that PFs with  $N_p = 50$  gives comparable estimation accuracy with EnKF with  $N_p = 5$ . This shows that if the posterior distribution of the parameters of the non-linear system is Gaussian distribution EnKF is the sub-optimal filter. This directs us to select PFs in the case of the system's parameters whose posterior distributions are multimodal.

From Tables 4 we compare the estimation accuracy  $\epsilon$  and the computational time  $\tau$  with the number of realization of the particles  $N_p$  for different PFs and EnKF. The comparison is relative to UKF. Regardless of the computational time for the estimators EnKF with  $N_p \geq 100$  converged to estimation error  $\approx 0.9$  times the estimation error of UKF. At  $N_p = 100$  the computational time for EnKF is about  $\approx 30$  times that of UKF. For the realization of particles  $N_p \geq 100$  all the estimators' estimation accuracy converged to a single value representing a sub-optimal solution achieved by the Bayesian inference. This shows that the UKF and EnKF are better estimators than PFs for the air-cooled hydro generator system. From Section VI we conclude that keeping the same estimation accuracy of the filters the performance of UKF is worst than EnKF and PFs in the case of the estimation of the stator iron temperature. As a final concluding remark, we choose UKF based on the *fair* estimation accuracy and the *fastest* computational time with temperature estimation under standard deviation of  $\sigma \approx 0.2^\circ\text{C}$ .

## REFERENCES

[1] T. Øyvang, J. K. Nøland, G. J. Hegglid, and B. Lie, "Online model-based thermal prediction for flexible control of an air-cooled hydrogenerator," *IEEE Trans. Ind. Electron.*, vol. 66, no. 8, pp. 6311–6320, Aug. 2019.

[2] M. Pandey, "Model fitting and state estimation for thermal model of synchronous generator," M.S. thesis, Univ. South-Eastern Norway, Notodden, Norway, 2019.

[3] D. Simon, *Optimal State Estimation: Kalman, H Infinity, and Nonlinear Approaches*. Hoboken, NJ, USA: Wiley, 2006.

[4] N. Gordon, "Beyond the Kalman filter: Particle filters for tracking applications," in *Proc. 7th Int. Conf. Inf. Fusion*, 2004, pp. 1–15.

[5] F. Gustafsson, "Particle filter theory and practice with positioning applications," *IEEE Aerosp. Electron. Syst. Mag.*, vol. 25, no. 7, pp. 53–82, Jul. 2010.

[6] L. Tiancheng, B. Miodrag, and D. M. Petar, "Resampling methods for particle filtering: Classification, implementation, and strategies," *Signal Process. Mag.*, vol. 32, no. 3, pp. 70–86, May 2015.

[7] J. M. Giron-Sierra, *Digital Signal Processing With MATLAB Examples*, vol. 3. Cham, Switzerland: Springer, 2017.

[8] R. E. Kalman, "A new approach to linear filtering and prediction problems," *J. Basic Eng.*, vol. 82, pp. 35–45, Oct. 1960.

[9] S. J. Julier and J. K. Uhlmann, "New extension of the Kalman filter to non-linear systems," in *Signal Processing, Sensor Fusion, and Target Recognition VI*, vol. 3068. Bellingham, WA, USA: SPIE, 1997, pp. 182–193.

[10] G. Evensen, "The ensemble Kalman filter: Theoretical formulation and practical implementation," *Ocean Dyn.*, vol. 53, no. 4, pp. 343–367, Nov. 2003.

[11] D. L. Alspach and H. W. Sorenson, "Nonlinear Bayesian estimation using Gaussian sum approximations," *IEEE Trans. Autom. Control*, vol. AC-17, no. 4, pp. 439–448, Aug. 1972.

[12] K. K. Kottakki, M. Bhushan, and S. Bhartiya, "An improved Gaussian sum unscented Kalman filter," *IFAC Proc. Volumes*, vol. 47, no. 1, pp. 355–362, 2014.

[13] C. Campestrini, T. Heil, S. Kosch, and A. Jossen, "A comparative study and review of different Kalman filters by applying an enhanced validation method," *J. Energy Storage*, vol. 8, pp. 142–159, Nov. 2016.

[14] J. Keller, H.-J. H. Franssen, and G. Marquart, "Comparing seven variants of the ensemble Kalman filter: How many synthetic experiments are needed?" *Water Resour. Res.*, vol. 54, no. 9, pp. 6299–6318, Sep. 2018.



**MADHUSUDHAN PANDEY** received the M.Sc. degree in electrical power engineering from the University of South-Eastern Norway (USN), Norway, in 2019. Since 2019, he has been a Ph.D. Researcher with TMCC, USN, Porsgrunn, Norway. His research interests include modeling, control, optimization of dynamic systems, and integration of dispatchable renewable energy sources with variable renewable energy sources.



**BERNT LIE** (Member, IEEE) received the Ph.D. degree in engineering cybernetics from the Norwegian University of Science and Technology (NTNU), Norway, in 1990. From 1987 to 1991, he was an Assistant and an Associate Professor at NTNU. In 1992, he joined at the University of South-Eastern Norway, where he is currently a Professor of informatics and a Leader with the Telemark Modeling and Control Center. His research interests include control relevant modeling and advanced control, with applications mainly within the process and energy industries.

...

# Appendix F

## DAEs of different kinds of Surge Tanks and Drat Tubes

### F.1 Simple surge tank

$$\frac{dm}{dt} = \dot{m}_i - \dot{m}_e \quad (\text{F.1})$$

$$\dot{m}_i = \rho \dot{V} \quad (\text{F.2})$$

$$\dot{m}_e = 0 \quad (\text{F.3})$$

$$m = \rho A \ell \quad (\text{F.4})$$

$$\ell = h \left( \frac{H}{L} \right) \quad (\text{F.5})$$

$$\frac{d\mathcal{M}}{dt} = \dot{\mathcal{M}}_i - \dot{\mathcal{M}}_e + F \quad (\text{F.6})$$

$$\dot{\mathcal{M}}_i = \dot{m}_i v \quad (\text{F.7})$$

$$v = \frac{\dot{V}}{A} \quad (\text{F.8})$$

$$\mathcal{M} = mv \quad (\text{F.9})$$

$$F = F_p - F_{g|\dot{V}} - F_f \quad (\text{F.10})$$

$$F_p = (p_m - p_a)A \quad (\text{F.11})$$

$$F_{g|\dot{V}} = mg \frac{H}{L} \quad (\text{F.12})$$

$$F_f = \frac{1}{2} \rho v |v| A_w \frac{f_D}{4} \quad (\text{F.13})$$

$$A_w = \pi D \ell \quad (\text{F.14})$$

where  $f_D$  is the Darcy's friction factor expressed in terms of Reynolds' number as

$$f_D = \begin{cases} \frac{64}{N_{\text{Re}}} & N_{\text{Re}} < 2100 \\ aN_{\text{Re}}^3 + bN_{\text{Re}}^2 + cN_{\text{Re}} + d & 2100 \leq N_{\text{Re}} \leq 2300 \\ \frac{1}{\left(2 \log_{10} \left( \frac{\epsilon}{3.7D} + \frac{5.7}{N_{\text{Re}}^{0.9}} \right)\right)^2} & N_{\text{Re}} > 2300 \end{cases}$$

where Reynolds' number  $N_{\text{Re}}$  is

$$N_{\text{Re}} = \frac{\rho v D}{\mu},$$

$\mu$  is the dynamic viscosity of the fluid,  $\epsilon$  is the pipe roughness height. For the region  $2100 \leq N_{\text{Re}} \leq 2300$ ,  $f_D$  is calculated by using cubic interpolation with coefficients  $a, b, c$ , and  $d$ , differentiable at the boundaries.

## F.2 Sharp orifice type surge tank

$$\frac{dm}{dt} = \dot{m}_i - \dot{m}_e \quad (\text{F.15})$$

$$\dot{m}_i = \rho \dot{V} \quad (\text{F.16})$$

$$\dot{m}_e = 0 \quad (\text{F.17})$$

$$m = \rho A \ell \quad (\text{F.18})$$

$$\ell = h \left( \frac{H}{L} \right) \quad (\text{F.19})$$

$$\frac{d\mathcal{M}}{dt} = \dot{\mathcal{M}}_i - \dot{\mathcal{M}}_e + F \quad (\text{F.20})$$

$$\dot{\mathcal{M}}_i = \dot{m}_i v \quad (\text{F.21})$$

$$v = \frac{\dot{V}}{A} \quad (\text{F.22})$$

$$\mathcal{M} = mv \quad (\text{F.23})$$

$$F = F_p - F_{g|\dot{V}} - F_f \quad (\text{F.24})$$

$$F_p = (p_m - p_a) A \quad (\text{F.25})$$

$$F_{g|\dot{V}} = mg \frac{H}{L} \quad (\text{F.26})$$

$$F_f = \frac{1}{2} \rho v |v| \left( A_w \frac{f_D}{4} + A \phi_{\text{so}} \right) \quad (\text{F.27})$$

$$A_w = \pi D \ell \quad (\text{F.28})$$

where  $\phi_{\text{so}}$  depends on  $N_{\text{Re}}$ , and the diameter of the surge tank and the orifice.

For  $N_{Re} < 2500$  :

$$\phi_{so} = \left[ 2.72 + \left( \frac{D_i}{D_o} \right)^2 \left( \frac{120}{N_{Re}} - 1 \right) \right] \cdot \phi_{so}^0$$

For  $N_{Re} \geq 2500$  :

$$\phi_{so} = \left[ 2.72 + \left( \frac{D_i}{D_o} \right)^2 \cdot \frac{4000}{N_{Re}} \right] \cdot \phi_{so}^0$$

where,

$$\phi_{so}^0 = \left[ 1 - \left( \frac{D_i}{D_o} \right)^2 \right] \left[ \left( \frac{D_i}{D_o} \right)^4 - 1 \right].$$

$f_D$  is calculated as in Section F.1.

### F.3 Throttle valve type surge tank

$$\frac{dm}{dt} = \dot{m}_i - \dot{m}_e \quad (\text{F.29})$$

$$\dot{m}_i = \rho \dot{V} \quad (\text{F.30})$$

$$\dot{m}_e = 0 \quad (\text{F.31})$$

$$\frac{d\mathcal{M}}{dt} = \dot{\mathcal{M}}_i - \dot{\mathcal{M}}_e + F \quad (\text{F.32})$$

$$F = F_p - F_{g|\dot{V}} - F_f \quad (\text{F.33})$$

$$\dot{\mathcal{M}}_i = \dot{m}_i v \quad (\text{F.34})$$

$$\dot{\mathcal{M}}_e = 0 \quad (\text{F.35})$$

$$v = \frac{\dot{V}}{\left( \frac{A+A_t}{2} \right)} \quad (\text{F.36})$$

$$\mathcal{M} = mv \quad (\text{F.37})$$

$$F_{g|\dot{V}} = mg \frac{H}{L} \quad (\text{F.38})$$

where  $m$ ,  $F_p$  and  $F_f$  for the throttle valve surge tank varies depending upon the water level inside the surge tank as above or below the throat.



**F.3.1 For  $\ell \leq L_t$ : When the water level is at the throat or below the throat**

$$m = \rho A_t \ell \quad (\text{F.39})$$

$$F_p = (p_m - p_a) A_t \quad (\text{F.40})$$

$$F_f = \frac{1}{2} \rho v |v| A_w \frac{f_D}{4} \quad (\text{F.41})$$

where  $A_w = \pi D_t \ell$ .

**F.3.2 For  $\ell > L_t$ : When water level inside the surge tank is above the throat**

$$m = \rho (A_t L_t + A (\ell - L_t)) \quad (\text{F.42})$$

$$F_p = (p_m - p_j) A_t + (p_j - p_a) A \quad (\text{F.43})$$

$$p_j = p_a + \rho g (\ell - L_t) \frac{H}{L} \quad (\text{F.44})$$

$$F_f = \frac{1}{2} \rho v |v| \left( A_w \frac{f_D}{4} + A \phi_{tv} \right) \quad (\text{F.45})$$

where where  $A_w = \pi (D_t L_t + D (\ell - L_t))$  and  $\phi_{tv}$  is calculated based on the direction of velocity.

**F.3.2.1 For  $v \geq 0$ ,  $\phi_{tv} = \phi_{se}$**

In this case the flow of water is considered to be from the manifold towards the free water surface of the surge tank. The generalized friction factor  $\phi_{se}$  is calculated considering a *square expansion* type pipe fitting and depends on the Reynolds number [20, p. 245].

For  $N_{Re} < 4000$ :

$$\phi_{se} = 2 \left[ 1 - \left( \frac{D_o}{D_i} \right)^4 \right].$$

For  $N_{Re} \geq 4000$ :

$$\phi_{se} = (1 + 0.8 f_D) \left[ 1 - \left( \frac{D_o}{D_i} \right)^2 \right].$$

**F.3.2.2** For  $v < 0$ ,  $\phi_{tv} = \phi_{sr}$

In this case the flow of water in this case is considered to be from the top of the surge tank to the bottom direction. The friction factor is calculated considering *square reduction* type pipe fitting.

For  $N_{Re} < 2500$  :

$$\phi_{sr} = \left(1.2 + \frac{160}{N_{Re}}\right) \left[ \left(\frac{D_i}{D_o}\right)^4 - 1 \right].$$

For  $N_{Re} \geq 2500$  :

$$\phi_{sr} = (0.6 + 0.48f_D) \left(\frac{D_i}{D_o}\right)^2 \left[ \left(\frac{D_i}{D_o}\right)^2 - 1 \right].$$

## F.4 Conical diffuser

$$\frac{dm}{dt} = 0 \quad (\text{F.46})$$

$$m = \rho V \quad (\text{F.47})$$

$$V = \frac{\pi H}{12} (D_i^2 + D_e^2 + D_i D_e) \quad (\text{F.48})$$

$$\frac{d\mathcal{M}}{dt} = F \quad (\text{F.49})$$

$$\mathcal{M} = mv \quad (\text{F.50})$$

$$v = \frac{\dot{V}}{A} \quad (\text{F.51})$$

$$A = \frac{\pi \left(\frac{D_i + D_e}{2}\right)^2}{4} \quad (\text{F.52})$$

$$F = F_p + F_{g|\dot{V}} - F_f \quad (\text{F.53})$$

$$F_p = (p_i - p_e)A \quad (\text{F.54})$$

$$F_{g|\dot{V}} = mg \cos \theta \quad (\text{F.55})$$

$$F_f = \frac{1}{2} \rho v |v| A_w \left( \frac{f_D}{4} + A \phi_{cd} \right) \quad (\text{F.56})$$

$$A_w = \pi D H \quad (\text{F.57})$$

$$\phi_{cd} \approx 0.23 \left(1 - \frac{D_i}{D_o}\right)^2. \quad (\text{F.58})$$

## F.5 Moody spreading pipes

$$\frac{dm}{dt} = 0 \quad (\text{F.59})$$

$$m = \rho V \quad (\text{F.60})$$

$$V = A_m L_m + 2A_b L_b \quad (\text{F.61})$$

$$\frac{d\mathcal{M}}{dt} = F \quad (\text{F.62})$$

$$\mathcal{M} = mv \quad (\text{F.63})$$

$$v = \frac{\dot{V}}{A_m} \quad (\text{F.64})$$

$$F = F_p + F_{g|\dot{V}} - F_f \quad (\text{F.65})$$

$$F_p = p_i A_i - p_e A_e \cos \frac{\theta}{2} \quad (\text{F.66})$$

$$F_{g|\dot{V}} = m_m g + 2m_b g \cos \frac{\theta}{2} \quad (\text{F.67})$$

$$m_m = \rho A_m L_m \quad (\text{F.68})$$

$$m_b = 2\rho A_b L_b \quad (\text{F.69})$$

$$F_f = F_{f,m} + 2F_{f,b} \cos \frac{\theta}{2} + 2 \cdot \frac{1}{2} \rho v_m |v_m| A \phi_{ms} \quad (\text{F.70})$$

$$v_m = \frac{\dot{V}}{A_i} \quad (\text{F.71})$$

$$F_{f,m} = \frac{1}{2} \rho v_m |v_m| A_{w,m} \frac{f_{D,m}}{4} \quad (\text{F.72})$$

$$F_{f,b} = \frac{1}{2} \rho v_b |v_b| A_{w,b} \frac{f_{D,b}}{4} \quad (\text{F.73})$$

$$v_b = 2 \frac{A_i}{A_o} v_m \quad (\text{F.74})$$

$$A_{w,m} = \pi D L_m \quad (\text{F.75})$$

$$A_{w,b} = \pi D L_b \quad (\text{F.76})$$

$$\phi_{ms} = 1 + \frac{v_b}{v_m} - 2 \frac{v_b}{v_m} \cos \theta - \phi_{ms}^0 \left( \frac{v_b}{v_m} \right)^2 \quad (\text{F.77})$$

where  $\phi_{ms}^0$  is calculated as in Table F.1.

Table F.1:  $\phi_{ms}^0$  for different value of  $\theta$  .

$\theta$	15	30	45	60	90
$\phi_{ms}^0$	0.04	0.16	0.36	0.64	1

**Modelling Tool for Hydropower  
Systems, with Analysis and Design**  
Madhusudhan Pandey

**Doctoral dissertations at the  
University of South-Eastern Norway  
no. 173**

ISBN: 978-82-7206-801-0 (print)  
ISBN: 978-82-7206-802-7 (online)

**usn.no**